





Universitat Autònoma de Barcelona

ADVERTIMENT. L'accés als continguts d'aquesta tesi queda condicionat a l'acceptació de les condicions d'ús establertes per la següent llicència Creative Commons:  http://cat.creativecommons.org/?page_id=184

ADVERTENCIA. El acceso a los contenidos de esta tesis queda condicionado a la aceptación de las condiciones de uso establecidas por la siguiente licencia Creative Commons:  <http://es.creativecommons.org/blog/licencias/>

WARNING. The access to the contents of this doctoral thesis it is limited to the acceptance of the use conditions set by the following Creative Commons license:  <https://creativecommons.org/licenses/?lang=en>



**Universitat Autònoma
de Barcelona**

Departament de Química

Facultat de Ciències

**PHOTOACTIVABLE COORDINATION POLYMER
NANOPARTICLES FOR BIOLOGICAL AND
DEVICE APPLICATIONS**

Junda Zhang

Ph.D. Thesis

Ph.D. in Materials Science

2022

Supervisors:

Dr. Claudio Roscini

Dr. Fernando Novio Vázquez

Tutor:

Dr. Fernando Novio Vázquez

Memòria presentada per aspirar al Grau de Doctor per Junda Zhang.

Junda Zhang

Vist i plau,

Dr. Claudio Roscini (Director)

Dr. Fernando Novio Vázquez (Director)

Dr. Fernando Novio Vázquez (Tutor)

Bellaterra, 5 de Setembre del 2022

ABSTRACT

Coordination polymer nanoparticles (CPNs), as a new growing family of nanoparticles have piqued the interest of researchers because of their intriguing properties. For decades, scientists have been attracted by the versatility and tunability of the infinite combination of metal nodes and organic linkers as precursors of self-assembled materials. Because of such unlimited possibilities that allow achieving novel properties, nanoscale coordination chemistry is regarded as one of the most adaptable methodologies for the preparation of new nanostructured materials. The CPNs properties and characteristics can be fine-tuned thanks to the synthetic flexibility of coordination chemistry making them excellent materials for different applications. Moreover, their chemical versatility allows constructing sophisticated systems combining different organic or metal-organic units that can offer new properties with interesting applications in energy storage, photocatalysis, molecular electronics, sensors, or nanomedicine. Interestingly, the use of light-responsive building blocks allows obtaining photoactive CPNs, which activate remotely their properties under spatial and temporal control.

In this thesis work the attention was focused on the synthesis of photoactive new organic compounds as CPNs precursors, the manufacture of functional nanomaterials and the investigation of potential applications of these nanoparticles, based on their intrinsic properties and their interaction with light. Thus, the research carried out in this PhD thesis work can be classified in three main topics, described in the Chapters 3, 4 and 5:

In Chapter 3, it is described the design and the synthesis of a novel family of photoactive Ru-based CPNs. These were obtained through the polymerization of a photoactive Ru(II) monomer, known to be a prodrug of anticancer drug. The visible light irradiation of the obtained CPNs resulted on the controlled release of an aquated Ru complex, of significantly higher cytotoxicity of the precursor. An extensive *in vitro* study of these CPNs, demonstrated their potential use in photoactivated chemotherapy (**PACT-CPNs**).

In Chapter 4, a new family of CPNs capable to undergo photons upconversion (UC) was designed and synthesized and their potential application in various technological fields was explored. In the first part of this chapter, it is reported the synthesis of two pairs of dyes, acting as sensitizers and emitters, able to produce visible-to-visible and near-infrared-to-visible UC. In the second part, the synthesis of the upconverting CPNs (**UC-CPNs**), hosting both sensitizer and emitter molecules as constitutive building blocks, was optimized. Apart from the analysis of their physicochemical and photophysical properties, the CPNs were integrated into a

polymeric matrix to obtain UC water-borne inks and transparent films where UC is preserved in air atmosphere.

Finally, in Chapter 5, CPNs made by carboxylic acid-terminated diphenylanthracene were obtained and coated with gold nanostructures. These CPNs are synthesized to *i*) trap and store high amount per particle of molecular oxygen upon irradiation of the anthracene, through the formation of the corresponding endoperoxide, *ii*) release the singlet oxygen ($^1\text{O}_2$) at will, upon thermal or photothermal heating. The sudden thermal or photothermal release of $^1\text{O}_2$ has potential application for photodynamic therapy (**PDT-CPNs**).

The results reported in this Thesis have been partially described in the following publications:

Chapter 3:

- (1) **Photoactivable ruthenium-based coordination polymer nanoparticles for light-induced chemotherapy.** Junda Zhang, Vadde Ramu, Xue-Quan Zhou, Carolina Frias, Daniel Ruiz-Molina, Sylvestre Bonnet, Claudio Roscini, Fernando Novio. *Nanomaterials* **2021**, 11(11), 3089. doi: 10.3390/nano11113089

Table of contents

Table of content

Chapter 1.....	0
<i>General Introduction</i>	0
1.1 Macro-to-nano materials & coordination chemistry	1
1.2 Metal–organic frameworks (MOFs) and coordination nanoparticle polymers (CPNs)	3
1.3 Synthetic routes	5
1.3.1 Conventional methods	5
<i>Nanoscale precipitation</i>	5
<i>Solvothermal synthesis</i>	6
<i>Reverse microemulsion method</i>	7
<i>Surfactant molecules assistance</i>	7
1.4 CPNs for biological and technological applications	8
1.4.1 CPNs for biological applications	8
1.4.1.1 Drug encapsulation and release approaches	10
<i>pH-sensitive CPNs</i>	12
<i>Photosensitizers-based CPNs</i>	12
<i>Redox-activated CPNs</i>	13
1.4.2 Technological applications of CPNs	13
1.4.2.1 Light-harvesting materials of CPNs	13
1.4.2.2 White-light-emitting materials of CPNs	15
1.4.2.3 Catalytic materials of CPNs	15
1.5 Scope of the Thesis	16
1.6 Reference	17
Chapter 2.....	23
<i>Objectives</i>	23
Chapter 3.....	25

<i>Photoactivable Ruthenium-Based Coordination Polymer Nanoparticles for Light-Induced Chemotherapy</i>	25
3.1 Introduction	26
3.1.1 Ruthenium anticancer drugs	27
3.1.2 Photo-activatable Ru complexes for photodynamic therapy and photoactivated chemotherapy	28
<i>3.1.2.1 Photodynamic therapy</i>	28
<i>3.1.2.2 Photoactivated chemotherapy</i>	29
3.2 Objective	33
3.3 Results and discussion	35
3.3.1 Synthesis and characterization of RuBIX-CPNs and RuBIS-CPNs	35
3.3.2 Photoactivity of RuBIS-CPNs	41
3.2.5 Study of the RuBIS-CPNs in cells	48
3.4 Conclusions	53
3.5 Materials and methods	54
3.6 References	63
Chapter 4	70
<i>Upconverting Coordination Polymer Nanoparticles for Photochemical applications and Photophysical Applications</i>	70
4.1 Introduction	71
4.1.1 Upconverting Rare-earth-doped nanoparticles	71
4.1.2 Upconversion based on triplet-triplet annihilation (TTA-UC)	72
4.1.3 TTA-UC nanomaterials	75
<i>4.1.3.1 Liposomes and micelles based TTA-UC</i>	76
<i>4.1.3.2 Silica based TTA-UC</i>	77
<i>4.1.3.3 Polymer-based based TTA-UC</i>	78
4.1.3.4 Metal-organic coordination based TTA-UC	79
4.1.4 Applications of TTA-UC nanomaterials	81
<i>4.1.4.1 Biological applications</i>	81

4.1.4.2 OLED application	82
4.1.4.3 Energy applications	83
4.1.4.4 Anti-counterfeiting applications	84
4.2 Objective	85
4.3 Results and Discussions	86
4.3.1 Organic synthesis.....	87
4.3.2 Optical measurements of DPA-S-COOH and Pd-S-COOH	91
4.3.3 synthesis of VVUC-CPNs using Zn(OAc) ₂	93
4.3.4 VVUC-CPNs synthesis using ZrOCl ₂	94
4.3.5 Optimization of the UC emission/phosphorescence ratio in the UC-CPNs	95
4.3.6 Optical characterization of Os-S-COOH and CAEBD-S-COOH.....	99
4.3.7 Synthesis of the NVUC-CPNs.....	101
4.3.8 Optimization of the UC emission/phosphorescence ratio in the UC-CPNs	102
4.3.9 Upconversion application exploration.....	103
4.3.9.1 Upconversion-induced photochromic change	103
4.3.9.2 Upconversion-induced photopolymerization	104
4.3.9.3 Air-stable upconverting transparent films	105
4.3.9.4 Air-stable upconverting printed patterns for security inks	108
4.4 Conclusions	109
4.5 Materials and methods	110
4.6 Reference.....	165
Chapter 5.....	171
<i>Coordination polymers nanoparticles for singlet oxygen storage and release</i>	171
5.1 Introduction.....	172
5.1.1 Synthetic strategies for efficient photosensitizer design.....	174
5.1.1.1 Introducing heavy atoms.	174
5.1.1.2 Energy transfer-based strategies.....	174

5.1.1.3 <i>Activatable PSs</i>	175
5.1.2 Nanomaterials for PDT	176
5.1.2.1 Carbon-based nanomaterials for PDT	176
5.1.2.2 <i>Gold-based nanomaterials for PDT</i>	177
5.1.2.3 <i>MOFs-based nanomaterials for PDT</i>	178
5.2 Objectives	179
5.3 Result and discussion	180
5.3.1 DPA-S-COOH singlet oxygen trapping and releasing monitoring by NMR	180
5.3.2 Absorption change of DPA-S-COOH upon light irradiation	181
5.3.3 Photothermal induced fluorescence enhancement in molecular level	182
5.3.4 Photothermal induced fluorescence enhancement investigation in nanoscale level	183
5.4 Future work	184
5.5 Reference	185
Chapter 6	189
<i>General Conclusions</i>	189

Chapter 1

General Introduction

1.1 Macro-to-nano materials & coordination chemistry

Macroscopic constructions can be built to exact specifications using blueprints and schematics. On a microscopic level, techniques nearly identical to those used in macroscopic production can be encountered. Due to modern processes, microfabrication can manufacture finely integrated structures with ultra-high precision at this level. As a result, microscale objects with precise duplicates of their blueprints can be built and implemented in advanced tools and methodologies. However, after reducing the material size to the nanometer scale, perturbations and uncertainties based on thermal fluctuations and mutual component interactions begin to cause new and interesting effects. Thus, due to the reduced size, these materials have been endowed with some new capabilities, and thus have the potential to be exploited in various fields.¹ Normally, nanoscale manufacturing cannot follow a typical default process using for macro or micro components. The preparation of functional nanomaterials has to be done with the synergy of various factors that control the organization of the structure through different processes.

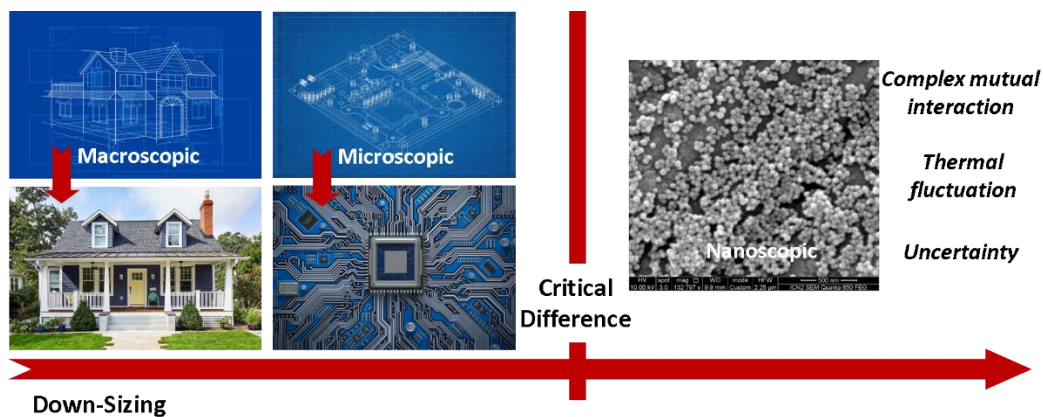


Figure 1.1: nanoscale fabrication is different from those in macroscale and microscale dimensions.

Matter at the nanoscale behaves differently from the common macroscopic world. Effects negligible at the macro- or microscopic level become important at the nanometer scale. The variations of some physical effects have different origin calling into question the validity of well known physical laws, since size and quantum effects play major roles. Typically, nanomaterials are materials with at least one dimension that measures 100 nanometers (nm) or less. Interestingly, the nanomaterials that have the same composition as known materials in bulk form may have different physico-chemical properties. For instance, opaque materials

become transparent (copper); inert materials become catalysts (platinum); stable materials turn combustible (aluminum); insulators become conductors (silicon). There are several processes to generate nanomaterials, classified as ‘top-down’ (bulk materials are broken into nano-sized particle normally using physical methods) and ‘bottom-up’ (nanoparticles are produced by building of atom by an atom, or molecule by molecule, through chemical processes).

Specifically, in the assembly of units at the nanoscale using bottom-up processes a series of phenomena that do not occur in other types of manufacturing processes should be taken into account. As the material size is produced at the nanoscale, the synthetic parameters require specific control to avoid uncontrolled interaction of the different components (building blocks), or the appearance of undesirable side reactions. Thus, the fabrication of functional materials at the nanoscale will be influenced by i) self-assembly of components, ii) atomic and molecular manipulation, iii) reaction conditions (i.e. reagents concentration, pH, type of solvent...) and iv) stability of the final product. In this scenario, some challenges of nanomaterials fabrication are the study of organization processes at the nanoscale for the production of advanced nanomaterials and nanosystems, the development of novel and unexpected properties, and the exploration of the new phenomena based on theoretical approximations.

Within the different materials that can be obtained at the nanoscale, polymers are playing a transcendental role allowing the design and generation of moldable structures with advances properties and functionalities in comparison with other materials. Specifically, coordination chemistry, where metal-to-ligand bonds become relevant, offers a powerful tool for the obtaining of polymeric materials (coordination polymers) with enormous potential applications in nanomaterials science. Thus coordination chemistry can be considered the basis of the bottom up synthesis of coordination polymers (**CPs**). The nanostructuring of the resulting polymers represent an interesting class of versatile materials comprised of metal nodes and functional or structural organic linkers, and represents a novel opportunity to develop a unique class of highly tailorable functional materials that combine the rich diversity of **CPs** with the advantages of nanomaterials. Apart from the interest in this coordination polymer nanoparticles (**CPNs**) for applications, such as catalysis, energy storage, or environmental remediation, there is an increasing interest in the development of biocompatible nanomaterials with applications in biomedicine based on the benefit from the characteristics of both inorganic and organic building blocks. Therefore, exploring new strategies to obtain novel **CPNs** with specific technological or biomedical applications, is needed.

One of the most interesting properties of these materials is their chemical versatility and flexibility, which allows the rational design of novel functional materials. The control over the reaction conditions and the rational selection of its components allows for the elaboration of a wide range of functional nanostructures. Metal-to-ligand bonds exhibit precise directional interactions, which may modulate the dimensionality of the resulting system and control the resulting extended structure. Extensive research is being focused on the design of new organic ligands for the formation of novel **CPs** with advanced properties.² Organic ligands can be designed and modified to allow the accurate adjustment of an specific structure or conformation and, depending on the combination organic ligands-metal node, the dimensionality of the final structure (1D-3D). Apart from the metal ion coordination, different non-covalent intermolecular interactions such as hydrogen bonding, π - π stacking and van der Waals forces, might take on relevance during the polymer assembly. These interactions are decisive for the final structure arrangement of the **CPs** in a specific coordination network.

1.2 Metal–organic frameworks (MOFs) and coordination nanoparticle polymers (CPNs)

High molecular weight compounds known as polymers are generated by the assembly of monomeric units together with covalent connections. Contrarily, coordination polymers are infinite systems constructed using metal ions and organic ligands as the primary fundamental units connected basically by coordination bonds and other types of connections such as supramolecular interactions. The coordination polymers can be defined as a compound with repeating coordination entities extending in one, two or three dimensions. Depending on their level of structuration (structural regularity/ crystallinity), two types of nanostructured coordination polymers can be considered: crystalline metal-organic frameworks (**MOFs**) and amorphous coordination polymer nanoparticles (**CPNs**). The **MOFs** contains potential voids and offer different dimensionalities and morphologies depending on the synthetic route and the nature of the intrinsic components. Because of crystals with extremely high porosity (from 1000 up to 10,000 m²/g)³ and good thermal and chemical, **MOFs** can be chemically functionalized to be used for a variety of purposes, including gas adsorption and separation,⁴⁻⁶ catalysis,⁷⁻⁸ luminescence,⁹⁻¹⁰ sensing,¹¹⁻¹² proton conduction,¹³⁻¹⁴ etc.

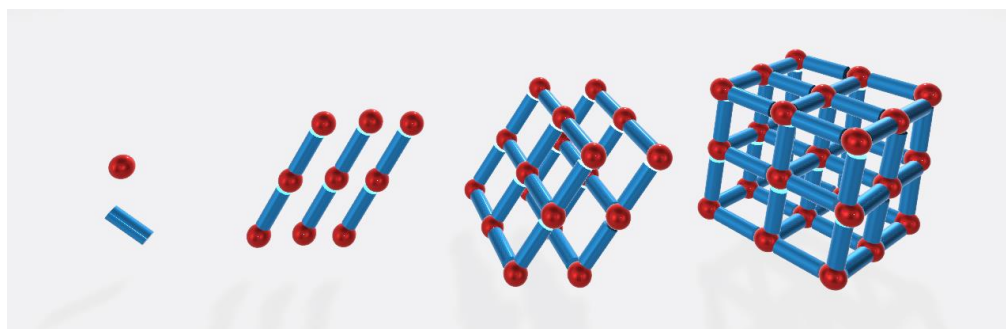


Figure 1.2: Schematic illustration of the different dimensionalities through the coordination between metals and ligands: (a) 1D, (b) 2D and (c) 3D.

Apart from **MOFs**, coordination nanoparticle polymers (**CPNs**), as one of two main branches of coordination polymers, typically adopt a spherical morphology to minimize the interfacial free energy between the particles, and exhibit amorphous structures becoming an option to **MOFs** lately. The first mention of **CPNs** was made in 2005¹⁵⁻¹⁶ and since then, there are a growing number of **CPNs**-related publications. There have been reports of metal-organic nanostructures with fascinating luminescent sensor properties,¹⁷⁻¹⁸ drug storage and release capabilities¹⁹⁻²⁰ and taken part as principal component in optical devices²¹⁻²². Comparing to the typical **MOFs**, **CPNs** exhibit a high extent of structure, size and morphology tunability affected by a variety of reaction conditions such as metal ions, organic ligands, synthetic technique, reaction temperature, solvent system, molar ratio, and pH value.²³⁻²⁸ Various approaches have been used for their synthesis, ranging from the use of sophisticated lab-on-a-chip devices²⁹ (Fig. 2a) or Dip-Pen Nanolithography (DPN)³⁰⁻³¹ (Fig. 2b) to other methods as reverse microemulsions.³² However, the most shared and simple approach is the synthesis of the **CPNs** using out-of-equilibrium one-pot reactions conditions, mainly by a reaction of organic ligands with metal ions in a solvent that promotes a fast precipitation of the resulting polymeric material. The resulting nanoparticles are usually amorphous and less porous than nano**MOFs** (**nMOFs**), with a spherical shape to lessen the interfacial free energy and average dimensions regulated by the addition rate of the ligands and stirring rate.³³ Concerning the area of application, **CPNs** have become relevant in different fields such as gas adsorption and separation processes, catalysis, sensor devices, photoluminescence, energy harvesting and conductivity.

1.3 Synthetic routes

MOFs and CPNs may be created as molecular nanomaterials using a limitless variety of metal and bridging ligands. The techniques utilized to synthesize MOFs and CPNs may be classified into four categories: nanoscale precipitation, solvothermal, surfactant-templated and reverse microemulsion (Figure 1.3). While the last three procedures have the potential to generate both amorphous and crystalline materials, the first approach often produces amorphous materials. In this part, we'll provide examples of these fundamental synthetic techniques.

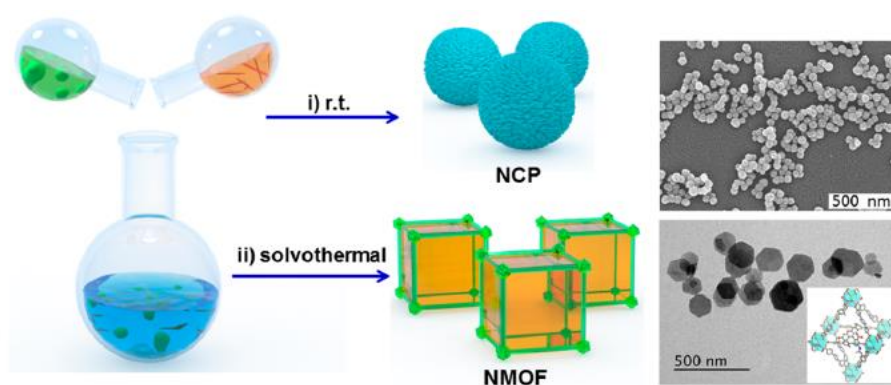


Figure 1.3: Surfactant-free synthesis by simply mixing precursors in appropriate solvents either at room temperature (i)³⁴ or at elevated temperature (ii).³⁵ Room-temperature synthesis typically yields amorphous CPNs, whereas solvothermal synthesis at elevated temperatures can afford both CPNs and crystalline MOFs.

1.3.1 Conventional methods

Nanoscale precipitation

Based on the fact that nanoparticles are insoluble in a particular solvent system while the individual precursors are still soluble, nanoparticles are created. For instance, Catechol-Based Pt(IV) coordination polymer nanoparticles were created using a method that has already been laid forth for comparable catechol-based nanoparticles.³⁶⁻³⁷ A platinum (IV) prodrug was dissolved in ethanol (EtOH), and iron acetate ($\text{Fe}(\text{OAc})_2$) in H_2O was added dropwise. A black solid in suspension was formed immediately with the addition of iron ions.³⁸ Also, Hybrid metal-phenol nanoparticles for imaging was synthesized by dissolving two ligands (1,4-Bis(imidazole-1-ylmethyl)-benzene and 3,4-dihydroxycinnamic acid) and subsequently, treating with an aqueous solution containing the metal salt. A schematic illustration is shown

in Figure 1.4 where is detailed the ligands and metal salts mixing together in an organic solvent for the formation of the CPNs nanosystems.

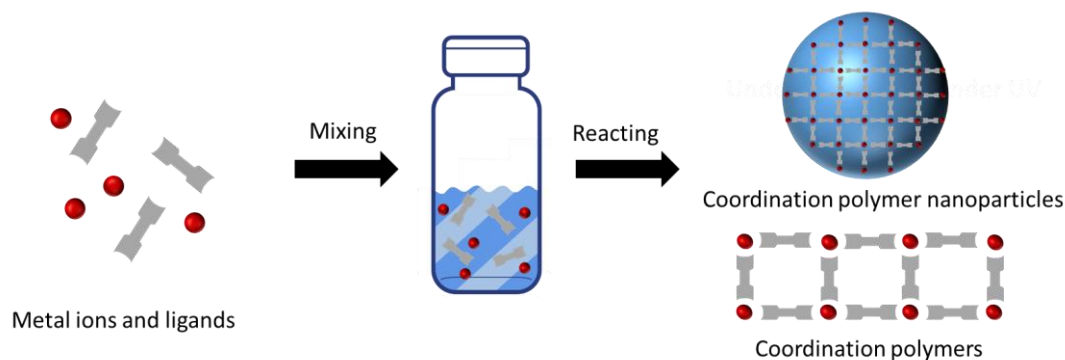


Figure 1.4: Schematic illustration of a one-pot synthesis reaction for the formation of coordination polymers.

Solvothermal synthesis

This method is the most widely used synthetic approach for MOFs synthesis because it enables relatively quick crystal development with high degrees of crystallinity, phase purity, and surface areas without the need for specialized equipment (Figure 1.5). This methodology uses mild conditions for a chemical reaction that takes place in a solvent, normally water, at a temperature higher than the boiling temperature of the solvent in a sealed vessel from several hours to days.^{40, 41, 42-43} Additionally, novel method has been emerging, such as microwave aided solvothermal synthesis which allows high quality metalorganic framework crystals to be synthesized in a short time. The size and shape of the crystals can be highly controlled, and the synthesis cycle can be significantly reduced for many practical applications, despite the fact that the microwave approach typically cannot provide crystals with a size great enough for single X-ray examination.⁴⁴

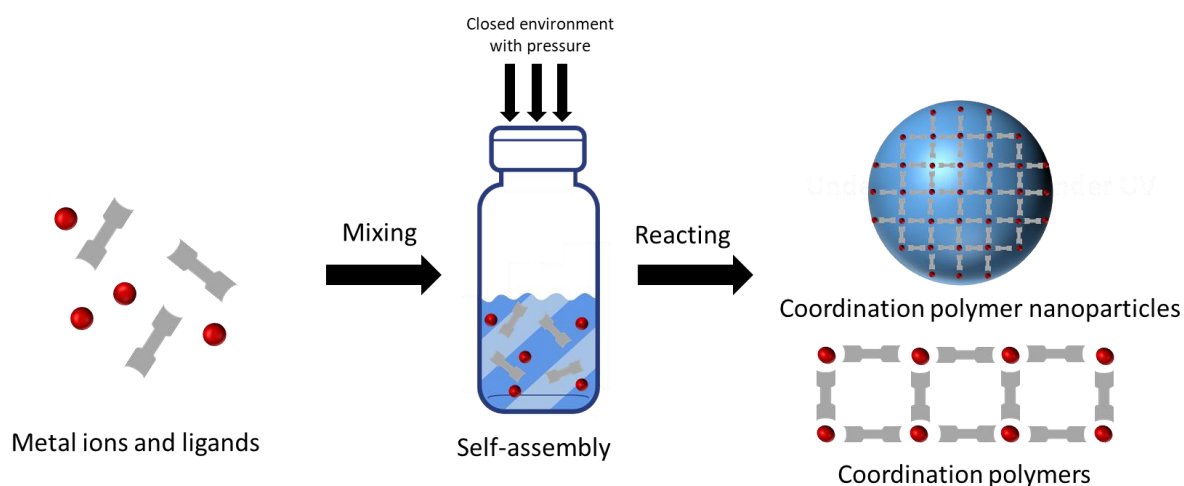


Figure 1.5: Schematic illustration of a hydro-/solvothermal approach for the formation of coordination polymers.

Reverse microemulsion method

Surfactants, co-surfactants, oil and water phases, and surfactants are extensively used to form the reverse micro-emulsion system. In an oil phase, surfactants generate reversed micelles where the hydrophilic moieties of the surfactant monomers encircle the water droplet. Each of these reversed micelles can be used as a tiny reactor. The limit of these micro-reactors causes them to collide and merge, which causes reactants in the droplet to react and generate precipitated products, the size of which may be adjusted.

Very known **MOFs** such as ZIF-8, as porous crystalline material, consisting of tetrahedral clusters of MN_4 linked by simple imidazolate ligands have a lot of potential applications in different areas such as gas sorption, separation, catalysis, and sensing, and it can be synthesized by reversed microemulsion according to the method described in the literature.⁴⁵

Surfactant molecules assistance

In reverse microemulsion conditions or solvothermal circumstances, surfactant molecules, such as polyvinylpyrrolidone (PVP), sodium dodecyl sulfate (SDS), PEG-400 (neutral), octanoic acid and cetyltrimethylammonium bromide (CTAB), can also serve as the template for the synthesis and modify the reaction speed and shape of **nMOFs/CPNs** during the reaction processes, because surfactants not only have low vapor pressure, great thermal and chemical stability, but also possess fascinating features (including neutral, acidic, anionic, basic, cationic, etc).⁴⁶ Mesostructured imidazolate frameworks (MIFs) with a basal spacing of approximately are created when methylimidazole (MeIM) and imidazole (IM) react with $Zn(OAc)_2$ in reverse microemulsion conditions (CTAB/n-heptane/1-hexanol/water). These MIFs are made up of 1D

zinc coordination polymers interspersed with CTAB.⁴⁷ Zhang and co-workers prepared four new three-dimensional (3D) crystalline heterometal-organic frameworks, [M(1,3,5-benzenetricarboxylate)Cu(py)₂] (M = Co, Mn, Ni and Zn) using PEG 400 surfactant thermal method and showing weak antiferromagnetic interactions between the nearest magnetic Co²⁺ ions, Mn²⁺ ions and Ni²⁺ ions revealed by magnetic studies.⁴⁶

1.4 CPNs for biological and technological applications

Coordination polymers, including **nMOFs** and **CPNs**, which are hybrid materials created by multidentate ligands with metal ions nodes, have several advantages, including as high porosity, large surface areas, and a variety of useful functions. Thus coordination polymers have been investigated for different kinds of applications, such as catalysis,⁴⁸ gas storage,^{4, 49} chemical sensing,⁵⁰ and biological applications.⁵⁰⁻⁵² In this introduction, we only summarize some of the most important achievements of **CPNs** in the field of biological applications including encapsulation and release approaches, and device applications.

1.4.1 CPNs for biological applications

Nanotherapy are developing quickly and are being used to overcome a number of problems compared to traditional delivery methods, including low oral bioavailability, lack of targeting, and poor water solubility. Emerging nanoscale targeting techniques have been developed as a result of developments in nanoscience and nanotechnology. Practical usage of a number of therapeutic nanocarriers has been authorized. To enhance their biodistribution and prolong their retention in the bloodstream, nanoparticles have been engineered for the suitable size and surface properties. As a result, nanocarriers are able to deliver loaded active drug to cancer sites by specifically using the distinct pathophysiology of tumors, such as their higher permeability and retention effect. Nanoparticles using for drug delivery can be created from a range of substances, such as lipids (liposomes), polymers (polymeric nanoparticles, micelles, or dendrimers), viruses (viral nanoparticles), and even organometallic compounds (nanotubes; Table 1).⁷⁷⁻⁷⁸

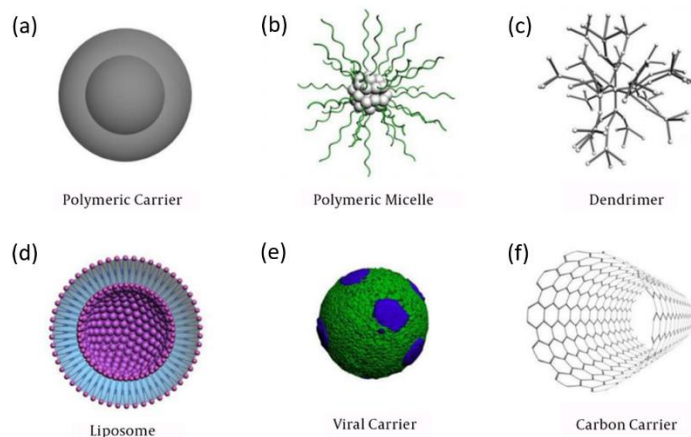


Figure 1.7: Types of nanocarriers for drug delivery. (a) Polymeric nanoparticles: polymeric nanoparticles in which drugs are conjugated to or encapsulated in polymers. (b) Polymeric micelles: amphiphilic block copolymers that form to nanosized core/shell structure in aqueous solution. The hydrophobic core region serves as a reservoir for hydrophobic drugs, whereas hydrophilic shell region stabilizes the hydrophobic core and renders the polymer to be water-soluble. (c) Dendrimers: synthetic polymeric macromolecule of nanometer dimensions, which is composed of multiple highly branched monomers that emerge radially from the central core. (d) Liposomes: self-assembling structures composed of lipid bilayers in which an aqueous volume is entirely enclosed by a membranous lipid bilayer. (e) Viral-based nanoparticles: in general structure are the protein cages, which are multivalent, self-assembles structures. (f) Carbon nanotubes: carbon cylinders composed of benzene rings.⁷⁷

Natural or artificial polymers have been used to create polymeric carriers (Figure 1). Drugs may be connected to or entrapped within polymeric carriers, depending on the techniques employed to prepare them.

Yan and co-workers presented the synthesis of multifunctional coordination-driven nanoparticles via the amphiphilic amino acid (9-fluorenylmethyloxycarbonyl-L-Leucine, Fmoc-L-L)-modulated self-assembly of a magnetic resonance imaging (MRI) contrast agent (Mn^{2+}) and photosensitive drug (chlorin e6, Ce6). The resulting Fmoc-L-L/ Mn^{2+} /Ce6 nanoparticles (FMCPNs) demonstrated a high inherent biocompatibility, considerable drug loading capacity reaching up to 36 wt%, robust stability, and PDT damage by releasing Ce6 following coordination of GSH with Mn(II) decreasing intracellular active GSH level. Additionally, MRI was utilized to confirm the in vivo anticancer effectiveness.⁷⁹

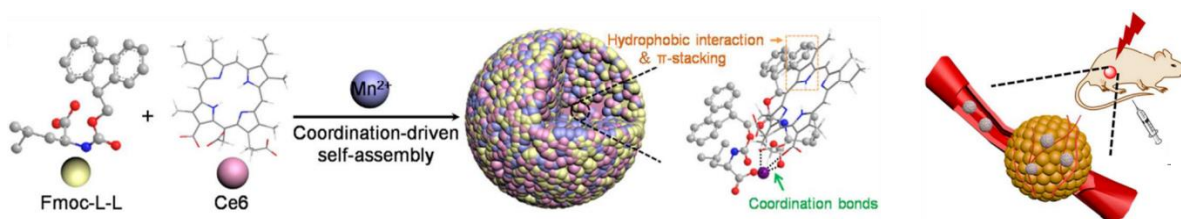


Figure 1.8: Schematic illustration of the fabrication process of FMCPNs via coordination-driven self-assembly and their responsive disassembly for MRI-guided PDT. Image extracted from reference.⁷⁹

Li and co-workers shared a brand-new, all-encompassing method for delivering Pt-based drugs to tumor cells by including them into **CPNs**. Firstly, through the use of poor solvent precipitation, **CPNs** were obtained by using Tb^{3+} and disuccinatocisplatin. Secondly amorphous silica shells of Pt are used to stabilize the Pt-based **CPNs** to effectively delay fast dissolution the Pt species' and control the release process and the thickness of silica shell is tunable by changing the reaction time and amount of reactants. Finally they bonded silyl-derived c(RGDfK), a short cyclic peptide sequence possessing high affinity for **Rv3** integrin, onto the surface of **CPNs** to improve uptake in vitro, which is elevated in several angiogenic malignancies (such as HT-29). Cytotoxicity of **CPNs-a** and **CPNs-b** that have different thickness of silica were evaluated and shown IC₅₀ (50% Inhibitory Concentration) values of 9.7 and 11.9 μ M, respectively, while our cisplatin standard had an IC₅₀ value of only 13.0 μ M.

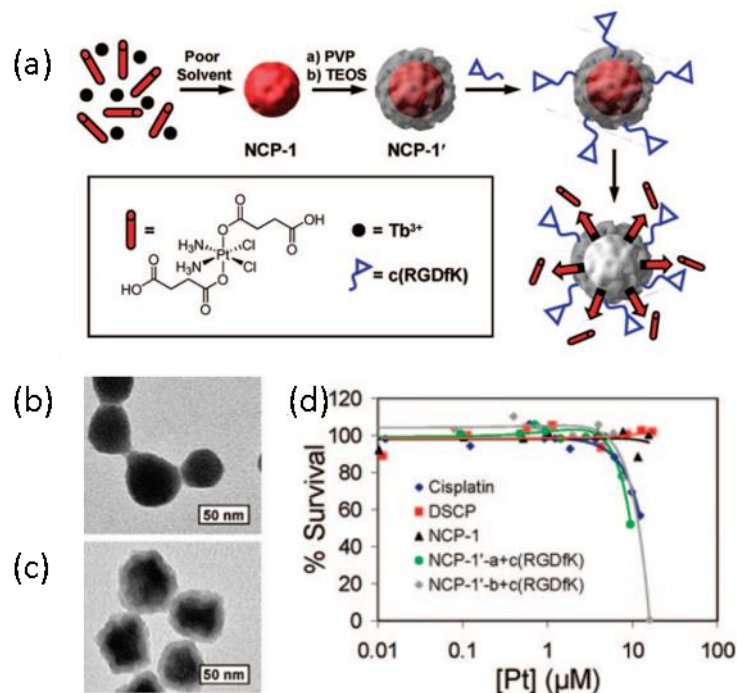


Figure 1.9: TEM micrograph for **CPNs**. (c) TEM and (C) SEM micrographs for **CPNs-b**. (d) In Vitro cytotoxicity assay curves for HT-29 cells obtained by plotting the % cell viability against the Pt concentration of various samples and cisplatin control³⁴

1.4.1.1 Drug encapsulation and release approaches

Drug encapsulation

Drugs may be physically or chemically entrapped inside a nanoparticle or as constituent parts of a polymeric unit. Physical containment includes guest encapsulation during **CPNs**

synthesis or in a pre-synthetic step, which is comprising active ingredients such magnetic nanoparticles, chemical dyes, or luminous quantum dots was first described in 2009 with efficiency up to 21%.⁵³ Wang and co-workers designed a novel gelatin-dopamin nano-gels (GDNGs) and the entrapment was simply carried out by mixing the model drug Dox and GDNGs in the presence of Fe^{3+} ions.⁵⁴ Huang and co-workers designed A novel targeted delivery strategy for in situ encapsulating anticancer medications that has been shown using coordination polymer spheres made from 1,10-(1,4-butanediyl)bis(imidazole) (bbi) and ferrous ions. and the encapsulation of DOX·HCl can be achieved by simply adding DOX·HCl.⁵⁵

With chemical method, it entails the integration of the active medication or functional molecules as a necessary component of the CPNs. Two distinct approaches may be used to accomplish this: i) using bio-active metal ions (such as Fe, Zn, Mn, Ag, or Gd) as linking components; or ii) using therapeutics as organic ligands.⁵⁶ Thanks to the application of the coordination-driven self-assembly approach to the field of DNA nanomaterials, Li and co-workers reported DNA-based CPNs are described (Scheme 1). The convenience and adaptability of this method were demonstrated by producing vast numbers of hybrid nanospheres in a single pot utilizing DNA molecules and Fe^{2+} ions. Also, Novio and co-workers created nanoparticles with controlled release, dual pH and redox sensitivity, and similar cytotoxicity to cisplatin against HeLa and GL261 cells by reacting a platinum (IV) prodrug with iron metal ions.³⁸

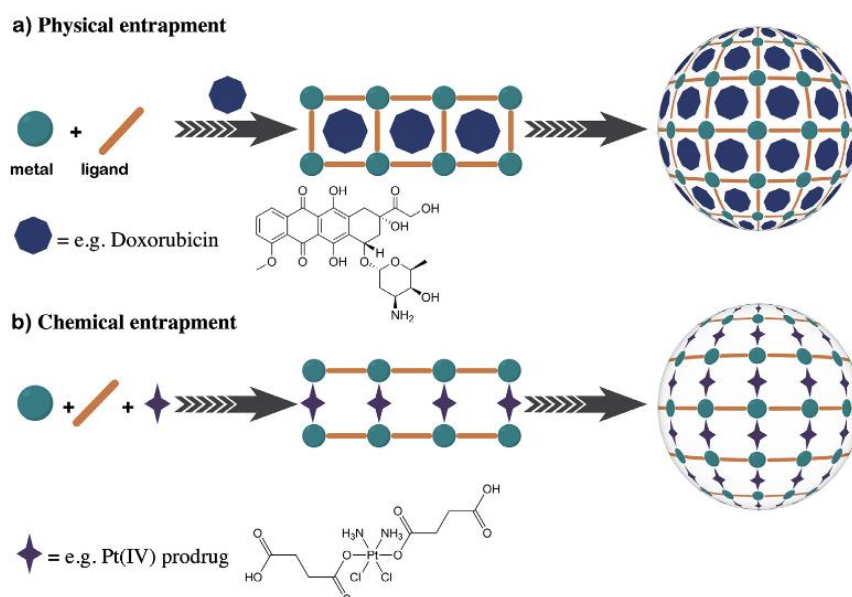


Figure 1.6: Representation of the two approaches used to encapsulate active drugs in NCPs: a) physical entrapment; b) chemical entrapment.⁵²

Drug release approaches:

Creating responsive **CPNs** that selectively administer the medicine in a smart and controllable way is another crucial challenge. Due to the great degree of tuneability in **CPNs** design, smart materials with responsive qualities can be developed, such as pH sensitive, redox- and light-responsive **CPNs**.

pH-sensitive CPNs

Utilizing the pH variations within intra- and extracellular environments in cancer cells, pH stimuli can be a critical key to control the **CPNs** drug delivery smartly. Thus, both metal nodes and ligands, as the two main components of **CPNs**, are possible to be the switch controlling a smart release. Chen and co-workers proposed a core-shell nanoparticles that consists Fe_3O_4 nanoclusters as the core and a Salphen- In^{3+} coordination polymer as the shell. In the presence of higher pH in intracellular environment the outer part of the material starts to be hydrolyzed and release free Salphen that subsequently coordinate with Fe ions that released from Fe_3O_4 to afford toxic anti-cancer drugs (Fe-salphen) realising a selective transformation from non-toxic materials to toxic ones preventing the cancer proliferation.⁵⁷ Sun and co-workers used Fe^{3+} , hydrocaffeic acid, and dopamine-modified hyaluronic acid to produce Fe-**CPNs** developing DOX-loaded Fe-**CPNs**. The pH-stimulated breakage of the Fe-DOX coordination bonds caused DOX release, which was further amplified by hyperpyrexia in the tumor-related area realizing chemotherapeutic application.⁵⁸

Photosensitizers-based CPNs

PDT (Photodynamic therapy) PACT (Photoactivated chemotherapy) and PTT (Photothermal therapy) are all noninvasive cancer treatments that have minimal side effects, little drug resistance, and little injury to surrounding healthy tissues.^{20, 59-61} For PDT, PACT and PTT, photosensitizers and light irradiation are the two primary components of the cancer treatment. In the last several decades, significant advancements have been achieved in the production of various photosensitizers, including cyanine-based **CPNs**,⁶²⁻⁶⁵ porphyrin-based **CPNs**⁶⁶⁻⁶⁹ and ruthenium complex-based **CPNs**⁷⁰⁻⁷² For example, Yin and his co-workers created a straightforward and reliable method for synthesizing ratio-tunable mixed-metal NCPs utilizing the precursors $\text{Ru}[4,4'-(\text{COOH})_2\text{bpy}]_3^{2+}$, high MR contrast of Gd^{3+} , and the high X-ray attenuation of Yb^{3+} to develop multimodality imaging probes.⁷³

Redox-activated CPNs

In addition to photosensitizers, chemical medications such as chemotherapeutic treatments like methotrexate (MTX) and cisplatin-prodrugs have also been used to create **CPNs**.⁷⁴⁻⁷⁵ However, because of the lack of selectivity from tumors and large drug dosage utilization, the molecular molecule cisplatin can have substantial adverse effects. To solve this problem, using therapeutic nanoc has been shown to be a useful and efficient means for enhancing the tumor uptake of drugs. Utilizing Pt (IV) in its oxidized state as prodrugs rather than cisplatin is another effective and beneficial tactic [95]. When present in a tumor context, these oxidized Pt(IV) prodrugs can undergo a reduction process with GSH to become physiologically active Pt(II) complexes, which are inactive in normal tissue environments.⁷⁶

1.4.2 Technological applications of CPNs

1.4.2.1 Light-harvesting materials of CPNs

Light-harvesting materials are attracting researchers' attention and are been widely used in different areas, such as optical devices, electrical devices and solar cell devices.⁸⁰⁻⁸² In recent years, materials⁸³, such as hydrogels,⁸⁴ porous nanocarriers, biomolecule-based composites, coordination-driven assemblies have been described and investigated. **CPNs**, as one of options above, are simple to be manufactured using the methodologies mention in Chapter 1.3.1. in Mixing metal ions and multidentate ligands and possible surfactants in a solution, **CPNs** can be afforded with round-shape or formless materials through a fast or slow precipitaion process. Finally, all the components are trapped within the **CPNs** chemically.

Qu and co-workers designed **CPNs** that consist of nuclestides (Guanosine 5'-monophosphate (GMP)) and lanthanide ions (Tb^{3+} or Eu^{3+}). Due to the high capacity of this **CPNs**, a "light switch molecule" (N-methyl mesoporphyrin IX (NMM)) was chosen and then incorporated within the **CPNs**.⁸⁵ As the most fluorescent dyes do, fluorescence of NMM is quenched in aqueous solution. However, the inner structure of **CPNs** offers a hydrophobic environment for the NMM and also, with the presence of G-quadruplex DNA and the Sr^{2+} -promoted GMP ensemble,⁸⁶⁻⁸⁷ the fluorescence intensity of GMP was enhance significantly. Also, the optical changes of the **CPNs** could be interpreted as binary logic gates.^{85, 88}

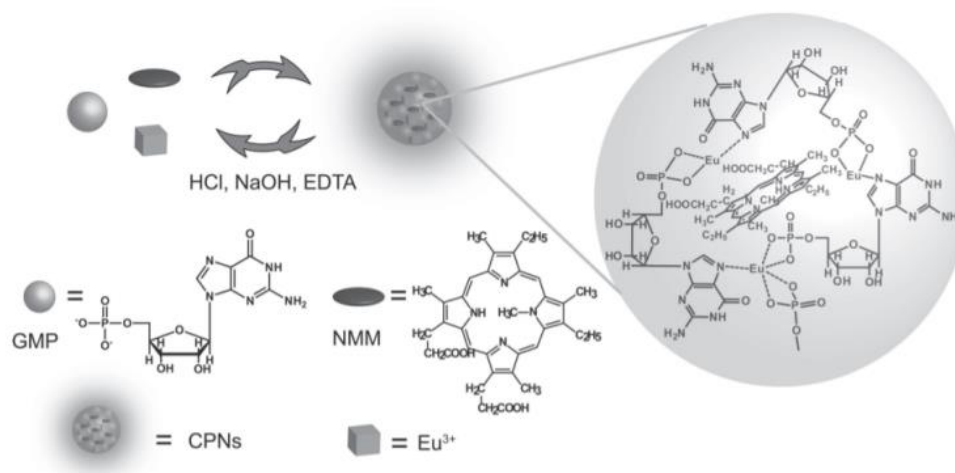


Figure 1.10: Schematic illustration of coordination polymer nanoparticles formation through the self-assembly of GMP and lanthanide ions. NMM was confined in the adaptive supramolecular networks and showed intense luminescence. The properties were used to construct versatile logic gates. Image extracted from the reference.⁸⁵

The same group presented another type of **CPNs** that consist of guanosine 5'-monophosphate (GMP), Thioflavin (ThT), thiazole orange (TO) and nucleic acid binders through self-assembly. They were chosen as the model's FRET donor-acceptor pair because they had adequate optical characteristics and were readily available on the market. ThT and TO are essentially non-fluorescent in aqueous solution, but when attached to nucleic acids, they exhibit strong absorption efficiency and fluorescence quantum yield.⁸⁹⁻⁹⁰ Additionally, it has been discovered that adding ThT and TO to GMP/lanthanide ions **CPNs**, increased the fluorescence intensity of those substances. By adjusting the proportion of donor and acceptor in particles, the optical properties may be modified, suggesting a tunable strategy for building arrays of light-harvesting systems.⁹¹

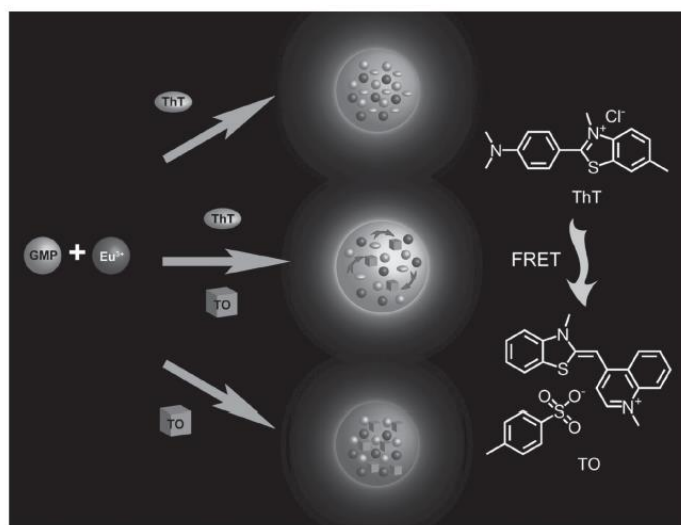


Figure 1.11:Construction of an artificial light-harvesting system by encapsulating two dyes into the coordination polymer nanoparticles through self-assembly. Image extracted from the reference.⁹¹

1.4.2.2 White-light-emitting materials of CPNs

White-light-emitting materials with high luminous brightness, environmental friendliness and many other advantages,⁹² have gained continuous attention and can be applied in various fields. Yang and co-workers synthesized Ir-1 and Ir-2 (chemical structures exhibited in Figure 1) and fabricated CPNs by employing $Y(OAc)_3$ salt as metallic nodes and bridging parts (Ir-1 and Ir-2 both with carboxylic group). Due to the empty 4f orbitals of Y^{3+} , f-f transitions will not take place and emit nothing in ultraviolet region but phosphorescent emission. Through adding different amount of Ir-1 and Ir-2, the energy transfer between them can be precisely adjusted. As a result, the color of the emission can be changed from blue to yellow.

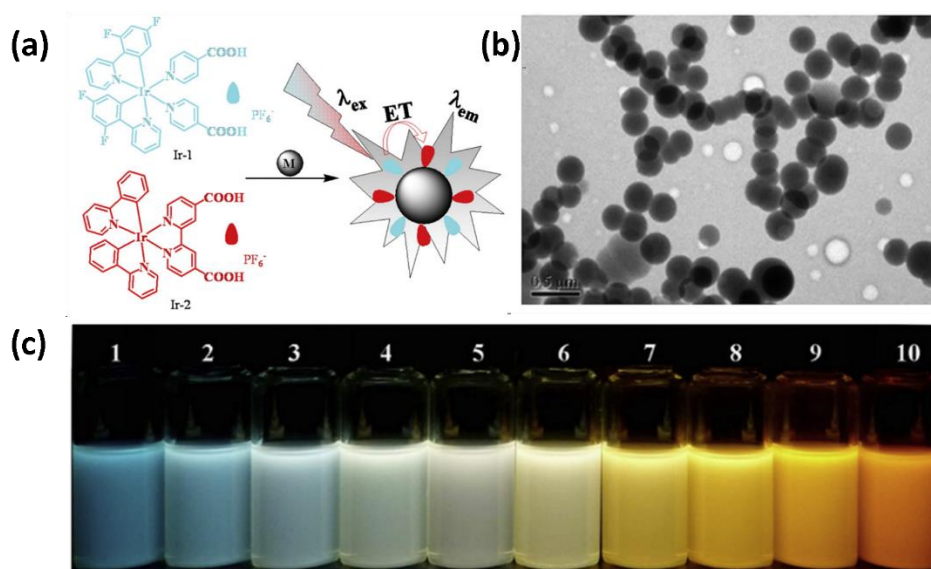


Figure 1.12: (a) The molecular structure of two iridium complexes and schematic representation of energy transfer in NCPs. (b) Representative SEM image of CPNs. (c) Phosphorescent photographs, from 1 to 10, doping ratio of Ir-1 and Ir-2: 100:0, 99.9:0.01, 99.8:0.02, 99.7:0.03, 99.6:0.04, 99.5:0.05, 99:0.1, 96:0.4, 90:10, 0:100. Images extracted from the reference.⁹³

1.4.2.3 Catalytic materials of CPNs

Apart from biological and device application, CPNs can also be used for other technological applications, such as catalysis. Zhong and co-workers designed a series of nucleotide-hybrid metal coordination polymers (CPs) constructed by guanosine 5'-monophosphate (GMP) and eight different metals with *Candida antarctica* lipase B (CALB) was encapsulated inside for enzymatic esterification. The result revealed that that, most of the present CPs encapsulated CALB (CALB@CPs) samples were highly selective for ester-

ification while poor in glycerolysis reaction. They exhibited quite poor performance in glycerolysis, however, they (most of them) showed good performance in esterification of fatty acids and glycerol for TAG synthesis.⁹⁴

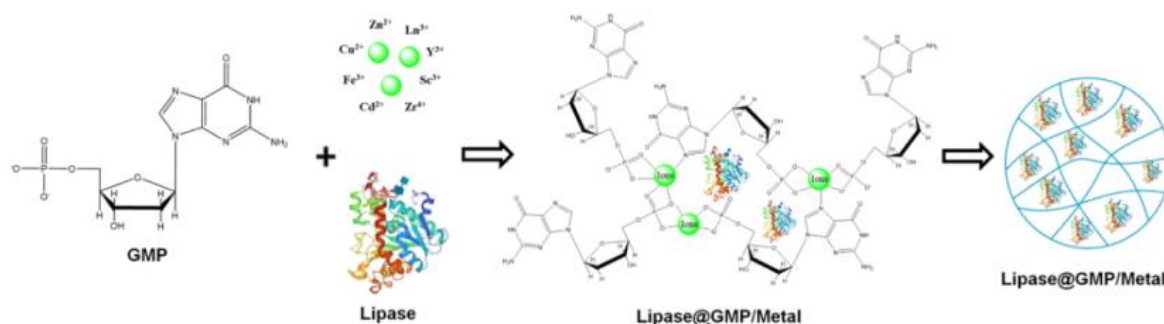


Figure 1.13: A scheme for preparing co-immobilized lipases by in situ self-assembly of GMP and metal ions. GMP, guanosine 50-monophosphate. Image extracted from the reference.⁹⁴

Additionally, Lang and co-workers presented the synthesis of Ag-based CPNs which exhibited good catalytic activity towards the photodegradation of nitrobenzene and other derivatives in aqueous solution under UV light irradiation.⁹⁵ In another example, Cao and co-workers described ultrasmall metal nanoparticles (MNPs) were decorated on soluble porous coordination polymers (CPs) with high metal loadings. The solubility of the composite and the size of the MNPs can be controlled by varying the ratio of the precursors to the supports. The soluble CPs can serve as a platform to homogenize heterogeneous MNPs catalysts, which exhibited excellent activity and recyclability in C–H activation and Suzuki reactions. This strategy combines the advantages of homogeneous and heterogeneous catalysis and may bring new inspiration to catalysis.⁹⁶

1.5 Scope of the Thesis

Coordination Polymer Nanoparticles		
Chapter 3	Chapter 4	Chapter 5
<i>Photoactivable Ruthenium-Based Coordination Polymer Nanoparticles</i>	<i>Upconverting Coordination Polymer Nanoparticles</i>	<i>DPA-S-COOH Based Coordination Polymer Nanoparticles</i>
Biological application (Chemotherapy)	Device application (Solar concentrator)	Biological application (PDT)

Figure 1.14: Schematic representation of the structure followed in this Thesis.

For the development of this Thesis, the work was based on two main challenges:

- i. The first one consists of the design and synthesis of novel **CPNs**. The rational design was based on the formation of **CPNs**. In all the cases, the synthesized nanostructures in the form of colloidal suspensions in water were explored.

In the **Chapter 3**, the obtaining of ruthenium-based **CPNs** with photoactivable property and the quantification of the drug release upon the light irradiation.

In the **Chapter 4**, the rational design of the dyes for TTA upconversion and the construction of the upconversion coordination polymer nanoparticles and optimization of materials optical properties.

In the **Chapter 5**, the obtaining of the DPA-S-COOH based coordination polymer nanoparticles.

- ii. The second challenge was related on the validation of the developed materials in their specific applications, such as drug delivery (**Chapter 3**), emissive device (**Chapter 4**) and PDT (**Chapter 5**).

1.6 Reference

1. Ariga, K.; Malgras, V.; Ji, Q.; Zakaria, M. B.; Yamauchi, Y., Coordination nanoarchitectonics at interfaces between supramolecular and materials chemistry. *Coord. Chem. Rev.* **2016**, *320-321*, 139-152.
2. Du, M.; Li, C.-P.; Liu, C.-S.; Fang, S.-M., Design and construction of coordination polymers with mixed-ligand synthetic strategy. *Coord. Chem. Rev.* **2013**, *257 (7-8)*, 1282-1305.
3. Horcajada, P.; Serre, C.; Vallet-Regí, M.; Sebban, M.; Taulelle, F.; Férey, G., Metal-organic frameworks as efficient materials for drug delivery. *Angew. Chem.* **2006**, *118 (36)*, 6120-6124.
4. Fan, W.; Zhang, X.; Kang, Z.; Liu, X.; Sun, D., Isoreticular chemistry within metal-organic frameworks for gas storage and separation. *Coord. Chem. Rev.* **2021**, *443*, 213968.
5. Li, B.; Dong, J.-P.; Zhou, Z.; Wang, R.; Wang, L.-Y.; Zang, S.-Q., Robust lanthanide metal-organic frameworks with "all-in-one" multifunction: Efficient gas adsorption and separation, tunable light emission and luminescence sensing. *J. Mater. Chem. C* **2021**, *9 (10)*, 3429-3439.
6. Brandt, P.; Nuhnen, A.; Öztürk, S.; Kurt, G.; Liang, J.; Janiak, C., Comparative Evaluation of Different **MOF** and Non-**MOF** Porous Materials for SO₂ Adsorption and Separation Showing the Importance of Small Pore Diameters for Low-Pressure Uptake. *Advanced Sustainable Systems* **2021**, *5 (4)*, 2000285.
7. Li, D.; Xu, H.-Q.; Jiao, L.; Jiang, H.-L., Metal-organic frameworks for catalysis: State of the art, challenges, and opportunities. *EnergyChem* **2019**, *1 (1)*, 100005.

8. Hao, M.; Qiu, M.; Yang, H.; Hu, B.; Wang, X., Recent advances on preparation and environmental applications of **MOF**-derived carbons in catalysis. *Sci. Total Environ.* **2021**, *760*, 143333.
9. Yin, H.-Q.; Yin, X.-B., Metal–organic frameworks with multiple luminescence emissions: designs and applications. *Acc. Chem. Res.* **2020**, *53* (2), 485-495.
10. Yang, G. L.; Jiang, X. L.; Xu, H.; Zhao, B., Applications of **MOFs** as luminescent sensors for environmental pollutants. *Small* **2021**, *17* (22), 2005327.
11. Karmakar, A.; Samanta, P.; Dutta, S.; Ghosh, S. K., Fluorescent “Turn-on” Sensing Based on Metal–Organic Frameworks (**MOFs**). *Chemistry—An Asian Journal* **2019**, *14* (24), 4506-4519.
12. Zhao, S. N.; Wang, G.; Poelman, D.; Voort, P. V., Luminescent Lanthanide **MOFs**: A Unique Platform for Chemical Sensing. *Materials (Basel)* **2018**, *11* (4), 572.
13. Cai, Y. Y.; Yang, Q.; Zhu, Z. Y.; Sun, Q. H.; Zhu, A. M.; Zhang, Q. G.; Liu, Q. L., Achieving efficient proton conduction in a **MOF**-based proton exchange membrane through an encapsulation strategy. *Journal of Membrane Science* **2019**, *590*, 117277.
14. Kanj, A. B.; Chandresh, A.; Gerwien, A.; Grosjean, S.; Bräse, S.; Wang, Y.; Dube, H.; Heinke, L., Proton-conduction photomodulation in spiropyran-functionalized **MOFs** with large on–off ratio. *Chemical Science* **2020**, *11* (5), 1404-1410.
15. Oh, M.; Mirkin, C. A., Chemically tailorable colloidal particles from infinite coordination polymers. *Nature* **2005**, *438* (7068), 651-4.
16. Sun, X.; Dong, S.; Wang, E., Coordination-induced formation of submicrometer-scale, monodisperse, spherical colloids of organic– inorganic hybrid materials at room temperature. *J. Am. Chem. Soc.* **2005**, *127* (38), 13102-13103.
17. Xue, S.-F.; Zhang, J.-F.; Chen, Z.-H.; Han, X.-Y.; Zhang, M.; Shi, G., Multifunctional fluorescent sensing of chemical and physical stimuli using smart riboflavin-5'-phosphate/Eu³⁺ coordination polymers. *Anal. Chim. Acta* **2018**, *1012*, 74-81.
18. Li, Q.; Wang, C.; Tan, H.; Tang, G.; Gao, J.; Chen, C.-H., A turn on fluorescent sensor based on lanthanide coordination polymer nanoparticles for the detection of mercury (II) in biological fluids. *RSC Adv.* **2016**, *6* (22), 17811-17817.
19. García-Pardo, J.; Novio, F.; Nador, F.; Cavaliere, I.; Suárez-García, S.; Lope-Piedrafita, S.; Candiota, A. P.; Romero-Gimenez, J.; Rodríguez-Galván, B.; Bové, J., Bioinspired theranostic coordination polymer nanoparticles for intranasal dopamine replacement in parkinson’s disease. *ACS nano* **2021**, *15* (5), 8592-8609.
20. Zhang, J.; Ramu, V.; Zhou, X. Q.; Frias, C.; Ruiz-Molina, D.; Bonnet, S.; Roscini, C.; Novio, F., Photoactivable Ruthenium-Based Coordination Polymer Nanoparticles for Light-Induced Chemotherapy. *Nanomaterials (Basel)* **2021**, *11* (11), 3089.
21. Morritt, G.; Michaels, H.; Freitag, M., Coordination polymers for emerging molecular devices. *Chemical Physics Reviews* **2022**, *3* (1), 011306.
22. Dutta, B.; Dey, A.; Maity, S.; Sinha, C.; Ray, P. P.; Mir, M. H., Supramolecular Assembly of a Zn (II)-Based 1D Coordination Polymer through Hydrogen Bonding and $\pi \cdots \pi$ Interactions: Crystal Structure and Device Applications. *ACS omega* **2018**, *3* (9), 12060-12067.
23. Zheng, S. T.; Zuo, F.; Wu, T.; Irfanoglu, B.; Chou, C.; Nieto, R. A.; Feng, P.; Bu, X., Cooperative Assembly of Three-Ring-Based Zeolite-Type Metal–Organic Frameworks and Johnson-Type Dodecahedra. *Angew. Chem. Int. Ed.* **2011**, *50* (8), 1849-1852.
24. Lv, X.-L.; Wang, K.; Wang, B.; Su, J.; Zou, X.; Xie, Y.; Li, J.-R.; Zhou, H.-C., A base-resistant metalloporphyrin metal–organic framework for C–H bond halogenation. *J. Am. Chem. Soc.* **2017**, *139* (1), 211-217.
25. Ren, C.-X.; Cai, L.-X.; Chen, C.; Tan, B.; Zhang, Y.-J.; Zhang, J., π -Conjugation-directed highly selective adsorption of benzene over cyclohexane. *J. Mater. Chem. A* **2014**, *2* (24), 9015-9019.
26. Cao, L.-H.; Wei, Y.-L.; Yang, Y.; Xu, H.; Zang, S.-Q.; Hou, H.-W.; Mak, T. C., Crystal structures and properties of Cd (II) coordination polymers supported by a new chiral aromatic polycarboxylate ligand. *Crystal growth & design* **2014**, *14* (4), 1827-1838.

27. Sun, J. K.; Tan, B.; Cai, L. X.; Chen, R. P.; Zhang, J.; Zhang, J., Polycatenation-Driven Self-Assembly of Nanoporous Frameworks Based on a 1D Ribbon of Rings: Regular Structural Evolution, Interpenetration Transformation, and Photochemical Modification. *Chemistry—A European Journal* **2014**, *20* (9), 2488-2495.
28. Ren, C. X.; Ji, M.; Yao, Q. X.; Cai, L. X.; Tan, B.; Zhang, J., Targeted functionalization of porous materials for separation of alcohol/water mixtures by modular assembly. *Chemistry* **2014**, *20* (45), 14846-52.
29. Puigmartí-Luis, J., Microfluidic platforms: a mainstream technology for the preparation of crystals. *Chem. Soc. Rev.* **2014**, *43* (7), 2253-2271.
30. Bellido, E.; Gonzalez-Monje, P.; Guardingo, M.; Novio, F.; Sánchez, A.; Montero, M.; Molnár, G.; Bousseksou, A.; Ruiz-Molina, D., Nanoscale coordination polymers obtained in ultrasmall liquid droplets on solid surfaces and its comparison to different synthetic volume scales. *RSC Adv.* **2016**, *6* (80), 76666-76672.
31. Guardingo, M.; González-Monje, P.; Novio, F.; Bellido, E.; Busqué, F.; Molnár, G.; Bousseksou, A.; Ruiz-Molina, D., Synthesis of nanoscale coordination polymers in femtoliter reactors on surfaces. *ACS nano* **2016**, *10* (3), 3206-3213.
32. Bousseksou, A.; Molnár, G.; Salmon, L.; Nicolazzi, W., Molecular spin crossover phenomenon: recent achievements and prospects. *Chem. Soc. Rev.* **2011**, *40* (6), 3313-3335.
33. Imaz, I.; MasPOCH, D.; Rodríguez-Blanco, C.; Pérez-Falcón, J. M.; Campo, J.; Ruiz-Molina, D., Valence-tautomeric metal-organic nanoparticles. *Angew. Chem.* **2008**, *120* (10), 1883-1886.
34. Rieter, W. J.; Pott, K. M.; Taylor, K. M.; Lin, W., Nanoscale coordination polymers for platinum-based anticancer drug delivery. *J. Am. Chem. Soc.* **2008**, *130* (35), 11584-5.
35. He, C.; Lu, K.; Lin, W., Nanoscale metal-organic frameworks for real-time intracellular pH sensing in live cells. *J. Am. Chem. Soc.* **2014**, *136* (35), 12253-12256.
36. Novio, F.; Lorenzo, J.; Nador, F.; Wnuk, K.; Ruiz-Molina, D., Carboxyl Group (CO₂H) Functionalized Coordination Polymer Nanoparticles as Efficient Platforms for Drug Delivery. *Chemistry—A European Journal* **2014**, *20* (47), 15443-15450.
37. Nador, F.; Wnuk, K.; García-Pardo, J.; Lorenzo, J.; Solorzano, R.; Ruiz-Molina, D.; Novio, F., Dual-Fluorescent Nanoscale Coordination Polymers via a Mixed-Ligand Synthetic Strategy and Their Use for Multichannel Imaging. *ChemNanoMat* **2018**, *4* (2), 183-193.
38. Mao, X.; Calero-Perez, P.; Montpeyo, D.; Bruna, J.; Yuste, V. J.; Candiota, A. P.; Lorenzo, J.; Novio, F.; Ruiz-Molina, D., Intranasal Administration of Catechol-Based Pt(IV) Coordination Polymer Nanoparticles for Glioblastoma Therapy. *Nanomaterials (Basel)* **2022**, *12* (7), 1221.
39. Suarez-Garcia, S.; Esposito, T. V.; Neufeld-Peters, J.; Bergamo, M.; Yang, H.; Saatchi, K.; Schaffer, P.; Hafeli, U. O.; Ruiz-Molina, D.; Rodriguez-Rodriguez, C., Hybrid Metal-Phenol Nanoparticles with Polydopamine-like Coating for PET/SPECT/CT Imaging. *ACS Appl. Mater. Interfaces* **2021**, *13* (9), 10705-10718.
40. Parvathikar, S.; Luz, I.; Carpenter, M.; Bellamy, T.; Amato, K.; Carpenter, J.; Gilmore, D.; Lail, M., Solvothermal synthesis of MOF-derived supported Ru nanocatalysts for low-temperature ammonia synthesis. *Catal. Today* **2022**, *387*, 23-27.
41. Eddaoudi, M.; Kim, J.; Rosi, N.; Vodak, D.; Wachter, J.; O'Keeffe, M.; Yaghi, O. M., Systematic design of pore size and functionality in isorecticular MOFs and their application in methane storage. *Science* **2002**, *295* (5554), 469-472.
42. Seo, J. S.; Whang, D.; Lee, H.; Jun, S. I.; Oh, J.; Jeon, Y. J.; Kim, K., A homochiral metal-organic porous material for enantioselective separation and catalysis. *Nature* **2000**, *404* (6781), 982-986.
43. Dybtsev, D. N.; Nuzhdin, A. L.; Chun, H.; Bryliakov, K. P.; Talsi, E. P.; Fedin, V. P.; Kim, K., A homochiral metal-organic material with permanent porosity, enantioselective sorption properties, and catalytic activity. *Angew. Chem.* **2006**, *118* (6), 930-934.
44. Ni, Z.; Masel, R. I., Rapid production of metal-organic frameworks via microwave-assisted solvothermal synthesis. *J. Am. Chem. Soc.* **2006**, *128* (38), 12394-5.

45. Sun, W.; Zhai, X.; Zhao, L., Synthesis of ZIF-8 and ZIF-67 nanocrystals with well-controllable size distribution through reverse microemulsions. *Chem. Eng. J.* **2016**, *289*, 59-64.
46. Gao, J.; He, M.; Lee, Z. Y.; Cao, W.; Xiong, W.-W.; Li, Y.; Ganguly, R.; Wu, T.; Zhang, Q., A surfactant-thermal method to prepare four new three-dimensional heterometal-organic frameworks. *Dalton Trans.* **2013**, *42* (32), 11367-11370.
47. Amo-Ochoa, P.; Welte, L.; Gonzalez-Prieto, R.; Sanz Miguel, P. J.; Gomez-Garcia, C. J.; Mateo-Marti, E.; Delgado, S.; Gomez-Herrero, J.; Zamora, F., Single layers of a multifunctional laminar Cu(I,II) coordination polymer. *Chem. Commun.* **2010**, *46* (19), 3262-4.
48. Wang, C.; An, B.; Lin, W., Metal-organic frameworks in solid-gas phase catalysis. *ACS Catalysis* **2018**, *9* (1), 130-146.
49. Li, H.; Li, L.; Lin, R.-B.; Zhou, W.; Zhang, Z.; Xiang, S.; Chen, B., Porous metal-organic frameworks for gas storage and separation: Status and challenges. *EnergyChem* **2019**, *1* (1), 100006.
50. Yan, B., Photofunctional MOF-based hybrid materials for the chemical sensing of biomarkers. *J. Mater. Chem. C* **2019**, *7* (27), 8155-8175.
51. Velásquez-Hernández, M. d. J.; Linares-Moreau, M.; Astria, E.; Carraro, F.; Alyami, M. Z.; Khashab, N. M.; Sumbly, C. J.; Doonan, C. J.; Falcaro, P., Towards applications of bioentities@ MOFs in biomedicine. *Coord. Chem. Rev.* **2021**, *429*, 213651.
52. Suárez-García, S.; Solórzano, R.; Alibés, R.; Busqué, F.; Novio, F.; Ruiz-Molina, D., Antitumour activity of coordination polymer nanoparticles. *Coord. Chem. Rev.* **2021**, *441*, 213977.
53. Imaz, I.; Hernando, J.; Ruiz-Molina, D.; Maspoch, D., Metal-organic spheres as functional systems for guest encapsulation. *Angew. Chem. Int. Ed.* **2009**, *48* (13), 2325-2329.
54. Fan, C.; Wang, D.-A., Novel gelatin-based nano-gels with coordination-induced drug loading for intracellular delivery. *Journal of Materials Science & Technology* **2016**, *32* (9), 840-844.
55. Gao, P. F.; Zheng, L. L.; Liang, L. J.; Yang, X. X.; Li, Y. F.; Huang, C. Z., A new type of pH-responsive coordination polymer sphere as a vehicle for targeted anticancer drug delivery and sustained release. *J. Mater. Chem. B* **2013**, *1* (25), 3202-3208.
56. Amorín-Ferré, L.; Busqué, F.; Bourdelande, J. L.; Ruiz-Molina, D.; Hernando, J.; Novio, F., Encapsulation and release mechanisms in coordination polymer nanoparticles. *Chemistry—A European Journal* **2013**, *19* (51), 17508-17516.
57. Xu, S.; Liu, J.; Li, D.; Wang, L.; Guo, J.; Wang, C.; Chen, C., Fe-salphen complexes from intracellular pH-triggered degradation of Fe₃O₄@ Salphen-In(III) CPPs for selectively killing cancer cells. *Biomaterials* **2014**, *35* (5), 1676-1685.
58. Li, J.; Zhang, C.; Gong, S.; Li, X.; Yu, M.; Qian, C.; Qiao, H.; Sun, M., A nanoscale photothermal agent based on a metal-organic coordination polymer as a drug-loading framework for effective combination therapy. *Acta Biomaterialia* **2019**, *94*, 435-446.
59. Baskaran, R.; Lee, J.; Yang, S. G., Clinical development of photodynamic agents and therapeutic applications. *Biomater Res* **2018**, *22* (1), 25.
60. Sun, W.; Li, S.; Haupler, B.; Liu, J.; Jin, S.; Steffen, W.; Schubert, U. S.; Butt, H. J.; Liang, X. J.; Wu, S., An Amphiphilic Ruthenium Polymetallo-drug for Combined Photodynamic Therapy and Photochemotherapy In Vivo. *Adv. Mater.* **2017**, *29* (6), 1603702.
61. Liu, Y.; Bhattarai, P.; Dai, Z.; Chen, X., Photothermal therapy and photoacoustic imaging via nanotheranostics in fighting cancer. *Chem. Soc. Rev.* **2019**, *48* (7), 2053-2108.
62. Sheng, Z.; Hu, D.; Zheng, M.; Zhao, P.; Liu, H.; Gao, D.; Gong, P.; Gao, G.; Zhang, P.; Ma, Y.; Cai, L., Smart human serum albumin-indocyanine green nanoparticles generated by programmed assembly for dual-modal imaging-guided cancer synergistic phototherapy. *ACS Nano* **2014**, *8* (12), 12310-22.
63. Xiong, X.; Song, F.; Wang, J.; Zhang, Y.; Xue, Y.; Sun, L.; Jiang, N.; Gao, P.; Tian, L.; Peng, X., Thermally activated delayed fluorescence of fluorescein derivative for time-resolved and confocal fluorescence imaging. *J. Am. Chem. Soc.* **2014**, *136* (27), 9590-7.
64. Yang, Y.; Zhu, W.; Dong, Z.; Chao, Y.; Xu, L.; Chen, M.; Liu, Z., 1D coordination polymer nanofibers for low-temperature photothermal therapy. *Adv. Mater.* **2017**, *29* (40), 1703588.

65. Lin, H.; Li, S.; Wang, J.; Chu, C.; Zhang, Y.; Pang, X.; Lv, P.; Wang, X.; Zhao, Q.; Chen, J.; Chen, H.; Liu, W.; Chen, X.; Liu, G., A single-step multi-level supramolecular system for cancer sonotheranostics. *Nanoscale Horiz* **2019**, *4* (1), 190-195.
66. Liu, M.; Wang, L.; Zheng, X.; Liu, S.; Xie, Z., Hypoxia-triggered nanoscale metal-organic frameworks for enhanced anticancer activity. *ACS Appl. Mater. Interfaces* **2018**, *10* (29), 24638-24647.
67. Xing, R.; Zou, Q.; Yuan, C.; Zhao, L.; Chang, R.; Yan, X., Self-assembling endogenous biliverdin as a versatile near-infrared photothermal nanoagent for cancer theranostics. *Adv. Mater.* **2019**, *31* (16), 1900822.
68. Chao, Y.; Liang, C.; Yang, Y.; Wang, G.; Maiti, D.; Tian, L.; Wang, F.; Pan, W.; Wu, S.; Yang, K.; Liu, Z., Highly Effective Radioisotope Cancer Therapy with a Non-Therapeutic Isotope Delivered and Sensitized by Nanoscale Coordination Polymers. *ACS Nano* **2018**, *12* (8), 7519-7528.
69. Zhang, P.; Wang, J.; Chen, H.; Zhao, L.; Chen, B.; Chu, C.; Liu, H.; Qin, Z.; Liu, J.; Tan, Y.; Chen, X.; Liu, G., Tumor Microenvironment-Responsive Ultrasmall Nanodrug Generators with Enhanced Tumor Delivery and Penetration. *J. Am. Chem. Soc.* **2018**, *140* (44), 14980-14989.
70. Zhou, Z.; Li, D.; Yang, H.; Zhu, Y.; Yang, S., Synthesis of d-f coordination polymer nanoparticles and their application in phosphorescence and magnetic resonance imaging. *Dalton Trans.* **2011**, *40* (44), 11941-11944.
71. Wang, L.; Song, B.; Khalife, S.; Li, Y.; Ming, L.-J.; Bai, S.; Xu, Y.; Yu, H.; Wang, M.; Wang, H., Introducing seven transition metal ions into terpyridine-based supramolecules: self-assembly and dynamic ligand exchange study. *J. Am. Chem. Soc.* **2020**, *142* (4), 1811-1821.
72. Wang, L.; Xie, Z.; Dang, S.; Sun, Z. M., Self-Assembly of Tunable Heterometallic Ln-Ru Coordination Polymers with Near-Infrared Luminescence and Magnetocaloric Effect. *Chemistry—A European Journal* **2017**, *23* (12), 2852-2857.
73. Wang, Y. M.; Liu, W.; Yin, X. B., Multifunctional mixed-metal nanoscale coordination polymers for triple-modality imaging-guided photodynamic therapy. *Chem. Sci.* **2017**, *8* (5), 3891-3897.
74. Wu, Y.; Xu, L.; Qian, J.; Shi, L.; Su, Y.; Wang, Y.; Li, D.; Zhu, X., Methotrexate-Mn 2+ based nanoscale coordination polymers as a theranostic nanoplatform for MRI guided chemotherapy. *Biomaterials science* **2020**, *8* (2), 712-719.
75. Poon, C.; He, C.; Liu, D.; Lu, K.; Lin, W., Self-assembled nanoscale coordination polymers carrying oxaliplatin and gemcitabine for synergistic combination therapy of pancreatic cancer. *J. Controlled Release* **2015**, *201*, 90-9.
76. Liu, J.; Wu, M.; Pan, Y.; Duan, Y.; Dong, Z.; Chao, Y.; Liu, Z.; Liu, B., Biodegradable nanoscale coordination polymers for targeted tumor combination therapy with oxidative stress amplification. *Adv. Funct. Mater.* **2020**, *30* (13), 1908865.
77. Khodabandehloo, H.; Zahednasab, H.; Ashrafi Hafez, A., Nanocarriers Usage for Drug Delivery in Cancer Therapy. *Iran J Cancer Prev* **2016**, *9* (2), e3966.
78. Dadwal, A.; Baldi, A.; Kumar Narang, R., Nanoparticles as carriers for drug delivery in cancer. *Artificial cells, nanomedicine, and biotechnology* **2018**, *46* (sup2), 295-305.
79. Zhang, H.; Liu, K.; Li, S.; Xin, X.; Yuan, S.; Ma, G.; Yan, X., Self-Assembled Minimalist Multifunctional Theranostic Nanoplatform for Magnetic Resonance Imaging-Guided Tumor Photodynamic Therapy. *ACS Nano* **2018**, *12* (8), 8266-8276.
80. Liu, Q.; Gerling, L. G.; Bernal-Tezca, F.; Toudert, J.; Li, T.; Zhan, X.; Martorell, J., Light harvesting at oblique incidence decoupled from transmission in organic solar cells exhibiting 9.8% efficiency and 50% visible light transparency. *Advanced energy materials* **2020**, *10* (17), 1904196.
81. Park, S. Y.; Labanti, C.; Luke, J.; Chin, Y. C.; Kim, J. S., Organic Bilayer Photovoltaics for Efficient Indoor Light Harvesting. *Advanced Energy Materials* **2022**, *12* (3), 2103237.
82. Vicente, A. T.; Araújo, A.; Mendes, M. J.; Nunes, D.; Oliveira, M. J.; Sanchez-Sobrado, O.; Ferreira, M. P.; Águas, H.; Fortunato, E.; Martins, R., Multifunctional cellulose-paper for light harvesting and smart sensing applications. *J. Mater. Chem. C* **2018**, *6* (13), 3143-3181.

83. Sun, Y.; Giebink, N. C.; Kanno, H.; Ma, B.; Thompson, M. E.; Forrest, S. R., Management of singlet and triplet excitons for efficient white organic light-emitting devices. *Nature* **2006**, *440* (7086), 908-12.
84. Rao, K. V.; Datta, K.; Eswaramoorthy, M.; George, S. J., Light-Harvesting Hybrid Hydrogels: Energy-Transfer-Induced Amplified Fluorescence in Noncovalently Assembled Chromophore-Organoclay Composites. *Angew. Chem. Int. Ed.* **2011**, *50* (5), 1179-1184.
85. Pu, F.; Ju, E.; Ren, J.; Qu, X., Multiconfigurable logic gates based on fluorescence switching in adaptive coordination polymer nanoparticles. *Adv. Mater.* **2014**, *26* (7), 1111-7.
86. Hu, D.; Ren, J.; Qu, X., Metal-mediated fabrication of new functional G-quartet-based supramolecular nanostructure and potential application as controlled drug release system. *Chemical Science* **2011**, *2* (7), 1356-1361.
87. Chen, J.; Liu, X.; Suo, Z.; Gao, C.; Xing, F.; Feng, L.; Zhao, C.; Hu, L.; Ren, J.; Qu, X., Right-/left-handed helical G-quartet nanostructures with full-color and energy transfer circularly polarized luminescence. *Chem. Commun.* **2020**, *56* (56), 7706-7709.
88. Pu, F.; Wu, L.; Ju, E.; Ran, X.; Ren, J.; Qu, X., Artificial Light-Harvesting Material Based on Self-Assembly of Coordination Polymer Nanoparticles. *Adv. Funct. Mater.* **2014**, *24* (28), 4549-4555.
89. Mohanty, J.; Barooah, N.; Dhamodharan, V.; Harikrishna, S.; Pradeepkumar, P.; Bhasikuttan, A. C., Thioflavin T as an efficient inducer and selective fluorescent sensor for the human telomeric G-quadruplex DNA. *J. Am. Chem. Soc.* **2013**, *135* (1), 367-376.
90. Lubitz, I.; Zikich, D.; Kotlyar, A., Specific high-affinity binding of thiazole orange to triplex and G-quadruplex DNA. *Biochemistry* **2010**, *49* (17), 3567-74.
91. Pu, F.; Wu, L.; Ju, E.; Ran, X.; Ren, J.; Qu, X., Artificial Light-Harvesting Material Based on Self-Assembly of Coordination Polymer Nanoparticles. *Adv. Funct. Mater.* **2014**, *24* (28), 4549-4555.
92. Li, J.; Yan, J.; Wen, D.; Khan, W. U.; Shi, J.; Wu, M.; Su, Q.; Tanner, P. A., Advanced red phosphors for white light-emitting diodes. *J. Mater. Chem. C* **2016**, *4* (37), 8611-8623.
93. Qin, L.; Zhu, Y.; Yang, H.; Ding, L.; Sun, F.; Shi, M.; Yang, S., White-light phosphorescence from binary coordination polymer nanoparticles. *Mater. Chem. Phys.* **2013**, *139* (2-3), 345-349.
94. Chen, W.; Xu, L.; Zhong, N., Encapsulation of CALB by nucleotide/metal ions coordination nanoparticles: highly selective catalysis of esterification while poor performance in glycerolysis reaction. *J. Sci. Food Agric.* **2022**, *102* (5), 1812-1822.
95. Wu, X.-Y.; Qi, H.-X.; Ning, J.-J.; Wang, J.-F.; Ren, Z.-G.; Lang, J.-P., One silver(I)/tetraphosphine coordination polymer showing good catalytic performance in the photodegradation of nitroaromatics in aqueous solution. *Applied Catalysis B: Environmental* **2015**, *168-169*, 98-104.
96. Huang, Y. B.; Wang, Q.; Liang, J.; Wang, X.; Cao, R., Soluble Metal-Nanoparticle-Decorated Porous Coordination Polymers for the Homogenization of Heterogeneous Catalysis. *J. Am. Chem. Soc.* **2016**, *138* (32), 10104-7.

Chapter 2

Objectives

Accordingly with the described in the introduction, the two main general objectives set for this Thesis are:

To design functional coordination polymers consist of therapeutic drug for possible biological application.

To design functional coordination polymers consist of fluorescent dyes for possible technological and biological application.

To achieve the first objective, the following specific objectives were set:

- I. To synthesize and characterize photoactivable ruthenium-based coordination polymer nanoparticles.
- II. To investigate the drug release profile and potentials for biological applications, such as drug release quantification, cell uptake, cytotoxicity measurement, etc.
- III. To study the *in vitro* behaviour of the coordination polymer nanoparticles upon light irradiation.

To achieve the second objective, the following specific objectives were set:

- I. To design, synthesize and characterize fluorescent dyes.
- II. To synthesize and characterize the light-responsive coordination polymer nanoparticles
- III. To investigate the possible technological and biological applications, such as emissive device and photodynamic therapy

Chapter 3

Photoactivable Ruthenium-Based Coordination Polymer Nanoparticles for Light-Induced Chemotherapy

3.1 Introduction

According to the WHO (world health organization), cancer is a leading cause of death worldwide, accounting for nearly 10 million deaths in 2020. The most common in 2020 (in terms of new cases of cancer) were: breast (2.26 million cases); lung (2.21 million cases); colon and rectum (1.93 million cases); prostate (1.41 million cases); skin (non-melanoma) (1.20 million cases); and stomach (1.09 million cases). The research of chemotherapeutic drugs for cancer treatment based on transition metals has always been one of the most interesting hotspots,¹⁻⁵ as consequence of the obvious benefits obtained from the long-term and widely used cisplatin [$\text{cis-Pt}(\text{NH}_3)_2\text{Cl}_2$] in clinical application. The unexpected discovery by Rosenberg and collaborators of the antitumor activity of cisplatin in the 1960s impelled an intense research with this compound and its analogs for the treatment of many cancers.⁶⁻⁷ Although cisplatin and its derivatives are efficacious against most of cancers, they present poor selectivity to tumor tissues and causes non-cancer cell toxicity with subsequent severe adverse effects.⁸⁻¹⁰ Along with cisplatin, oxaliplatin and carboplatin constitute the first generation of the Pt-based anti-cancer drugs with evident therapeutic effects on different types of tumors, such as breast, lungs, ovarian, and colorectal. Since these drugs are causing apoptosis to cancer cells and healthy cells at the same time, serious undesirable effects are showing up during the therapeutic processes, including cardiotoxicity, nephrotoxicity, neurotoxicity and myelosuppression. Besides, during treatment, the resistance of tumors to Pt-based drugs lowers the efficacy of therapy or even causing treatment failure (Figure 3.1).¹¹⁻¹²

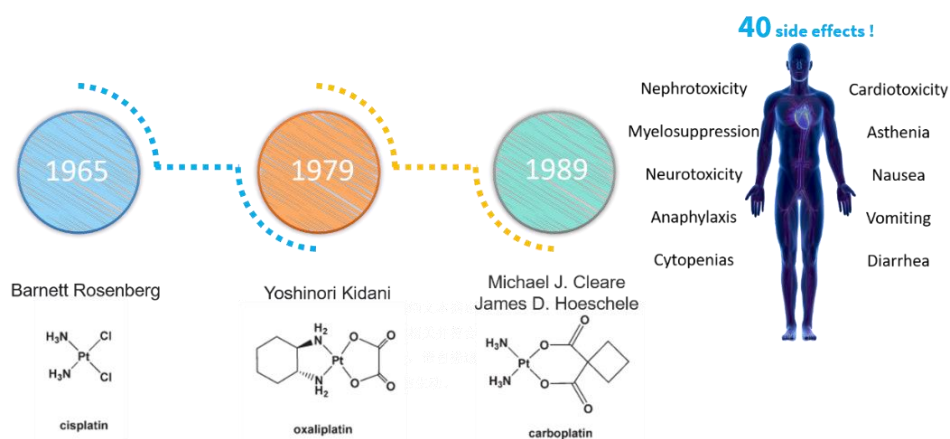


Figure 3.1: Chemical structures of cisplatin, oxaliplatin and carboplatin and the possible side effects caused by using platinum-based anti-cancer drug during therapeutic process

Different strategies have been used to solve the problems associated to the use of Pt(II) complexes, such as using targeting drug delivery systems and reduction responsive Pt(IV) prodrugs.¹³⁻¹⁴ In addition, many nontoxic (in the dark) photoactivable Pt(IV) agents have been

reported, which can release cytotoxic Pt(II) species upon light irradiation.¹⁵ These kinds of prodrugs are used in photoactivated chemotherapy (PACT), which can trigger and limit the therapeutic effect within the tumor tissues by spatio-temporal control of irradiation, thus reducing the side effects.¹⁶⁻¹⁷ Compared to traditional photodynamic therapy (PDT),¹⁸ a phototherapy that normally is oxygen-dependent, PACT offers an oxygen-independent mechanism, more suitable for hypoxic tumors, where the concentration of oxygen is notably low.¹⁹

3.1.1 Ruthenium anticancer drugs

Other transition metal complexes, especially ruthenium (Ru) complexes, have been presented as an interesting alternative to platinum drugs owing to their potential anticancer properties and selective cytotoxic activity.²⁰ As a transition metal in group 8, the second row of the transition metal series, ruthenium has two main oxidation states, Ru(II) and Ru(III). Since the highest oxidation state is relatively unstable inside the cell, due to the low oxygen content caused by the fast metabolism in tumor sites (Figure 3.2),²¹⁻²⁴ the reduction of ruthenium's oxidation state from Ru(III) to Ru(II) takes place readily attacking the cancer cells. On the other hand, the healthy cells are not affected by the highest oxidation state. Also, ruthenium compounds theoretically possess unique biochemical features allowing them to accumulate preferentially in neoplastic tissues.²⁵

Till now, several Ru(III) complexes as chemotherapeutic agents have already entered clinical trials, such as NAMI-A, KP1019, and KP1339 (Figure 3.2). NAMI-A was the first approved Ru complex to reach clinical investigations and showed success in phase I clinical studies though showed only limited efficacy in the phase II stage, which resulted in the failure of the clinical investigations.²⁶ KP1019 has attracted lots of attention as promising anticancer drug alternative, although it has some drawbacks, such as poor solubility limited in phase I and low cytotoxicity *in vitro*. Instead, a more soluble sodium salt, KP1339, was developed to break the limitation for the further applications and is currently undergoing clinical trials.^{11, 27-32}

Also, more attentions has been focused on the photoactivation of Ru(II) complexes. Thus, the first Ru(II)-based photosensitizer for PDT, the TLD1433, has entered human clinical trials.³³ Different studies have also demonstrated that Ru(II) complexes may have potential as PACT agents.¹¹ Compared to Pt(IV) complexes, Ru(II)-based PACT agents have some promising

advantages such as the easy-tunable molecular structures, rich photochemical properties, while the octahedral structures may endow them with good activity against cisplatin-resistant cancer cells.³⁴⁻³⁵



- Accumulation preferentially in tumors rather than normal tissues
- Remaining its relatively inactive Ru(III) oxidation state until it reaches the tumor site
- Greater efficacy against cancer metastases than against primary tumors

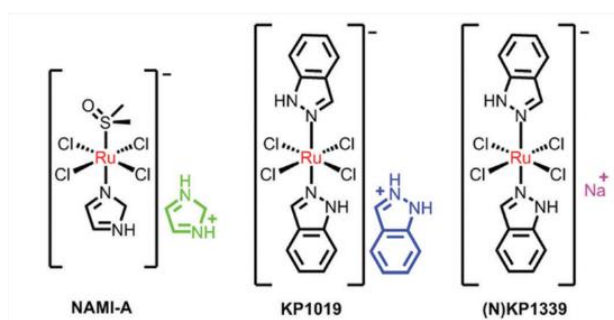


Figure 3.2: Advantage of ruthenium anticancer drug and chemical structures of NAMI-A, KP1019 and KP1339

3.1.2 Photo-activatable Ru complexes for photodynamic therapy and photoactivated chemotherapy

Photoactivation is an important and efficient way to improve selectivity and reduce the side-effect of Ru complexes in cancer therapy. An ideal photoactivatable Ru metallodrug should be non-toxic in the dark but become toxic to cancer cells when they are delivered to tumor tissue and activated by light, providing photodynamic(PDT) or/and PACT activity.³⁶⁻³⁷

3.1.2.1 Photodynamic therapy

Photodynamic therapy (PDT) is a two-stage treatment that combines light energy with a drug (photosensitizer) designed to destroy cancerous and precancerous cells after light activation.³⁸⁻⁴³ To achieve PDT, three essential factors are required:

Light: light is used to excite molecules to higher electronic excited states, which possess the energy to undergo processes not possible in the ground state. In PDT, it is normally desired to induce excitation of the photoactive agent by using radiation of the visible or near infrared (NIR) spectral region, to avoid the absorption of the biological tissues and assure deeper

penetration. due to the complexity of the samples related to the biological imaging, criteria for assessing phototoxicity cannot be set. To minimize the negative influence on the biological objects during observation, practical assessments and standards have to be setup and ultraviolet with high energy and shallow penetration depth should be avoided to the greatest extent possible. no

A photosensitizer: Normally, a photosensitizer is activated by light (usually from a laser source). The optimum scenario is that the photosensitizer is nontoxic until it is activated by light irradiation in the targeted tissue. Although there is a large variety of photosensitizers that have been tested out *in vivo* and *in vitro*, very few have shown promising properties.⁴⁴⁻⁴⁶ Rapid clearance, selectivity for tumor cells, chemical and physical stability, activation at wavelengths with optimal tissue penetration are all crucial parameters for the photosensitizer.

Oxygen: When the photosensitizers are irradiated they populate an excited state, normally a singlet, which after intersystem crossing (ISC), triplet excited states are forming. The triplet excited states usually have quite long lifetime (from μs to s) and their energy is released through two main paths. In a Type 1 mechanism, the triplets react with a substrate to form radicals that can further react with oxygen to produce reactive oxygen species (ROS).⁴⁷⁻⁴⁹ In Type 2 mechanism, the triplet are quenched by the ground state molecular oxygen ($^3\text{O}_2$), which is sensitized to produce highly reactive oxygen radical and singlet oxygen ($^1\text{O}_2$).⁵⁰ Both Type 1 and Type 2 reactions can occur simultaneously, and the ratio between these processes depends on the type of photosensitizers and the surrounding.^{47, 49}

In addition to treat cancer, PDT also has been used to treat bacterial, fungal and viral infections.⁵¹⁻⁵² Also, different studies have shown that PDT can also trigger the body's immune response,⁵³⁻⁵⁴ affording another means to help destroy cancerous and precancerous cells.

3.1.2.2 Photoactivated chemotherapy

Photoactivated chemotherapy (PACT) is a new name for “photocaged” compounds, which were firstly introduced by organic chemists Engels and Kaplan in 1970s using photocleavable moiety to protect bioactive center.⁵⁵⁻⁵⁶ PACT compounds can be activated by light, which

involves bonds cleavage or redox reaction. This irreversible reaction allows biological reactions and toxic ligand release to realize therapy (Figure 3.3).⁵⁷⁻⁶⁰

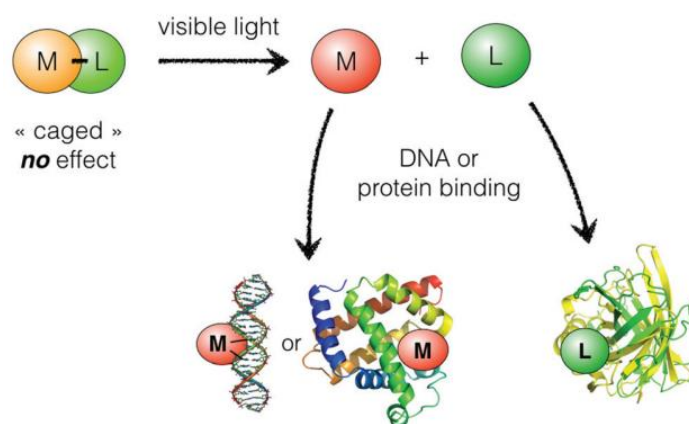


Figure 3.3: General principle of photoactivated chemotherapy. M represents a metal-based compound and L a ligand. Before light irradiation both compounds cage each other. Cleavage of the M–L bond occurs either via photoreduction, photosubstitution, or radical mechanisms. Either the fragment M or L, or both, may bear some biological activity. Image extracted from reference.⁶¹

Compared to PDT, PACT allows the oxygen-independent activation of drugs, which then also works under hypoxic conditions. This feature makes it potentially more versatile than Type II PDT, which requires the presence of a significant amount of molecular oxygen to generate enough reactive $^1\text{O}_2$ species to induce cytotoxicity.^{16-17, 37, 57, 62-67} PACT facilitates the control over when and where a drug is activated, resulting in a notable specificity of drug action.

For PACT, metal complexes are normally used. The effect of light on metal complexes and the subsequent effects on biomolecules, particularly DNA, is well-documented. Light can alter the electronic structure of molecules and induce changes in both physical and chemical properties. The generated excited state is typically short-lived; however, as the molecule returns to the ground state, the energy can be dissipated in different ways, in the form of light or heat, induce a chemical modification of the structure or transferred to another species.¹⁷ Metal complexes have excited states that can be normally obtained upon irradiation with UV-vis light. Transition metal complexes with d^3 and d^6 electronic configurations are particularly promising, due to their photophysical properties and the relative non-lability of complexes.⁶⁸ PACT agents can be activated through different mechanisms:⁶¹

Photoreduction: In the reductive environment, mostly Pt(IV) or Co(III) based complex will undergo reduction, yielding cytotoxic Pt(II) or Co(II) species and one or more organic ligands.⁶⁹⁻⁷⁰

C-C bond cleavage: This process is caused by a response of neighboring metal center upon irradiation, which has been widely used for many photocaged compounds.⁷¹⁻⁷²

Photosubstitution: This is a nonredox reaction involving ligand exchange. Chemically speaking, d6 metal ions, such as Ru(II), Rh(III), Ir(III), or Re(I), undergo photosubstitution upon light irradiation, which generates triplet excited states of metal-to-ligand character (³MLCT) and subsequently interconverts to a highly dissociative excited metal-centered triplet state (³MC) resulting in substitution of mostly water molecule (aquation) with a free ligand(s) release.^{36-37, 57}

New Pt(IV) complexes have also been developed as PACT compounds that absorb in UVA (320–400 nm) or high-energy visible light (400–450 nm), which damage cells and have shallow penetration depth.^{58, 73} However Ru-based complexes can be activated at higher wavelengths and closer to the phototherapeutic window.^{36-37, 57} Before bring the these PACT agents to the clinical use, there are still some challenges needed to be handled, such as water solubility, preferential accumulation in tumours,⁷⁴ precise controlled release of the drug,^{73, 75-76} increase of the biocompatibility while minimizing residual toxicity in the dark⁷⁷⁻⁷⁹ and improvement of their fast clearance from the bloodstream,⁸⁰ must be faced without compromising photoinduced activation.

To overcome most of these limitations, an interesting approximation consists on the incorporation of photolabile complexes in nanoparticles (NPs),⁸¹⁻⁸² included Ru-based complexes, for their application in photoinduced therapies.⁸³ For instance, Wu *et al.* have reported the covalent link of Ru to block copolymers (Figure 3.4)^{37, 84} that stabilize photoactivatable ruthenium complexes under physiological conditions.⁸⁵ This strategy includes ruthenium-containing block copolymer units that self-assemble into nanoparticles in aqueous solution with excellent uptake *in vitro* and *in vivo* results. The inhibition of cancer cells was related to the generation of singlet oxygen (¹O₂) upon irradiation with red-light.^{36, 86}

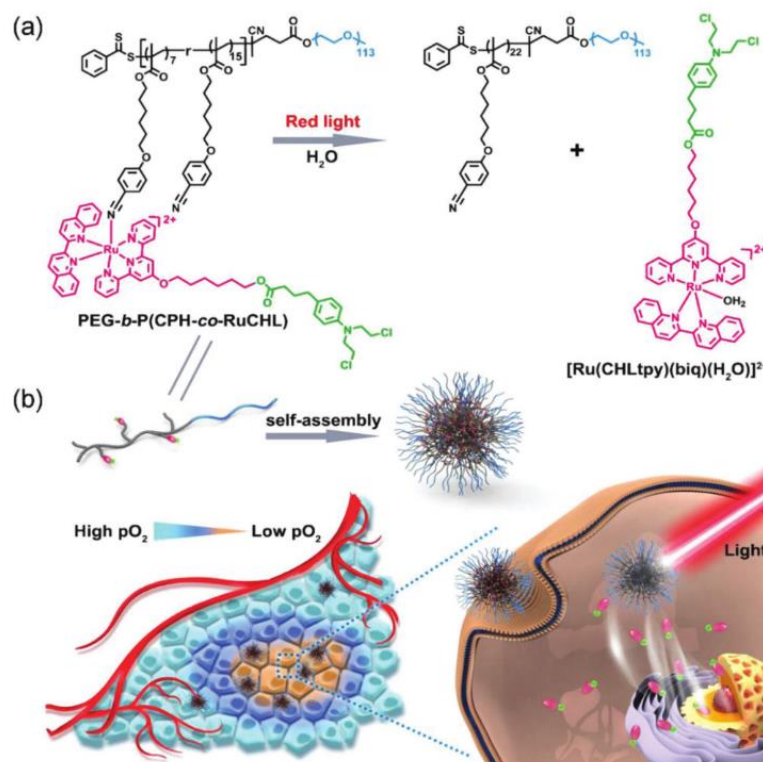


Figure 3.4: Structure and photoreaction of the metallopolymer PEG-b-P(CPH-co-RuCHL). The green and purple parts in the chemical structures represent the drug (CHL) moiety and the Ru complex moiety. Red light induces the release of the drug–Ru complex conjugate [Ru(CHLtpy)(biq)(H₂O)]²⁺. b) Self-assembly of PEG-b-P(CPH-co-RuCHL) and its phototherapy in hypoxic tumor environment. Images extracted from reference.³⁷

Other approaches involve the conjugation of photocleavable Ru complexes to the surface of upconverting NPs.⁸⁷⁻⁹⁰ Zhou *et al* have synthesized Bovine serum albumin (BSA) coated lanthanide-doped upconversion nanoparticles (NaYF₄:Yb:Tm@NaYF₄ (UCNPs)) loaded using a Ru(II) PACT agent [Ru(dip)₂(spc)]⁺. The resulting UCNP@BSA@Ru nanoparticles can peel off [Ru(dip)₂(spc)]⁺ upon dual light irradiation (980 or 470nm). Also, UCNP@BSA@Ru nanoparticles showed good photo-cytotoxicity towards a series of cancer cell lines (Figure 3.5).

Nonetheless, the encapsulation of photoactive Ru-based complexes is in its fledgling stage, so there is a growing interest to develop novel nanoparticles that allow a proper fine-tune structure/function correlations and adapt it for their use in photoactivated chemotherapy.⁹¹

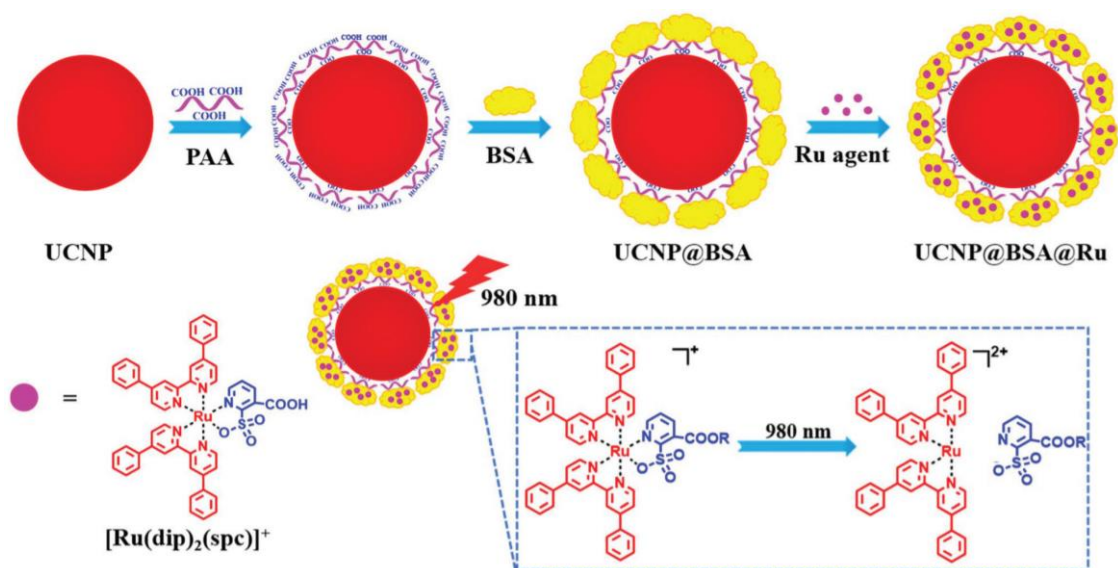


Figure 3.5: Schematic illustration of the fabrication of UCNP@BSA@Ru nanoparticles and their PACT action upon 980 nm irradiation. Image extracted from reference⁸⁷.

3.2 Objective

The general objective of this work was the preparation of non-cytotoxic Ru-based coordination polymer nanoparticles (CPNs) with photoactivated chemotherapy properties, promoted by visible light. For this we aimed to use a coordination polymer where the backbone of the polymer is constituted by the complex $[\text{Ru}(\text{biqbp})_2(\text{dms})\text{Cl}]\text{Cl}$ monomer (complex **1**, where biqbp stands for 6,6'-bis[N-(isoquinolyl)-1-amino]-2,2'-bipyridine), linked through Ru center and bis(imidazol-1-yl)hexane (**BIS**) or bis(imidazol-1-ylmethyl)benzene (**BIX**) spacers to afford Ru-BIS-based CPNs (**RuBIS-CPNs**) and Ru-BIX-based CPNs (**RuBIX-CPNs**). The choice of this compound as a monomer was dictated by the results of previous studies, carried out by the group of Prof. Silvestre Bonnet (Leiden university), which proved the non-toxic anti-cancer drug precursor complex **1** that can be converted efficiently into the cytotoxic aqueous active species $[\text{Ru}(\text{biqbp})(\text{H}_2\text{O})_2]^{2+}$ through photosubstitution (aquation) (Figure 3.6). The **BIS** or **BIX** acts as a bridging ligand between the monomeric complex without affecting its property and the alkyl chain provide the amorphous character to the polymer, within the nanoparticles (Figure 3.7).

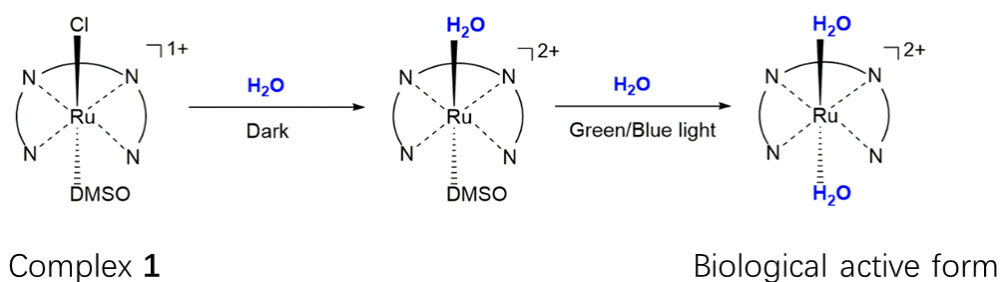


Figure 3.6: Ligand exchange processes upon dilution of complex **1**

Similar CPNs (e.g. Pt (IV)-based CPNs) have already been successfully demonstrated to be highly performing as biocompatible contrast agents and antitumoral application.⁹²⁻⁹³ Thus this nanostructure is expected to offer good colloidal stability, scalability, cellular internalization, and even more noticeably high payloads, as the prodrug constitutes the backbone of the nanoparticles polymer itself.⁹⁴ All these advantages turn out to be really helpful to reduce the dose, the irradiation intensity required to activate the anticancer drug diffusion, and therefore any side effect. Though, in spite these advantages, the number of ruthenium-based coordination polymers with antitumor applications is rather limited and none of them have been shown photoactivable properties.

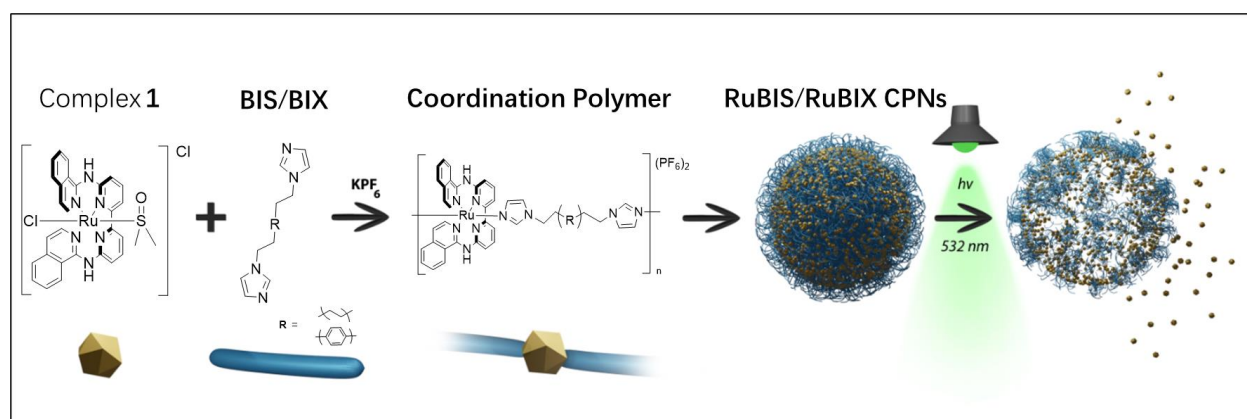


Figure 3.7: Scheme of synthesis and photoactivation process of Ru-based coordination polymer nanoparticles (**RuBIX** and **RuBIS-CPNs**).

3.3 Results and discussion

3.3.1 Synthesis and characterization of RuBIX-CPNs and RuBIS-CPNs

The polymerization process was performed using two different ligands acting as linking agent of the monomeric unit, through the coordination to the Ru: **BIX** or **BIS**. These two ligands were chosen because they are nontoxic and relatively flexible.⁹⁵⁻⁹⁷ To obtain the corresponding photoactive **RuBIS-CPNs** and **RuBIX-CPNs**, the polymerization was carried out following a methodology previously described for the synthesis of other Zn^{2+} , Fe^{2+} and Co^{2+} based **CPNs** of relevance in biological applications.^{95-96, 98-99}

Complex **1** was refluxed in water under N_2 atmosphere and then mixed with the ethanol solutions of **BIX** or **BIS** ligand, slowly injected in the Ru-complex solution, while refluxing. The refluxing time after the addition of the ligands was varied between xx and xx h, as it was observed that it affected the size of the **CPNs**, as shown below. After refluxing, and cooling down to room temperature a saturated KPF_6 solution was added to the mixture to obtain a brown precipitate (Figure 3.8). The solids obtained from the two syntheses was centrifuged, washed with cold ethanol, and freeze-dried for subsequent storage and characterization.

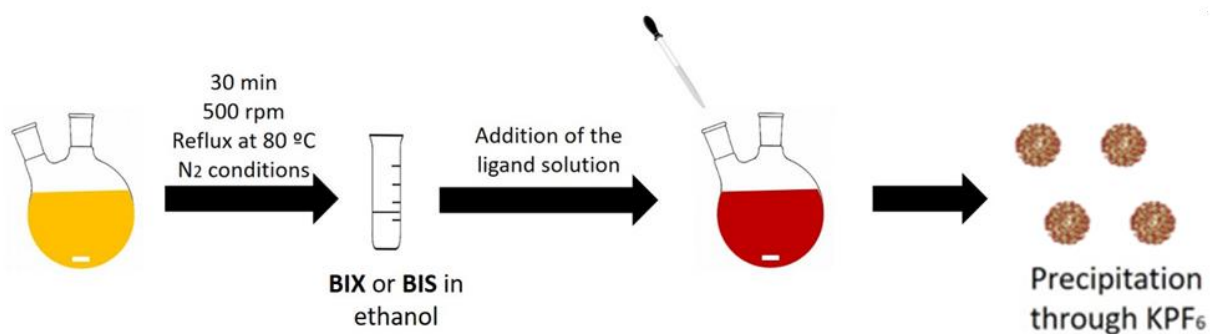


Figure 3.8: Schematic of the **RuBIX** and **RuBIS-CPNs** synthesis.

Before studying the PACT properties chemical, morphological and optical characterization of the solid was carried out. FTIR of the freeze-dried solid showed the presence of the peaks associated to **BIX** (2952 cm^{-1} and 498 cm^{-1}) or **BIS** (3000 cm^{-1} , 1509 cm^{-1} and 1472 cm^{-1})¹⁰⁰ and of complex **1** (1532 cm^{-1} and 1098 cm^{-1}). More importantly, the appearance of new bands for both **RuBIX-CPNs** (825 cm^{-1} and 443 cm^{-1}) and **RuBIS-CPNs** (839 cm^{-1} and 432 cm^{-1}), assigned to the antisymmetric stretching modes of PF_6 and Ru-N,

respectively, which confirmed the coordination of the **BIX** and **BIS** ligand to complex **1** and the presence of PF_6^- as a counterion (Figure 3.9).¹⁰¹

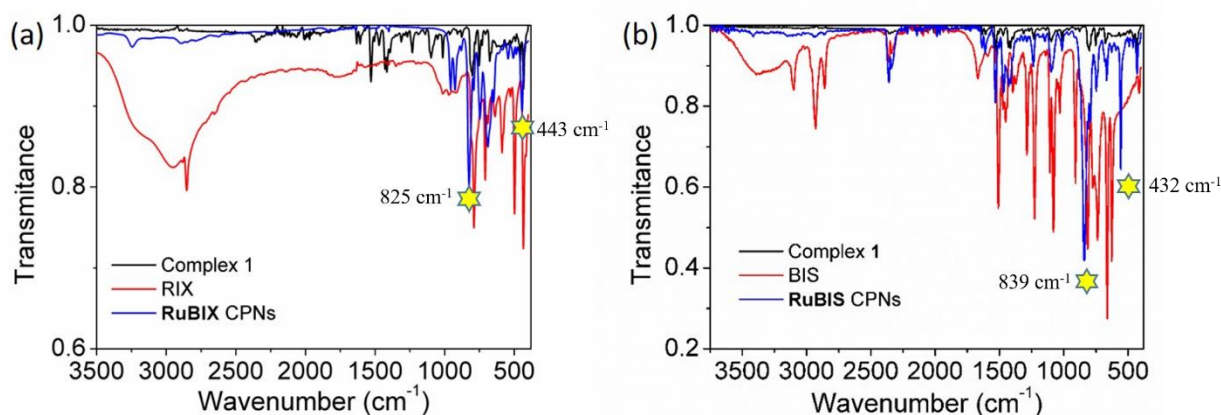


Figure 3.9: FTIR spectrum of (a) **RuBIX** and (b) **RuBIS-CPNs** compared to the complex **1**, **BIS** and **BIX** FTIR spectra.

The scanning electron microscopy (SEM) analysis of **RuBIX-CPNs** revealed the formation of spherical particles with a rough surface and an average diameter of 210 ± 37 nm (Figure 3.10a), in agreement with the dynamic light scattering (DLS) measurements, showing a hydrodynamic diameter of 214 ± 103 nm (Figure 3.10d). When **RuBIS-CPNs** were obtained after 2h (refluxing time after ligand addition), similar dimensions and size distribution as for **RuBIS-CPNs** (200 nm, Figure 3.10b) were obtained, though these showed a smoother surface. Moreover, for these **RuBIS-CPNs** it was noticed that the size could be significantly decreased by reducing the reaction time. Indeed by shortening the reaction time to 1 hour the average hydrodynamic diameter of the **RuBIS-CPNs** in Milli-Q[®] water was reduced to 93 ± 46 nm (Figure 3.10c), in agreement with the average size of 50 ± 12 nm found by SEM (Figure 3.10e). This size tunability and reduction provided by the synthetic method is highly important, as it allows making these **CPNs** small enough enhance the cellular uptake, required for the

application of these **PACT-CPNs** in biological systems.

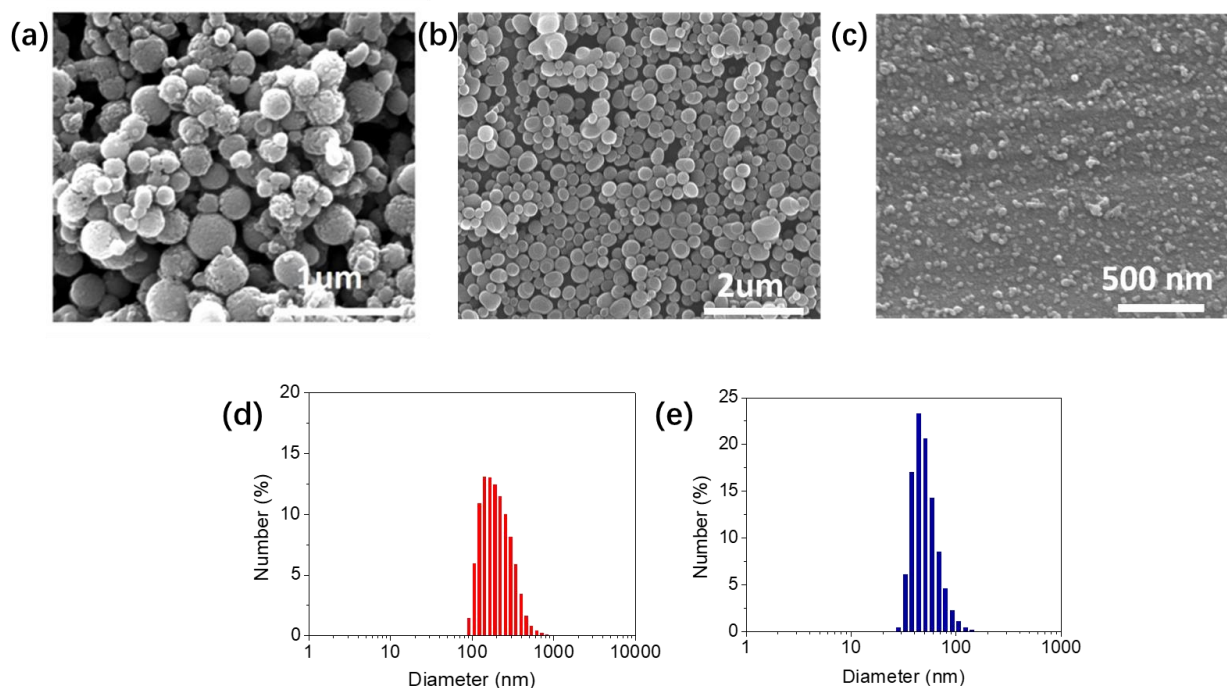


Figure 3.10: (a) Representative SEM images of (a) **RuBIX-CPNs**, (b) **RuBIS-CPNs** (2 hours reaction), **RuBIS-CPNs** (1 hours reaction) dispersed in Milli-Q[®] water, scale bar: 1 μm, 2 μm and 500 nm respectively. DLS measurements for a 50 ug/mL of (d) **RuBIX-CPNs**, (e) **RuBIS-CPNs** (1 hours reaction) suspension in Milli-Q[®] water.

For the same reason, before performing further characterization of the **PACT-CPNs**, we aimed to investigate their colloidal and chemical stability in aqueous media relevant for biological applications. For this it was chosen a phosphate buffered saline (PBS) aqueous solution, containing bovine serum albumin (BSA) protein (20 mg/mL).

It was observed that when the **RuBIX-CPNs** were kept in this medium during 2.5 h, they lost their shape forming unstructured material, as shown by SEM image (Figure 3.11a). and The loss of the nanostructure was possibly related to the coordination exchange with phosphate in PBS. DLS analysis of the **RuBIX-CPNs** suspension upon time revealed a size increase, which was ascribed to the formation of aggregates. These results indicated that **RuBIX-CPNs** are not stable in the simulated physiological media (Figure 3.11b). On the other hand, **RuBIS-CPNs** showed colloidal stability in BSA-containing (20 mg/mL) PBS solution for at least 24 h as corroborated by DLS analysis. Therefore, because their colloidal and chemical stability, the **RuBIS-CPNs** were chosen for further studies (Figure 3.11c).

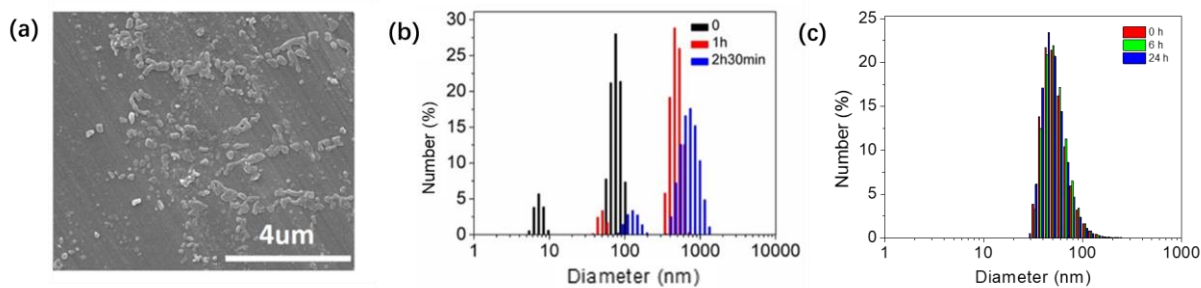


Figure 3.11: (a) Representative SEM image of **RuBIX-CPNs** dispersed in PBS buffer containing 20 mg/mL BSA. DLS monitoring measurements for a 50 ug/mL (b) **RuBIX-CPNs** (2.5 h) and (c) **RuBIS-CPNs** (24h) suspension in PBS buffer containing BSA (20 mg/mL).

Inductively coupled plasma mass spectrometry (ICP-MS) analysis of the **RuBIS-CPNs** showed a content of Ru in the **CPNs** of 6.9 ± 0.2 wt% (Figure 3.2.4a). Finally, the lack of diffraction peaks in the X-ray powder diffraction (XRD) indicated the amorphous nature, of the obtained **RuBIS-CPNs** (Figure 3.11b).

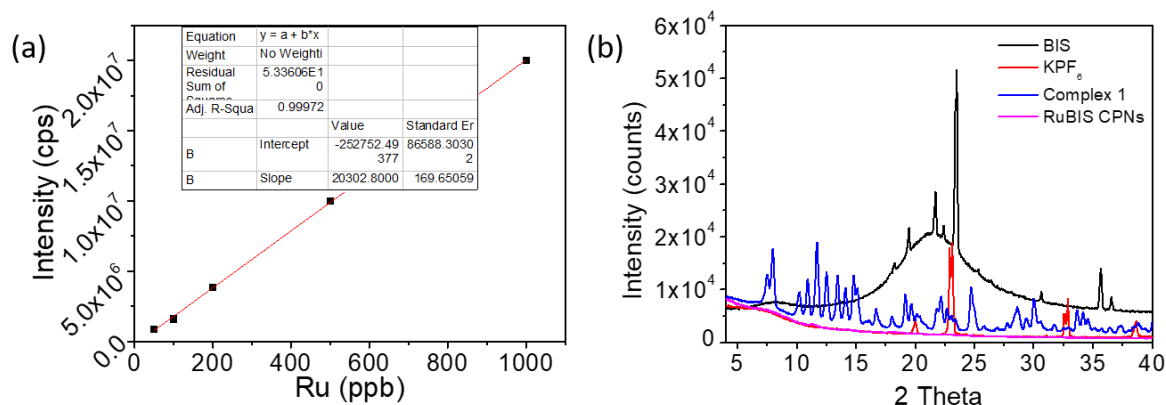


Figure 3.12: (a) Inductively coupled plasma mass spectrometry (ICP-MS): the calibration curve of the Ru. From this curve and the signal intensity related to the Ru in the **CPNs** allowed to determine a percentage of Ru in the **CPNs** of 6.9 ± 0.2 wt%. (b) X-Ray Diffractometry of BIS ligand (black), KPF_6 (red), complex 1 (blue), and **RuBIS-CPNs** (pink)

To quantify the exact amount of each component in **RuBIS-CPNs**, nuclear magnetic resonance (NMR) technique was used. However, the slow rotational correlation time in NMR of these nanoparticles in a colloidal solution makes it difficult to obtain a quantitative NMR spectrum. To accomplish this, the **RuBIS-CPNs** were dissolved in deuterated dimethyl sulfoxide solvent ($(CD_3)_2SO$) containing a certain quantity of deuterium chloride (DCl) to

decompose the nanoparticles into the molecular entities and thus obtain sharp signals that allow quantifying the ligand-to-ligand ratio. To make sure that different spectra are comparable, the same ratio DCl/(CD₃)₂SO was used (50 μL DCl/mL (CD₃)₂SO).

In order to have precise quantification, fluoroacetonitrile (CH₂FCN) that has H and F atoms was chosen as the internal reference. After testing out the ¹H NMR spectra of dissolved **RuBIS-CPNs**, complex **1**, **BIS**, and CH₂FCN, the ¹H NMR spectrum of dissolved **RuBIS-CPNs** showed the typical pick from each component (a,b,c peaks assigned from the spectrum of **BIS**, and e,f peaks from complex **1**, Figure 3.13a). From ¹⁹F NMR spectra of dissolved **RuBIS-CPNs**, it proved the presence of PF₆⁻.

$$P_{sample} = \frac{S_{sample}}{S_{std}} \times \frac{N_{std}}{N_{sample}} \times \frac{m_{std}}{m_{sample}} \times \frac{M_{sample}}{M_{std}} \times P_{std}$$

S = Integrated area of the peak, N = Number of protons (Number of hydrogen atoms in the functional group), m = Prepared mass, M = Molecular weight, P = Purity

With the equation presented above, it allowed us proposing the chemical formula [[Ru(biqbpy)]_{1.5}(bis)](PF₆)₃. The characterization analysis was successfully performed for at least three different batches of **RuBIS-CPNs** to assure the reproducibility of the synthetic methodology.

The stoichiometric deviation from theoretical expected ratio of the components for a linear polymer ([Ru(biqbpy)]:**BIS** = 1:1) is quite archetypal for **CPNs**. This is attributed to the out-of-equilibrium synthetic conditions that lead to the fast precipitation process of oligomeric species with different stoichiometry.^{93, 95-96, 102-103} In any case, the Ru-complex payload was as high as 41 wt%, which is more than 4-fold higher than most conventional metallodrug-loaded polymer carriers known to date (typically less than 10%).¹⁰⁴

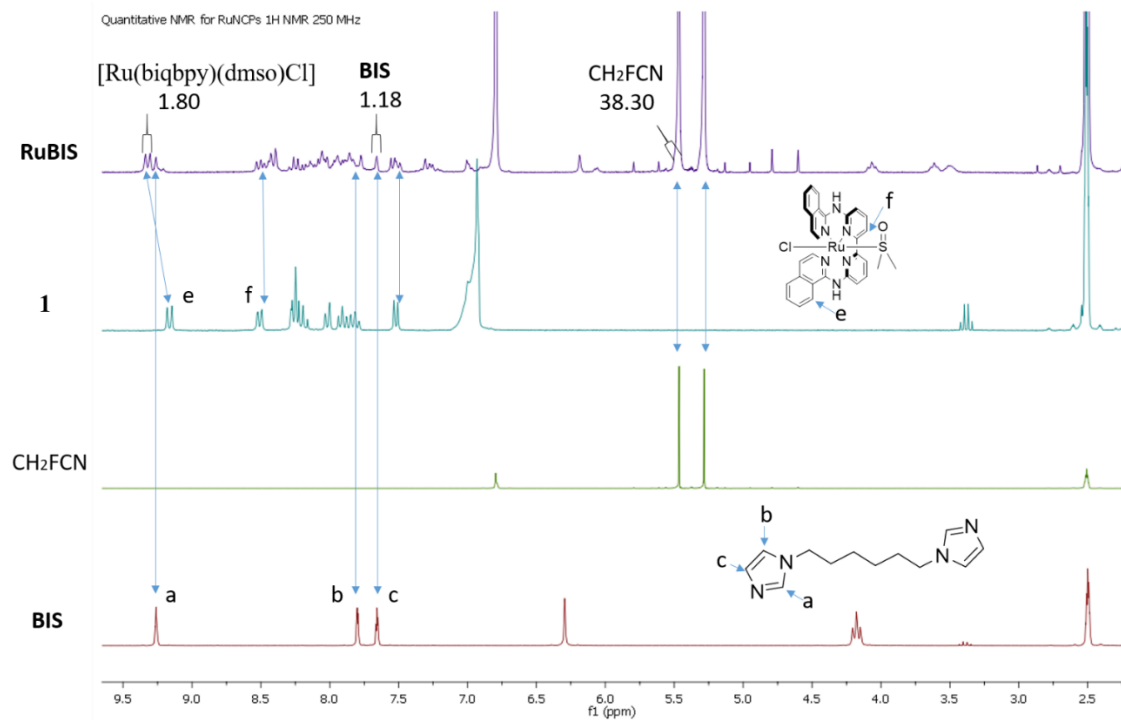


Figure 3.13a: ¹H NMR spectra of (top to bottom) **RuBIS-CPNs**, complex **1**, CH₂FCN (internal reference) and **BIS**.

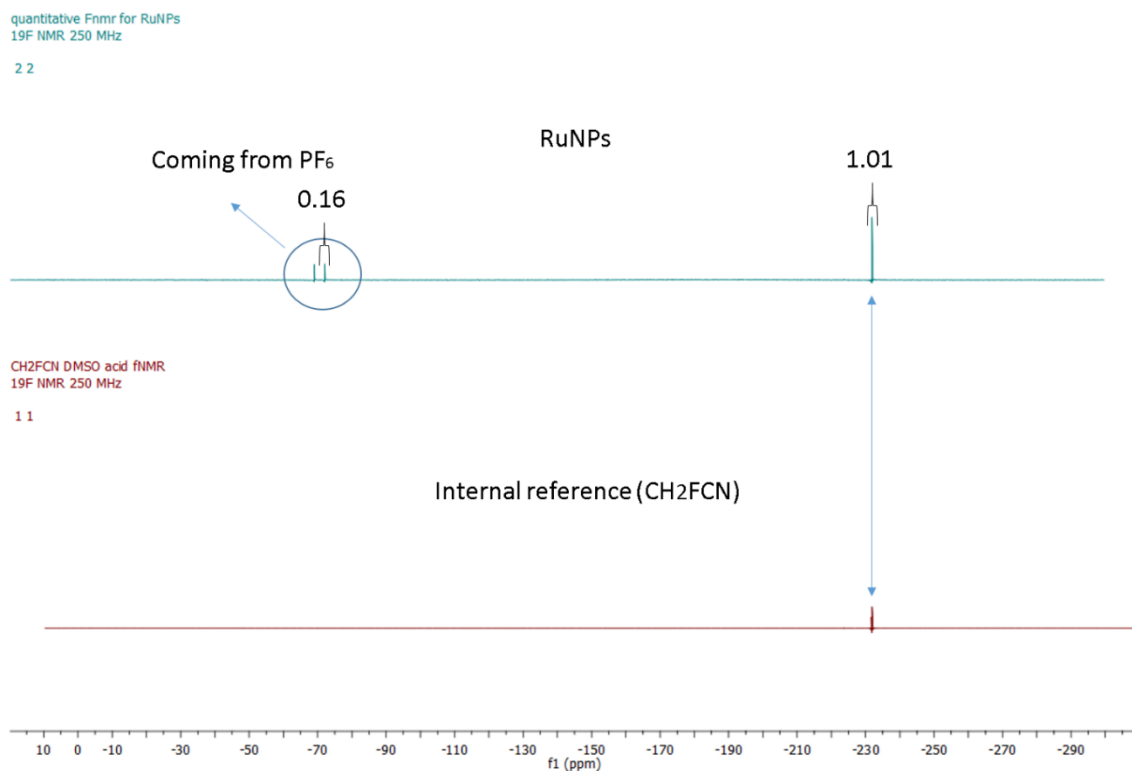


Figure 3.13b: ¹⁹F NMR spectra of **RuBIS-CPNs** and CH₂FCN (internal reference)

3.3.2 Photoactivity of RuBIS-CPNs

After the chemical and morphological characterization of the **RuBIS-CPNs**, the next step consisted of the investigation of their behaviour upon absorption of light. The photoactivity of the **RuBIS-CPNs** was monitored by both UV-Vis spectroscopy and high-performance-liquid-chromatography (HPLC).

Monitorization by UV-Vis

UV-Vis spectroscopy of fresh-made PBS suspensions of the **RuBIS-CPNs** showed an absorption band with a maximum at $\lambda_{\max} = 315$ nm and two shoulders at $\lambda_{\text{abs}} = 365$ nm and 439 nm, which extended up to 600 nm (Figure 3.14, black curve, time = 0 min). No spectral changes were observed in the dark upon time (3 h and 10 min). The DLS measurement was carried out along with the absorption measurement to monitor the size change, which turned out a size maintaining.

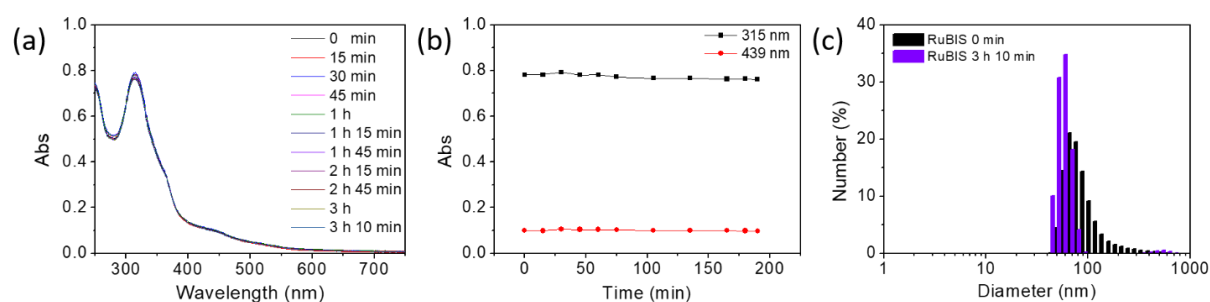


Figure 3.14: (a) Evolution of the UV-vis absorption spectra of a PBS suspension of **RuBIS-CPNs** in the dark over time. (b) Plot of absorption intensity at 315 and 439 nm of the **RuBIS-CPNs** suspension in the dark. (c) DLS tracing results of the **RuBIS-CPNs** suspension in PBS solution recorded at 0 min and 3 h 10 min.

On the other hand, significant spectral changes were found under irradiation. For these experiments two different irradiation wavelengths were selected: i) 450 nm, close to the **CPNs** absorption maximum in the visible region and ii) 532 nm, taking advantage of the tail of the broad absorption band. This last wavelength should be not only suitable for triggering the photosubstitution reactions but is also less harmful than blue light to living cells and allows deeper penetration in biological tissues.

Irradiation with 450 nm (0.35 W/cm^2) for the first 10 min showed a red-shift of the main band, from $\lambda_{\max} = 315$ to 326 nm and an intensity increase of the shoulder at $\lambda_{\text{abs}} = 439$ nm (Figure 3.15a,b). Irradiation for longer periods (up to 2.5 h) evidenced an intensity decrease of both bands, and of the shoulder at $\lambda_{\text{abs}} = 365$ nm, until its disappearance (Figure 3.15a,b).

Moreover, an isosbestic point at $\lambda_{\text{iso}} = 406$ nm was observed for the spectra recorded during the second period of irradiation. These results suggest that two different processes are occurring before and after the 10 min irradiation and that the intermediate species is interconverting in the final product. This time-dependent two-step process was tentatively explained by an initial fast formation of photoinduced intermediate species ($t_{\text{irradiation}} \leq 10$ min) and its subsequent slower photochemical reaction ($t_{\text{irradiation}} > 10$ min) leading to the formation of the final photoproduct.

Irradiation with green light ($\lambda_{\text{exc}} = 532$ nm, 0.42 W/cm²) yielded similar results though the spectral changes occurred more slowly possibly due to the lower absorption of the **RuBIS-CPNs** at this wavelength. A red shift from $\lambda_{\text{max}} = 315$ to 326 nm and an increase of intensity at $\lambda_{\text{abs}} = 439$ nm was observed for the first 15 min of irradiation, while longer irradiation periods (up to 3 h) induced a decrease of the two bands (326 nm and 439 nm) and the formation of an isosbestic point (Figure 3.14c,d). The similar evolution of the UV-Vis spectra observed for the molecular complex **1** under blue and green light irradiations,⁵⁷ suggested a similar photo-induced process towards the active photoproduct.

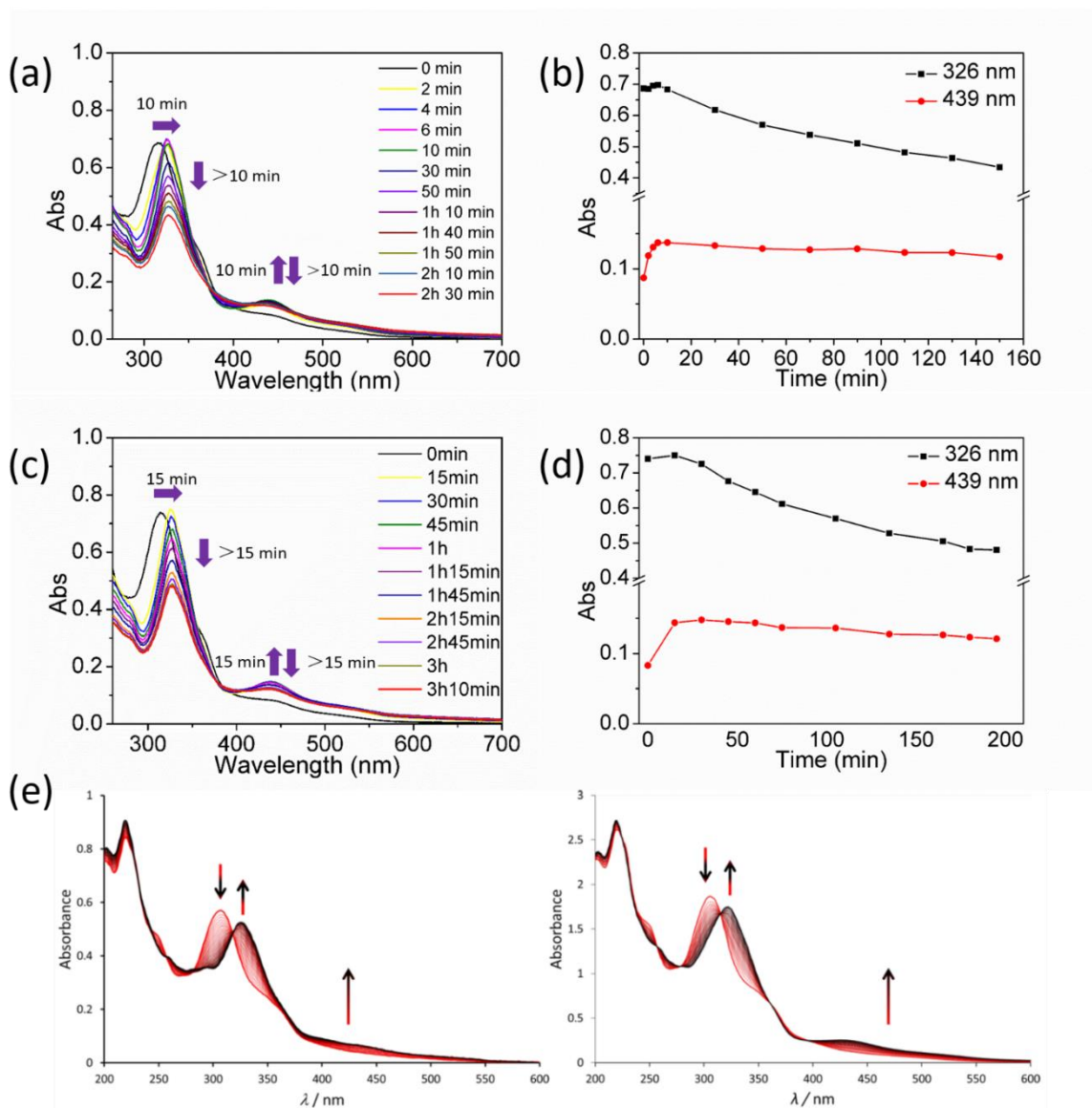


Figure 3.15: (a) Evolution of the UV-vis spectra of a PBS suspension of **RuBIS-CPNs**, upon blue light irradiation ($\lambda_{ex} = 450$ nm). (b) Plot of absorption changes at 326 nm (black) 439 nm (red). (c) Evolution of the UV-vis spectra of a PBS suspension of **RuBIS-CPNs**, upon green light irradiation ($\lambda_{ex} = 450$ nm). (d) Plot of absorption changes at 326 nm (black) 439 nm (red). (e) Evolution of the UV-vis absorbance spectra of a solution of complex 1, upon 450 nm blue (left) or 530 nm green light (right) irradiation under argon. Image extracted from reference.⁵⁷

HPLC studies

In order to get more information on the photoactivated process in which undergo the **RuBIS-CPNs**, it was decided to analyse the photoproducts of the irradiated **CPNs** with high-performance-liquid-chromatography (HPLC).

Its intrinsic selectivity and sensitivity compared to ^1H NMR or UV-Vis spectroscopy allows the determination and quantification of the photoproducts as well as to differentiate the final Ru-containing products, more specifically than with inductively-coupled plasma mass spectrometry (ICP-MS).^{36-37, 105-106} For the HPLC studies it was decided to use only 532 nm light as it was confirmed to induce photoreaction of the **RuBIS-CPNs** and is more relevant for biological application than the 450 nm light.

In order to discriminate the formation of the photoproduct, from the possible by-products, it was first decided to irradiate a stock solution of molecular complex **1** in water. The photoreactivity of this complex was previously studied by Bonnet and coworkers who concluded the conversion of the complex **1** to the active aqueous photoproduct was quantitative under green light irradiation.⁵⁷ Therefore, if the **RuBIS-CPNs** were releasing the same photoproduct, it should have had the same retention time in the HPLC. Because of the quantitative conversion of complex **1** into the aqueous compound, a calibration curve of the photoproduct could be obtained ($R^2 = 0.996$) irradiating solutions of different concentrations of the complex **1** (1 mg/mL) with green light (1.1 W/cm^2) for 20 h, a time period considered sufficient to complete the photoconversion. The resulting irradiated solution showed a single peak at retention time 18.3 min assigned to the active complex $[\text{Ru}(\text{biqbpy})(\text{H}_2\text{O})_2]^{2+}$, as confirmed by ESI mass spectrometry with the corresponding $m/z = 271.0$ (calc. $m/z = 270.8$) (Figure 3.16a,b). With dilution of irradiation solution, several different concentrations (0.1, 0.5, 1.0, 5.0, 10.0, 20.0 $\mu\text{g/mL}$) have been made for a calibration curve (Figure 3.16c). In addition, the absorption of the isolated active complex (drug) has been measured and compared to the **RuBIS-CPNs** to indicate the spectrum change (Figure 3.16d).

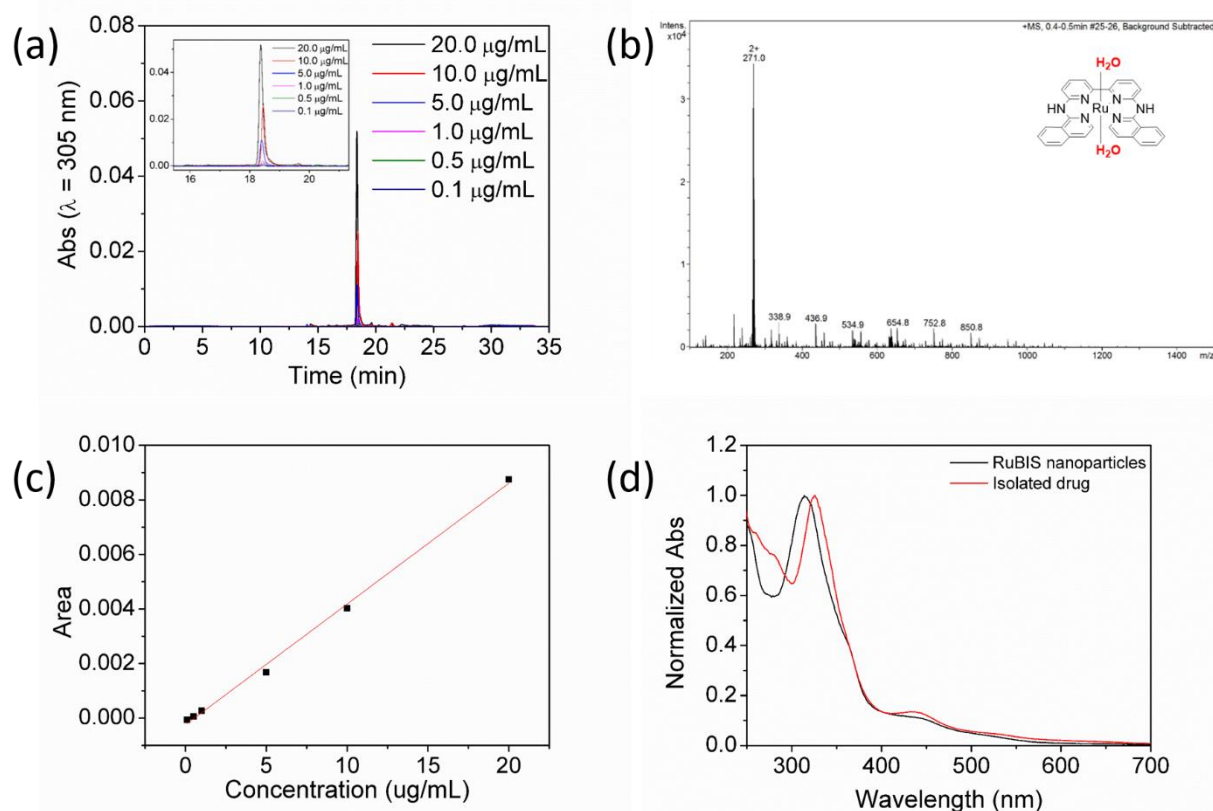


Figure 3.16: (a) The whole chromatogram of fully activated drug $[\text{Ru}(\text{biqbpy})(\text{H}_2\text{O})_2]^{2+}$ converted from $[\text{Ru}(\text{biqbpy})(\text{dmsO})\text{Cl}]\text{Cl}$ at different concentrations. (b) Mass spectrometry of the fractions: retention times = 18.3 min, m/z ($[\text{Ru}(\text{biqbpy})]^{2+}$) = 271.0 (calc. m/z = 270.8). (c) The drug ($[\text{Ru}(\text{biqbpy})(\text{H}_2\text{O})_2]^{2+}$) calibration curve. (d) UV-vis of isolated drug ($[\text{Ru}(\text{biqbpy})(\text{H}_2\text{O})_2]^{2+}$) collected from HPLC and **RuBIS-CPNs** before light irradiation.

Once the retention time of the aqueous product was determined and the calibration curve was obtained colloidal suspensions of **RuBIS-CPNs** in PBS buffer was irradiated ($\lambda_{\text{exc}} = 532$ nm, 1.1 W/cm^2 and 24 h) and aliquots at different irradiation times were taken, filtered and analysed by HPLC. To assure the detection of the released complex, the concentration of the initial suspension was increased with respect to that used in UV-Vis experiments up to $200 \mu\text{g/mL}$ and the irradiation time enlarged.

Three different peaks with retention times of 14.7, 16.9 and 18.3 min, associated to different species, appeared after 30 min (Figure 3.17a). Continuous irradiation up to 6 h induced a notable increase of the peak at 18.3 min while the two others decreased until almost disappearing after 20 h (Figure 3.17b). The formation of intermediate species at shorter irradiation times and their decrease upon prolonged irradiation to form a final product resembles the behaviour observed with UV-Vis experiments (the different conversion times observed by UV-Vis vs. HPLC for the intermediates and final photoproduct were ascribed to the different **CPNs** concentrations used in each case). To get more detailed information on the

intermediate as well as the final photoproduct chemical composition, mass spectrometry was used. Analysis of intermediate fractions collected at retention times of 14.7 and 16.9 min revealed oligomeric species that may come from larger fragments. One of them (16.9 min) could be determined as $\{[\text{Ru}_2(\text{biqbpy})_2\text{bis}(\text{MeOH})_2](\text{PF}_6)_2\}^{2+}$ (found $m/z = 828.8$ calc. $m/z = 828.7$) (Figure 3.18a), while for the other intermediate (14.7 min) a final structure could not be achieved (Figure 3.18b,c). The fraction collected at retention time of 18.3 min was expected to be the target active complex $[\text{Ru}(\text{biqbpy})(\text{H}_2\text{O})_2]^{2+}$ (Figure 3.16a,b), as indeed confirmed by mass spectrometry. Using the calibration curve previously obtained with this bis-aqua product, it was possible to quantitatively determine that after 24 h of green light irradiation of a 200 $\mu\text{g}/\text{mL}$ **RuBIS-CPNs** suspension (PBS buffer release), 1.1 $\mu\text{g}/\text{mL}$ solution of the activated complex was obtained.

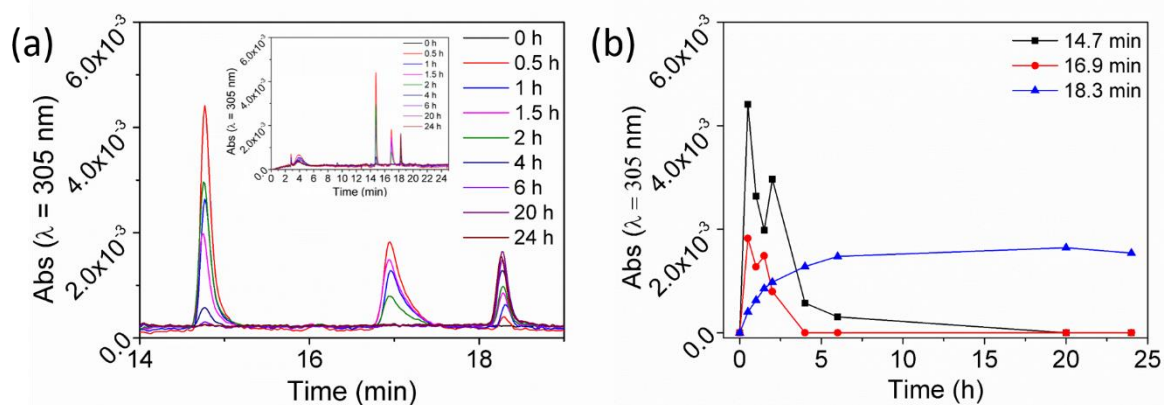


Figure 3.17: (a) Time-dependent HPLC evolution under irradiation of a **RuBIS-CPNs** colloidal suspension (200 $\mu\text{g}/\text{mL}$) (Inset) the whole chromatogram of the drug release of **RuBIS-CPNs** (0 – 35 min). (b) Plot of the time-dependent variation of each component (retention times) upon irradiation. Detection wavelength: $\lambda = 305$ nm.

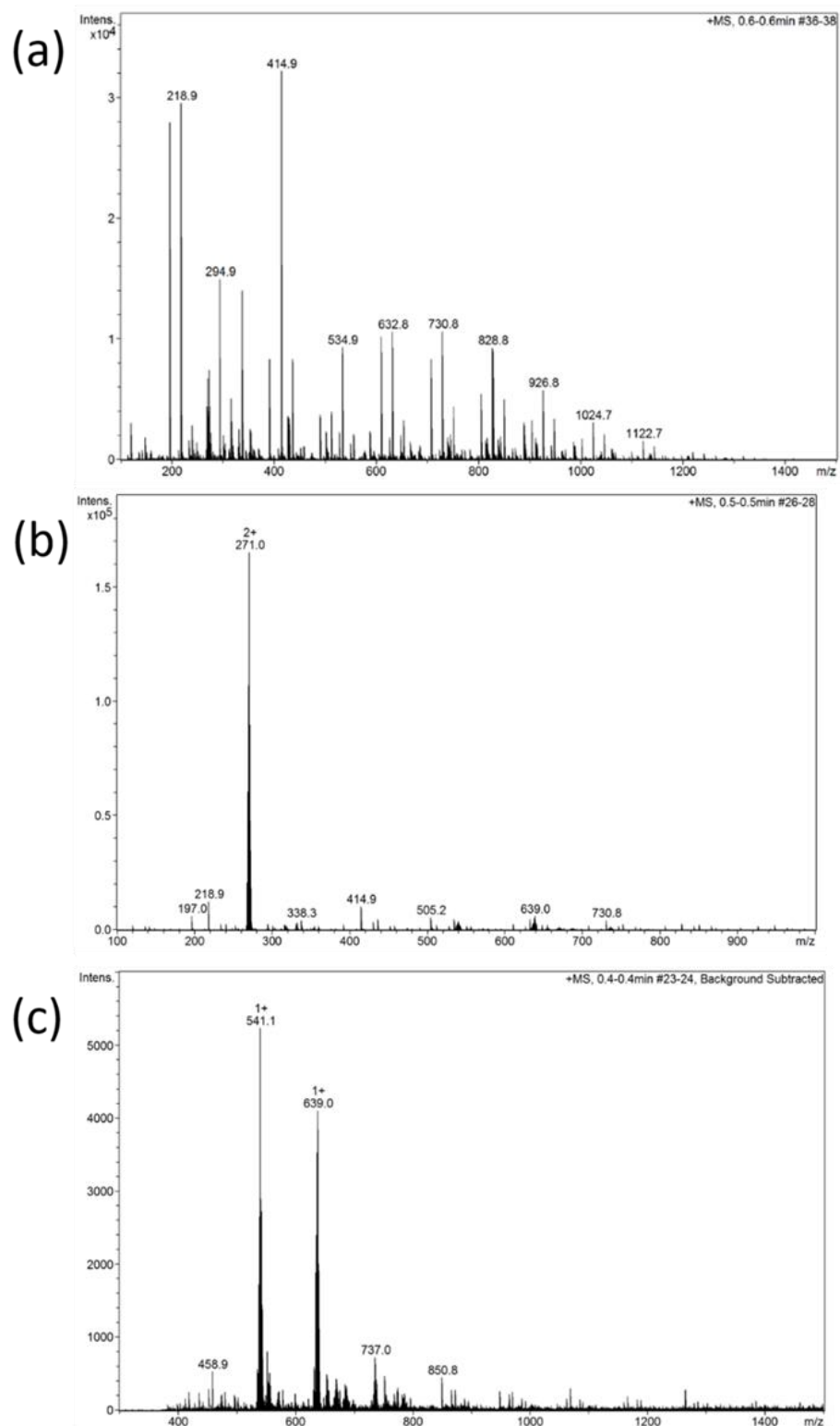


Figure 3.17: Mass spectra of samples with (a) retention time = 16.9 min, $\{[\text{Ru}_2(\text{biqbpy})_2\text{BIS}(\text{MeOH})_2](\text{PF}_6)_2\}^{2+}$ with $m/z = 828.8$ (calc. $m/z = 828.7$), (b,c) retention time = 14.7 min give peaks at $m/z = 271.0$ and 541.1 corresponding to $[\text{Ru}(\text{biqbpy})]^{2+}$ (calc. $m/z = 270.8$) and $[\text{Ru}(\text{biqbpy})]^{1+}$ (calc. $m/z = 541.0$) respectively;

3.2.5 Study of the RuBIS-CPNs in cells

After demonstrating the photoactivity of the **RuBIS-CPNs** and their ability to release the aqueous cytotoxic product, it was aimed to investigate the behaviour of these **CPNs** in biological environment. For this it was first studied the uptake of the **CPNs** and their cytotoxicity and later it was determined the increase of cytotoxicity after irradiation. This part of the work was carried out by our collaborators at the Leiden University.

Cellular uptake measurements

Skin non-melanoma A431 cells were incubated in the dark for 2 h with **RuBIS-CPNs** and the amount of Ru in the cells was quantified using ICP-MS. To better define the role of the nanostructuration on the internalization and phototherapy we repeated these experiments with a related molecular complex $[\text{Ru}(\text{biqppy})(\text{N-methylimidazole})_2](\text{PF}_6)_2$ (complex **2**), especially synthesized as reference study. Complex **2**, a mononuclear analogue of complex **1** coordinated with 2 axial methylimidazole ligands, was selected as reference molecular complex for **RuBIS-CPNs** due to the analogous ruthenium coordination sphere in both systems which facilitates and makes more suitable the comparative studies.

Complex **2** was obtained with 80% yield, upon reaction of complex **1** with an excess of 1-methylimidazole (ratio 1:10) in EtOH under reflux and N_2 atmosphere (for more information see materials and methods section). Remarkably, the time-dependent UV-Vis evolution of complex **2** under green light irradiation (Figure 3.18) is very similar to that previously observed for complex **1** (Figure 3.15e),⁵⁷ validating its use for further biological studies.

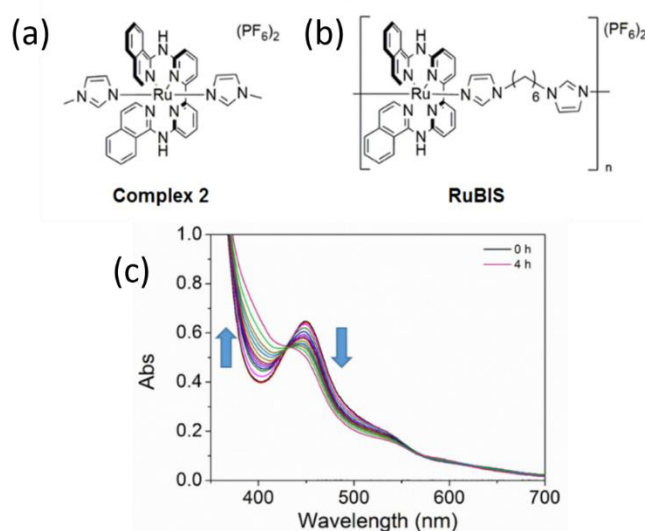


Figure 3.18: (a,b) Chemical representation of complex **2** and **RuBIS-CPNs**. (c) Evolution of the UV-vis absorbance spectra of a solution of complex **2**, upon green light ($\lambda_{\text{exc}} = 532 \text{ nm}$, 0.42 W/cm^2) irradiation.

As can be seen in Figure 3.19, complex **2** uptake is of 16 ng Ru/million cell, which is a value comparable to similar molecular Ru complexes previously reported.⁵⁷ **RuBIS-CPNs** were taken up by cells A431 up to 11 times more (183 ng Ru/million cell). Such difference was tentatively assigned to the different internalization mechanisms. To confirm it, additional Ru quantification studies were performed co-incubating **RuBIS-CPNs** or complex **2** with the endocytosis inhibitors NaN₃, NH₄Cl, or Dynasore, which are inhibitors of active uptake, endocytosis, and dynamin-dependent endocytosis, respectively. The cellular uptake of **RuBIS-CPNs** was decreased in the presence of Dynasore (96.3 ng Ru/million cells), ammonium chloride (101 ng Ru/million cells), and sodium azide (138 ng Ru/million cells). For the mononuclear complex **2** the opposite result was observed, with a higher uptake (i.e. xxx, xxx, and xxx ng Ru/million cell, respectively) in the presence of the same inhibitors. Overall, these results suggested that endocytosis-related processes may be involved in cellular uptake of **RuBIS-CPNs**, as reported previously for other nanoparticles,¹⁰⁷ while for complex **2** different mechanisms probably take place.¹⁰⁸

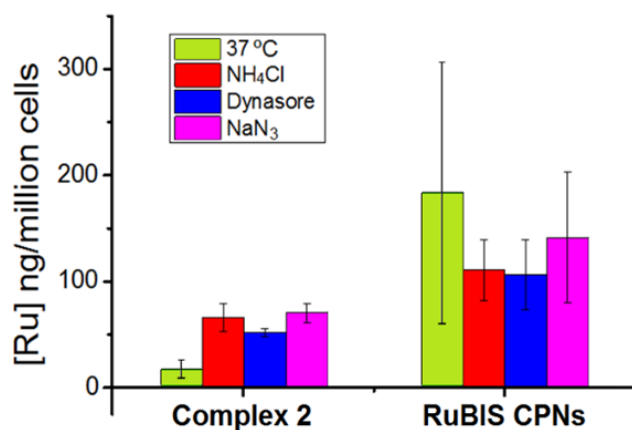


Figure 3.19: Cellular uptake quantification for Ru content in A431 cells treated the complex **2** (19 µg/mL) or **RuBIS-CPNs** (25 µg/mL) nanoparticles for 2 hours in presence or absence of uptake inhibitors: ammonium chloride, Dynasore, or sodium azide endocytosis.

(Photo)cytotoxicity studies

Once proved the **RuBIS-CPNs** were successfully internalized in the cells, it was investigated the cytotoxicity of the particles in the dark and after irradiation, when the aqueous active complex is released. Again, the cytotoxicity study was carried out comparing the values to the reference complex **2**.

RuBIS-CPNs dispersions (from 0.7 ng/mL to 2.83 µg/mL based on Ru content) or complex **2** solutions (from 1.0 ng/mL to 5.0 µg/mL based on Ru content) were prepared in Opti-MEM medium, which is..... In order to fully dissolve the complex **2**, the minimum

amount of DMSO (< 0.5 %) was also added. The **RuBIS-CPNs** suspensions and the complex **2** solutions were seeded in human skin (A431) and lung cancer (A549) cell lines. For the study it was followed method described in previous reports.¹⁰⁹ The cells were seeded at $t = 0$, treated at $t = 24$ h, irradiated with green light ($\lambda_{exc} = 520$ nm, 39.3 J/cm²) for 1 h at 48 h, and cell viability was quantified at $t = 96$ h using standard sulforhodamine B (SRB) assay. Half-effective growth inhibition concentration (EC₅₀ in μ M) values at $t = 96$ h are shown in Figure 3.20 and dose-response curves are shown in Figure 3.21. Cisplatin, known to be highly cytotoxic, was also tested under the same conditions and used as control.

Cell Type	Light Dose/J/cm ²	RuBIS CPNs			Complex 2			Cisplatin		
		EC ₅₀ (μ M)	CI [a]	PI [b]	EC ₅₀ (μ M)	CI [a]	PI [b]	EC ₅₀ (μ M)	CI [a]	PI [b]
A431	0	11.9	+0.46 -n.a.	2.4	28.1	+0.06 -0.60	1.7	3.0	+0.45 -0.41	1.1
	39.3	5.0	+0.04 -0.04		16.3	+0.55 -0.32		3.3	+0.31 -0.28	
A549	0	9.1	+0.09 -0.08	1.8	28.3	+1.16 -0.74	1.0	3.0	+0.15 -0.15	1.0
	39.3	5.0	+0.02 -0.02		27.5	+0.43 -0.37		3.0	+0.17 -0.17	

Figure 3.20: Phototoxicity assay outline: cells were incubated in the dark for 48 h, and the Cytotoxicity of **RuBIS-CPNs** and complex **2** in A431 and A549 cancer cell lines in the dark and under green light ($\lambda_{exc} = 520$ nm, 39.3 J/cm²) irradiation [a] Confidence interval, [b] photo indices. EC50 values are expressed in μ M as half-maximal effective concentration (95% confidence interval are also given in μ M).

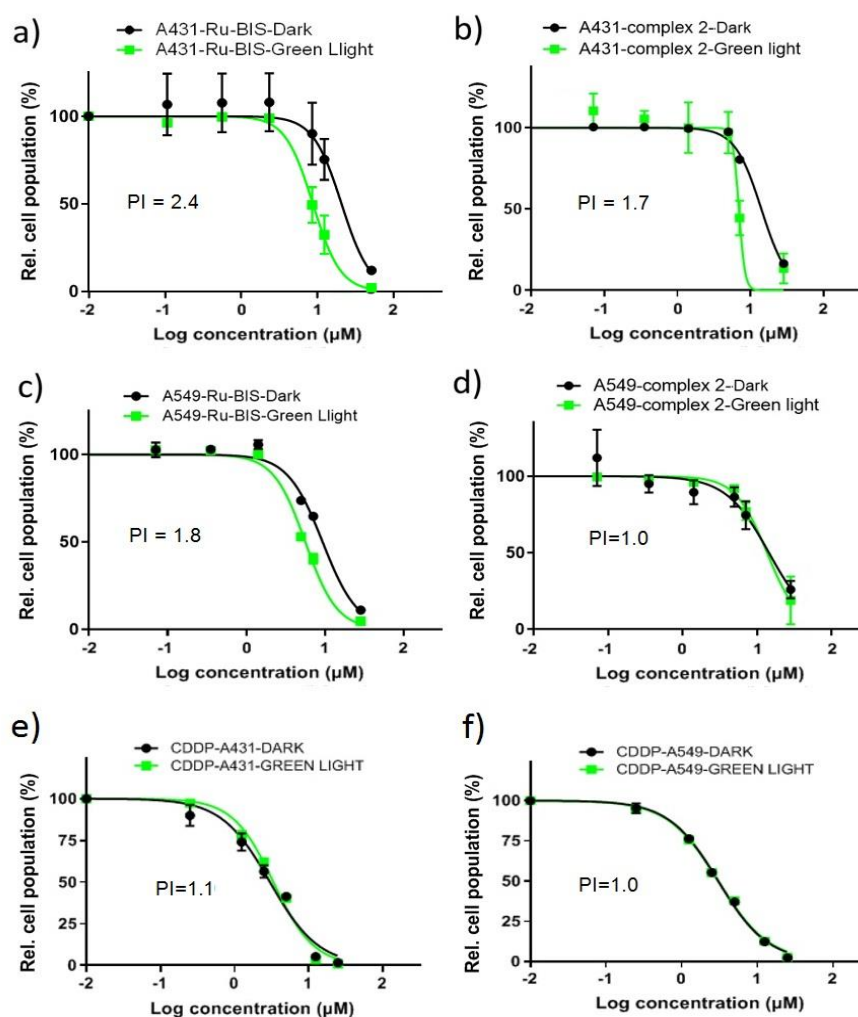


Figure 3.21: Comparative dose-response curves and calculated phototoxicity index (PI) after 1h irradiation with green light (green data points) and in the dark (black data points) for: A431 cell line in presence of **RuBIS-CPNs** (a) or the complex 2 (b); A549 cell line in presence of **RuBIS-CPNs** (c) or the complex 2 (d); and cisplatin (CDDP) cytotoxicity dose - response curves for A431 (e) and A549 (f) cell lines. Phototoxicity assay outline: cells were incubated in the dark for 48 h, and the plates were irradiated for 60 min with green light ($\lambda_{\text{exc}} = 520 \text{ nm}$, power density 10.92 mW/cm^2 , light dose = 39.3 J/cm^2). SRB assay was performed at $t=96\text{h}$. Data points represent the average of triplicates (confidence interval of 95% in M)

Interestingly, the EC_{50} values for **RuBIS-CPNs** in the dark ($\text{EC}_{50,\text{dark}}$) were $11.88 \mu\text{M}$ and $9.10 \mu\text{M}$, while these values decrease under irradiation ($\text{EC}_{50,\text{light}}$) to $4.95 \mu\text{M}$ and $5.04 \mu\text{M}$ for A431 and A549 cells, respectively (Table 3.1). Therefore, there is a remarkable difference in EC_{50} values for the **RuBIS-CPNs** with and without irradiation, showing a cell-dependent phototoxicity index (PI) values of 2.4 and 1.8 towards A431 and A549 cells, respectively. In both cases PI values of **RuBIS-CPNs** are higher than those of the molecular complex 2 (1.7 and 1.0, respectively). From these data, the following considerations deserve to be mentioned. First, the $\text{EC}_{50,\text{dark}}$ of **RuBIS-CPNs** was higher than that of complex 2, which was expected as it is possibly related to the significant higher uptake. Second, the $\text{EC}_{50,\text{light}}$ values of model complex 2 were $16.33 \mu\text{M}$ and $27.52 \mu\text{M}$ in A431 and A549 cells, respectively, up to 3-5 five times higher than those found for **RuBIS-CPNs**, confirming the positive nanostructuring

effect on the enhancement of phototoxicity. These results imply that less amount of Ru is required to photoinduce efficient chemotherapeutic effect, minimizing cells death for non-irradiated cells. Moreover, the obtained $EC_{50,light}$ values are similar to previously described monomeric complexes⁵⁷ but using almost half irradiation dose, which is also an additional advantage given the possible undesirable side effects that may appear from using high irradiation doses. And last but not least, $EC_{50,dark}$ values for **RuBIS-CPNs** are 3-4 times higher than those of cisplatin (3.01 and 3.04 μ M), i.e. less toxic; while $EC_{50,light}$ values of **RuBIS-CPNs** were close to those obtained for the photo-independent gold-standard cisplatin ($EC_{50} = 3.01 \mu$ M and 3.04μ M in A431 and A549, respectively), which equates their effectiveness to drugs commercially used today. Cytotoxicity of the bis-imidazol (bis) and methylimidazole ligands are considered negligible since previous evaluation in our group using concentrations ranging from 0 to 100 μ g/mL in different cell lines (Figure 3.22) corroborated their very low cytotoxic effect at the highest concentration assayed (100 μ g/mL).

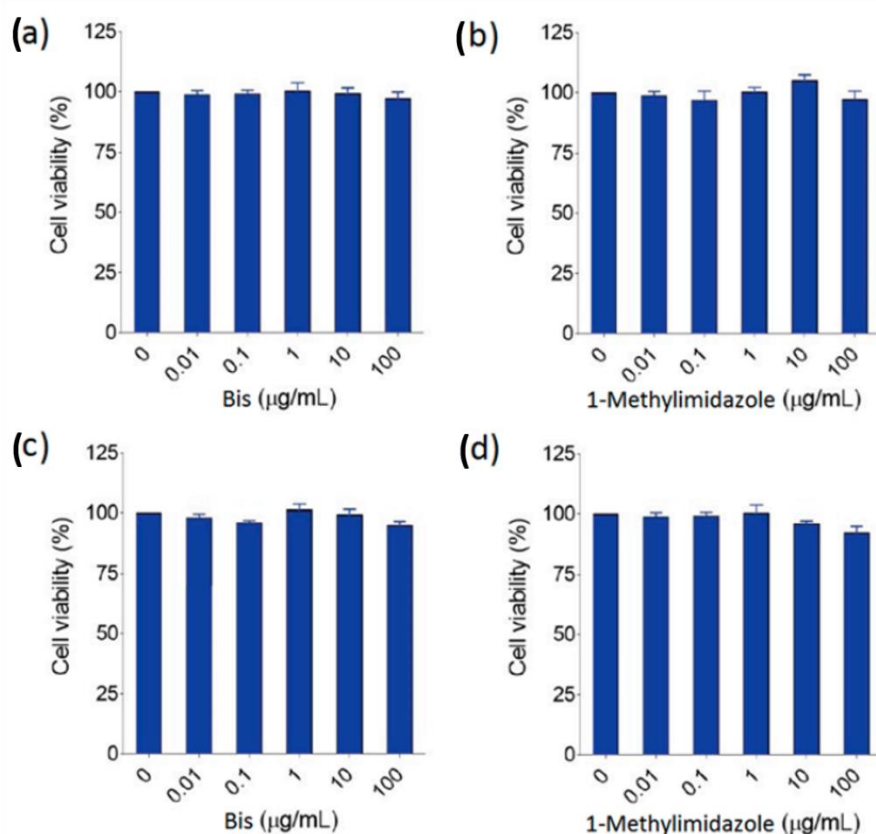


Figure 3.22: Cell viability studies of BIS and N-methylimidazole free ligands in (a,b) non-malignant human fibroblast cells (1Br3G) and (c,d) HeLa cell lines at different concentrations ranging from 0 to 100 μ g/mL. Cell viability was evaluated at 48h by a resazurin - based assay using the PrestoBlue cell viability reagen

Singlet oxygen production

To discard PDT as possible origin of the photoactivity instead of PACT, the production of singlet oxygen ($^1\text{O}_2$) upon green light irradiation of **RuBIS-CPNs** was quantified. For this, the common method is to measure the near-infrared emission intensity of $^1\text{O}_2$ (1270 nm) in CD_3OD though in this case to mimic the cell culture conditions, the value of singlet oxygen quantum yield (ϕ_Δ) was indirectly determined in Opti-MEM medium using a selective water-soluble $^1\text{O}_2$ probe, *i.e.*, 9,10-anthracenediyl-bis(methylene)-dimalonic acid (ABMDMA). In the dark, this dye absorbs light at 378 nm while in the presence of photo-generated $^1\text{O}_2$ a less conjugated endoperoxide is formed, leading to a decrease of the absorbance at 378 nm.¹¹⁰ The rose Bengal dye was used as reference, as it produces $^1\text{O}_2$ with a known quantum yield $\phi_\Delta = 0.76$ ¹¹¹ under green light irradiation. When **RuBIS-CPNs** (25 $\mu\text{g/mL}$) were mixed with ABMDMA (100 μM) in Opti-MEM, no changes in the absorption spectra were observed with or without green light irradiation ($\lambda_{\text{exc}} = 520$ nm, see , contrary to rose Bengal (Figure 3.23).¹¹² The same study was performed in the same way for complex **2**. In both cases the results excluded $^1\text{O}_2$ production, as expected for photosubstituted active ruthenium compounds.

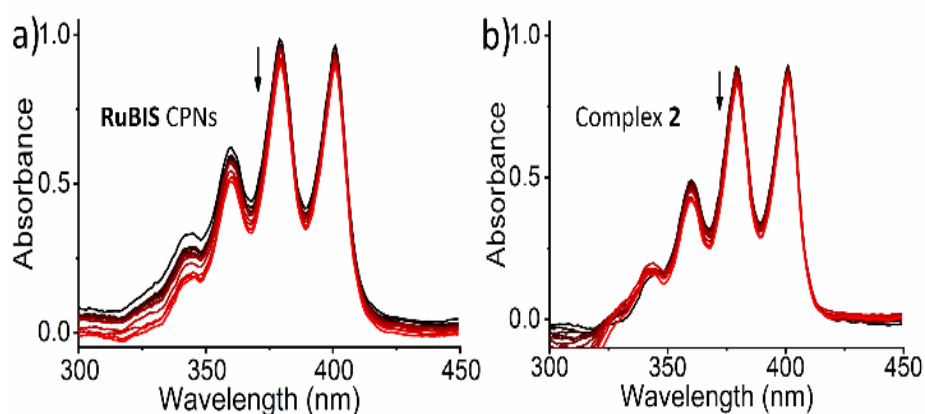


Figure 3.23: The absorption spectral changes of ABMDMA following green light irradiation in the presence of a) **RuBIS-CPNs** (25 $\mu\text{g/mL}$), b) complex **2** (19 $\mu\text{g/mL}$). The $^1\text{O}_2$ generation studied in Opti-MEM medium.

3.4 Conclusions

We have successfully designed and synthesized light-sensitive coordination polymer nanoparticles (**CPNs**) based on the polymerization of a Ru(II) polypyridyl prodrug **1** with a photocleavable bis-imidazole linking ligand **BIS**. Precise control of the reaction conditions has allowed to obtain reproducible and narrow **CPNs** size distributions around 50 ± 12 nm, with the prodrug being the backbone of the constituting polymer, allowing remarkable Ru-complex

content well over those already described for other nanoencapsulation systems. The photoactivation of the **RuBIS-CPNs** showed controlled release of the anticancer Ru complex $[\text{Ru}(\text{biqbpy})(\text{H}_2\text{O})_2]^{2+}$ upon green (532 nm) irradiation, while they were stable in cell-growing medium in the dark, reducing the cell dead population and side effects in its inactivated form. Interestingly, the dose of light necessary to obtain enough cytotoxic complex from **RuBIS-CPNs** *in vitro* (39.3 J/cm^2) is notably lower compared to previous values published for similar green light photoactivated ruthenium systems (75 J/cm^2).⁵⁷ Moreover, *in vitro* studies demonstrated that **RuBIS-CPNs** have an 11-fold increased uptake in comparison to related monomeric complexes thanks to the energy-dependent endocytosis uptake pathway triggered by the **CPNs** formulation. This fact determined a substantial increase in phototoxicity index in comparison with monomeric species and a light selective cytotoxic effect close to the gold standard cisplatin. All in all, **RuBIS-CPNs** demonstrates the potential of photoactivated **CPNs** for PACT anticancer treatments.

3.5 Materials and methods

Reagents and Instrumentation

Solvents were purchased from Sigma–Aldrich and used as received and complex **1** was provided by the group of Prof. Silvestre Bonnet (Leiden university). Fourier transform infrared (FTIR) spectra were carried out with a Tensor 27/PMA50FTIR Spectrometer in a range of $4000\text{--}400 \text{ cm}^{-1}$. Dynamic light scattering (DLS) for the determination of the particle-size distributions and the zeta potential values were measured in a ZetaSizer nano ZS (ZEN3600, Malvern Instruments, Ltd., Malvern, UK). Scanning Electron Microscopy (SEM) images were obtained on a scanning electron microscope (FEI Quanta 650 FEG, The Netherlands). The samples were casted on aluminum holders following by evaporation and later a thin platinum layer was sprayed to increase the conductivity of samples. Ultraviolet–visible spectroscopy (UV-vis) study was carried out in the Agilent Cary 60 spectrophotometer, in the dark using a 1 cm quartz cuvette with a stirring bar, containing 2 mL of **RuBIS-CPNs** ($20 \mu\text{g/mL}$). Time-dependent UV-Vis spectra during irradiation were recorded at regular time intervals (specified in the spectra) after irradiation of the stirred sample with a continuous beam of a green ($\lambda = 532 \text{ nm}$, 30 mW, 0.42 mW/cm^2) or blue laser (450 nm, 100 mW, 0.35 mW/cm^2) set in front of the cuvette.

Synthesis and characterization of the photoactive materials

Synthesis of complex 2

[Ru(biqbpy)(dmsO)Cl]Cl (50.0 mg, 0.072 mmol) was dissolved in EtOH and H₂O (5 mL, v/v = 1/1). Then 1-methylimidazole (60.0 mg, 0.73 mmol) was injected in the mixture and refluxed for 12 h under N₂ protection. The reaction mixture was cooled to room temperature. Ice cold water (5 mL) and KPF₆ (20 mg) were then added to the reaction mixture, dark brown precipitate was thus formed and filtered. After column chromatography (SiO₂, Ethyl acetate / MeOH = 10:1), 2 (50 mg, 80 %) [Ru(biqbpy)(N-methylimidazole)₂](PF₆)₂ complex (complex 2) was obtained as dark brown solid.

¹H NMR (360 MHz, (CD₃)₂SO) δ 10.73 (s, 2H), 8.93 (d, J = 8.1 Hz, 2H), 8.46 (d, J = 7.7 Hz, 2H), 8.21 (d, J = 6.7 Hz, 2H), 8.12 (t, J = 8.0 Hz, 2H), 7.93 (ddd, J = 23.1, 18.0, 7.3 Hz, 8H), 7.41 (d, J = 6.6 Hz, 2H), 7.32 (s, 2H), 6.86 (s, 2H), 6.08 (s, 2H), 3.35 (s, 6H). ¹³C NMR (91 MHz, (CD₃)₂SO) δ 156.28, 151.20, 150.01, 145.50, 140.25, 135.81, 135.58, 131.80, 129.28, 128.82, 127.86, 123.77, 122.69, 120.21, 118.81, 116.06, 115.79, 34.22. MS-ESI (m/z): [M]⁺ Calcd. for C₃₆H₃₂N₁₀Ru⁺ 705.8, found 705.2. Elem. Anal. Calcd. for C₃₆H₃₂F₁₂N₁₀P₂Ru·3H₂O : C, 40.55; H, 3.60; N, 13.51 Found: C, 40.72; H, 3.62; N, 12.95. (Figure 3.24-3.27)

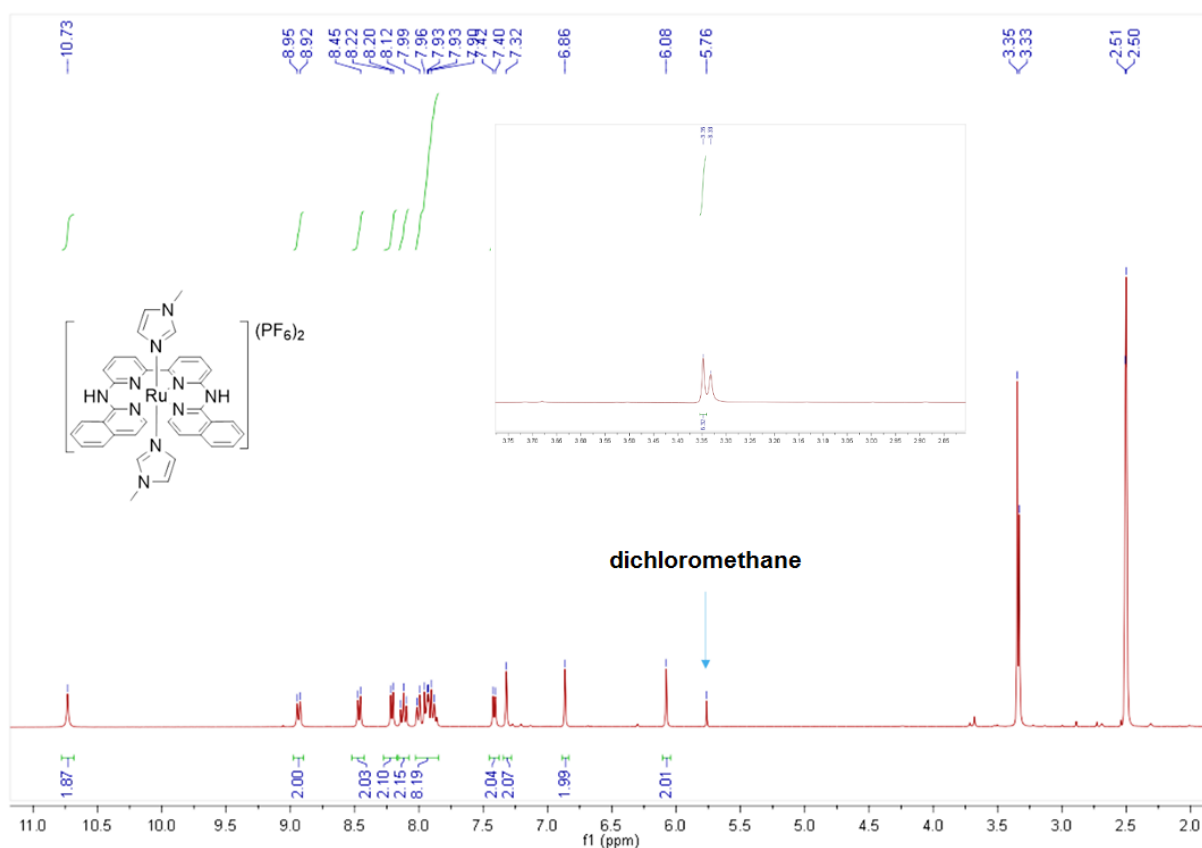


Figure 3.24: ^1H -NMR spectrum of complex **2** in $(\text{CD}_3)_2\text{SO}$.

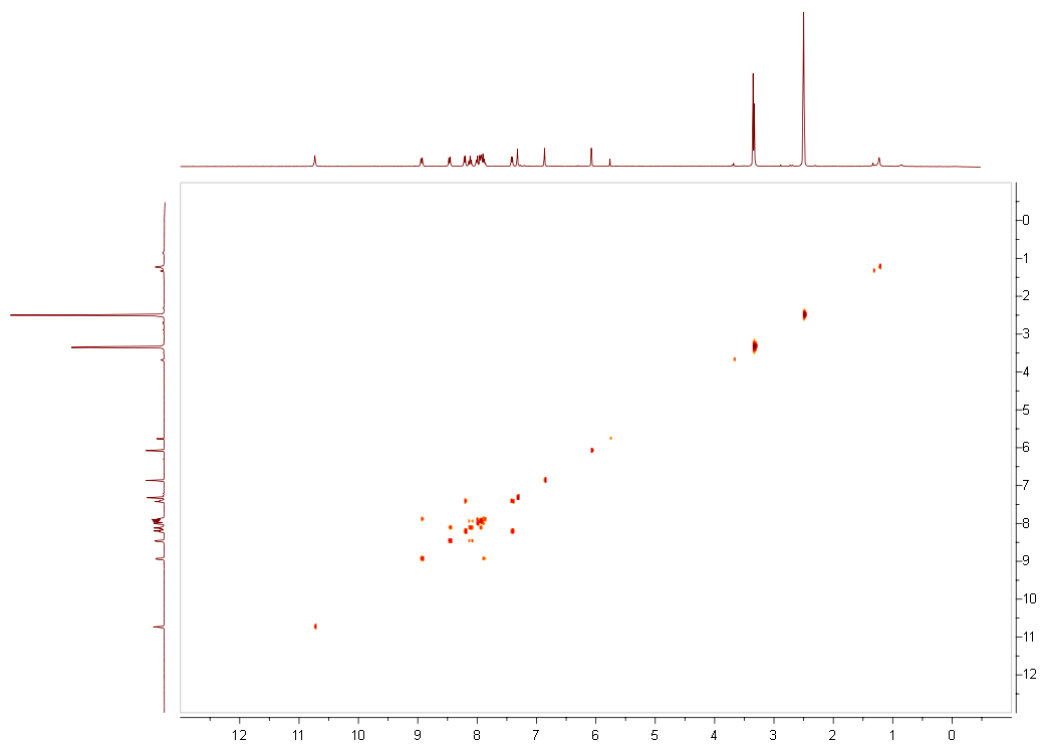


Figure 3.25: COSY spectrum of complex **2** in $(\text{CD}_3)_2\text{SO}$.

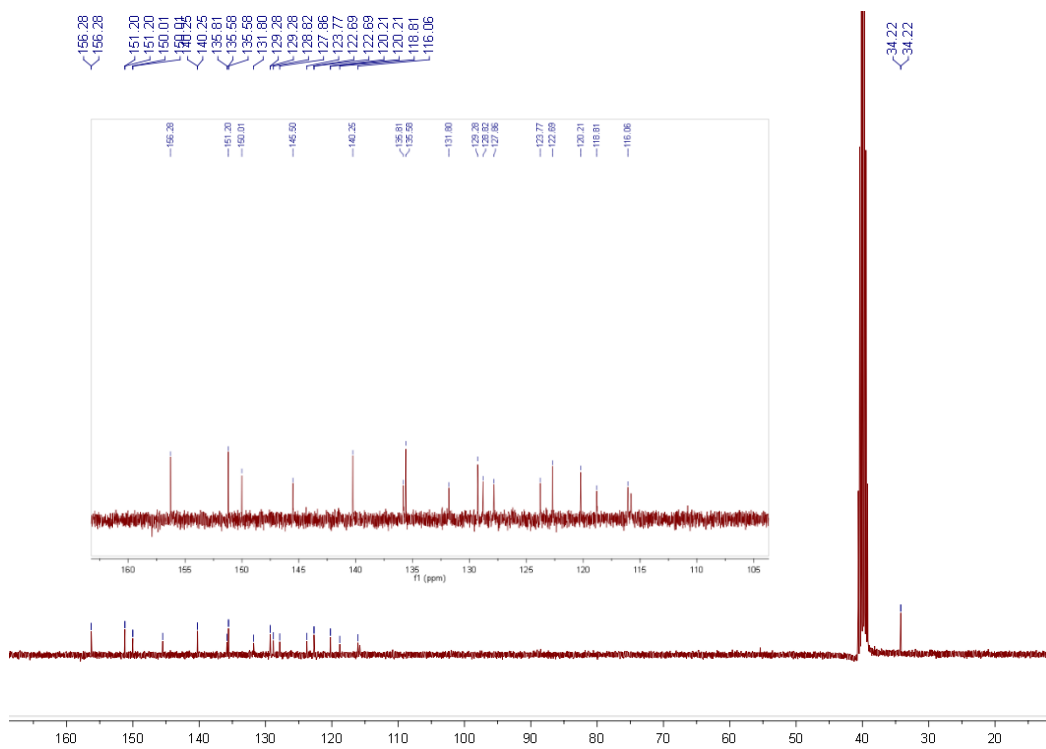


Figure 3.26: ^{13}C -NMR spectrum of complex **2** in $(\text{CD}_3)_2\text{SO}$.

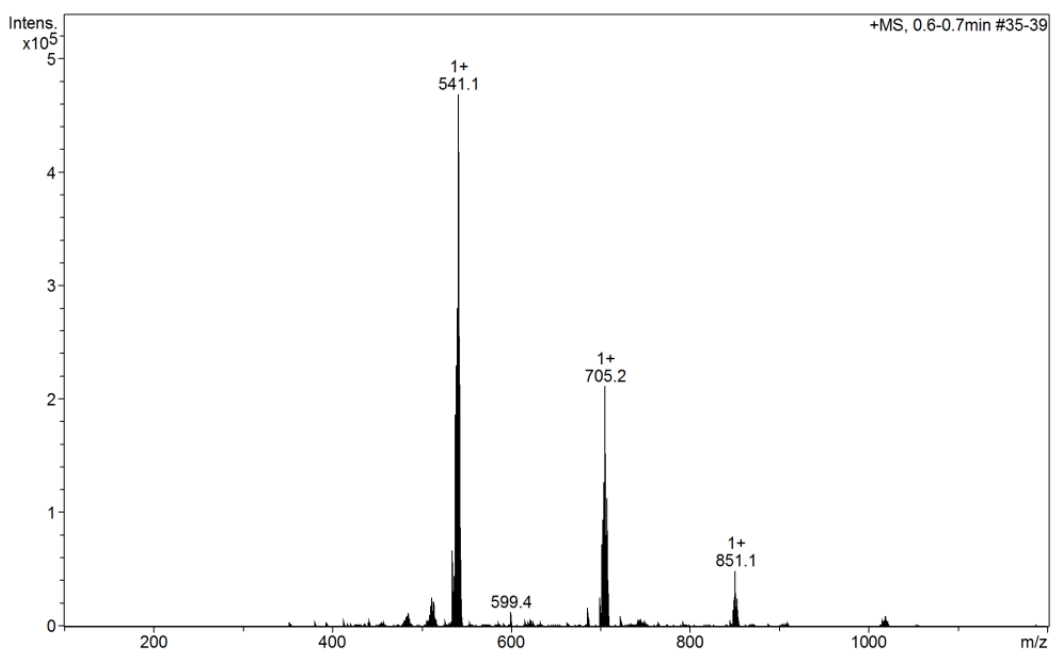


Figure 3.27: Mass spectrum of complex **2**.

Synthesis of coordination nanoparticles RuBIS-CPNs

$[\text{Ru}(\text{biqbpy})(\text{dmsO})\text{Cl}]\text{Cl}$ (complex **1**, 10.9 mg, 15.8 μmol) was firstly dissolved in a 2-necked round-bottom flask (10 mL) in 1 mL Milli-Q[®] water and N_2 atmosphere at 80 $^\circ\text{C}$ for 10 min. **BIS** (3.4 mg, 15.8 μmol) was dissolved in 1 mL Milli-Q[®] water and injected to the reaction slowly and the colour of the reaction changed from orange to dark brown. The reaction was stirred at 80 $^\circ\text{C}$ at 600 rpm for 1 h in dark conditions. After 1 h, 0.5 mL of saturated KPF_6 water solution was added to the mixture which precipitated. The solid was purified through three times centrifugation (10 min, 4300 rpm) and washed with Milli-Q[®] water. Finally, the as obtained solid was freeze-dried and stored as a powder (13.0 mg, yield = 92.8 wt%).

HPLC methodology for RuBIS-CPNs releasing quantification

Time-dependent HPLC evolution under irradiation of a **RuBIS** colloidal suspension (200 $\mu\text{g}/\text{mL}$) were performed with stirring and aliquots at different irradiation times were taken, filtered and analysed by HPLC. Calibration curve was performed using different concentrations (0.1, 0.5, 1, 5, 10 and 20 $\mu\text{g}/\text{mL}$) of a stock solution of the $[\text{Ru}(\text{biqbpy})(\text{H}_2\text{O})_2]^{2+}$ activated complex. The stock solution was obtained from the irradiation with green light (100 mW, 1.1 mW/cm^2) of complex **1** (1 mg/mL) dissolved in PBS solution for 20 h to make sure that Ru complex was fully converted to the active form through photocleavage and photosubstitution

process. Analyses were performed using a HPLC Waters 2695 separation module coupled to a Waters 2487 UV-Vis detector. The column used was a Restek® C-18 (250 mm x 4.6 mm). Eluent A was a 0.1% (v/v) H₃PO₄ aqueous solution and eluent B was acetonitrile absolute (HPLC grade). Before the analysis, the column was pre-equilibrated using the starting conditions of the method (99 % A (v/v)) for 10 min, followed by a gradual decrease of A from 100 % to 40 % (v/v) in the first 20 min and lasting 5 min. Then, the mobile phase reduced to 20 % A (v/v) in 1 minute and lasted 4 min. At the end, mobile phase was increased to 100 % A (v/v) in 1 min to elute residues and this ratio was kept for additional 5 min. For the next injection, mobile phase was reset to the initial conditions (A:B) 100:0 (v/v) and kept for 10 min to equilibrate. The flow rate was set at 1.0 mL/min at temperature. This method was used for both calibration curve and quantification of active complex release from **RuBIS-CPNs**.

Quantitative ¹H NMR and ¹⁹F NMR for component analysis of RuBIS-CPNs

7 mg of **RuBIS-CPNs** were dissolving in 6 mL deuterated dimethyl sulfoxide solvent ((CD₃)₂SO) containing deuterium chloride (DCl) to decompose the nanoparticles into the molecular entities. Same ratio (DCl/ (CD₃)₂SO) was used for comparison (50 μL DCl / mL (CD₃)₂SO) (Internal reference: 9 mg).

Cell culturing

Human skin (A431) and lung cancer (A549) cell lines were tested. Cells were cultured in Dulbecco's Modified Eagle's Medium (DMEM) "complete" (i.e. DMEM with phenol red, supplemented with Fetal-Calf Serum (FCS, 10.0 % v/v), Penicillin-Streptomycin (PS solution; 0.2 % v/v), and GlutaMax (GM, 0.9 % v/v)). Both cell lines were cultured under humidified conditions (37 °C atmosphere containing 7.0 % CO₂) in 75 cm² flasks and sub-cultured (1:3–1:6) upon reaching 70–80 % confluency (approximately once per week). Media were refreshed every 3 days; cells were passaged for 4–8 weeks maximum.

Cell-irradiation setup

The same cell-irradiation system was used as published previously from our group¹¹³ that consisted of a Ditabis thermostat (980923001) fitted with two flat-bottomed microplate thermoblocks (800010600) and a 96-LED array fitted to a standard 96-well plate. The $\lambda_{exc} =$

520 nm LED with power density (10.9 mW/cm²) (OVL-3324), fans (40 mm, 24 V DC, 9714839), and power supply (EA-PS 2042-06B) were obtained from Farnell.

Cytotoxicity assay

Cells were seeded at t = 0 h in 96-well plates at a density of A549 (5x10³ / mL) and A431(8 x10³ / mL) in Opti-MEM complete without phenol red (100 µL) and incubated for 24 h at 37 °C/, under 7% of CO₂. After this period, aliquots (100 µL) of six different concentrations between 50 ng/mL to 50 µg/mL (0.7 ng/mL to 2.83 µg/mL based on metal content) of freshly prepared stock **RuBIS-CPNs** suspension or **2** solution in Opti-MEM were added to three adjacent wells as triplicate. Minimum amount of DMSO (<0.5%) was used to dissolve the compounds, which does not harm the cells in each well, including in the control wells. Plates were incubated in the dark for an additional 24 h. After this period the plates were irradiated for 60 min with green light ($\lambda_{exc} = 520$ nm, power density 10.92 mW/cm², light dose = 39.3 J/cm²). After irradiation, all plates were incubated in the dark for an additional 48 h either in normoxia or hypoxic incubator. The cells were then fixed by adding cold (4 °C) TCA (10 % w/v; 100 µL) in each well. Next, TCA was removed from the wells, and the plates were gently washed with water (×5), stained with SRB (0.6 % w/v in acetic acid (1 % v/v; 100 µL) for 30 min, washed with acetic acid (1 % v/v; ≈300 µL), and air-dried overnight. The SRB dye was solubilized with Tris-base (10 mM; 200 µL), and the absorbance in each well was read at $\lambda=510$ nm by using a M1000 Tecan Reader.

The SRB absorbance data was used to calculate the fraction of viable cells in each well (Excel and GraphPad Prism software). The absorbance data were averaged from triplicates for each concentration. Relative cell viabilities were calculated by dividing the average absorbance of the treated wells by the average absorbance of the untreated wells. Three independent biological replicates were completed for each cell line (three different passage numbers per cell line). The average cell viability of the three biological replicates was plotted versus log (concentration) [µM], with the standard deviation error of each point. By using the dose–response curve for each cell line under dark and irradiated conditions, the effective concentration (EC₅₀) was calculated by fitting the curves to a non-linear regression function with fixed maximum (100 %) and minimum (0 %), as relative cell viability, and obtaining a variable Hill slope, which resulted in the simplified two-parameter Hill-slope equation (1)]

$$Y = 100 / (1 + 10^{((\log_{10} EC_{50} - X) \cdot \text{Hill Slope}))} \dots \dots \dots \text{eq (1)}$$

Cellular uptake measurements

A431 cells (5×10^5) were seeded in 12-well plates, incubated for 24 h under normoxic conditions, treated with **RuBIS-CPNs** (25 $\mu\text{g/mL}$) or **2** (19 $\mu\text{g/mL}$) for 2 h. Then cells were washed thrice with cold (4 $^\circ\text{C}$) PBS (3 x 2 mL) to remove any compound attached outside the cells. Then the cells were trypsinized and collected into 2 mL Eppendorf tube in Opti-MEM media. Cells were counted on a BioRad cell-counting board, carefully washed once with cold PBS to remove trypsin. Collected cells were then centrifuged at 3000 rpm for 5 min. The resulting cell pellet was digested using in 65 % HNO_3 at 100 $^\circ\text{C}$ overnight in a hot air oven. Once back to room temperature the total volume was completed to 10 mL using Milli-Q water. The ruthenium content and the standard deviation values of these solutions were analyzed on the duplicate experimental results using the Perkin Elmer NexION 2000 of inductively coupled plasma mass spectrometer (ICP-MS).

Endocytosis inhibition studies

A431 cells (5×10^5 cells) were seeded in 12-well plates, incubated for 24 h under normoxic conditions, and then treated with NaN_3 (active uptake inhibitor, 15.4 mM), NH_4Cl (20 mM) or Dynasore (dynamin-dependent endocytosis inhibitor, 80 μM) for 1 h; alternatively, the cells were incubated at 4 $^\circ\text{C}$ for 1 h. After that, the cells were incubated with either **RuBIS-CPNs** (50 $\mu\text{g/mL}$) or complex **2** (38 $\mu\text{g/mL}$) for 3 h in the regular incubator for the inhibitor samples, or at 4 $^\circ\text{C}$ for the low temperature samples. The cells were then treated like in the normal cellular uptake study.

ICP-MS analysis

Nitric acid (65%, Suprapur®, Merck) was used in the sample digestion process, while diluted (1%) nitric acid was used as a carrying solution throughout the ICP measurements. National Institute of Standards and Technology (NIST)-traceable 1000 mg/L elemental standards were used (TraceCERT®, Fluka) for preparation of calibration and internal standards. Approximately 18 $\text{M}\Omega \text{ cm}^{-1}$ water (MiliQ) was used in all sample preparation and analysis steps. Calibration standards were prepared in a Secuflow fume hood (SCALA) to prevent contamination by atmospheric particulates. The standard samples and measurement samples were analysed for trace elements using the NexION® 2000 (PerkinElmer) ICP-MS equipped with a concentric glass nebulizer and Peltier-cooled glass spray chamber. An SC2 DX

autosampler (PerkinElmer) was connected to the ICP-MS for sample introduction. Syngistix™ Software for ICP-MS (v.2.5, PerkinElmer) was used for all data recording and processing. Five trace elemental calibration standards for ICP-MS analysis were prepared using NIST-traceable 1000 mg/L Ru standard: 0, 1, 4, 20, 100 µg/L. Another set of calibration standard for Ru: 0, 0.1, 0.5, 2.5, 10 µg/L were prepared for samples that were anticipated to contain low-level Ru. Samples were analyzed without dilution in the original delivery containers to minimize the possibility of contamination. 10 µg/L Rh and In were used as internal standard. To check the calibration, samples were analyzed through a blank measurement and a repeated measurement of one of the calibration standards. For the calibration curves with correlation coefficient (Cor.Coeff) higher than 0.999 were accepted.

Singlet oxygen $^1\text{O}_2$ production studies

Singlet oxygen generation measurements were conducted in cell-growing medium using 9, 10-anthracenediyl-bis(methylene) dimalonic acid (ABMDMA) as $^1\text{O}_2$ -specific probe. ABMDMA is a hydrophilic anthracene derivative which reacts with $^1\text{O}_2$ to produce the corresponding endoperoxide,¹¹⁴ thereby lowering the absorbance at 400 nm. For the experiment, 0.1 mM of ABMDMA (in Opti-MEM) was mixed with **RuBIS-CPNs** (25 µg/mL) which was previously dispersed in Opti-MEM cell culture media. The resulting samples were taken into a 3 mL quartz cuvette to record the absorbance in the dark or following green light irradiation ($\lambda_{\text{exc}} = 520 \text{ nm}$, 39.3 J/cm^2). Absorption spectra were recorded initially every 30 seconds during the first 1 minute of continuous light irradiation and successively every 1 min interval during 6 min. The reference rose Bengal dye caused significant changes to the absorption spectra of ABMDMA at 400 nm (Figure 3.28), which indicated the production of $^1\text{O}_2$ with a quantum yield of $\Phi_{\Delta} = 0.68$.¹¹¹

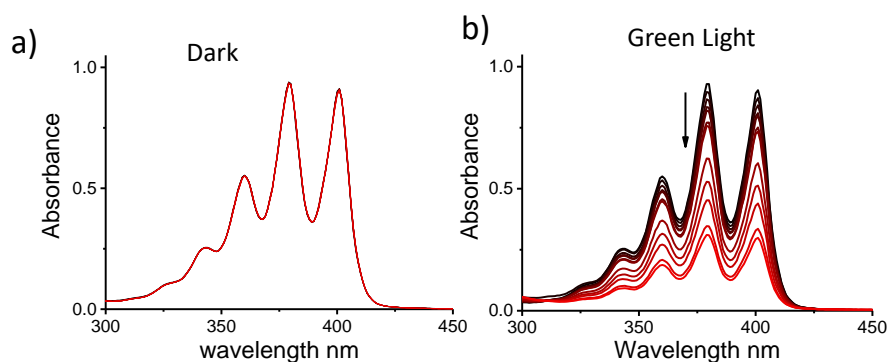


Figure 3.28: Absorption spectral changes of ABMDMA in the dark (a) or following green light irradiation with the light of dose 39.3 J/cm^2 (b) in the presence of Rose Bengal ($0.1 \text{ }\mu\text{M}$).

Determining the required irradiation time for RuBIS-CPNs and complex 2 activation

Mock irradiation experiments were performed in the conditions of the cytotoxicity assay, but in absence of cells, to determine the irradiation time necessary to activate **RuBIS-CPNs** and complex **2** in the cytotoxicity assay. The highest concentration (50 $\mu\text{g/mL}$) of **RuBIS-CPNs** was added (200 μL) in transparent 96-well plates. Samples were irradiated for 60 min with green light ($\lambda_{\text{exc}} = 520 \text{ nm}$, 39.3 J/cm^2) and absorption changes at 440 and 390 nm for **RuBIS-CPNs** and complex **2** was followed vs. irradiation time. The complete activation of both compounds was achieved after 60 min of continuous irradiation (light dose 39.3 J/cm^2) (Figure 3.29).

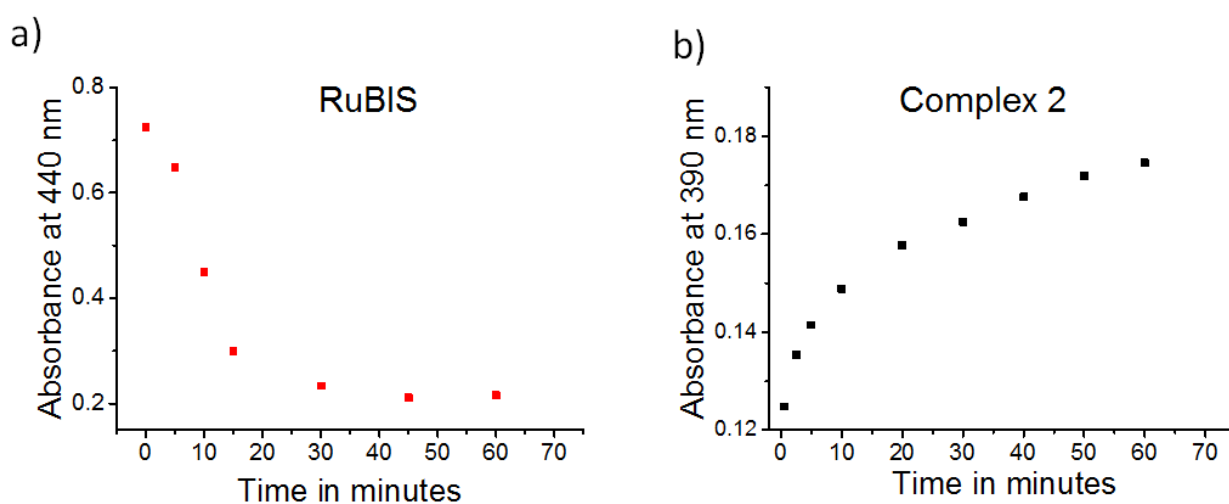


Figure 3.29: Mock irradiation studies for (a) **RuBIS-CPNs** and (b) complex **2** was conducted in cell culturing Opti-MEM media at 37 °C in air without the cells to know the light intensity and duration of time for the complete activation of these compounds. Conditions: 50 $\mu\text{g/mL}$ of **RuBIS-CPNs** or complex **2** (200 μL), light irradiation $\lambda_{\text{exc}} = 520 \text{ nm}$, 39.3 J.cm^{-2} .

3.6 References

1. Omondi, R. O.; Ojwach, S. O.; Jaganyi, D., Review of comparative studies of cytotoxic activities of Pt (II), Pd (II), Ru (II)/(III) and Au (III) complexes, their kinetics of ligand substitution reactions and DNA/BSA interactions. *Inorg. Chim. Acta* **2020**, *512*, 119883.
2. Ma, D. L.; Wu, C.; Wu, K. J.; Leung, C. H., Iridium(III) Complexes Targeting Apoptotic Cell Death in Cancer Cells. *Molecules* **2019**, *24* (15), 2739.
3. Ohata, J.; Ball, Z. T., Rhodium at the chemistry–biology interface. *Dalton Trans.* **2018**, *47* (42), 14855-14860.
4. Das, U.; Kar, B.; Pete, S.; Paira, P., Ru (II), Ir (III), Re (I) and Rh (III) based complexes as next generation anticancer metallopharmaceuticals. *Dalton Trans.* **2021**.
5. Mjos, K. D.; Orvig, C., Metallodrugs in medicinal inorganic chemistry. *Chem. Rev.* **2014**, *114* (8), 4540-63.
6. Lippert, B., Chemistry and biochemistry of a leading anticancer drug. *Verlag Helvetica Chimica Acta, Zürich* **1999**.
7. Romero-Canelon, I.; Sadler, P. J., Next-generation metal anticancer complexes: multitargeting via redox modulation. *Inorg. Chem.* **2013**, *52* (21), 12276-91.
8. Suntharalingam, K.; Song, Y.; Lippard, S. J., Conjugation of vitamin E analog α -TOS to Pt (IV) complexes for dual-targeting anticancer therapy. *Chem. Commun.* **2014**, *50* (19), 2465-2468.
9. Graf, N.; Bielenberg, D. R.; Kolishetti, N.; Muus, C.; Banyard, J.; Farokhzad, O. C.; Lippard, S. J., α V β 3 integrin-targeted PLGA-PEG nanoparticles for enhanced anti-tumor efficacy of a Pt (IV) prodrug. *ACS nano* **2012**, *6* (5), 4530-4539.
10. Zheng, Y. R.; Suntharalingam, K.; Johnstone, T. C.; Yoo, H.; Lin, W.; Brooks, J. G.; Lippard, S. J., Pt(IV) prodrugs designed to bind non-covalently to human serum albumin for drug delivery. *J. Am. Chem. Soc.* **2014**, *136* (24), 8790-8.
11. Zeng, L.; Gupta, P.; Chen, Y.; Wang, E.; Ji, L.; Chao, H.; Chen, Z. S., The development of anticancer ruthenium(II) complexes: from single molecule compounds to nanomaterials. *Chem. Soc. Rev.* **2017**, *46* (19), 5771-5804.
12. Dhar, S.; Gu, F. X.; Langer, R.; Farokhzad, O. C.; Lippard, S. J., Targeted delivery of cisplatin to prostate cancer cells by aptamer functionalized Pt(IV) prodrug-PLGA-PEG nanoparticles. *Proc Natl Acad Sci U S A* **2008**, *105* (45), 17356-61.
13. Johnstone, T. C.; Suntharalingam, K.; Lippard, S. J., The Next Generation of Platinum Drugs: Targeted Pt(II) Agents, Nanoparticle Delivery, and Pt(IV) Prodrugs. *Chem. Rev.* **2016**, *116* (5), 3436-86.
14. Deng, Z.; Wang, N.; Ai, F.; Wang, Z.; Zhu, G., Nanomaterial-mediated platinum drug-based combinatorial cancer therapy. *View* **2021**, *2* (1), 20200030.
15. Imran, M.; Ayub, W.; Butler, I. S., Photoactivated platinum-based anticancer drugs. *Coord. Chem. Rev.* **2018**, *376*, 405-429.
16. Imberti, C.; Zhang, P.; Huang, H.; Sadler, P. J., New Designs for Phototherapeutic Transition Metal Complexes. *Angew. Chem. Int. Ed. Engl.* **2020**, *59* (1), 61-73.
17. Farrer, N. J.; Salassa, L.; Sadler, P. J., Photoactivated chemotherapy (PACT): the potential of excited-state d-block metals in medicine. *Dalton Trans* **2009**, (48), 10690-701.
18. Guo, D.; Xu, S.; Huang, Y.; Jiang, H.; Yasen, W.; Wang, N.; Su, Y.; Qian, J.; Li, J.; Zhang, C.; Zhu, X., Platinum(IV) complex-based two-in-one polyprodrug for a combinatorial chemo-photodynamic therapy. *Biomaterials* **2018**, *177*, 67-77.
19. Eales, K. L.; Hollinshead, K. E.; Tennant, D. A., Hypoxia and metabolic adaptation of cancer cells. *Oncogenesis* **2016**, *5* (1), e190.
20. Lee, S. Y.; Kim, C. Y.; Nam, T.-G., Ruthenium complexes as anticancer agents: A brief history and perspectives. *Drug Design, Development and Therapy* **2020**, *14*, 5375.
21. Moreno-Sánchez, R.; Rodríguez-Enríquez, S.; Marín-Hernández, A.; Saavedra, E., Energy metabolism in tumor cells. *The FEBS journal* **2007**, *274* (6), 1393-1418.

-
22. Crowther, M.; Brown, N. J.; Bishop, E. T.; Lewis, C. E., Microenvironmental influence on macrophage regulation of angiogenesis in wounds and malignant tumors. *J Leukoc Biol* **2001**, *70* (4), 478-90.
23. Brown, J. M.; Wilson, W. R., Exploiting tumour hypoxia in cancer treatment. *Nat Rev Cancer* **2004**, *4* (6), 437-47.
24. Dang, C. V.; Kim, J.-w.; Gao, P.; Yustein, J., The interplay between MYC and HIF in cancer. *Nature Reviews Cancer* **2008**, *8* (1), 51-56.
25. Antonarakis, E. S.; Emadi, A., Ruthenium-based chemotherapeutics: are they ready for prime time? *Cancer Chemother. Pharmacol.* **2010**, *66* (1), 1-9.
26. Bergamo, A.; Zorzet, S.; Gava, B.; Sorc, A.; Alessio, E.; Iengo, E.; Sava, G., Effects of NAMI-A and some related ruthenium complexes on cell viability after short exposure of tumor cells. *Anti-Cancer Drugs* **2000**, *11* (8), 665-672.
27. Kladnik, J.; Kljun, J.; Burmeister, H.; Ott, I.; Romero-Canelon, I.; Turel, I., Towards Identification of Essential Structural Elements of Organoruthenium(II)-Pyridylthioamido Complexes for Anticancer Activity. *Chemistry* **2019**, *25* (62), 14169-14182.
28. Zhao, Z.; Gao, P.; You, Y.; Chen, T., Cancer-Targeting Functionalization of Selenium-Containing Ruthenium Conjugate with Tumor Microenvironment-Responsive Property to Enhance Theranostic Effects. *Chemistry* **2018**, *24* (13), 3289-3298.
29. Hartinger, C. G.; Zorbas-Seifried, S.; Jakupec, M. A.; Kynast, B.; Zorbas, H.; Keppler, B. K., From bench to bedside--preclinical and early clinical development of the anticancer agent indazolium trans-[tetrachlorobis(1H-indazole)ruthenate(III)] (KP1019 or FFC14A). *J. Inorg. Biochem.* **2006**, *100* (5-6), 891-904.
30. Gransbury, G. K.; Kappen, P.; Glover, C. J.; Hughes, J. N.; Levina, A.; Lay, P. A.; Musgrave, I. F.; Harris, H. H., Comparison of KP1019 and NAMI-A in tumour-mimetic environments. *Metallomics* **2016**, *8* (8), 762-73.
31. Mital, M.; Ziora, Z., Biological applications of Ru(II) polypyridyl complexes. *Coord. Chem. Rev.* **2018**, *375*, 434-458.
32. Jakupec, M. A.; Kandioller, W.; Schoenhacker-Alte, B.; Trondl, R.; Berger, W.; Keppler, B. K., Trends and Perspectives of Ruthenium Anticancer Compounds (Non-PDT). In *Ruthenium Complexes*, 2018; pp 271-291.
33. Monro, S.; Colon, K. L.; Yin, H.; Roque, J., 3rd; Konda, P.; Gujar, S.; Thummel, R. P.; Lilge, L.; Cameron, C. G.; McFarland, S. A., Transition Metal Complexes and Photodynamic Therapy from a Tumor-Centered Approach: Challenges, Opportunities, and Highlights from the Development of TLD1433. *Chem. Rev.* **2019**, *119* (2), 797-828.
34. Jakubaszek, M.; Goud, B.; Ferrari, S.; Gasser, G., Mechanisms of action of Ru (II) polypyridyl complexes in living cells upon light irradiation. *Chem. Commun.* **2018**, *54* (93), 13040-13059.
35. Hu, X.; Liu, N. Y.; Deng, Y. Q.; Wang, S.; Liu, T.; Liu, X. W., Photoinduced DNA Cleavage and Photocytotoxic of Phenanthroline-Based Ligand Ruthenium Compounds. *Molecules* **2021**, *26* (11), 3471.
36. Sun, W.; Li, S.; Haupler, B.; Liu, J.; Jin, S.; Steffen, W.; Schubert, U. S.; Butt, H. J.; Liang, X. J.; Wu, S., An Amphiphilic Ruthenium Polymetallo-drug for Combined Photodynamic Therapy and Photochemotherapy In Vivo. *Adv. Mater.* **2017**, *29* (6), 1603702.
37. Sun, W.; Wen, Y.; Thiramanas, R.; Chen, M.; Han, J.; Gong, N.; Wagner, M.; Jiang, S.; Meijer, M. S.; Bonnet, S.; Butt, H.-J.; Mailänder, V.; Liang, X.-J.; Wu, S., Red-Light-Controlled Release of Drug-Ru Complex Conjugates from Metallopolymer Micelles for Phototherapy in Hypoxic Tumor Environments. *Adv. Funct. Mater.* **2018**, *28* (39), 1804227.
38. Berndt-Paetz, M.; Schulze, P.; Stenglein, P. C.; Weimann, A.; Wang, Q.; Horn, L.-C.; Riyad, Y. M.; Griebel, J.; Hermann, R.; Glasow, A., Reduction of Muscle-Invasive Tumors by Photodynamic Therapy with Tetrahydroporphyrin-Tetratosylat in an Orthotopic Rat Bladder Cancer Model Effective Bladder Tumor Growth Control by PDT with THPTS. *Molecular Cancer Therapeutics* **2019**, *18* (4), 743-750.

-
39. Marcus, S. L., Clinical photodynamic therapy: the continuing evolution. In *Photodynamic therapy*, CRC Press: 2020; pp 219-268.
40. Dougherty, T. J.; Marcus, S. L., Photodynamic therapy. *European Journal of Cancer* **1992**, *28* (10), 1734-1742.
41. Robertson, C. A.; Evans, D. H.; Abrahamse, H., Photodynamic therapy (PDT): a short review on cellular mechanisms and cancer research applications for PDT. *Journal of Photochemistry and Photobiology B: Biology* **2009**, *96* (1), 1-8.
42. Braathen, L. R.; Szeimies, R.-M.; Basset-Seguín, N.; Bissonnette, R.; Foley, P.; Pariser, D.; Roelandts, R.; Wennberg, A.-M.; Morton, C. A., Guidelines on the use of photodynamic therapy for nonmelanoma skin cancer: an international consensus. *Journal of the American Academy of Dermatology* **2007**, *56* (1), 125-143.
43. Christensen, E.; Warloe, T.; Kroon, S.; Funk, J.; Helsing, P.; Soler, A.; Stang, H.; Vatne, Ø.; Mørk, C., Guidelines for practical use of MAL-PDT in non-melanoma skin cancer. *Journal of the European Academy of Dermatology and Venereology* **2010**, *24* (5), 505-512.
44. Lu, K.; He, C.; Lin, W., Nanoscale Metal-Organic Framework for Highly Effective Photodynamic Therapy of Resistant Head and Neck Cancer. *J. Am. Chem. Soc.* **2014**, *136* (48), 16712-16715.
45. Dąbrowski, J. M.; Arnaut, L. G., Photodynamic therapy (PDT) of cancer: from local to systemic treatment. *Photochem. Photobiol. Sci.* **2015**, *14* (10), 1765-1780.
46. Sandell, J. L.; Zhu, T. C., A review of in-vivo optical properties of human tissues and its impact on PDT. *Journal of biophotonics* **2011**, *4* (11-12), 773-787.
47. Sun, J.; Du, K.; Diao, J.; Cai, X.; Feng, F.; Wang, S., GSH and H₂O₂ Co-Activatable Mitochondria-Targeted Photodynamic Therapy under Normoxia and Hypoxia. *Angew. Chem.* **2020**, *132* (29), 12220-12226.
48. Garcia-Diaz, M.; Huang, Y.-Y.; Hamblin, M. R., Use of fluorescent probes for ROS to tease apart Type I and Type II photochemical pathways in photodynamic therapy. *Methods* **2016**, *109*, 158-166.
49. Sui, C.; Tan, R.; Chen, Y.; Yin, G.; Wang, Z.; Xu, W.; Li, X., MOFs-Derived Fe-N Codoped Carbon Nanoparticles as O₂-Evolving Reactor and ROS Generator for CDT/PDT/PTT Synergistic Treatment of Tumors. *Bioconjugate Chem.* **2021**, *32* (2), 318-327.
50. Wang, W.; Wang, L.; Li, Z.; Xie, Z., BODIPY-containing nanoscale metal-organic frameworks for photodynamic therapy. *Chem. Commun.* **2016**, *52* (31), 5402-5405.
51. Kharkwal, G. B.; Sharma, S. K.; Huang, Y. Y.; Dai, T.; Hamblin, M. R., Photodynamic therapy for infections: clinical applications. *Lasers in surgery and medicine* **2011**, *43* (7), 755-767.
52. Rajesh, S.; Koshi, E.; Philip, K.; Mohan, A., Antimicrobial photodynamic therapy: An overview. *Journal of Indian Society of Periodontology* **2011**, *15* (4), 323.
53. Denis, T. G. S.; Aziz, K.; Waheed, A. A.; Huang, Y.-Y.; Sharma, S. K.; Mroz, P.; Hamblin, M. R., Combination approaches to potentiate immune response after photodynamic therapy for cancer. *Photochem. Photobiol. Sci.* **2011**, *10* (5), 792-801.
54. Huang, Y.-Y.; Tanaka, M.; Vecchio, D.; Garcia-Diaz, M.; Chang, J.; Morimoto, Y.; Hamblin, M. R., Photodynamic therapy induces an immune response against a bacterial pathogen. *Expert review of clinical immunology* **2012**, *8* (5), 479-494.
55. Kaplan, J. H.; Forbush III, B.; Hoffman, J. F., Rapid photolytic release of adenosine 5'-triphosphate from a protected analog: utilization by the sodium: potassium pump of human red blood cell ghosts. *Biochemistry* **1978**, *17* (10), 1929-1935.
56. Engels, J.; Schlaeger, E. J., Synthesis, structure, and reactivity of adenosine cyclic 3', 5'-phosphate-benzyltriesters. *J. Med. Chem.* **1977**, *20* (7), 907-911.
57. van Rixel, V. H. S.; Siewert, B.; Hopkins, S. L.; Askes, S. H. C.; Busemann, A.; Siegler, M. A.; Bonnet, S., Green light-induced apoptosis in cancer cells by a tetrapyrridyl ruthenium prodrug offering two trans coordination sites. *Chem. Sci.* **2016**, *7* (8), 4922-4929.
58. Farrer, N. J.; Woods, J. A.; Salassa, L.; Zhao, Y.; Robinson, K. S.; Clarkson, G.; Mackay, F. S.; Sadler, P. J., A Potent Trans-Diimine Platinum Anticancer Complex Photoactivated by Visible Light. *Angew. Chem.* **2010**, *122* (47), 9089-9092.

59. Presa, A.; Brissos, R. F.; Caballero, A. B.; Borilovic, I.; Korrodi-Gregório, L.; Pérez-Tomás, R.; Roubeau, O.; Gamez, P., Photoswitching the cytotoxic properties of platinum (II) compounds. *Angew. Chem. Int. Ed.* **2015**, *54* (15), 4561-4565.
60. Sgambellone, M. A.; David, A.; Garner, R. N.; Dunbar, K. R.; Turro, C., Cellular toxicity induced by the photorelease of a caged bioactive molecule: design of a potential dual-action Ru (II) complex. *J. Am. Chem. Soc.* **2013**, *135* (30), 11274-11282.
61. Bonnet, S., Why develop photoactivated chemotherapy? *Dalton Trans.* **2018**, *47* (31), 10330-10343.
62. Burke, C. S.; Byrne, A.; Keyes, T. E., Targeting Photoinduced DNA Destruction by Ru(II) Tetraazaphenanthrene in Live Cells by Signal Peptide. *J. Am. Chem. Soc.* **2018**, *140* (22), 6945-6955.
63. Shi, G.; Monro, S.; Hennigar, R.; Colpitts, J.; Fong, J.; Kasimova, K.; Yin, H.; DeCoste, R.; Spencer, C.; Chamberlain, L.; Mandel, A.; Lilge, L.; McFarland, S. A., Ru(II) dyads derived from α -oligothiophenes: A new class of potent and versatile photosensitizers for PDT. *Coord. Chem. Rev.* **2015**, *282-283*, 127-138.
64. Zhang, C.; Guan, R.; Liao, X.; Ouyang, C.; Rees, T. W.; Liu, J.; Chen, Y.; Ji, L.; Chao, H., A mitochondria-targeting dinuclear Ir-Ru complex as a synergistic photoactivated chemotherapy and photodynamic therapy agent against cisplatin-resistant tumour cells. *Chem. Commun.* **2019**, *55* (83), 12547-12550.
65. Lameijer, L. N.; Hopkins, S. L.; Breve, T. G.; Askes, S. H.; Bonnet, S., d- Versus l-Glucose Conjugation: Mitochondrial Targeting of a Light-Activated Dual-Mode-of-Action Ruthenium-Based Anticancer Prodrug. *Chemistry* **2016**, *22* (51), 18484-18491.
66. Wong, D. Y. Q., Induction of immunogenic cell death by chemotherapeutic platinum complexes. In *Rethinking Platinum Anticancer Drug Design: Towards Targeted and Immuno-chemotherapeutic Approaches*, Springer: 2018; pp 131-145.
67. Lv, W.; Zhang, Z.; Zhang, K. Y.; Yang, H.; Liu, S.; Xu, A.; Guo, S.; Zhao, Q.; Huang, W., A mitochondria-targeted photosensitizer showing improved photodynamic therapy effects under hypoxia. *Angew. Chem. Int. Ed.* **2016**, *55* (34), 9947-9951.
68. Mesmaeker, A. K.-D.; Lecomte, J.-P.; Kelly, J. M., Photoreactions of metal complexes with DNA, especially those involving a primary photo-electron transfer. *Electron Transfer II* **1996**, 25-76.
69. Presa, A.; Vázquez, G.; Barrios, L. A.; Roubeau, O.; Korrodi-Gregório, L.; Pérez-Tomás, R.; Gamez, P., Photoactivation of the Cytotoxic Properties of Platinum(II) Complexes through Ligand Photoswitching. *Inorg. Chem.* **2018**, *57* (7), 4009-4022.
70. Renfrew, A. K.; Bryce, N. S.; Hambley, T., Cobalt (III) Chaperone Complexes of Curcumin: Photoreduction, Cellular Accumulation and Light-Selective Toxicity towards Tumour Cells. *Chemistry—A European Journal* **2015**, *21* (43), 15224-15234.
71. Klán, P.; Solomek, T.; Bochet, C. G.; Blanc, A.; Givens, R.; Rubina, M.; Popik, V.; Kostikov, A.; Wirz, J., Photoremovable protecting groups in chemistry and biology: reaction mechanisms and efficacy. *Chem. Rev.* **2013**, *113* (1), 119-191.
72. Joshi, T.; Pierroz, V.; Mari, C.; Gemperle, L.; Ferrari, S.; Gasser, G., A Bis (dipyridophenazine)(2-(2-pyridyl) pyrimidine-4-carboxylic acid) ruthenium (II) Complex with Anticancer Action upon Photodeprotection. *Angew. Chem.* **2014**, *126* (11), 3004-3007.
73. Mackay, F. S.; Woods, J. A.; Heringová, P.; Kašpárková, J.; Pizarro, A. M.; Moggach, S. A.; Parsons, S.; Brabec, V.; Sadler, P. J., A potent cytotoxic photoactivated platinum complex. *Proc. Natl. Acad. Sci. U. S. A.* **2007**, *104* (52), 20743-20748.
74. Tahmasbi Rad, A.; Chen, C.-W.; Aresh, W.; Xia, Y.; Lai, P.-S.; Nieh, M.-P., Combinational Effects of Active Targeting, Shape, and Enhanced Permeability and Retention for Cancer Theranostic Nanocarriers. *ACS Appl. Mater. Interfaces* **2019**, *11* (11), 10505-10519.
75. Mari, C.; Pierroz, V.; Ferrari, S.; Gasser, G., Combination of Ru(ii) complexes and light: new frontiers in cancer therapy. *Chemical Science* **2015**, *6* (5), 2660-2686.
76. Barry, N. P. E.; Sadler, P. J., Challenges for Metals in Medicine: How Nanotechnology May Help To Shape the Future. *ACS Nano* **2013**, *7* (7), 5654-5659.

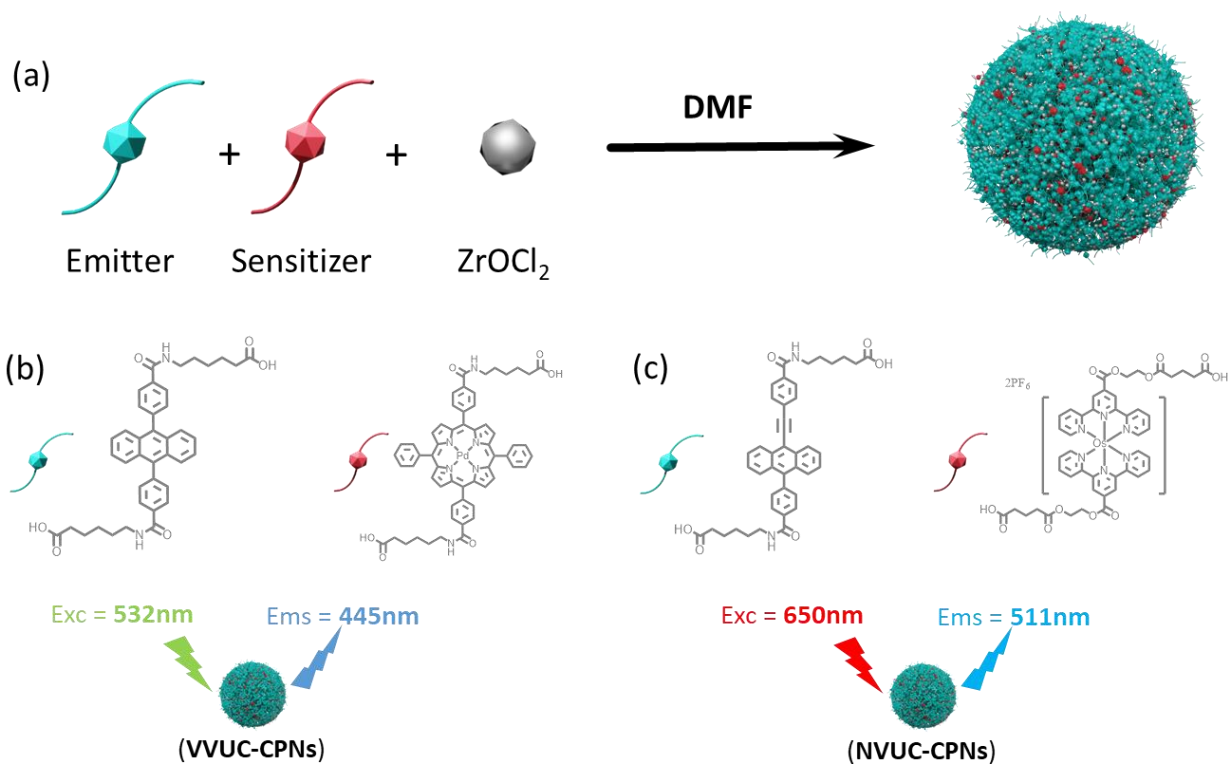
-
77. Mulcahy, S. P.; Li, S.; Korn, R.; Xie, X.; Meggers, E., Solid-phase synthesis of tris-heteroleptic ruthenium(II) complexes and application to acetylcholinesterase inhibition. *Inorg. Chem.* **2008**, *47* (12), 5030-5032.
78. Vyas, N. A.; Bhat, S. S.; Kumbhar, A. S.; Sonawane, U. B.; Jani, V.; Joshi, R. R.; Ramteke, S. N.; Kulkarni, P. P.; Joshi, B., Ruthenium(II) polypyridyl complex as inhibitor of acetylcholinesterase and A β aggregation. *Eur. J. Med. Chem* **2014**, *75*, 375-381.
79. Alatrash, N.; Narh, E. S.; Yadav, A.; Kim, M.-J.; Janaratne, T.; Gabriel, J.; MacDonnell, F. M., Synthesis, DNA Cleavage Activity, Cytotoxicity, Acetylcholinesterase Inhibition, and Acute Murine Toxicity of Redox-Active Ruthenium(II) Polypyridyl Complexes. *ChemMedChem* **2017**, *12* (13), 1055-1069.
80. H Koch, J.; Rogers, W. P.; Dwyer, F. P.; C Gyarfas, E., The Metabolic Fate of Tris-1,10-Phenanthroline 106Ruthenium (II) Perchlorate, a Compound With Anticholinesterase and Curare-Like Activity. *Aust. J. Biol. Sci.* **1957**, *10* (3), 342.
81. Poynton, F. E.; Bright, S. A.; Blasco, S.; Williams, D. C.; Kelly, J. M.; Gunnlaugsson, T., The development of ruthenium(ii) polypyridyl complexes and conjugates for in vitro cellular and in vivo applications. *Chem. Soc. Rev.* **2017**, *46* (24), 7706-7756.
82. Villemin, E.; Ong, Y. C.; Thomas, C. M.; Gasser, G., Polymer encapsulation of ruthenium complexes for biological and medicinal applications. *Nat. Rev. Chem.* **2019**, *3* (4), 261-282.
83. Karges, J.; Li, J.; Zeng, L.; Chao, H.; Gasser, G., Polymeric Encapsulation of a Ruthenium Polypyridine Complex for Tumor Targeted One- and Two-Photon Photodynamic Therapy. *ACS Appl. Mater. Interfaces* **2020**, *12* (49), 54433-54444.
84. Sun, W.; Zeng, X.; Wu, S., Photoresponsive ruthenium-containing polymers: potential polymeric metallodrugs for anticancer phototherapy. *Dalton Trans* **2018**, *47* (2), 283-286.
85. Chen, M.; Sun, W.; Kretzschmann, A.; Butt, H. J.; Wu, S., Nanostructured polymer assemblies stabilize photoactivatable anticancer ruthenium complexes under physiological conditions. *J. Inorg. Biochem.* **2020**, *207*, 111052.
86. Sun, W.; Parowatkin, M.; Steffen, W.; Butt, H. J.; Mailander, V.; Wu, S., Ruthenium-Containing Block Copolymer Assemblies: Red-Light-Responsive Metallopolymers with Tunable Nanostructures for Enhanced Cellular Uptake and Anticancer Phototherapy. *Adv. Healthc. Mater.* **2016**, *5* (4), 467-73.
87. Zhang, C.; Guo, X.; Da, X.; Yao, Y.; Xiao, H.; Wang, X.; Zhou, Q., UCNP@BSA@Ru nanoparticles with tumor-specific and NIR-triggered efficient PACT activity in vivo. *Dalton Trans* **2021**, *50* (22), 7715-7724.
88. Meijer, M. S.; Natile, M. M.; Bonnet, S., 796 nm Activation of a Photocleavable Ruthenium(II) Complex Conjugated to an Upconverting Nanoparticle through Two Phosphonate Groups. *Inorg. Chem.* **2020**, *59* (20), 14807-14818.
89. Chen, Y.; Jiang, G.; Zhou, Q.; Zhang, Y.; Li, K.; Zheng, Y.; Zhang, B.; Wang, X., An upconversion nanoparticle/Ru(ii) polypyridyl complex assembly for NIR-activated release of a DNA covalent-binding agent. *RSC Adv.* **2016**, *6* (28), 23804-23808.
90. Ruggiero, E.; Habtemariam, A.; Yate, L.; Mareque-Rivas, J. C.; Salassa, L., Near infrared photolysis of a Ru polypyridyl complex by upconverting nanoparticles. *Chem. Commun.* **2014**, *50* (14), 1715-8.
91. Soliman, N.; McKenzie, L. K.; Karges, J.; Bertrand, E.; Tharaud, M.; Jakubaszek, M.; Guerineau, V.; Goud, B.; Hollenstein, M.; Gasser, G.; Thomas, C. M., Ruthenium-initiated polymerization of lactide: a route to remarkable cellular uptake for photodynamic therapy of cancer. *Chem. Sci.* **2020**, *11* (10), 2657-2663.
92. Suárez-García, S.; Solórzano, R.; Alibés, R.; Busqué, F.; Novio, F.; Ruiz-Molina, D., Antitumour activity of coordination polymer nanoparticles. *Coord. Chem. Rev.* **2021**, *441*, 213977.
93. Adarsh, N. N.; Frias, C.; Ponnoth Lohidakshan, T. M.; Lorenzo, J.; Novio, F.; Garcia-Pardo, J.; Ruiz-Molina, D., Pt(IV)-based nanoscale coordination polymers: Antitumor activity, cellular uptake and interactions with nuclear DNA. *Chem. Eng. J.* **2018**, *340*, 94-102.

-
94. Novio, F.; Lorenzo, J.; Nador, F.; Wnuk, K.; Ruiz-Molina, D., Carboxyl Group (CO₂H) Functionalized Coordination Polymer Nanoparticles as Efficient Platforms for Drug Delivery. *Chem. - Eur. J.* **2014**, *20* (47), 15443-15450.
95. Nador, F.; Wnuk, K.; García-Pardo, J.; Lorenzo, J.; Solorzano, R.; Ruiz-Molina, D.; Novio, F., Dual-Fluorescent Nanoscale Coordination Polymers via a Mixed-Ligand Synthetic Strategy and Their Use for Multichannel Imaging. *ChemNanoMat* **2018**, *4* (2), 183-193.
96. Borges, M.; Yu, S.; Laromaine, A.; Roig, A.; Suárez-García, S.; Lorenzo, J.; Ruiz-Molina, D.; Novio, F., Dual T1/T2 MRI contrast agent based on hybrid SPION@coordination polymer nanoparticles. *RSC Adv.* **2015**, *5* (105), 86779-86783.
97. Imaz, I.; Rubio-Martínez, M.; García-Fernández, L.; García, F.; Ruiz-Molina, D.; Hernando, J.; Puentes, V.; Maspoch, D., Coordination polymer particles as potential drug delivery systems. *Chem. Commun.* **2010**, *46* (26), 4737-4739.
98. Imaz, I.; Rubio-Martínez, M.; García-Fernández, L.; García, F.; Ruiz-Molina, D.; Hernando, J.; Puentes, V.; Maspoch, D., Coordination polymer particles as potential drug delivery systems. *Chem. Commun.* **2010**, *46* (26), 4737-9.
99. Lee, S.; Lee, J. H.; Kim, J. C.; Lee, S.; Kwak, S. K.; Choe, W., Porous Zr₆L₃ Metallocage with Synergetic Binding Centers for CO₂. *ACS Appl. Mater. Interfaces* **2018**, *10* (10), 8685-8691.
100. Barsukova, M.; Goncharova, T.; Samsonenko, D.; Dybtsev, D.; Potapov, A., Synthesis, Crystal Structure, and Luminescent Properties of New Zinc(II) and Cadmium(II) Metal-Organic Frameworks Based on Flexible Bis(imidazol-1-yl)alkane Ligands. *Crystals* **2016**, *6* (10), 132.
101. Elsayed, S. A.; Jean-Claude, B. J.; Butler, I. S.; Mostafa, S. I., Synthesis, structural characterization and anticancer activity of some new complexes of 6-amino-4-hydroxy-2-thiopyrimidine. *J. Mol. Struct.* **2012**, *1028*, 208-214.
102. Novio, F.; Lorenzo, J.; Nador, F.; Wnuk, K.; Ruiz-Molina, D., Carboxyl group (-CO₂H) functionalized coordination polymer nanoparticles as efficient platforms for drug delivery. *Chemistry* **2014**, *20* (47), 15443-50.
103. Solorzano, R.; Tort, O.; Garcia-Pardo, J.; Escriba, T.; Lorenzo, J.; Arnedo, M.; Ruiz-Molina, D.; Alibes, R.; Busque, F.; Novio, F., Versatile iron-catechol-based nanoscale coordination polymers with antiretroviral ligand functionalization and their use as efficient carriers in HIV/AIDS therapy. *Biomater. Sci.* **2018**, *7* (1), 178-186.
104. Aryal, S.; Hu, C. M.; Zhang, L., Polymer--cisplatin conjugate nanoparticles for acid-responsive drug delivery. *ACS Nano* **2010**, *4* (1), 251-8.
105. Zayat, L.; Noval, M. G.; Campi, J.; Calero, C. I.; Calvo, D. J.; Etchenique, R., A new inorganic photolabile protecting group for highly efficient visible light GABA uncaging. *Chembiochem* **2007**, *8* (17), 2035-8.
106. Kasparkova, J.; Kostrohova, H.; Novakova, O.; Krikavova, R.; Vanco, J.; Travniczek, Z.; Brabec, V., A Photoactivatable Platinum(IV) Complex Targeting Genomic DNA and Histone Deacetylases. *Angew. Chem. Int. Ed. Engl.* **2015**, *54* (48), 14478-82.
107. Manzanares, D.; Ceña, V., Endocytosis: The Nanoparticle and Submicron Nanocompounds Gateway into the Cell. *Pharmaceutics* **2020**, *12* (4), 371.
108. Li, Z.; Zhang, Y.; Zhu, D.; Li, S.; Yu, X.; Zhao, Y.; Ouyang, X.; Xie, Z.; Li, L., Transporting carriers for intracellular targeting delivery via non-endocytic uptake pathways. *Drug. Deliv.* **2017**, *24* (sup1), 45-55.
109. Vichai, V.; Kirtikara, K., Sulforhodamine B colorimetric assay for cytotoxicity screening. *Nat. Protoc.* **2006**, *1* (3), 1112-6.
110. Yu, G.; Zhang, M.; Saha, M. L.; Mao, Z.; Chen, J.; Yao, Y.; Zhou, Z.; Liu, Y.; Gao, C.; Huang, F.; Chen, X.; Stang, P. J., Antitumor Activity of a Unique Polymer That Incorporates a Fluorescent Self-Assembled Metallacycle. *J. Am. Chem. Soc.* **2017**, *139* (44), 15940-15949.
111. Lutkus, L. V.; Rickenbach, S. S.; McCormick, T. M., Singlet oxygen quantum yields determined by oxygen consumption. *J. Photochem. Photobiol., A* **2019**, *378*, 131-135.

-
112. Peterson, J. C.; Arrieta, E.; Ruggeri, M.; Silgado, J. D.; Mintz, K. J.; Weisson, E. H.; Leblanc, R. M.; Kochevar, I.; Manns, F.; Parel, J. M., Detection of singlet oxygen luminescence for experimental corneal rose bengal photodynamic antimicrobial therapy. *Biomed. Opt. Express* **2021**, *12* (1), 272-287.
113. Hopkins, S. L.; Siewert, B.; Askes, S. H.; Veldhuizen, P.; Zwier, R.; Heger, M.; Bonnet, S., An in vitro cell irradiation protocol for testing photopharmaceuticals and the effect of blue, green, and red light on human cancer cell lines. *Photochem. Photobiol. Sci.* **2016**, *15* (5), 644-53.
114. Chen, Z. A.; Kuthati, Y.; Kankala, R. K.; Chang, Y. C.; Liu, C. L.; Weng, C. F.; Mou, C. Y.; Lee, C. H., Encapsulation of palladium porphyrin photosensitizer in layered metal oxide nanoparticles for photodynamic therapy against skin melanoma. *Sci. Technol. Adv. Mater.* **2015**, *16* (5), 054205.

Chapter 4

Upconverting Coordination Polymer Nanoparticles for Photochemical applications and Photophysical Applications



4.1 Introduction

Photon upconversion (UC) is the generation of high-energy luminescence through sequential absorption of two or more photons of lower energy.¹⁻⁴ For this reason it is also named anti-Stokes type emission. An example of UC is the conversion of infrared radiation to visible light.⁵⁻⁸ UC can take place with both organic and inorganic materials, through a number of different mechanisms. Organic molecules that can achieve photon upconversion through triplet-triplet annihilation (TTA-UC) are typically polycyclic aromatic hydrocarbons (PAHs) which are a class of chemicals that occur naturally in coal, crude oil, and gasoline, such as phenanthrene, pyrene, anthracene etc. Inorganic materials capable of photon upconversion often contain ions of d-block or f-block elements. Examples of these ions are Er^{3+} , Yb^{3+} , Tm^{3+} , Os^{4+} , and so on.⁹⁻¹³

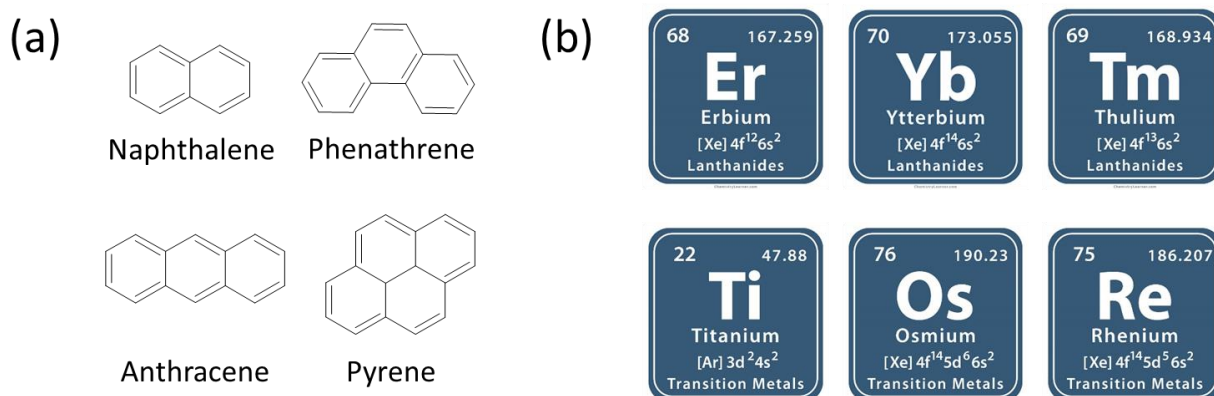


Figure 4.1: (a) Chemical structures of naphthalene, phenanthrene, anthracene and pyrene; (b) Chemical elements of erbium, ytterbium, thulium, titanium, osmium and rhenium.

4.1.1 Upconverting Rare-earth-doped nanoparticles

Ln^{3+} ions have several long-living electronic states which enable Ln-doped nanoparticles to undergo multiphoton absorption and energy transfer processes which yield upconversion. Depending on the type of Ln used and their combinations, UC emission occurs through different mechanisms, which are illustrated in Figure 4.2: excited-state absorption (ESA), energy transfer upconversion (ETU), cooperative sensitization upconversion (CSU), photon avalanche (PA) and energy migration upconversion (EMU),^{1, 3, 13-14}. Compared to the fluorescence of traditional dyes and quantum dots that are affected by the size and chemical surroundings, the UC emission of Ln-based materials only results from shielding effect. Additionally, with the good features of Ln-based UC, such as fixed energy levels, high

resistance photobleaching, long-living lifetimes, large anti-Stokes shifts and highly efficient conversion of NIR photons to visible/UV photons, several kinds of Ln-doped nanoparticles have been developed, for example Ln-doped mesoporous silica,¹⁵ surface-modified Ln-doped nanoparticles,¹⁶ core-shell-structured Ln-doped nanoparticles-incorporated polymer,¹⁷ which can be applied for anticounterfeiting,¹⁸⁻¹⁹ fingerprint detection,¹⁹ transparent displays,²⁰ solar cells,²¹ photoisomerization,²² the biological applications.²³⁻²⁴ However, Ln-based materials have some drawbacks such as narrow absorption bands, low quantum yield (QY), high cytotoxicity, and a high power excitation needed (10^3 - 10^5 mW/cm²), which hinder its applications to some extent.²⁵

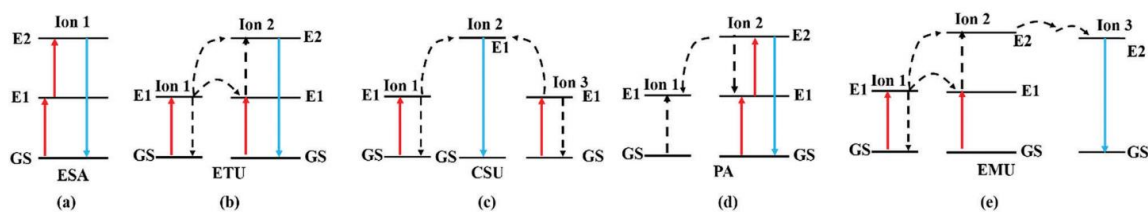


Figure 4.2: Upconversion processes for Ln-doped UCPNs. GS: ground state; E1 and E2: electronic excited states; ESA: excited-state absorption; ETU: energy transfer UC; CSU: cooperative sensitization UC; PA: photon avalanche; EMU: energy migration upconversion. Image extracted from reference.¹

4.1.2 Upconversion based on triplet-triplet annihilation (TTA-UC)

TTA mostly occurs with organic molecular dyes and was first introduced by Parker and Hatchard in 1962 described as a delayed fluorescence observed from solutions of anthracene and phenanthrene.²⁶⁻²⁷ Later on, TTA was used to obtain UC, which consists of a series of bimolecular processes and energy transfer steps that efficiently turn two low frequency photons into one photon of higher energy. TTA systems consist of one absorbing species, the sensitizer, and one emitting species, the emitter (or annihilator). Emitters are typically required to have these characteristics:

- (1) The excitation light can't excite the emitters, (2) A high fluorescence QY. (3) the energy of triplet state lower than the sensitizers. Sensitizers are also demanded to meet the following requirements: (1) High consistency of excitation light and the absorption of sensitizers, (2) An efficient intersystem crossing (ISC) to generate enough triplet states, (3) A relatively slow phosphorescence decay to transfer energy.

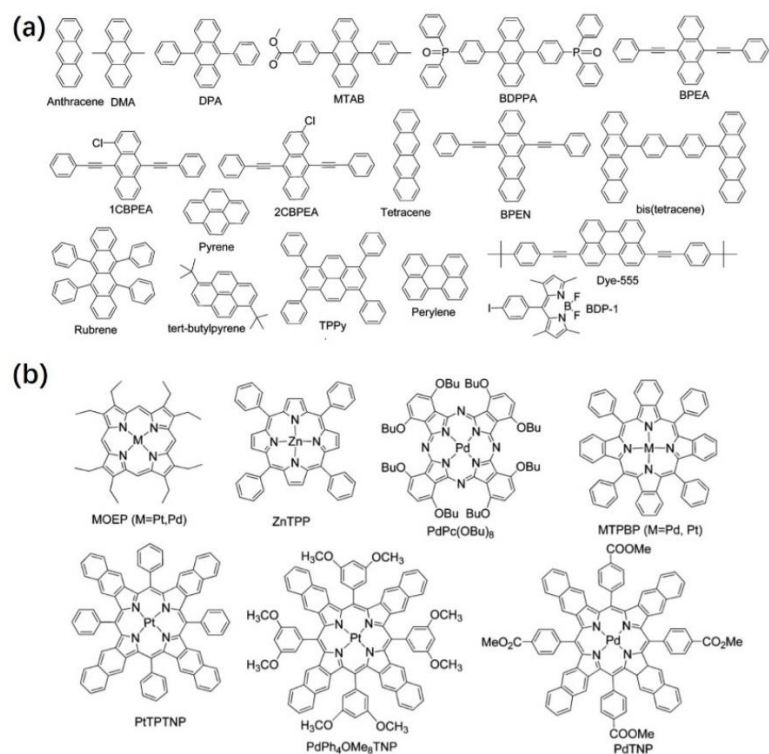


Figure 4.3: (a) Chemical structures of reported annihilators. (b) Chemical structures of porphyrin and phthalocyanine complexes used as sensitizers. Images extracted from reference.²⁸

In a sensitization *via* ISC process, singlet state of sensitizer (S_{s1}) is populated by photon excitation. Subsequently, triplet excited state (T_{s1}) is forming by ISC. Along with the triplet excited state energy transferring from the sensitizer to an emitter molecule, known as triplet-triplet energy transfer (TTET), triplet excited state of emitter (T_{e1}) is populated. When enough triplet excited states of the emitter molecules are generated, collisions between triplet take place with a second energy transfer process, known as triplet-triplet annihilation (TTA), which yields an emitter molecule in the ground state and one in a high-energy singlet excited state (S_{e1}) which later on relaxes to the ground state as a delayed fluorescence that has higher energy than the photons initially absorbed.^{1-3, 11} The overall balance sees two lower energy photons are required to produce one higher frequency photons (Figure 4.4).

To achieve efficient TTA-UC, several requirements have to be fulfilled:

(1) Due to the biomolecular process of TTA, the sum of energy of two sensitizer triplet states (T_{s1}) has to be higher to the emitter singlet state (S_{e1}) in order to accomplish the annihilation process. (2) Efficient ISC is needed for the sensitizers to generate adequate amount of triplet excited state (T_{s1}). (3) Long-living triplet state are required for both sensitizers and

emitters for effective TTET and TTA. (4) The presence of oxygen affects all the triplet-state-involved processes. Thus, a degassed environment is needed.²⁹⁻³¹

To evaluate the efficacy of sensitized system, a term “upconversion QY (Φ_{uc})” was proposed, which refers to a ratio of the transmitted light to the absorbed light, which can also be collectively shown in the equation ($\Phi_{uc} = \Phi_{ISC}\Phi_{TTET}\Phi_{TTA}\Phi_E$) by multiplying individual processes of TTA-UC. Where Φ_{ISC} stands for the QY of intersystem crossing (ISC). Φ_{TTE} stands for the triplet-triplet energy transfer between sensitizers and emitters (TTET). Φ_{TTA} stands for the QY of triplet-triplet annihilation. Φ_E stands for the QY of emitters. Therefore, theoretically and ideally, the maximum $\Phi_{uc} = 50\%$ (Φ_{ISC} , Φ_{TTET} , and Φ_E are 100% and $\Phi_{TTA}=50\%$ due to bimolecular process).

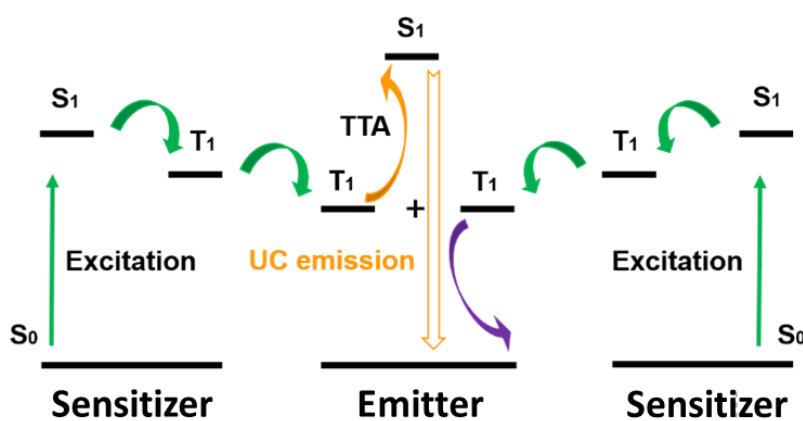


Figure 4.4: Schematic illustration of the TTA-UC *via* ISC

To improve the efficacy of UC emission, another process has been found, which is to avoid having ISC to reduce energy loss. In the 1940s,³²⁻³³ Lewis and Kasha investigated the singlet-to-triple (S-T) absorption as a reverse process of phosphorescence, and in late 1960s, the S-T absorption of transition metal complexes has been extensively studied and several Os polypyridyl complexes have shown S-T absorption in the NIR region.³⁴⁻³⁷ Thus, low excitation intensities can be used and S-T-TTA UC is able to have a larger anti-stokes shift converting.³⁸⁻⁴² The mechanism can be described that, in a sensitization *via* S-T process, triplet state of sensitizer (T_{s1}) is populated directly by photon excitation. Subsequently, the triplet excited state energy transfers from the sensitizer to an emitter molecule to afford triplet excited state (T_{e1}). Finally the two triplet states of emitter collide to accomplish TTA (Figure 4.5).

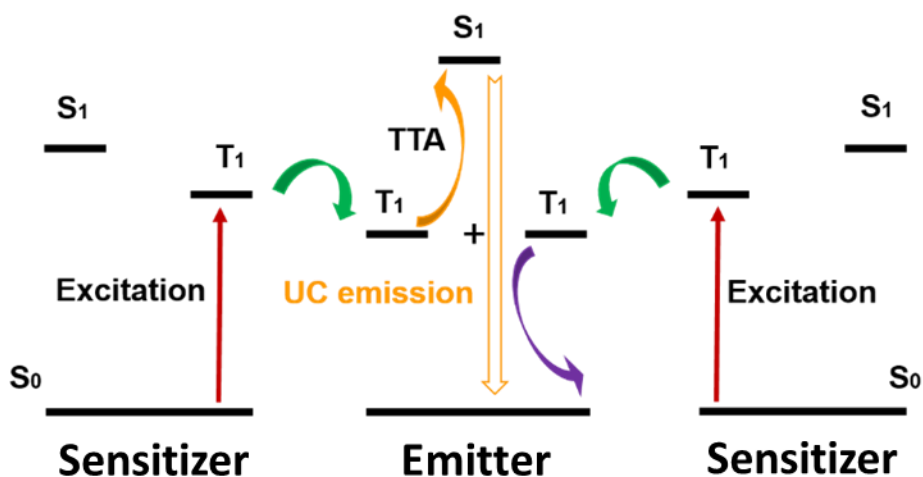


Figure 4.5: Schematic illustration of the photoactivatable S-T-TTA UC

4.1.3 TTA-UC nanomaterials

In the early stage, most of research on TTA-UC was carried out in organic liquid solutions (e.g. dimethylformamide, acetonitrile, and toluene) of the sensitizers and emitters. The liquid environment assures molecular diffusion of the fluorophores and thus a higher efficiency of the bimolecular processes (i.e. TTET and TTA) involved in the UC.⁴³⁻⁴⁴. These fundamental studies were very useful to obtain information on the UC mechanism, to increase the UC efficiency and to develop novel types of sensitizer/emitter pairs upconverting light from/to different spectral regions. However, to make TTA-UC applicable in different fields, solid materials undergoing TTA-UC in air atmosphere are required. Thus, more recently, researchers have started investigating solutions to obtain solid TTA-UC materials, facing important challenges to assure efficient UC: (1) the lack of mobility of photosensitizers and emitters in rigid matrices dramatically limits the diffusion-controlled bimolecular triplet-triplet energy transfer (TTET) and triplet-triplet annihilation (TTA) processes, with negative impact in the overall UC efficiency.^{2, 45-46} (2) The aggregation of photosensitizers and emitters is more frequent in the solid state and can negatively impact the optical properties (e.g. emission QY) of the materials because of aggregation-caused-quenching (ACQ).⁴⁷⁻⁴⁹ (3) The dependency of the UC from the presence of atmospheric molecular oxygen, which is a very good quencher of the excited triplet states of the sensitizer and emitter, and thus of the UC process.

In liquid solutions containing TTA-UC can be preserved by purging an inert gas (e.g. Ar or N₂) or freeze-pump-thaw techniques, which expels the dissolved oxygen. Although these methods are useful for fundamental studies, they are not suitable for practical applications. .

The first case of efficient TTA-UC emission without requiring degassing procedures, was reported by Kim and coworkers,⁵⁰ who used a solution made of mixture of hexadecane and polyisobutylene (PIB), possibly because of the low oxygen impermeability of PIB. Similar to this, in later research, oxygen scavengers with reductive chemical structures consuming the singlet oxygen, such as soybean oil and bovine serum albumin, hyperbranched unsaturated polyphosphates, and oleic acid were used to implement TTA-UC under ambient settings.⁵¹⁻⁵³ Although oxygen scavenging media avoid the requirement for a deoxygenation procedure, most of these methods are still based on liquid solutions, which are not useful for most practical applications such as solar energy harvesting, bioimaging/biotherapy, anticounterfeiting technologies, OLEDs, etc.

With the rapid development of nanotechnology, many synthetic strategies to obtain TTA-UC in the solid state were reported in past few decades, which can be classified in different families, such as:

4.1.3.1 Liposomes and micelles based TTA-UC

To keep high concentration of both dyes, proximity of emitters and sensitizers, and good energy transfer, Liposomes employed as spherical vesicles of a bilayer are good candidates to accommodate TTA-UC.⁵⁴⁻⁵⁶ Also, liposomes have been approved for clinical use by the United States Food & Drug Administration (FDA).⁵⁷⁻⁵⁹ Thus, they are one of the first material considered to prepare nanostructured solid materials. For instance, Bonnet and coworkers synthesized liposomes using 1,2-dimyristoyl-sn-glycero-3-phosphocholine (DMPC) and sodium *N*-(carbonyl-methoxypolyethyleneglycol2000)-1,2-distearoyl-sn-glycero-phosphoethanolamine (DSPE-MPEG-2000), and used two pairs of dyes, to have red-to-blue (the sensitizer platinum octaethylporphyrin and 9,10-diphenylanthracene) and green-to-blue (palladium tetraphenyltetrabenzoporphyrin and perylene) upconversion with a layer of Ru-based photoactivable complex anchored on the surface of liposomes to realize upconversion-induced photoreaction (Figure 4.6).⁶⁰

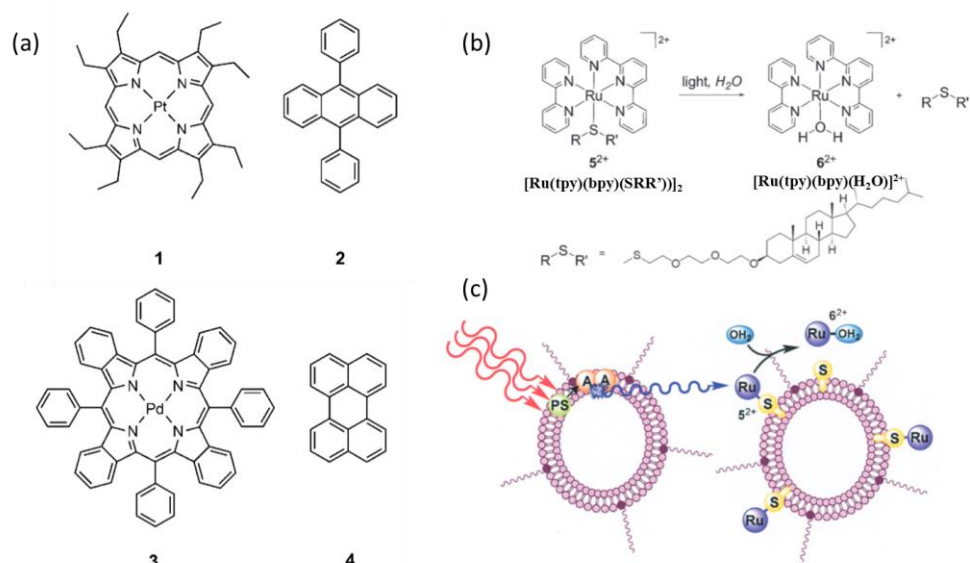


Figure 4.6: (a) Chemical structures of platinum octaethylporphyrin (1), 9,10 diphenylanthracene (2), palladium tetraphenyltetrabenzoporphyrin (3), and perylene (4). (b) Chemical structures of $[\text{Ru}(\text{tpy})(\text{bpy})(\text{SRR}')_2]^{2+}$ (5^{2+}) and $[\text{Ru}(\text{tpy})(\text{bpy})(\text{H}_2\text{O})]^{2+}$ (6^{2+}) and the conversion of 5^{2+} into 6^{2+} . (c) The TTA-UC process in the lipid bilayer, using a photosensitizer (PS) and an annihilator (A). Radiative energy transfer from the annihilator to complex 5^{2+} , denoted by a blue arrow, triggers light-induced hydrolysis of 5^{2+} to release 6^{2+} in solution. Images extracted from reference.⁶⁰

Beverina and coworkers also demonstrated a successful internalization of water-dispersible upconverting materials into the cytoplasm. The commercially available and FDA-approved surfactant Kolliphor EL® was employed as emulsifier for obtaining the solid upconverting nanomicelles.⁶¹ A further attempt was carried out by Yoda and coworkers, a new amphiphilic molecule that consists of hydrophilic sensitizer moiety and hydrophobic emitter moiety was synthesized for reverse micellar assembly providing a unique concept that will enhance future development of high performance TTA-UC systems.⁶²

4.1.3.2 Silica based TTA-UC

Silica is one of the most widely used matrix for a range of applications because of high chemical stabilities, large surface area, good compatibility, while offering easy synthesis with cheap starting materials.⁶³⁻⁶⁶ A growing interest of silica employed as TTA-UC substrate has been developed. Han and coworkers selected a iodized boron-dipyrromethene (BODIPY) dimer (BDP-F) and 9-phenylacetyleneanthracene (PEA) as a sensitizer and emitter respectively. After incorporation of the oxygen scavenger (methyl oleate oil) solution of the upconverting dyes in mesoporous silica nanoparticles. The silica based TTA-UC materials exhibited a good

UC and successful drug delivery. (Figure 4.7).⁶⁷ Also, Kim and coworkers employed hollow mesoporous silica microcapsules as carriers for aqueous phase photon upconversion. The high porosity feature of and hollow silica accommodate a good loading rate of TTA-UC medium. In presence of oxygen scavenger, the upconverting silica microcapsules are working in ambient environment.⁶⁸ Further, Kwon and coworkers reported self-assembling micelles with TTA-UC chromophores and oleic acid and later on encapsulated by silica shell, which has shown a red-to-blue upconversion process and demonstrated potential surface functionalization on nanocapsule surface and future application in aqueous phase.⁶⁹ However, silica-based TTA-UC materials still face the problems, such as the relatively low loading and the loss of the upconversion chromophore during encapsulation and surface functionalization.^{4, 68, 70} These challenges need to be tackled and more strategies have to be explored.

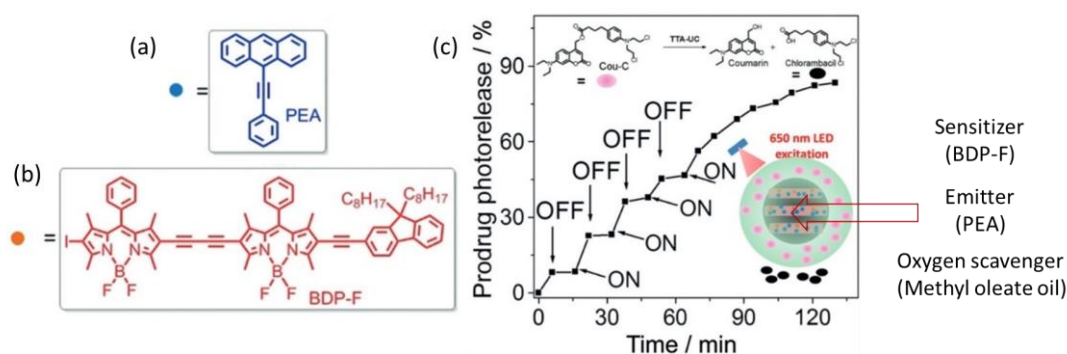


Figure 4.7: The molecular structure of (a) BDP-F and (b) PEA. (c) The TTA-UC regulated activation of Cou-C from TTA-core-shell structured nanocapsule with 650nm LED irradiation. “ON” and “OFF” indicate the initiation and termination of LED irradiation, respectively; working power density=100 mW/cm². Top inset: the photoactivation reaction of Cou-C. Bottom inset: illustration of a TTA-UC-mediated prodrug activation process in TTA silica based materials. Images extracted from reference⁶⁷

4.1.3.3 Polymer-based based TTA-UC

By incorporating upconversion chromophore into polymers, the local concentration of dyes can be maintained in a high level also with a good mobility. In addition, due to the advantages of polymer, such as ease of synthesis, good biocompatibility and facile surface functionalization, a variety of polymer employed as matrixes/backbones have been investigated extensively for fabrication of TTA-UC solid materials. One of the first examples of polymer-based TTA-UC was reported by Baluschev and coworkers by incorporating metalloporphyrins into polyfluorene to present a solid upconverting film.⁷¹ Furthermore, polyurethane films were made to explore the TTA-UC process efficiency of a series of lately-developed bichromophoric triplet sensitizers featuring tris-

cyclometalated Ir(III), showing high value so far reported for the visible-to-UV TTA systems in solid matrices (Figure 4.8).⁷²

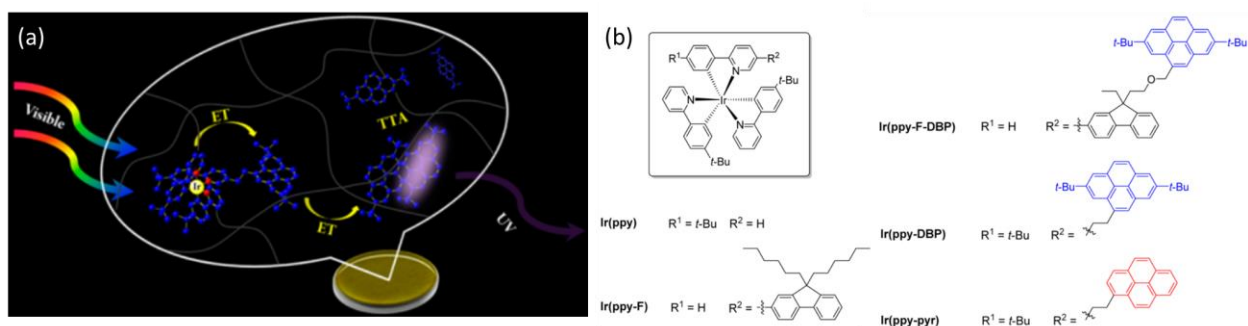


Figure 4.8: (a) Schematic illustration of the upconverting polyurethane films, (b) Chemical structures of studied sensitizers. Images extracted from reference⁷².

4.1.3.4 Metal-organic coordination based TTA-UC

Metal-organic coordination bonds that interconnect emitters and sensitizers by metal ions can fulfill the fast diffusion requirement for TTA-UC and allow a high exciton mobility through molecular aggregates, which is considered as a good strategy to develop solid state upconverting.⁷³⁻⁷⁴ Metal-organic frameworks (**MOFs**), as the well-known metal-organic coordination based crystalline materials have captured widespread research interests and recognized as potential candidates TTA-UC applications.⁷⁵⁻⁷⁶ Due to their synthetic tunability and chemical stability, **MOFs** have also been explored as a efficient energy transfer (ET) platform that may be favorable to triplet energy transfer. Howard and co-workers presented a sandwich-structure (A-B-A) **MOFs** and double-layer (A-B) **MOFs** where A and B stand for a layer of emitter **MOFs** and sensitizer **MOFs** respectively (Figure 4.9). Within the structure, after irradiation, triplets generated from the B layer can only flee out through A layers. Based on these multilayer materials, solid-state upconverting thin films can be achieved with UC thresholds lower than 1 mW/cm^2 .⁷⁷ Another example was presented by Zhou and coworkers, porous emitter-based Zr-**MOFs** were synthesized with a following encapsulation of different concentration of sensitizer to optimize the energy transfer and finally realize bioimaging.⁷⁵

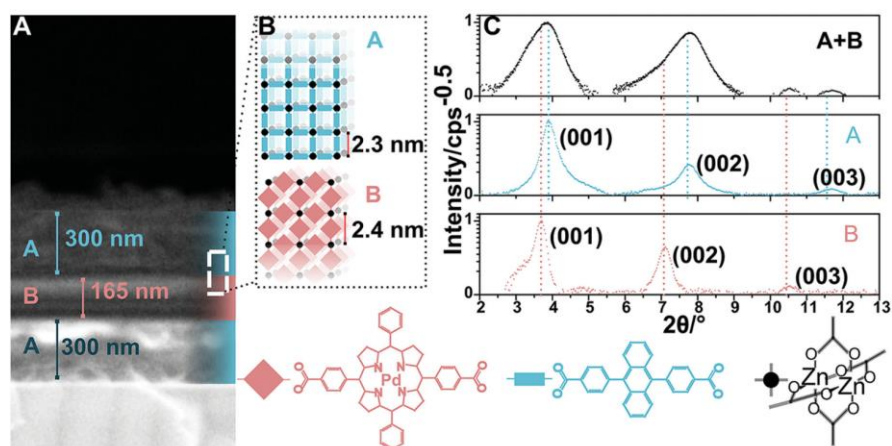


Figure 4.9: A) SEM cross-section of a three-layer emitter–sensitizer–emitter (A–B–A) SURMOF heterostructure on a Si substrate B) Schematic illustration of the heterostructure showing the layers are made from different organic linkers. B. C) Out-of-plane XRD diffractograms showing the first three orders of the diffraction peak in the (001) crystalline direction of MOFs prepared from Zn-emitter (A) and Zn-sensitizer (B) alone, plus the A–B–A heterojunction. Images extracted from reference⁷⁷

Apart from MOFs, Hanson and coworkers constructed an nanocrystalline ZrO_2/TiO_2 –organic interface with an outer layer that consists TTA-UC molecules linked through Zinc ions ((4,4'-(anthracene-9,10-diyl)bis(4,1-phenylene)diphosphonic acid DPPA as emitters and Pt(II)tetrakis(4-carboxyphenyl)porphyrin PtTCPP) as sensitizers) anchored on the surface of metal oxide. This hybrid system provides a new method for constructing layer through metal-organic coordination bonds (Figure 4.10).

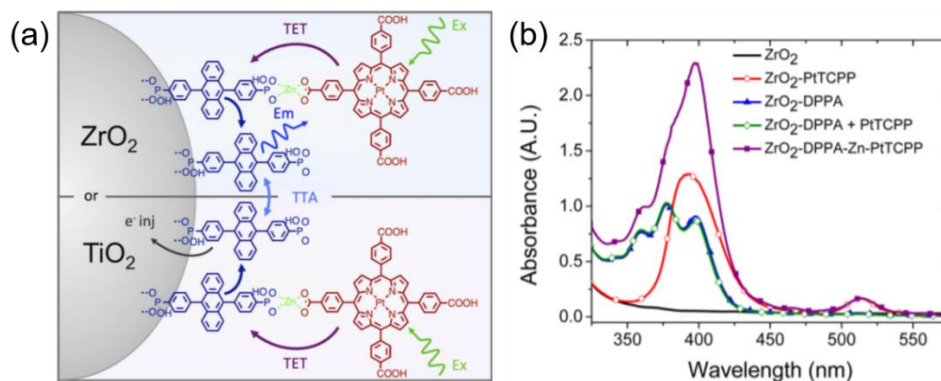


Figure 4.10: Schematic for the nanocrystalline ZrO_2/TiO_2 –organic interface where the chemical structure of DPPA (blue), Zn^{2+} ions (green) and PtTCPP (red) are shown. (b) Absorption spectra for ZrO_2 , ZrO_2 -DPPA, ZrO_2 -PtTCPP and ZrO_2 -DPPA after soaking in PtTCPP with (ZrO_2 -DPPA-Zn-PtTCPP) and without (ZrO_2 -DPPA + PtTCPP) $Zn(CH_3COO)_2$ pretreatment. Images extracted from reference.⁷⁸

4.1.4 Applications of TTA-UC nanomaterials

4.1.4.1 Biological applications

Bioimaging. *Bioimaging* relates to methods that non-invasively visualize biological processes in real time and aims to interfere as little as possible with life processes. However, standard fluorescence bioimaging, exploiting the Stokes-shift of the emitting molecules or nanoparticles, presents autofluorescence interference generated from the tissue themselves, excited with the same wavelength as that used to activate the fluorescent marker, and low penetration depths, especially if short wavelengths are used. Thus, to overcome these limitations, upconverting materials are promising alternatives by utilizing longer and more penetrating wavelengths as excitation light, while the anti-Stokes emissions and longer lifetimes prevents any be interference with the autofluorescence. Beverina and coworkers obtained water-dispersible TTA-UC-active nanomicelles for enhanced theranostics. The fabricated nanomicelles demonstrated effective emission at 10 mW/cm^2 . Using just one excitation light source, multichannel, high-contrast optical imaging of 3T3 cells was made possible by biocompatible materials made of the nanomicells (excitation at 532 nm). In the cytoplasmic region around the cell nucleus, upconverted emission (435 nm) was detected, and red light was produced from the stained dye, (phalloidin positive F actin). The internalization of the upconverting nanomicelles into the cytoplasm was successful, as seen by the combined confocal fluorescence image (Figure 4.11).⁷⁹

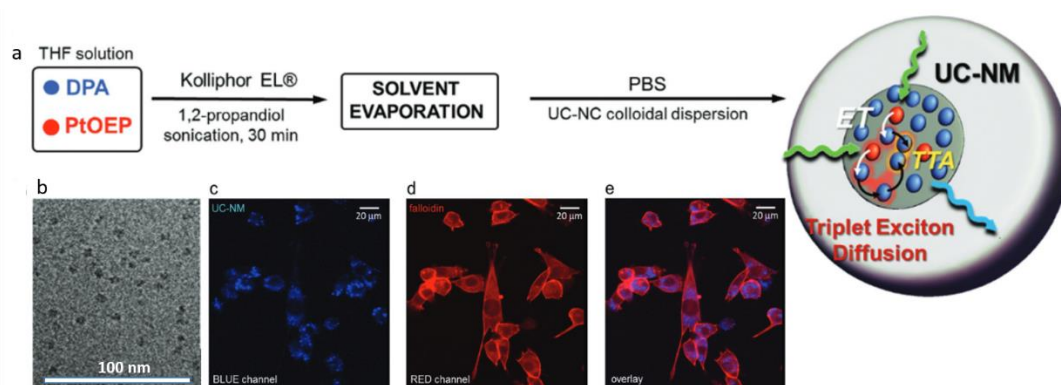


Figure 4.11: (a) Outline of the UC-NM self-assembly reaction scheme and sketch of the TTA-UC process in a single UC-NM. The up-converted photons are generated thanks to the diffusion (black arrows) and annihilation (TTA) of sensitized dark triplet excitons among the network of acceptors (Diphenyl anthracene, DPA, blue dots) embedded in the Kolliphor EL micelles. (b) Cryo-TEM images of UC-NMs loaded with a 100:1 DPA:PtOEP cargo. (c-e) Confocal fluorescence image of 3T3 cell stained with UC-NMs (blue) and phalloidin positive F actin (red) under laser excitation at 532 nm. Images extracted from reference.⁷⁹

Biotherapy. Compared to the traditional photoinduced drug delivery processes, higher energy excitations are needed, regarding to the wavelength of stokes shift. The high phototoxicity and shallow penetration depth are the main drawbacks hindering the further development. To coop with the problems, TTA-UC can be a perfect solution to step further in field of biological applications. Similar methods can be found from Han's group⁶⁷ and Bonnet's group⁶⁰⁸⁰, which is about the fabrication of TTA-UC materials that are closely attached with photoactivatable prodrug. After irradiation, the upconversion takes place and further trigger the photocleavage to realize drug delivery. Further attempt was carried out by Emrullahoglu and coworkers presenting two types of halogenated BODIPY-based photosensitisers (BOD-1 and BOD-2) with high yield of singlet oxygen. Significant upconversion was observed for **BOD-2** when combined with perylene as the emitter, at the same time with excellent photoactivity and photocytotoxicity both in solution and living cells, thereby making it a highly promising tool for imaging-guided PDT.⁸¹

4.1.4.2 OLED application

TTA-UC emission has long been considered potentially useful for OLED applications. An effective TTA mechanism in OLEDs was developed by Friend and coworkers.⁸² They designed TTA-UC dyes doped polymer LEDs representing the first application of DPA, perylene, rubrene and TIPS-pentacene as OLED emitters. Monkman and coworkers designed, and synthesized a series of carbazole and nitrile-substituted 1,3,5-triphenylbenzene (TPB) and investigated the influence of the substituent orientation on the properties of the compounds for the potential use for TTA OLED applications. The result turned out that para-conjugation (p-TPB-2Cz) and meta-conjugation (m-TPB-2Cz) exhibited outstanding performance in an OLED reaching an average quantum efficiency of 12.1% (Figure 4.12).⁸³

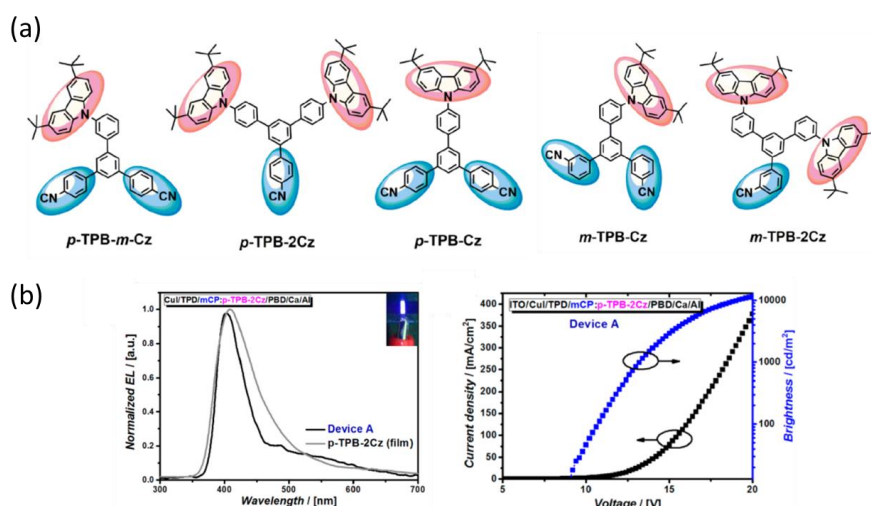


Figure 4.12: (a) Chemical Structures of the Carbazoyl- and Cyano-Substituted TPB Derivatives. (b) electroluminescence spectra of the fabricated device, and graph of the current density–voltage–luminance curves. Images extracted from reference.⁸³

4.1.4.3 Energy applications

In terms of energy applications, solar energy is adequate and free, but there is a lack of easy-manufactured energy capture devices. Perovskites or polythiophenes, as a class of energy conversion devices, are promising. However, due to the high bandgap, they sacrifice a large portion of the photons that are lower than the bandgap. TTA-UC materials can utilize the unused part of light and convert it into useful wavelength. Schmidt and coworkers reported the first example of combining a dye-sensitized solar cell (DSC) and TTA-UC system.⁸⁴ Also, Hanson and coworkers have investigated self-assembled bilayers for many years offering a promising strategy to directly harness photon upconversion via triplet–triplet annihilation (TTA-UC).^{85–88} To be specific, it is found that the bilayers solar cell exhibits efficient sensitizer-to-acceptor energy transfer and the photon-to-current efficiency. Additionally, the redox potential of the $\text{Co}^{2+/3+}$ mediator had a significant influence to I_{th} values (0.8 mW/cm^2) which is also the lowest value reported for any TTA-UC system (Figure 4.13).⁸⁸

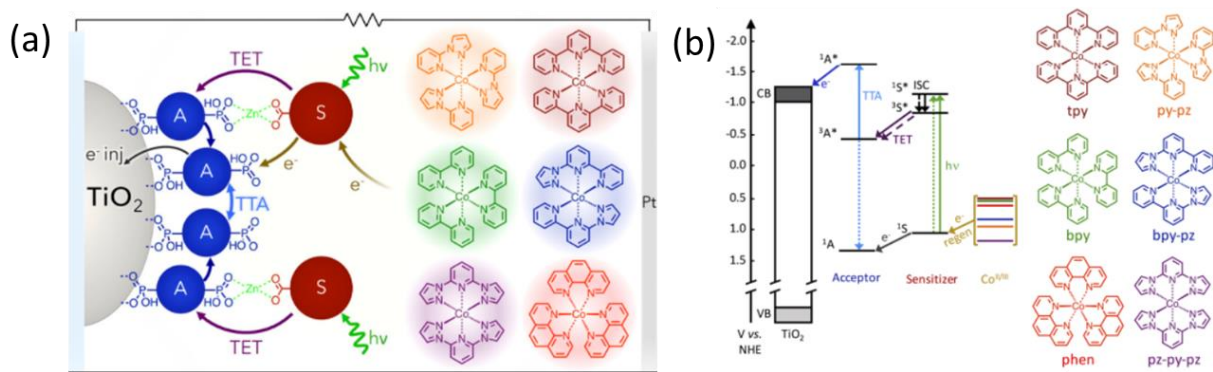


Figure 4.13: (a) Schematic illustration bilayer bilayers solar cell, (b) Electronic transitions and energetics for TiO₂, acceptor, sensitizer, and the mediators (vs NHE) alongside the structure of the CoII/III redox mediators. Images extracted from reference⁸⁸

4.1.4.4 Anti-counterfeiting applications

Product counterfeiting represents a large, growing risk to many global firms and people including currency, medicines, and documents, has long been a threat to public property. According to the “Counterfeiting and piracy in 2021 – the global impact”, the international trade in counterfeit and pirated products could have amounted to as much as \$509 billion in 2016, estimated to be 3.3% of world trade – up from \$461 billion in 2013, representing 2.5% of world trade. In this regard, a variety of anti-counterfeiting technologies have emerged on the market to boycott the increasing amount of counterfeiting. Upconversion materials, as a novel anti-counterfeiting alternative, exhibit multicolor optical properties, light power dependence excitation, and a near-infrared source of upconversion that is difficult to obtain, resulting in the difficulty of duplicating.⁸⁹ TTA-UC-based anti-counterfeiting technique was proposed by Kim and coworkers. They presented a new multilayer thin-film structure in which there are flexible and photostable TTA-UC thin films with layers of oxygen barrier (Polyvinyl alcohol, PVA), interference layer (striped layer) and host polymers.⁹⁰ Upon UV light irradiation, the luminescence of the striped layer will interfere with the patterned layer making it unreadable. However, upon 635 nm irradiation, only the TTA-UC layer glows enabling QR code recognizable to the smart phone (Figure 4.14).⁹⁰

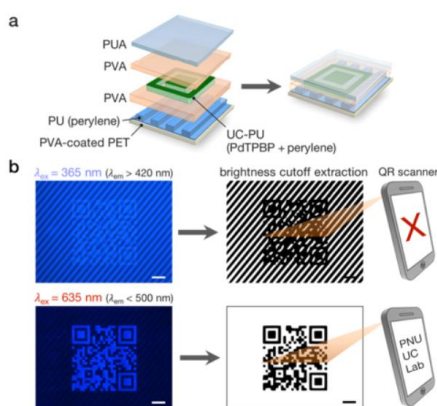


Figure 4.14: (a) Schematic showing the multilayers materials with a QR code doped with PdTPBP and perylene. (b) Fluorescence micrographs of this material under xenon lamp excitation at 365 nm and laser excitation at 635 nm, only the QR code in the bottom image can be read using a smart phone or a QR code scanner. Images extracted from reference.⁹⁰

4.2 Objective

Due to the many potential applications of solid state TTA-UC materials. Herein, we aim to have a new approach to accomplish TTA-UC in solid state upconverting coordination polymer nanoparticles (UC-CPNs), where the high content of the dyes in the amorphous material compensates the lack of mobility, in which the monomers consist of functionalized sensitizer and the emitter molecules with flexible alkyl chains, crosslinked by zirconium ions. Such strategy allows to have ratio tunable UC-CPNs with good colloidal stability and efficient TTET through a large excess of emitter, resulting in TTA-UC based solid materials possibly applied in photochemical and photophysical applications.

To obtain the upconverting CPNs (UC-CPNs), firstly three pairs of dyes have been design (Figure 4.15):

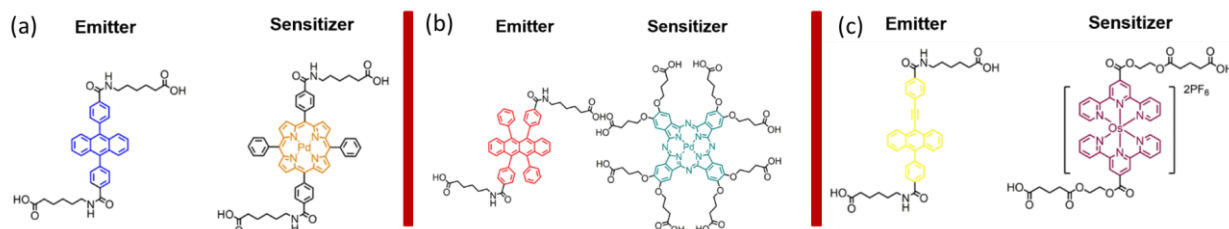


Figure 4.15: Chemical structures of functionalized (a) DPA (**DPA-S-COOH**) and palladium porphyrin (**Pd-S-COOH**), (b) rubrene (**RUB-S-COOH**) and phthalocyanine (**PAC-S-COOH**), (c) [4-((10-(4-carboxyphenyl)anthracene-9-yl)ethynyl)benzoic (**CAEBD-S-COOH**) and diterpyridine Osmium complex (**Os-S-COOH**).

(a) **DPA-S-COOH** and **Pd-S-COOH** are designed for visible-to-visible upconversion (VVUC) through ISC.

(b) **PAC-S-COOH** and **RUB-S-COOH** are designed for near infrared (NIR)-to-visible upconversion (NVUC) through ISC.

(c) **CAEBD-S-COOH** and **Os-S-COOH** are designed for near infrared (NIR)-to-visible upconversion (NVUC) through S-T

Secondly, with anticipated coordination properties of the molecules. **CPNs** will be made via coordination methods *e.g.* using metal ions. The schematic illustration is shown in Figure 4.16.

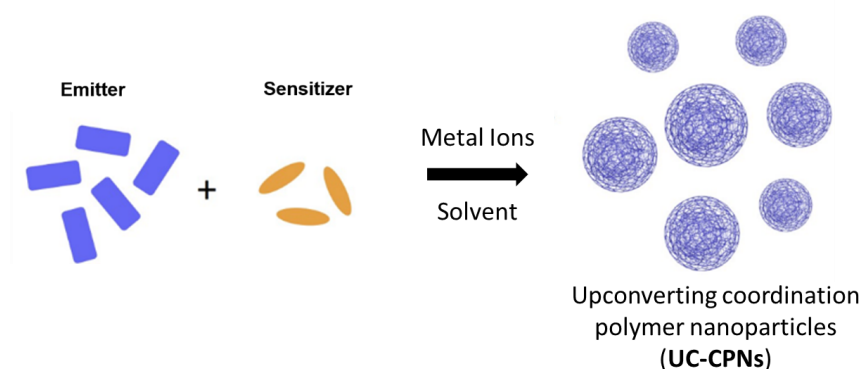


Figure 4.16: The schematic illustration of UC-CPNs synthesis.

Finally, with the obtained UC-CPNs, possible photochemical and photophysical application will be investigated, including upconversion-induced photochromism, upconversion-induced photopolymerization, film application and security ink.

4.3 Results and Discussions

The first part of this project consisted of the preparation of the dye pairs (sensitizer and emitter) required for the synthesis of the UC-CPNs. For this, we designed three pairs of dyes (**DPA-S-COOH & Pd-S-COOH**, **RUB-S-COOH & PAC-S-COOH**, and **CAEBD-S-COOH & Os-S-COOH**) which are well-known molecules for upconversion with excitation and emission wavelength spanning from NIR region to visible region. Due to the possibility of chemical functionalization on the molecules, it is worthy to explore that with the proposed strategy, if we can obtain the efficient UC-CPNs for further applications. It was decided to attach a spacer around 5 to 10 atoms between carboxylic groups and chromophores because a shorter spacer may increase rigidity to form crystalline and longer spacer will relatively reduce

the concentration of chromophores during particles formation and increase the distance between emitters and sensitizers, which is unfavorable for efficient energy transfer.

4.3.1 Organic synthesis

The first dyes synthesized, were the **DPA-S-COOH** and **Pd-S-COOH**, which were selected for the preparation of VVUC-CPNs. The chosen synthetic route is shown in Figure 4.17, 4.18.

DPA-S-COOH synthetic route

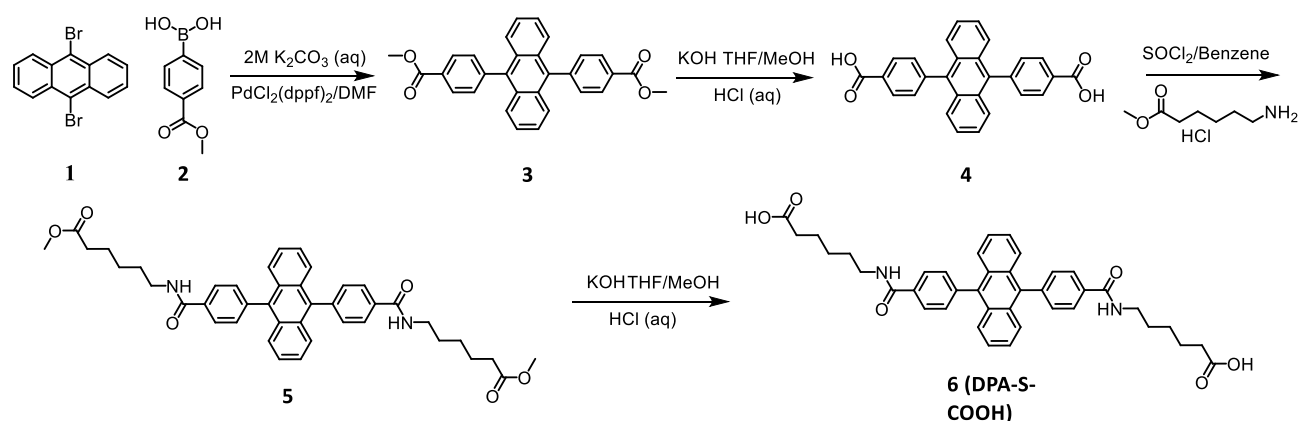


Figure 4.17: Synthetic route for **DPA-S-COOH**

Suzuki coupling (**1** and **2**) was used to have terminal ester groups on diphenylanthracene **3** with a yield of 67.7%. After hydrolysis with potassium hydroxide and further acidification using hydrochloric acid, the 4,4'-(anthracene-9,10-diyl) dibenzoic acid **3** was obtained with a yield of 90.1% following a react with alkyl chain to extend the length of the molecule to afford **5** with a yield of 75.9%. The final product **6** was collected by hydrolysing **5** with further acidification with a yield of 89% (5-step overall yield = 41.2%). Synthesis details are shown in the materials and methods section.

Pd-S-COOH synthetic route

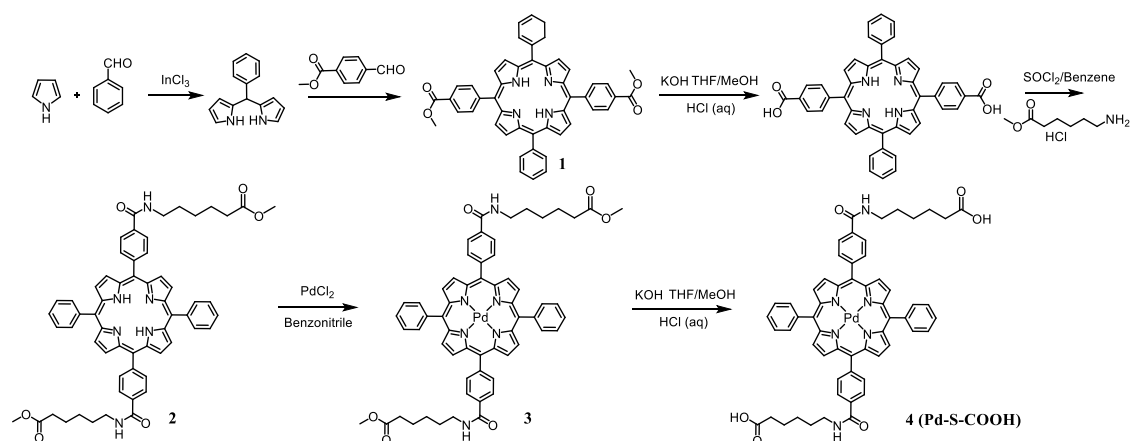


Figure 4.18: Synthetic route for **Pd-S-COOH**

Dipyrroliphenylmethane was synthesized using pyrrole and benzaldehyde in acidic condition with a yield of 76%. Afterwards 4-formylbenzoate was used to construct porphyrin ring with two terminal ester groups with a ver low yield of 7.1%. Following by KOH hydrolysis and HCl (aq) acidification, alkyl chain was introduced to afford **2** with a yield of 71.1%. Pd ion was introduced to coordiante with porphyrin by using PdCl_2 at high temprature with a yield of 72.2%. Due to the sensitivity of metallic phophyrin towards acidic environment, acidity was monitored carefully using pH indicator during the addition of hydrochloric acid and **4** was finally obtained with a yield of 91.7% (6-step overall yield 1.8%). Synthesis details are shown in the materials and methods section.

The second dyes synthesized, were the **RUB-S-COOH** and **PAC-S-COOH**, which were selected for the preparation of NVUC-CPNs. The chosen synthetic route is shown in Figure 4.19, 4.20.

RUB-S-COOH synthetic route

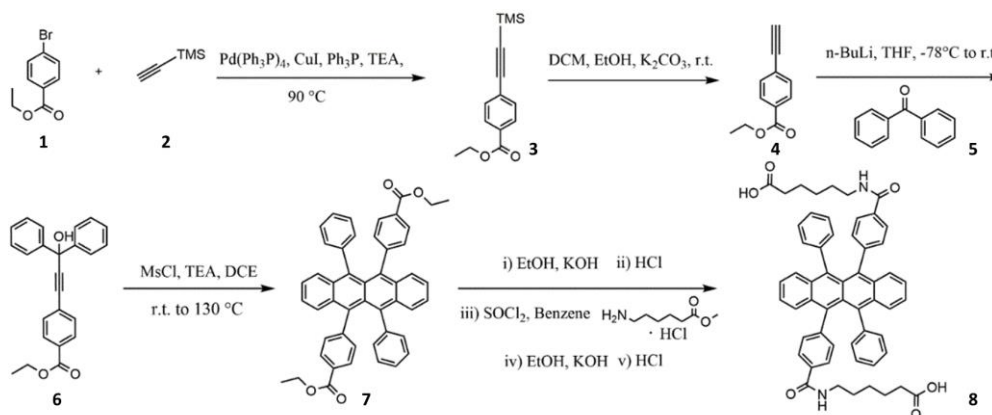


Figure 4.19: Synthetic route for **RUB-S-COOH**

The designed synthetic route has 5 steps in total. Since it is difficult to functionalize the benzene group on the rubrene core directly, the compound **RUB-S-COOH** had to be designed and synthesized from very beginning. Thus, ethyl 4-bromobenzoate was selected as the starting material with lower cost compared to the methyl-4-bromobenzoate. The first step is the Sonogashira cross-coupling reaction used in organic synthesis to form carbon–carbon bonds. It employs a palladium catalyst as well as copper co-catalyst to form a carbon–carbon bond between a terminal alkyne and an aryl or vinyl halide. The synthesis was carried out at 90 °C, yielding the corresponding product **3** with a yield of 96.7%. The second step consisted of the hydrolysis of the trimethylsilyl group so that the alkynyl hydrogen can be exposed for the next step, achieved with a yield of 86.7%. Later on, the hydrogen is deprotonated by using a strong base *n*-BuLi under -78 °C following a reaction with **5**, which involves electrophilic addition and ring arrangement with a yield of 23.5%.⁹¹ The last step contains the hydrolysis, acidification and side chain extension. Synthesis details are shown in the materials and methods section

PAC-S-COOH synthetic route

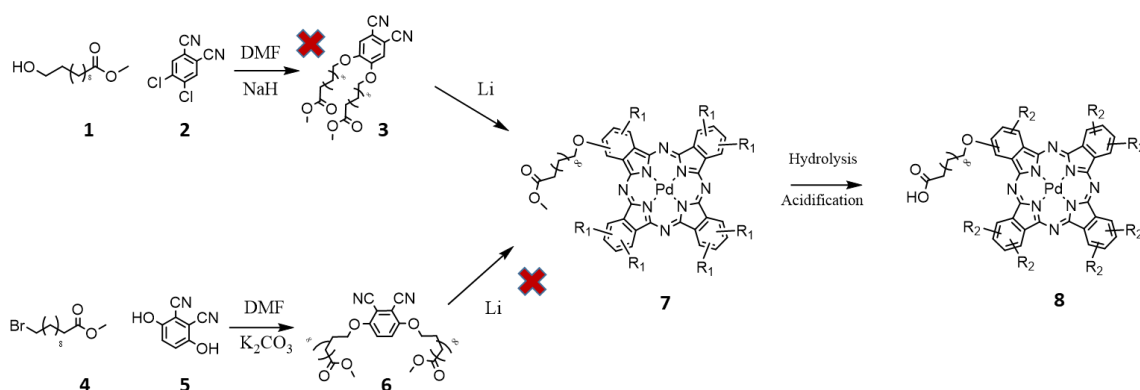


Figure 4.20: Synthetic route for **PAC-S-COOH**

The first step (**1** and **2**) is Williamson ether synthesis that is an S_N2 reaction in which a diphenol ion is a nucleophile that displaces a halide ion from an alkyl halide to give an ether. However, cyanide groups can also react with nucleophile, which resulted in a failure. Afterwards, a further trial was carried out by using **4** and **5**. Due to the slightly acidic nature of phenol and electron withdrawing property of cyanide groups, Williamson reaction undergoes successfully in a mild base environment to afford **6** with a yield of 68%. But the **7** can't be obtained probably because of the side-reduction of the ester groups taking place with Li. Thus the pair RUB-S-COOH and PAC-S-COOH was not considered for further investigation.

The third dyes synthesized, were the **CAEBD-S-COOH** and **Os-S-COOH**, which were selected for the preparation of NVUCCPNs. The chosen synthetic route is shown in Figure 4.21, 4.22.

CAEBD-S-COOH synthetic route

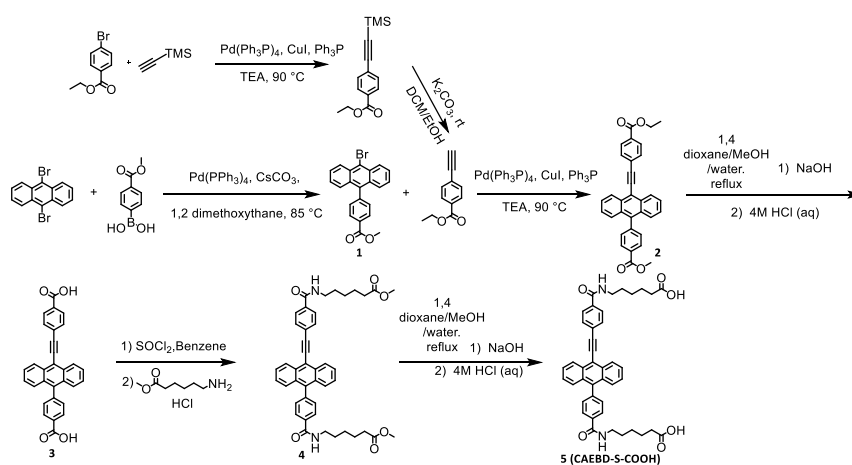


Figure 4.21: Synthetic route for **CAEBD-S-COOH**

Methyl 4-(10-bromoanthracen-9-yl)benzoate **1** was synthesized through Suzuki coupling reaction with 9,10-dibromoanthracene and (4 - (methoxycarbonyl) phenyl) boronic acid as starting materials with a yield of 45.7%. The second step is Sonogashira coupling to construct the core structure with two terminal ester groups **2** with a yield of 73% following by hydrolysis and acidification to obtain **3** with a yield of 91%. Afterwards, the same strategy was used to extend the length of the molecule to finally have two terminal carboxylic groups **5** with a yield of 89% (7-step overall yield of 23.4%). Synthesis details are shown in the materials and methods section.

Os-S-COOH synthetic route

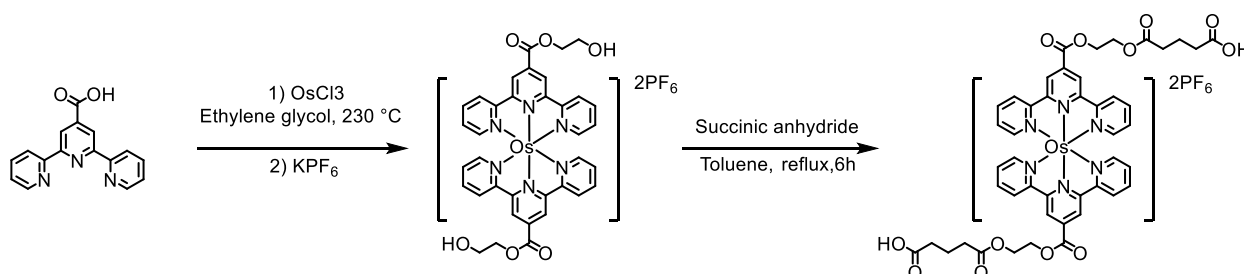


Figure 4.22: Synthetic route for **Os-S-COOH**

Ethylene glycol was chosen as reaction solvent. However apart from osmium coordination, the solvent can also react with carboxylic acid affording ester.³⁸ Taking advantage of the previous side-reaction, succinic anhydride was used to further extend the length of the spacer (2-step overall yield of 12.6%). Synthesis details are shown in the materials and methods section.

4.3.2 Optical measurements of DPA-S-COOH and Pd-S-COOH

Before the synthesis of upconverting nanoparticles, the absorption and emission of **DPA-S-COOH** and **Pd-S-COOH** were measured in DMF. **DPA-S-COOH** showed an absorption spectrum with the typical vibronic bands, with $\lambda_{Abs} = 375$ nm. The emission maximum of the **DPA-S-COOH** (extinction coefficient = 1.37×10^4 M⁻¹ cm⁻¹) ($\lambda_{exc} = 375$ nm) was recorded at $\lambda_{Ems} = 425$ nm. The absorption and emission spectra of **Pd-S-COOH** (extinction coefficient = 3.34×10^5 M⁻¹ cm⁻¹) showed a band at $\lambda_{Abs} = 523$ nm and a band at $\lambda_{Ems} = 700$ nm respectively upon 532nm excitation (Figure 4.23a-e). Additionally, the QY of **DPA-S-**

COOH and **Pd-S-COOH** were measured in DMSO using perylene as a standard reference, under N_2 environment ($QY_{DPA-S-COOH} = 98.9\%$, $QY_{Pd-S-COOH} = 1.4\%$, $\lambda_{exc} = 532$ nm, Figure 4.23f,g).

Once the optical properties of the dyes were characterized, the next step consisted in the investigation of the UC properties of solutions made by the two dyes. For this study, the concentration of **DPA-S-COOH** was set to 1×10^{-4} M, while the concentration of **Pd-S-COOH** was varied from 1×10^{-6} to 2×10^{-5} M. The resulting dimethyl sulfoxide (DMSO) solution was degassed by N_2 and irradiated with laser ($\lambda_{exc} = 532$ nm, 18mW) showing successful anti-Stokes emission ($\lambda_{Ems} = 435$ nm), which indicates that the pair is suitable for UC (Figure 4.23h).

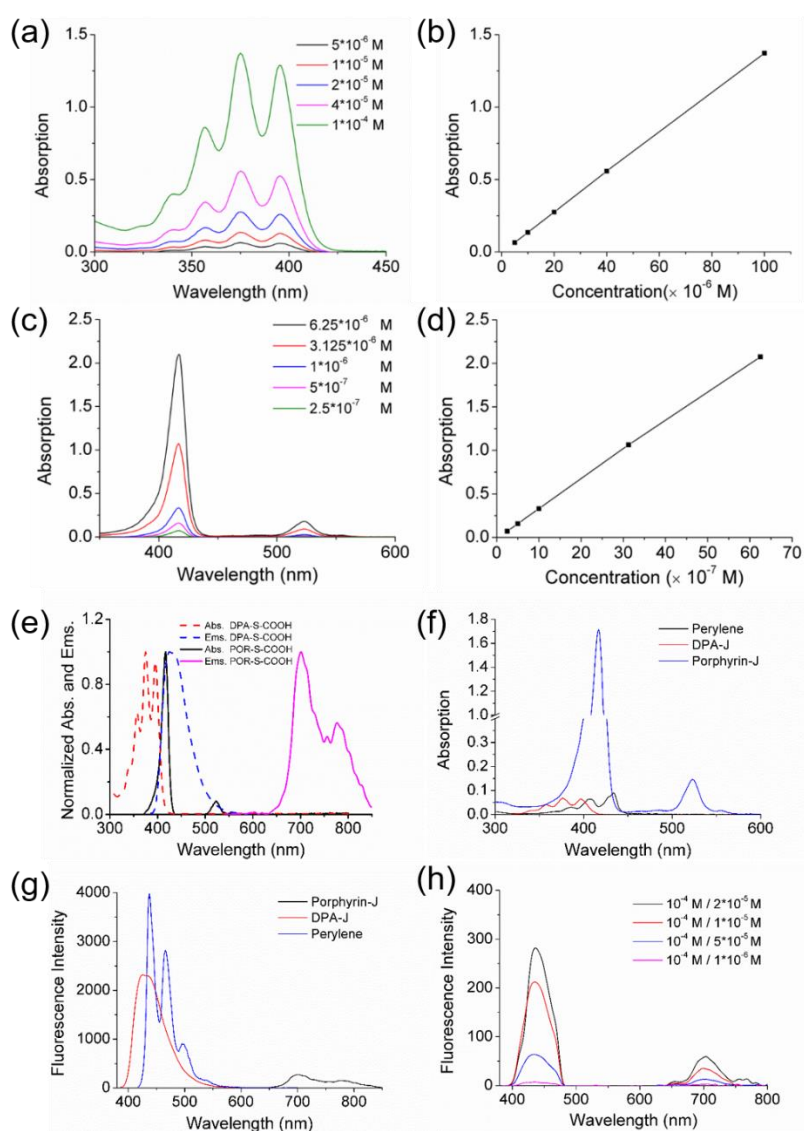


Figure 4.23: (a,c) UV-Vis spectra of **DPA-S-COOH** and **Pd-S-COOH** at various concentrations in DMF and (b,d) linear fitting of the absorbance at 375 nm and 416 nm. (e) Absorption and emission of two dyes. (f,g) Perylene in EtOH was used as a standard reference (absolute quantum efficiency $\Phi_{ref} = 0.92$ in aerated EtOH). The QY of two dyes was calculated with the

equation below. $\Phi = \Phi_{\text{ref}}(I/I_{\text{ref}}) (A_{\text{ref}}/A) (n^2/n_{\text{ref}}^2)$, where Φ is the QY, I is the integrated emission intensity, A is the absorbance at the excitation wavelength, and n is the refractive index of the solvent. The subscript ref refers to the reference fluorophore of known QY. (h) UCL spectra of **DPA-S-COOH** and **Pd-S-COOH** in different concentration ratio in DMSO under N_2 protection ($\lambda_{\text{exc}} = 532 \text{ nm}$, 18 mW)

4.3.3 synthesis of VVUC-CPNs using $Zn(OAc)_2$

$Zn(OAc)_2$ was used first to manufacture the particles due to the high coordination ability of carboxylic acid groups towards metallic ions. To begin, **DPA-S-COOH** and **Pd-S-COOH** were dissolved in DMF. When $Zn(OAc)_2$ was added, precipitates formed almost immediately. The particles were obtained as a white solid after removing excess $Zn(OAc)_2$ and unreacted compounds with several times DMF and water washing upon centrifugation. SEM images of the nanoparticles revealed that shape and size were not uniform showing an average size of $127 \pm 37 \text{ nm}$ (Figure 4.24a). Due to the ununiform morphology of particles, size distribution and stability of particles can be done only after using $0.2\mu\text{m}$ filter to remove aggregates. Figure 4.24b,c are showing good stability in 29h with an average size of $98 \pm 29 \text{ nm}$. FTIR of particles and different components indicated the successful synthesis of particles (Figure 4.24d).

With the observation of the UC luminescence of nanoparticles suspension showing an emission at 450 nm under N_2 atmosphere ($\lambda_{\text{exc}} = 532 \text{ nm}$), and a picture of cuvette showing a blue colour beam with a filter (Figure 4.24e,f), it can be concluded as an achievement of UC emission confirming that the proximity of the dyes permits the TTA-UC process and a success of coordination synthesis strategy.

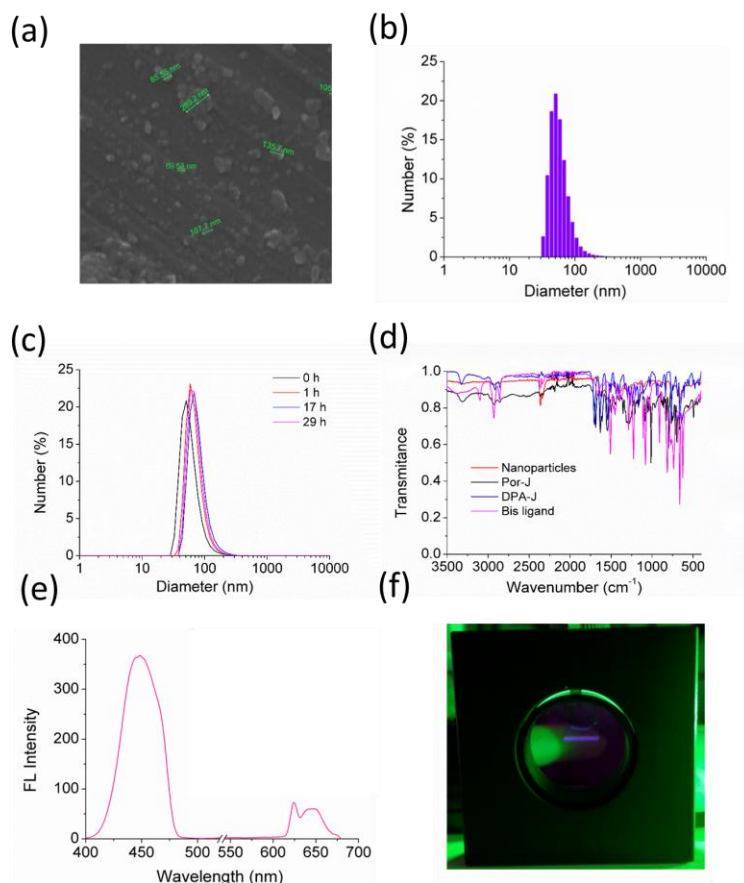


Figure 4.24: (a) Representative SEM image of Zn-based VVUC-CPNs. (b) DLS of upconversion nanoparticles Milli-Q® water suspension. (c) Stability of upconversion nanoparticles in Milli-Q® water. (d) FTIR of nanoparticles, DPA-S-COOH, Pd-S-COOH, and Bis ligand. (e) UC luminescence of Zn-based VVUC-CPNs Milli-Q® water suspension ($\lambda_{exc} = 532$ nm). (f) A picture of cuvette showing a blue colour beam with a filter ($\lambda_{exc} = 532$ nm).

4.3.4 VVUC-CPNs synthesis using $ZrOCl_2$

Once proved this strategy permitted obtaining nanoparticles with UC properties it was decided to improve their size and shape uniformity. For this, the synthesis was further optimized. $Zn(OAc)_2$ was used again with four different types of surfactants (Cetrimonium bromide (CTAB), sodium dodecyl sulfate (SDS), polyvinylpyrrolidone (PVP) and polyethylene glycols 2000 (PEG)). Additionally, due to inertness of metal oxides, $ZrOCl_2$ was chosen as crosslinking metal ion for substitution, with and without four different types of surfactants. The SEM images turned out that the assistance of surfactants did not improve the morphology when $Zn(OAc)_2$ was used (Figure 4.25a-d). With the addition of SDS (Figure 4.25g), the morphology of particles is flakes with size over 200 nm. The cases with and without surfactants all showed sphere morphology (Figure 4.25e,f,h,i). Finally, the synthesis with $ZrOCl_2$ and without adding surfactant was chosen for the future work.

	CTAB	PVP	SDS	PEG	control
Zn(OAc) ₂	(a)	(b)	(c)	(d)	
ZrOCl ₂	(e)	(f)	(g)	(h)	(i)

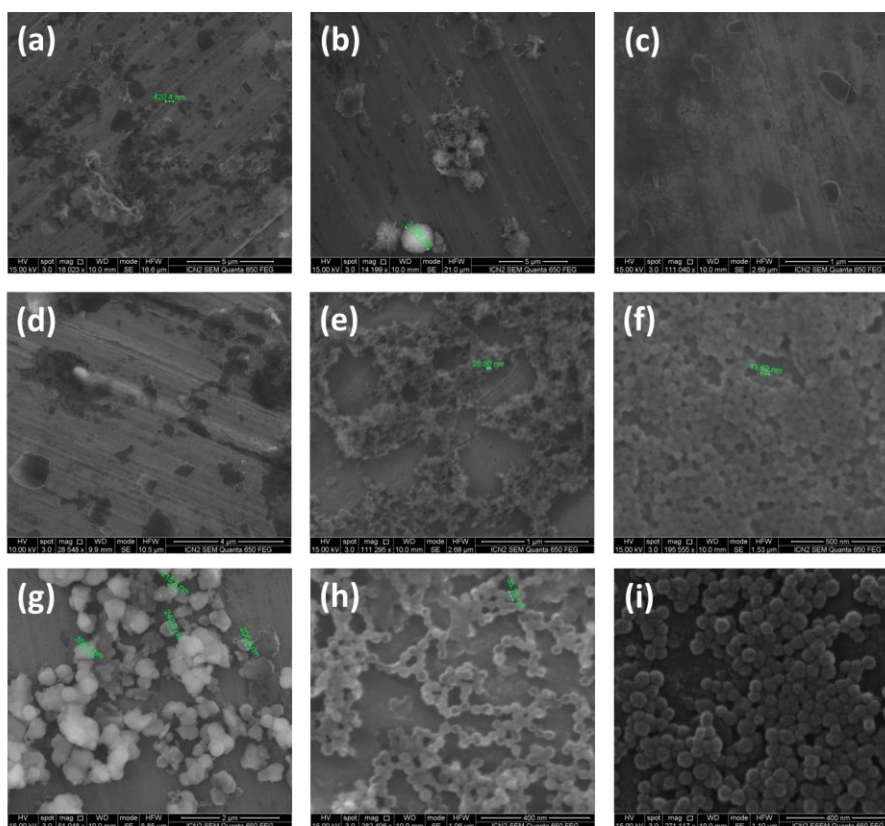


Figure 4.25: Representative SEM images of nanoparticles with addition of (a) CTAB, (b) PVP, (c) SDS, (d) PEG.

4.3.5 Optimization of the UC emission/phosphorescence ratio in the UC-CPNs

Once optimized the synthesis of the CPNs to have good size distribution, it was decided to improve the purity of the UC emission by increasing its intensity towards the competing phosphorescence emission. To do this, the efficiency of the TTET had to improved. To favour this, the distance between the donor and acceptor has to be minimized (less than 1 nm) for the effective overlap of wavefunctions for an electron exchange. Also, to assure the sensitizer triplet states energy is efficiently transferred to the emitter, the latter has to be present in large excess. Thus, new syntheses of the CPNs were carried out tuning the initial ratio of the sensitizer and emitter to study the effect on the UC/phosphorescence emission ratio.

The concentration of **DPA-S-COOH** was initially fixed to 1 mg/mL and the amount of **Pd-S-COOH** was set to a range between 0.3 and 5 μ g/mL having 5 different concentration (1:

1mg/mL & 0.3125 μ g/mL, **2**: 1mg/mL & 0.625 μ g/mL, **3**: 1mg/mL & 1.25 μ g/mL, **4**: 1mg/mL & 2.5 μ g/mL, **5**: 1mg/mL & 5 μ g /mL). All synthesis yielded the desired **CPNs** of size around 60.0 nm, as shown by SEM images. (Figure 4.26).

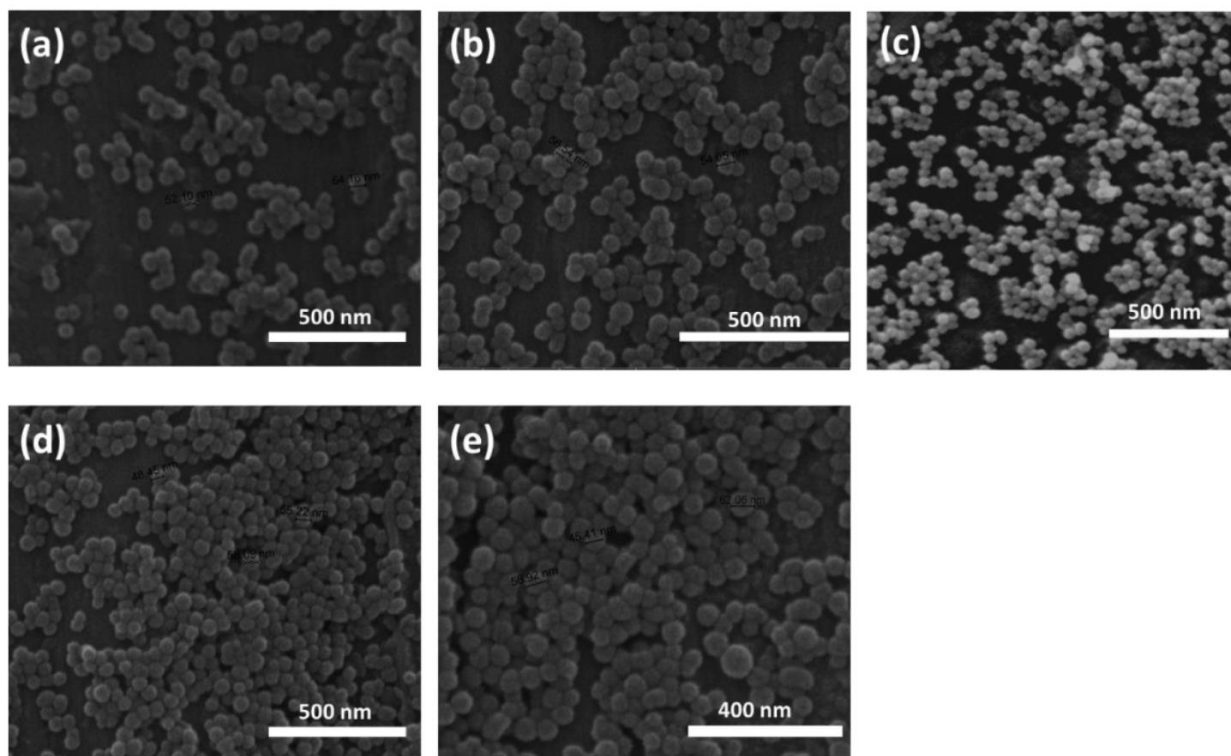


Figure 4.26: SEM images of (a)1, (b)2, (c)3, (d)4, (e)5

All obtained **CPNs** showed UC at $\lambda = 445$ nm upon green light irradiation ($\lambda_{exc} = 532$ nm), with residual phosphorescence luminescence (PL) at $\lambda = 653$ nm, indicating different efficiencies of triplet energy transfer and demonstrating the importance provided by the possibility of tuning the dyes ratio within a solid system (Figure 4.27a).

Among them, the batch **3** (made by using 1 mg/mL of DPA-S-COOH and 1.25 μ g /mL of **Pd-S-COOH**) showed an intensive upconversion emission with a highest integral ratio of UCL/PL = 6.54 (Figure 4.27b). The VVUC-**CPNs** suspension irradiated with 532 nm laser (100 mW/cm²), manifested blue light emission, visually confirming the upconversion (short-pass filter was used to remove excitation light and residual phosphorescence Figure 4.27c). Finally, high performance liquid chromatography (HPLC) was used to determine the concentration of the emitter molecules in the **CPNs**, while the inductively coupled plasma-mass spectrometry (ICP-MS) technique was used to quantify the concentration of sensitizers (through the Pd center) and Zr²⁺ ion. The ratio (*w*t%) of the dyes in the particles was **Pd-S-**

COOH/DPA-S-COOH = 0.06% (molar ratio is 1/2900) with polymer formula **DPA-S-COOH₂₉₀₀Pd-S-COOH₁Zr₅₆₉₀** (Figure 4.27d). This ratio was used for the rest of work.

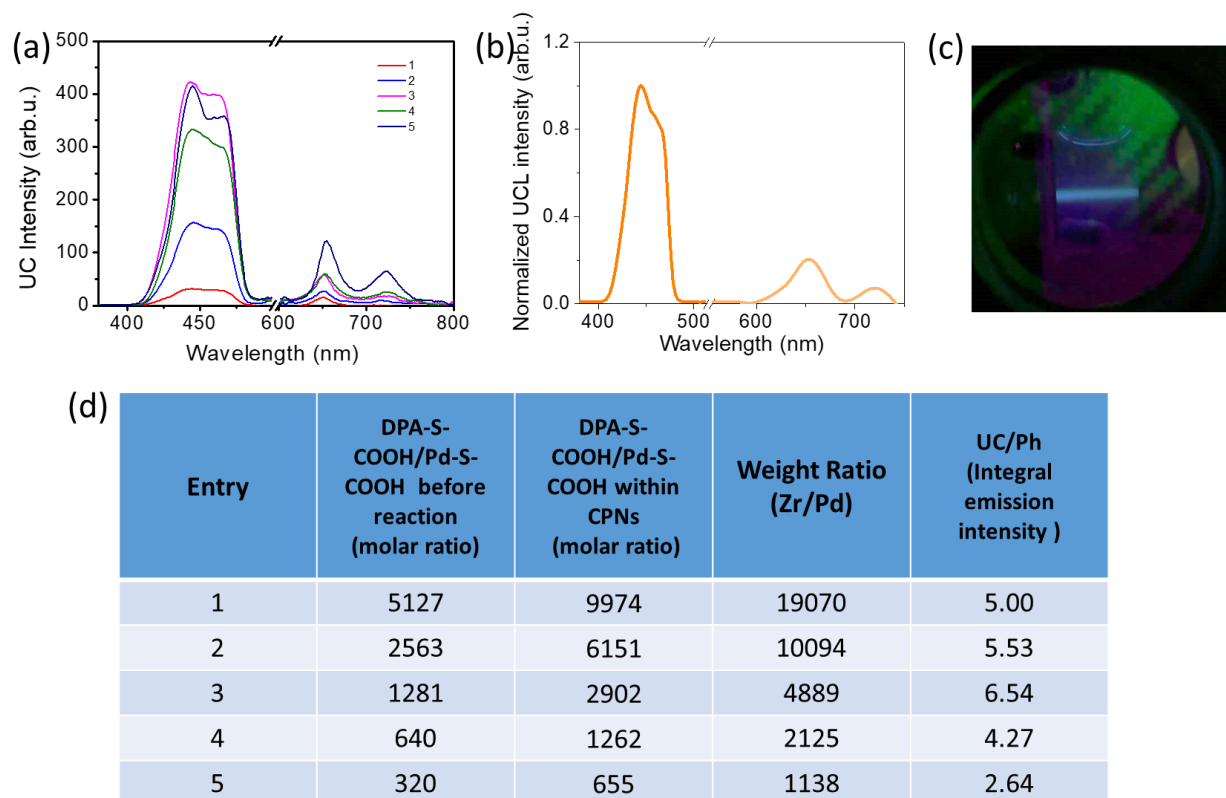


Figure 4.27: (a) Upconversion emission of five different VVUC-CPNs water suspensions ($\lambda_{exc} = 532$ nm) obtained by using different **DPA-S-COOH/Pd-S-COOH** ratio (1: 1mg/mL & 0.3125 μ g/mL, 2: 1mg/mL & 0.625 μ g/mL, 3: 1mg/mL & 1.25 μ g/mL, 4: 1mg/mL & 2.5 μ g/mL, 5: 1mg/mL & 5 μ g/mL). Magenta subtractive dichroic color filter, filter was used to cut the 532 nm excitation beam. (b) Emission spectrum and (c) Photograph of the emission of the aqueous suspension of VVUC-CPNs obtained from **DPA-S-COOH/Pd-S-COOH** = 1281 (entry 3) ($\lambda_{exc} = 532$ nm, N₂ atmosphere). Magenta subtractive dichroic color filter was used to cut the 532 nm excitation beam. (d) Quantification of 5 batch (1-5)

The CPNs with highest UC/phosphorescence ratio were further characterized. The shape of amorphous upconverting nanoparticles with an average size of 47.0 ± 8.0 was revealed by SEM images of VVUC-CPNs, Figure 4.28a). The size distribution of the resuspended UCCPNs in Milli-Q[®] water was estimated to be roughly 70 nm using dynamic light scattering (DLS, Figure 4.28b). X-ray powder diffraction (XRD) showed the absence of diffraction peaks which confirms the amorphous nature of the solid nanoparticles. This corroborates the 5-carbon alkyl chain was a sufficient length to break the crystalline order (Figure 4.28c). Fourier-transform infrared spectroscopy (FT-IR) showed a band at 1650 cm^{-1} and another medium intensity band at 1371 cm^{-1} ; the intensity and frequency of the bands indicate that they correspond to νCO_{asym} and νCO_{sym} vibrations, respectively. The former is shifted from 1705 cm^{-1} and the latter from 1440 cm^{-1} , observed in **DPA-S-COOH**, or from

1688 cm^{-1} and 1441 cm^{-1} of the **Pd-S-COOH** free ligands, indicating the coordination of the carboxyl groups of the ligands to the metal center (Figure 4.28d).⁹²⁻⁹⁴

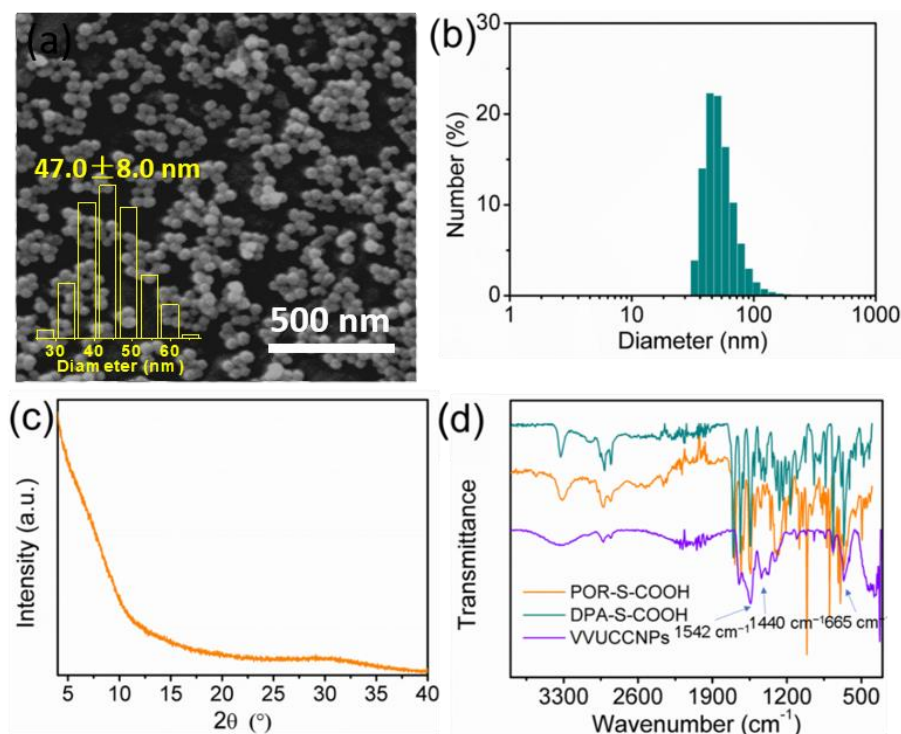


Figure 4.28: **Characterization of VVUCCPNs: (a) Representative SEM image, scale bar = 500 nm. (b) Size distribution of VVUCCPNs in MiliQ®. (c) X-ray powder diffraction (XRD) spectrum. (d) FTIR of two dyes and VVUCCPNs.**

To quantify the efficiency of the UC. For this, the excitation intensity threshold (I_{th}) and the QY (Φ_{UC}) were determined. The I_{th} is the incident light power density value above which the formed triplets of the emitter mainly undergo TTA as enough triplet states have been formed. In this regime the UC intensity increase passes to be quadratic to linear with respect to the incident light intensity. In the logarithm plot of the integrated UC intensity against the incident light power density, the I_{th} is determined as the intersection point between the fitting lines of the quadratic (at low intensities) and linear (at higher intensity) trends (Figure 4.29a). For our VVUC-CPNs the I_{th} was 90 mW/cm^2 , at which it was measured a relative $\Phi_{\text{UC}} = 0.65\%$.⁷⁵ This value has to be considered respect to a maximum value of $\Phi_{\text{UC}} = 50\%$, due to the bimolecular character of the UC process.⁹⁵⁻⁹⁶

To bring more light to this fact further spectroscopic data were obtained for these CPNs. The absorption spectrum of a VVUC-CPNs water suspension showed the characteristic **DPA-S-COOH** bands, but broadened and red-shifted, in addition to some light scattering (Figure 4.29b). Pd-S-COOH could not be detected due to its low contribution to the final

polymer molecular formula **DPA-S-COOH**₂₉₀₀**Pd-S-COOH**₁Zr₅₆₉₀. Moreover, the **DPA-S-COOH** emission ($\lambda_{\text{Exc}} = 375 \text{ nm}$) within the nanoparticles was slightly broader and red-shifted compared to that of a bulk DMF solution, suggesting some degree of aggregation of the dye in the nanoparticles (Figure 4.29c).

In the future, these values can be further improved, by slightly modifying the design of the monomeric molecules. Indeed, **CPNs** obtained from only **DPA-S-COOH** (**DPA-S-CPNs**) showed a fluorescence QY of 18.5% (Figure 4.29d) and the absolute fluorescence quantum yield of **DPA-S-COOH** ($\lambda_{\text{Exc}} = 375 \text{ nm}$) in **VVUC-CPNs** is 34.2% (Figure 4.29e), which is quite lower respect to the initial monomer, suggesting DPA aggregation in the particles. This means that TTA efficiency is reduced, lowering the overall value of the UC. The presence of bulky group in the structure of the DPA molecules is expected to prevent aggregation, while keeping high dye density.

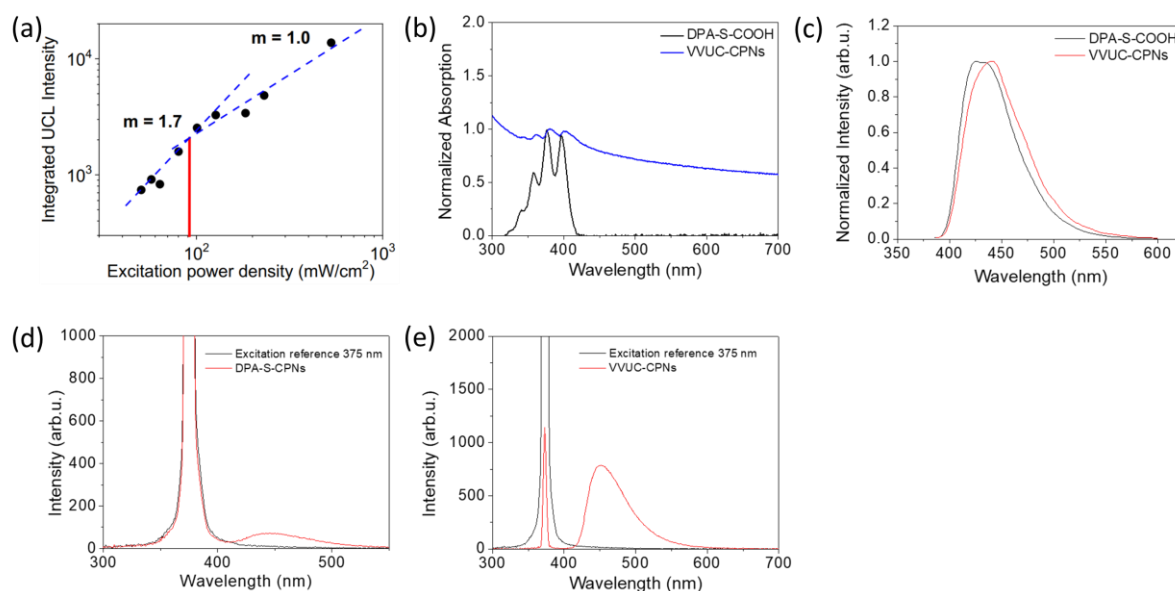


Figure 4.29: (a) logarithm plot of integrated UCL intensity against excitation power density. Excitation intensity threshold (I_{th}) was determined from the interception of the two fitting lines in the quadratic and linear regimes. (b) Absorption and (c) emission spectra of a DMF solution of **DPA-S-COOH** and **VVUC-CPNs** aqueous suspension ($\lambda_{\text{exc}} = 375 \text{ nm}$). Absolute fluorescence quantum yield of **DPA-S-COOH** in (d) **DPA-S-CPNs** (18.5%) and (e) **VVUC-CPNs** (34.2%), exciting at $\lambda_{\text{exc}} = 375 \text{ nm}$.

4.3.6 Optical characterization of **Os-S-COOH** and **CAEBD-S-COOH**

To demonstrate the universality of the approach, **UC-CPNs** were also designed to upconvert NIR radiation into visible light (**NVUC-CPNs**). For this we also investigated the use of sensitizers forming their triplets upon direct singlet-to-triplet absorption, without passing through the ISC, which competes unfavorably with vibrational relaxation when the singlet

excited state (S_1) is of lower energies. The monomers of choice was an Os complex (**Os-S-COOH**) as sensitizer, functionalized with succinic acid attached to the aromatic moiety through an ester bond, and the [4-((10-(4-carboxyphenyl)-anthracene-9-yl)-ethynyl)-benzoic acid derivative (**CAEBD-S-COOH**, emitter) chemically modified with a carboxylic acid-terminated alkyl chain, attached to the aromatic moiety through amide bond (Figure 1c). The optical properties of the dyes in DMF solutions matched with reported data of the respect parent molecules. **Os-S-COOH** (extinction coefficient = $2.12 \times 10^4 \text{ M}^{-1} \text{ cm}^{-1}$) has absorption and phosphorescent bands at $\lambda_{\text{Max}} = 680 \text{ nm}$ and $\lambda_{\text{Ems}} = 773 \text{ nm}$ ($\lambda_{\text{Exc}} = 650 \text{ nm}$), respectively. The absorption and fluorescence bands of **CAEBD-S-COOH** (extinction coefficient = $2.4 \times 10^4 \text{ M}^{-1} \text{ cm}^{-1}$) were at $\lambda_{\text{Max}} = 410 \text{ nm}$ and $\lambda_{\text{Ems}} = 455 \text{ nm}$ ($\lambda_{\text{Exc}} = 410 \text{ nm}$), respectively (Figure 4.3a-e). Irradiation with 650 nm laser of a degassed DMF solution of the sensitizer ($5 \times 10^{-4} \text{ M}$) and emitter (10^{-3} M) confirmed the upconverted emission (Figure 4.3f).

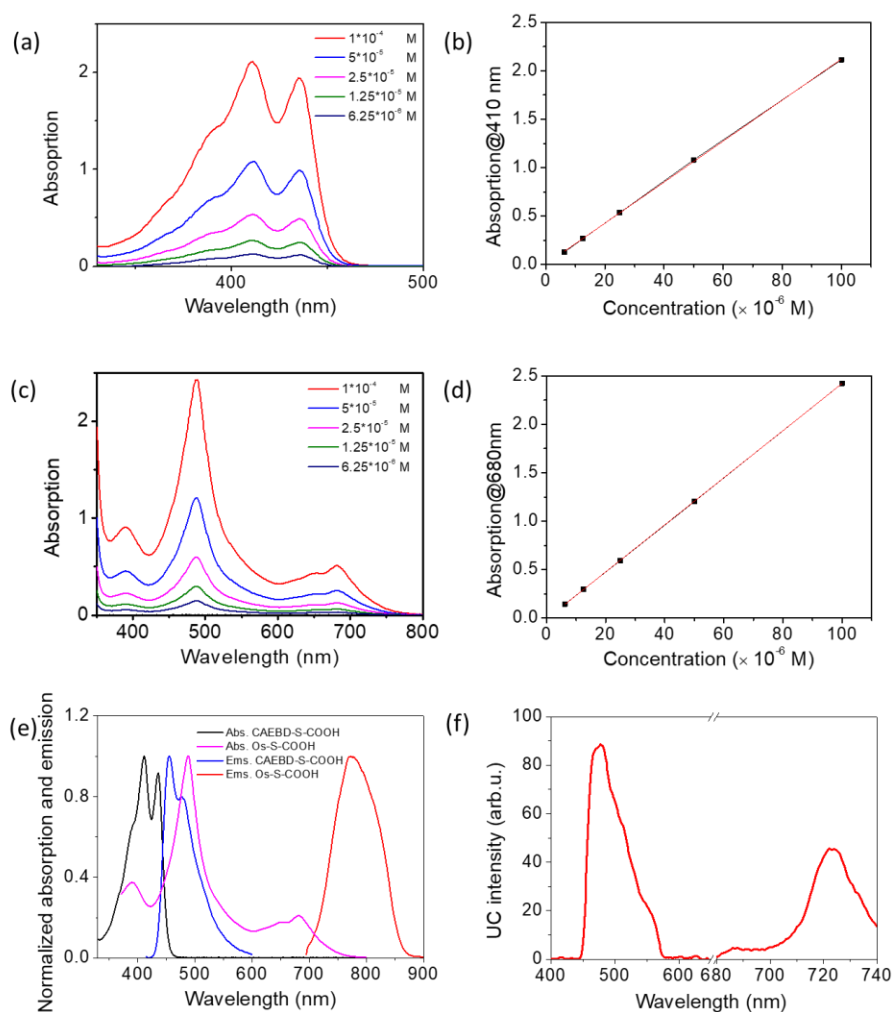


Figure 4.30: (a,c) UV-Vis absorption spectra of **CAEBD-S-COOH** and **Os-S-COOH** at various concentrations in DMF and (b,d) linear fitting of the absorbance at 410 nm and 680 nm, respectively. (e) Absorption and emission ($\lambda_{\text{Exc}} = 410 \text{ nm}$, $\lambda_{\text{Exc}} = 680 \text{ nm}$, respectively) spectra of **CAEBD-S-COOH** and **Os-S-COOH** in DMF. (f) UC emission of a degassed DMF solution

of the **Os-S-COOH** (5×10^{-4} M) and **CAEBD-S-COOH** (10^{-3} M), irradiated with 650 nm CW laser. Subtractive cyan dichroic filter was used.

4.3.7 Synthesis of the NVUC-CPNs

NVUC-CPNs have been synthesized using the same strategy. For characterisation, the solid was centrifuged, isolated, and freeze-dried. The shape of amorphous upconverting nanoparticles with an average size of 89.2 ± 12.8 nm was revealed by SEM images of VVUC-CPNs (Figure 4.31a). The size distribution of the resuspended UCCPNs in MiliQ® water was estimated to be roughly 120 nm using dynamic light scattering (DLS, Figure 4.31b). X-ray powder diffraction (XRD) showed the presence of an amorphous structure of the solid particles and the absence of any crystalline moiety (as it happens instead in MOF-based coordination polymers), which confirmed the 5-carbon alkyl chain was sufficient to break the crystalline order (Figure 4.31c). Fourier-transform infrared spectroscopy (FTIR) of VVUC-CPNs confirmed the coordination bonds between $-\text{COO}^-$ groups and the metal centers through the absorption bands at $\nu = 1540, 632 \text{ cm}^{-1}$,⁹²⁻⁹⁴ indicating the dyes coordination to the Zr in the CPNs (Figure 4.31d).⁹²⁻⁹⁴

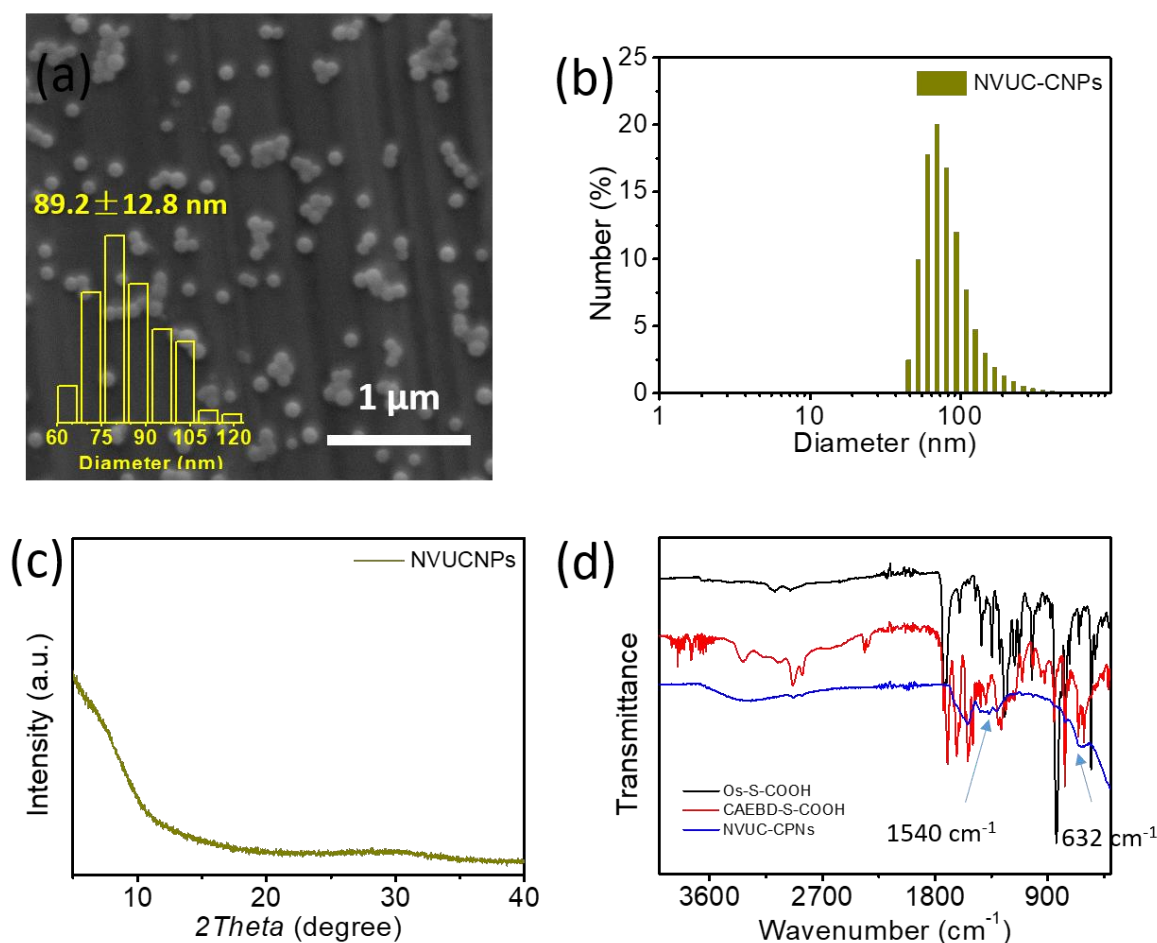


Figure 4.31: Characterization of NVUC-CPNs: (a) Representative SEM image, scale bar = 1 μm . (b) Size distribution of NVUC-CPNs in MilliQ[®]. (c) X-ray powder diffraction (XRD) spectrum. (d) FTIR of two dyes and NVUC-CPNs.

4.3.8 Optimization of the UC emission/phosphorescence ratio in the UC-CPNs

The concentration of CAEBD-S-COOH was initially fixed to 1.5 mg/mL and the amount of Os-S-COOH was set to a range (12.5 - 50 $\mu\text{g/mL}$). After obtaining the materials, optical properties of three batches were investigated in nitrogen environment (Figure 4.32a).

All batches have shown upconversion upon green light irradiation ($\lambda_{\text{exc}} = 650 \text{ nm}$) with different intensity of upconversion luminescence (UCL) at $\lambda = 511 \text{ nm}$ and residual phosphorescence luminescence (PL) at $\lambda = 773 \text{ nm}$ indicating different efficiency of triplet energy transfer and demonstrating the importance provided by the possibility of tuning the dyes ratio within a solid system.

Among them, the batch **2** (CAEBD-S-COOH 1.5 mg/mL & Os-S-COOH 25 $\mu\text{g/mL}$) showed an intensive upconversion emission with a highest integral ratio of UCL/PL = 7.31 (Figure 4.32b). The photo of the cuvette containing NVUC-CPNs suspension was taken upon irradiation with short-pass filter showing blue light emission, which is the proof of upconversion (Figure 4.32c). Finally, high performance liquid chromatography (HPLC) was used to determine the concentration of the emitter molecules in the CPNs, while the inductively coupled plasma-mass spectrometry (ICP-MS) technique was used to quantify the concentration of sensitizers (through the Os center) and finally afford polymer formula as **CAEBD-S-COOH₈₉Os-S-COOH₁Zr₂₃₆** (Figure 4.32d). This ratio was used for the rest of work.

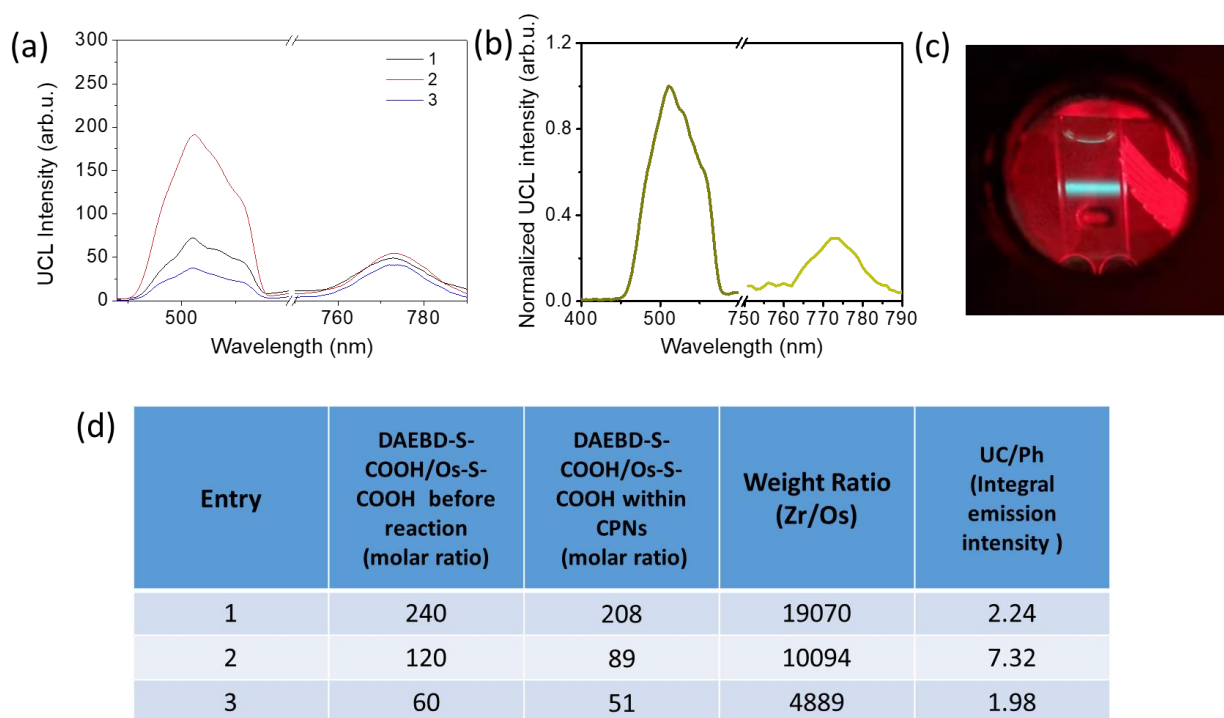


Figure 4.32: (a) Upconversion luminescence of 3 batches with different ratio between emitter and sensitizer (**1-3**, 1.5 mg/mL & 12.5 $\mu\text{g/mL}$, 1.5 mg/mL & 25 $\mu\text{g/mL}$, 1.5 mg/mL & 50 $\mu\text{g/mL}$). (b) Upconversion luminescence of batch **2** with the highest ratio between UCL/PL. (c) Photo of the cuvette with NVUC-CPNs upon 680 nm irradiation (Subtractive cyan dichroic filter was used). (d) Amount of **Os-S-COOH**, **CAEBD-S-COOH** and Zr^{2+} for the reactions and quantification of exact amount of each component within the particles in **1-3** batches, using HPLC for **CAEBD-S-COOH** and ICP-MS for **Os-S-COOH** and Zr^{2+} . Subtractive cyan dichroic filter was used.

4.3.9 Upconversion application exploration

Once demonstrated the viability of the **UC-CPNs** for different spectral ranges and good colloidal stability in MilliQ[®] water (Figure 4.19), we aimed to investigate the applicability of the **UC-CPNs** obtained. For this, it was decided to use the UC emission of the **CPNs** to:

- Induce reversible (photochromism) and irreversible (photopolymerization) photochemical processes,
- Fabricate nanomaterials with air-stable UC emission.

4.3.9.1 Upconversion-induced photochromic change

“Photochromism” is simply defined as a light-induced reversible change of color, which involves a reversible transformation of a chemical species between two forms by the absorption of electromagnetic radiation (photoisomerization).⁹⁷ To be specific, the stable initial form of photochrome is transformed by irradiation into an active form of photochromes, where the two

forms have different absorption spectra (Figure 4.33). The back reaction can occur thermally (Photochromism of type T) or photochemically (Photochromism of type P).

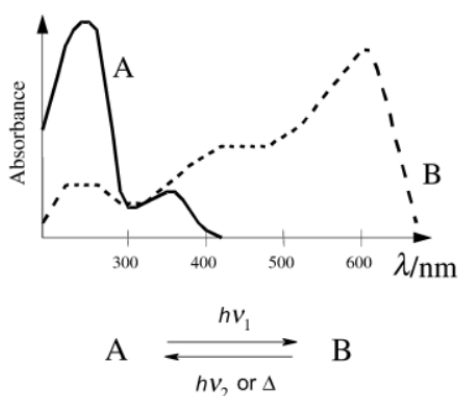


Figure 4.33: (a) Schematic of photochromism.

Due to the fast development of photochromism, both in the industrial and the academic fields, a growing interest has been found in fabricating functional photochromism (T-Type) material in the area of ophthalmic lenses and smart windows.⁹⁸ However, most of the T-Type photochromes absorb selectively in the UV and synthesizing molecules that absorb in the visible or NIR is not cost-friendly and straightforward. Therefore, UC would be a good solution for the photochromism, which extends the activation to visible and NIR of solar light as it is allowed a larger number of photons to be used.

Due to the upconversion emission of VVUC-CPNs is 410-480 nm ($\lambda_{\text{Max}} = 450$ nm), a variety of photochromic dyes have been evaluated upon 450 nm laser to see the colour change and recovery time. Finally, the graphite (GR) was chosen as the candidate for the experiment with an observation of colour change. However, colour changes haven't been observed even with a high concentration of VVUC-CPNs, the possible explanation will be the low intensity of upconverted emission that can't trigger the photochromism. In addition, we have found that high intensity of green light (532 nm) accelerates the colour recovery that hinders the photochromism.

4.3.9.2 Upconversion-induced photopolymerization

The application of photochemistry to polymer and material science has led to the development of complex yet efficient systems for polymerization, polymer postfunctionalization, and advanced materials production. Using light to activate chemical

reaction pathways in these systems not only leads to exquisite control over reaction dynamics, but also allows complex synthetic protocols to be easily achieved.⁹⁹⁻¹⁰² UC that converts long wavelength light to shorter emission has more advantages, such as deep penetrating depth to activate photopolymerization and more access to the LED or light sources. Thus, it would be interesting to use upconversion luminescence to trigger the photoinitiator generating reactive intermediate.

Herein, polymerization of 2-Hydroxyethyl methacrylate (HEMA) was attempted in the presence of VVUC-CPNs ($\lambda_{uc} = 450$ nm) and photoinitiators (Riboflavin, $\lambda_{Max} = 444$ nm).¹⁰³⁻¹⁰⁴ To be specific, different ratios between HEMA and solvent have been used (HEMA/solvent ratio 1.21 : 10, 5 : 1 and 1 : 0) to explore that how does different amount of HEMA affect the speed of polymerization. Additionally, 0.01M triethanolamine (TEOHA) was used as a coinitiator in aqueous solvents. The whole experiments were carried out under an N₂ protection conditions at 25 ° C, in the presence of 2-4mg/mL VVUC-CPNs and Riboflavin. Unfortunately, gellization has not been observed neither blue upconverting emission (The condition was set base on the reference and an observation of gellization under sunlight). The possible reason is that the upconverted emission from VVUC-CPNs is not enough to initiate the polymerization.

4.3.9.3 Air-stable upconverting transparent films

The first material consisted of a transparent polymeric film, of interest for OLEDs, solar cell and solar concentrator. The low size (< 100 nm) and narrow size distribution of CPNs prevent the light scattering and should allow the fabrication of highly transparent polymeric films embedding the nanoparticles (Figure 4.34), as the group Nanosfun demonstrated with low-size oil photochromic nanodroplets¹⁰⁵ and fluorescent solid lipid nanoparticles.¹⁰⁶ On the other hand, the aqueous medium in which they are dispersed offers the possibility to use the water-soluble film-forming polyvinyl alcohol (PVA) matrix, where UC organic dyes are normally not soluble, but which is also one of the most efficient oxygen barrier polymer and useful for UC.¹⁰⁷⁻¹⁰⁸

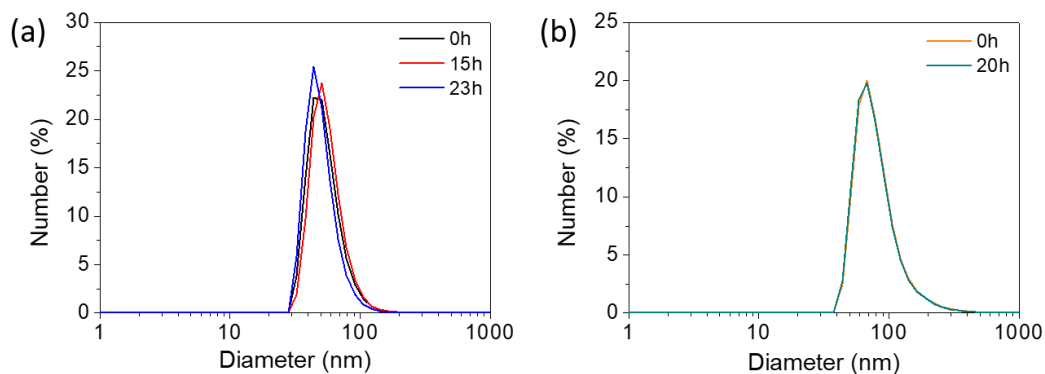


Figure 4.34: Colloidal stability of UC-CPNs in MilliQ® water (a) VVUC-CPNs, (b) NVUC-CPNs

PVA films were easily prepared by drop-casting a VVUC-CPNs and NVUC-CPNs suspensions in the presence of PVA and letting the water evaporate at room temperature (Figure 4.35a). Flexible, free-standing and highly transparent films could be peeled out from the container (Figure 4.35b). Thanks to, not only their small dimensions, but also their homogeneous distribution within the polymer, the resulting films showed high transparency ($\%T_{555\text{nm}} = 84$ and 75% T against air, respectively, Figure 4.35c). Most importantly, the films showed blue and greenish emissions, respectively, upon irradiation with 532 and 650 nm lasers under air atmosphere, confirming the generation of air-stable UC photons (Figure 4.35d,e). From here two facts deserve to be emphasized. First, the UC/phosphorescence ratio of VVUC-CPNs was even higher than the corresponding colloidal suspensions (Figure 4.35f), possibly due to a better protection from oxygen quenching by the PVA, which prevents the need of additional protective coatings, e.g. nanocellulose, or antioxidants, normally used to inhibit oxygen diffusion and/or quenching of the triplet states.¹³ And second, UC was observable using a relatively low amount of CPNs (0.67 wt.% respect to PVA), without needing rubber-type polymers or high dyes concentration (as normally happens in UC polymeric matrices)..³⁰⁻

31, 109-110

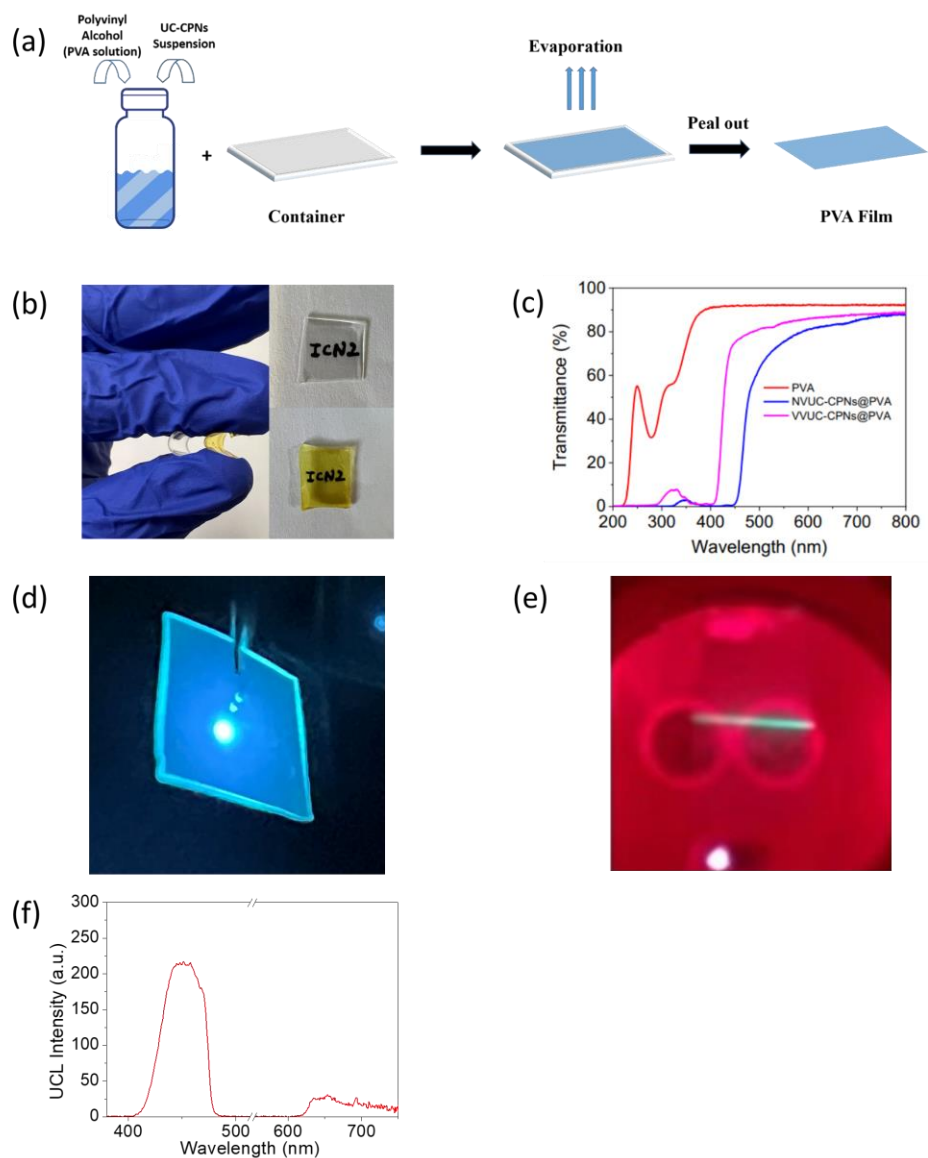


Figure 4.35: (a) Schematic of PVA film preparation. (b) VVUC-CPNs@PVA and NVUC-CPNs@PVA films bended with fingers, to show flexibility. (c) Transmittance of plain PVA, NVUC-CPNs@PVA and VVUC-CPNs@PVA films. Photographs of transparent (d) VVUC-CPNs@PVA and (e) NVUC-CPNs@PVA films showing UC emission under 532 nm and 650 nm CW laser irradiation, respectively. (f) UC emission of VVUC-CPNs@PVA film ($\lambda_{exc} = 532$ nm). Magenta subtractive dichroic color filter, filter was used to cut the 532 nm excitation beam.

Even more, localized irradiation with 532 nm CW laser at the center of the VVUC-CPNs@PVA film, yielded intense UC emission at the edges of the film (Figure 4.35d and Figure 4.36). This result demonstrated that the CPNs are small enough to minimize the scattering of light, which concentrates at the edges through total internal reflectance. These transparent films based on UC-CPNs are thus promising materials to obtain luminescent solar concentrators based on UC emission, desirable to avoid the typical dyes reabsorption of re-emitted light during its traveling to the edges.

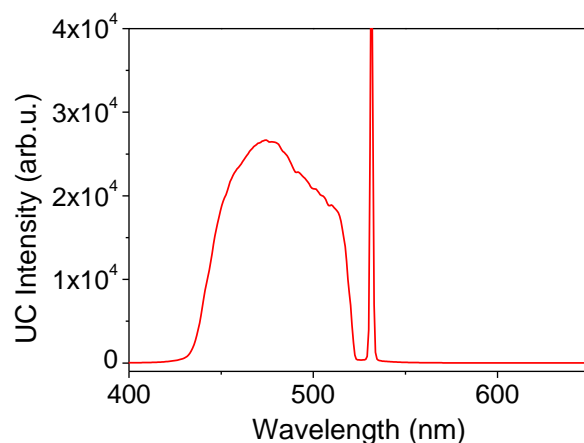


Figure 4.36: UC emission of VVUC-CPNs@PVA film ($\lambda_{Exc} = 532$ nm). Magenta subtractive dichroic color filter, filter was used to cut the 532 nm excitation beam.

4.3.9.4 Air-stable upconverting printed patterns for security inks

The good colloidal dispersion of our nanoparticles in aqueous suspensions was also successfully used to prepare water-based security inks. Both VVUC-CPNs and NVUC-CPNs could be easily patterned, in the presence of PVA binder, onto glass substrate through spray-coating and using a pre-patterned mask (with “UC” shape, Figure a), preserving their fluorescent properties under UV irradiation ($\lambda_{Exc} = 365$ nm, Figure b) and UC emissions under 532 and 650 nm light (Figure c).

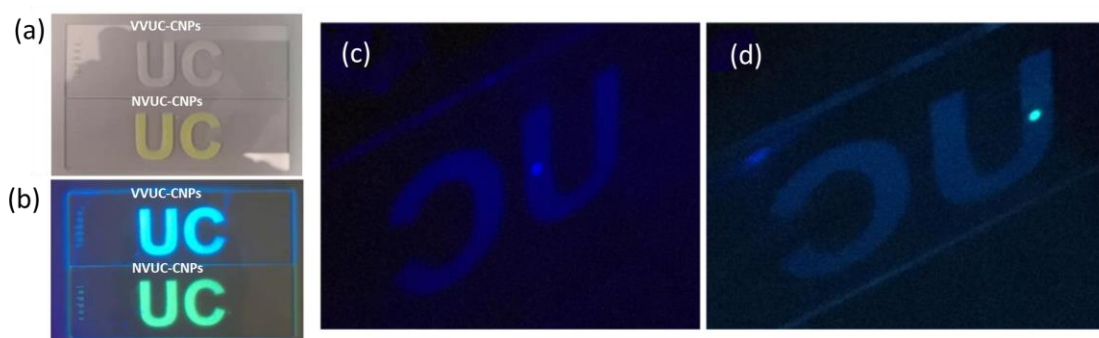


Figure 4.20: (a) Photograph of VVUC-CPNs and NVUC-CPNs spray-coated patterns under (a) ambient light and (b) UV irradiation ($\lambda_{exc} = 365$ nm). Photo of the UC emission of VVUC-CPNs- and NVUC-CPNs-based “UC” patterns, irradiated with (a) 532 nm and (b) 650 nm CW laser, respectively.

To prepare an encrypted label, a glass substrate was first spray-coated all over the surface with a suspension made of DPA-S-CPNs or CAEBD-S-CPNs (containing only DPA-S-COOH or CAEBD-S-COOH) and PVA, obtaining a uniform printed UV active substrate (background) with rough surfaces due to the PVA microcapsules formed upon spraying (Figure d). On top of this, the PVA/VVUC-CPNs or PVA/NVUC-CPNs aqueous suspensions were spray-coated on the respective prepared substrate, interposing the pre-patterned “UC” mask between the nozzle and the substrate (Figure a). When the scanning of the substrate surface with 532 and

650 nm CW lasers and pulsed 532 nm beam. UC emission only appears when the beam scans over the “UC” pattern, decrypting the hidden message.

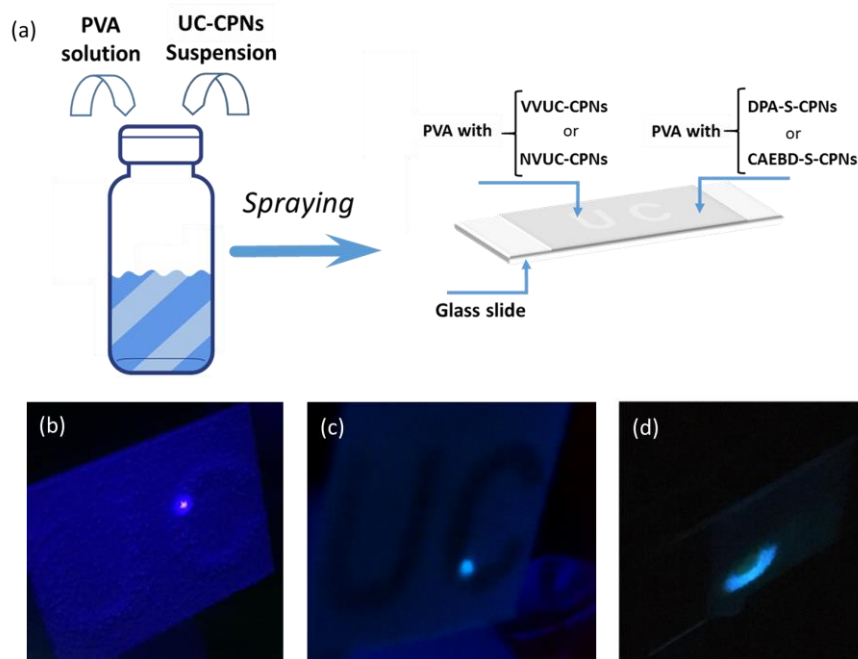


Figure 4.23: (a) Schematic of PVA film preparation. preparation of the material with UC-based encrypted message; photograph of spray-coated (b) **VVUC-CPNs** and (c) **NVUC-CPNs** patterns showing UC emission upon irradiation with 532 nm and 650 nm CW lasers, respectively, when the laser beam scans over the "UC" pattern. (d) **VVUC-CPNs** patterns scanning with 532 nm (pulsed Nd:YAG).

4.4 Conclusions

In conclusion, the introduction of alkyl chain within emitter and sensitizer ligands allowed us to synthesize UC amorphous nanoscale coordination polymers with high dye densities and easy dye-ratio tunability. This approach prevents dyes migration and phase segregation of the dyes in polymer material (matrix) and allows the optimization of the dye interactions and the consequent energy transfer processes involved in the TTA-UC. We proved the approach can be generalized to upconvert photons from/to different spectral regions and through distinct mechanisms (intersystem-crossing or direct singlet-to-triplet absorption). Moreover, given their chemical and colloidal stability in water, these CPNs could be considered the organic counterpart of the lanthanide-based inorganic UCNPs, but with lower excitation intensity thresholds. The system might be further improved through the addition of bulky group in the **DPA-S-COOH** structure to reduce aggregation, while preserving the high density in the CPNs to favor TTET and TTA. Finally, the combination with the water-soluble and oxygen-barrier PVA polymer, allowed us to obtain UC water-borne inks and transparent films where UC is preserved even at low CPNs concentration. The interest for these platforms was exemplified

by the development of anticounterfeiting patterns and luminescent solar concentrators, respectively.

4.5 Materials and methods

Reagents and Instrumentation

Solvents were purchased from Sigma–Aldrich and used as received and complex **1** was synthesized and characterized according to previously reported methodology [14]. Fourier transform infrared (FTIR) spectra were carried out with a Tensor 27/PMA50FTIR Spectrometer in a range of 4000–400 cm^{-1} . Dynamic light scattering (DLS) for the determination of the particle-size distributions and the zeta potential values were measured in a ZetaSizer nano ZS (ZEN3600, Malvern Instruments, Ltd., Malvern, UK). Scanning Electron Microscopy (SEM) images were obtained on a scanning electron microscope (FEI Quanta 650 FEG, The Netherlands). The samples were casted on aluminum holders following by evaporation and later a thin platinum layer was sprayed to increase the conductivity of samples.. Ultraviolet–visible spectroscopy (UV-vis) study was carried out in the Agilent Cary 60 spectrophotometer

HPLC methodology for UC-CPNs quantification

Chromatographic conditions: analyses were performed using a HPLC Waters 2695 separation module coupled to a Waters 2487 UV-Vis detector (suitable for dual detection 280 369nm). The column used was a Restek® C-18 (250 mm x 4.6 mm). Eluent A was a 0.1% (v/v) TFA aqueous solution and eluent B was acetonitrile absolute (HPLC grade). Before the analysis, the RP column was preequilibrated using the starting conditions of the method (99 % A (v/v)) for 10 min, followed by a gradual decrease of A from 100% to 0% (v/v) in first 15 min and lasting 4 min. Then, mobile phase was raised to 100 % A (v/v) in 3 min and lasting 3 min. Finally, mobile phase was reset to the initial conditions (A:B) 100:0 (v/v) and stayed for 10 min to equilibrate for the next injection. The flow rate was set at 1.0 mL/min and the column temperature was kept at 25 °C. The detection wavelengths were 280 and 369 nm. This method were for calibration curve of DPA-S-COOH and CAEBD-S-COOH and quantification of UC-CPNs.

ICP-AES analysis

UC-CPNs are determined by after dissolving the metals in aqua regia.

UC-CPNs synthesis

Dyes were dissolved in 2 ml anhydrous DMF with final addition of $ZrOCl_2$. The resulting mixture was stirred and heated at $90^\circ C$ for 15h. Precipitates were isolated by centrifugation with following 3 times DMF washing and 2 times water washing to remove unreacted compound.

Upconversion luminescence and phosphorescence measurement

1mg/mL UC-CPNs were dispersed in MiliQ® water in sealable quartz cuvette and the suspension was degassed by N_2 for 1.5h for upconversion measurement. Phosphorescence was measured using the same method after 1.5h degassing.

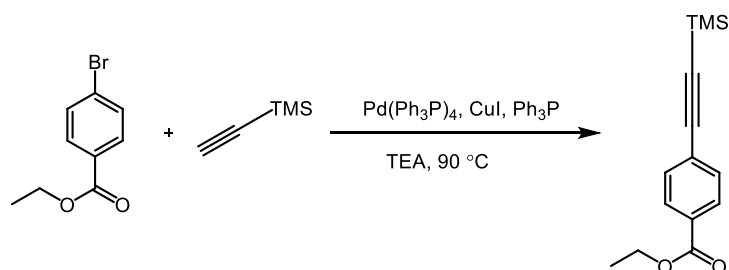
UC-CPNs Film preparation

2 mg/mL UC-CPNs were dispersed in 1 mL MiliQ®. The resulting suspension afterwards mixed with 1mL 20 wt% PVA solution with stirring for better dispersion. The mixture were poured into a container for film formation through evaporation.

Glass slide printing

2 mg/mL UC-CPNs were dispersed in 2 mL MiliQ®. The resulting suspension afterwards mixed with 2mL 10 wt% PVA solution with stirring for better dispersion. The mixture was used for

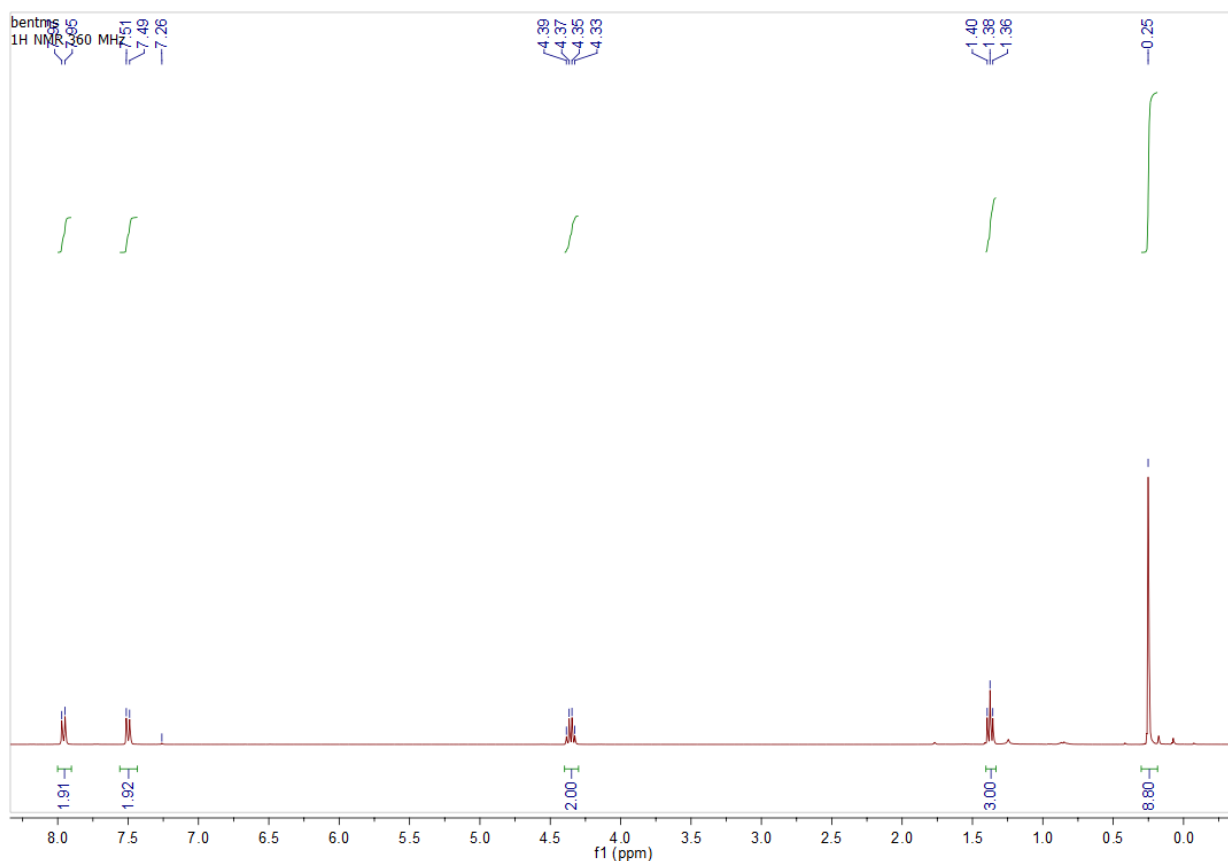
Synthesis and spectra



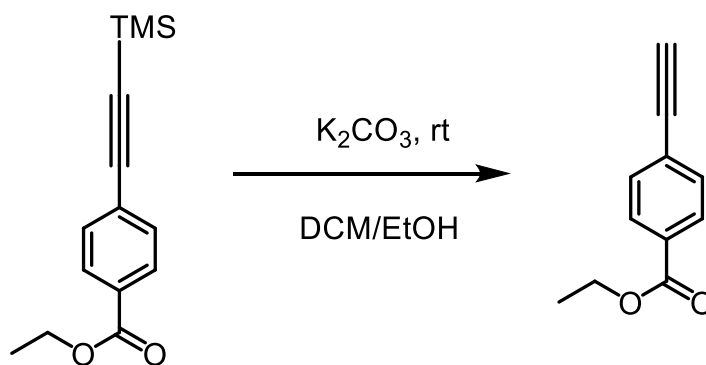
A mixture of ethyl 4-bromobenzoate (2.01 g, 8.77 mmol, 1.0 equiv), $Pd(PPh_3)_4$ (504 mg, 0.44 mmol, 0.05 equiv.), CuI (83 mg, 0.44 mmol, 0.05 equiv.) and PPh_3 (137 mg, 0.53 mmol, 0.06 equiv.) was dissolved in triethylamine (60 ml) under argon. Ethynyltrimethylsilane (1.03 g

10.49 mmol, 1.2 equiv) was added and the reaction mixture was heated at 90 °C for 17 hr. After cooling to rt, the mixture was filtered through CELITE and evaporated to dryness. The crude was purified by flash chromatography (HEX/DCM 10/1 to 2/1) to afford 2.08 g (96.7%) as a yellowish liquid. $R_f = 0.50$ (hexanes:DCM = 1:1)

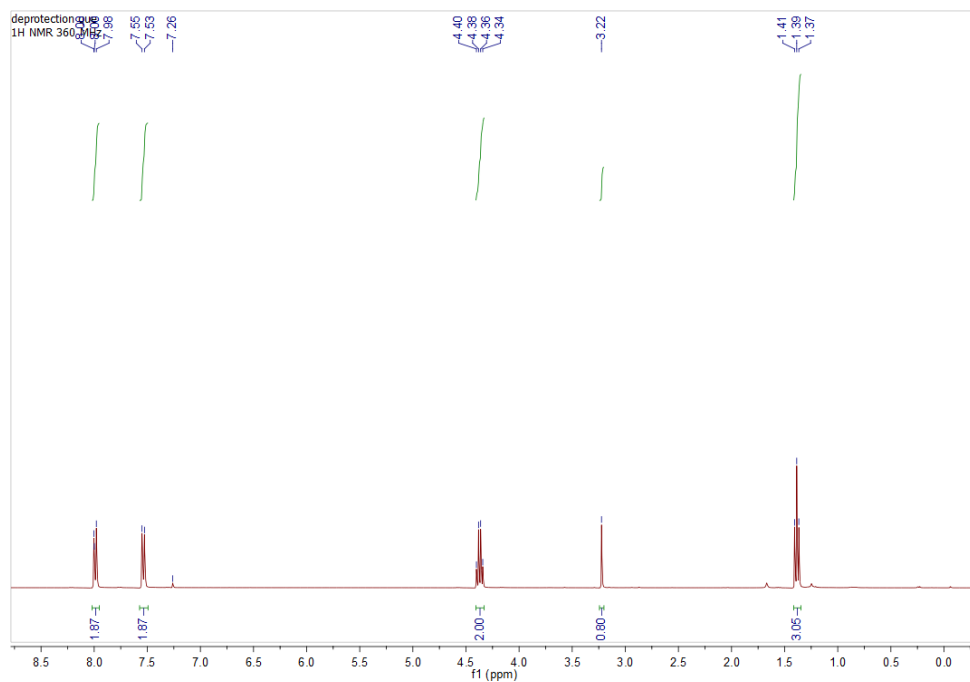
$^1\text{H NMR}$ (360 MHz, CDCl_3) $\delta = 7.96$ (d, $J=8.4$, 2H), 7.50 (d, $J=8.5$, 2H), 4.36 (q, $J=7.1$, 2H), 1.38 (t, $J=7.1$, 3H), 0.25 (s, 9H)



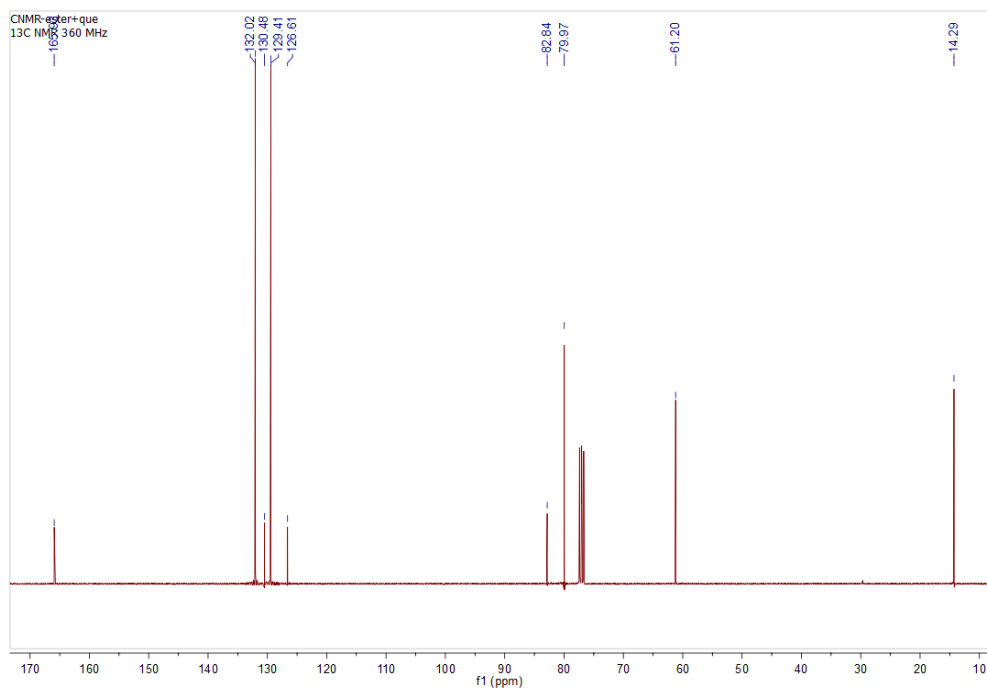
$^1\text{H NMR}$ spectrum of ethyl 4-((trimethylsilyl)ethynyl)benzoate



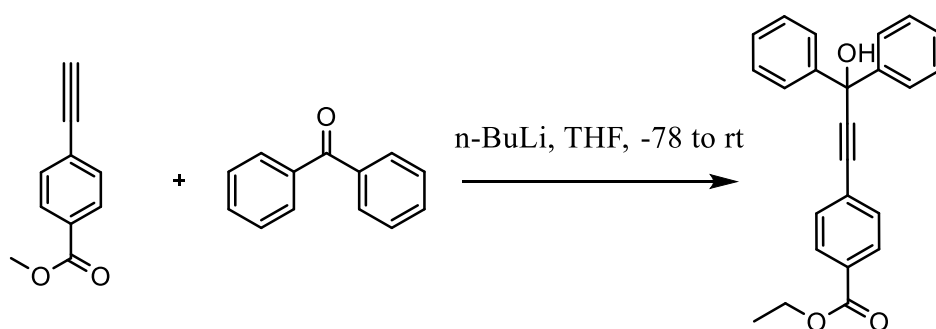
To a solution of K_2CO_3 (2.33 g, 16.8 mmol, 2.0 equiv.) in EtOH/DCM (50 mL/10 mL) mixture ethyl 4-((trimethylsilyl)ethynyl)benzoate (2.08 g, 8.4 mmol, 1.0 equiv.) was added under argon. The reaction mixture was stirred for 4 h at rt, then filtered and evaporated to dryness. The crude was purified by flash chromatography to afford 1.27 g (86.7%). $R_f = 0.40$ (hexanes:DCM 1:1) 1H NMR (360 MHz, $CDCl_3$) $\delta = 8.02 - 7.95$ (m, 2H), 7.54 (d, $J=8.3$, 2H), 4.37 (q, $J=7.1$, 2H), 3.22 (s, 1H), 1.39 (t, $J=7.1$, 3H). ^{13}C NMR (91 MHz, $CDCl_3$) $\delta = 165.93, 132.02, 130.48, 129.41, 126.61, 82.84, 79.97, 61.20$



1H NMR spectrum of ethyl 4-ethynylbenzoate

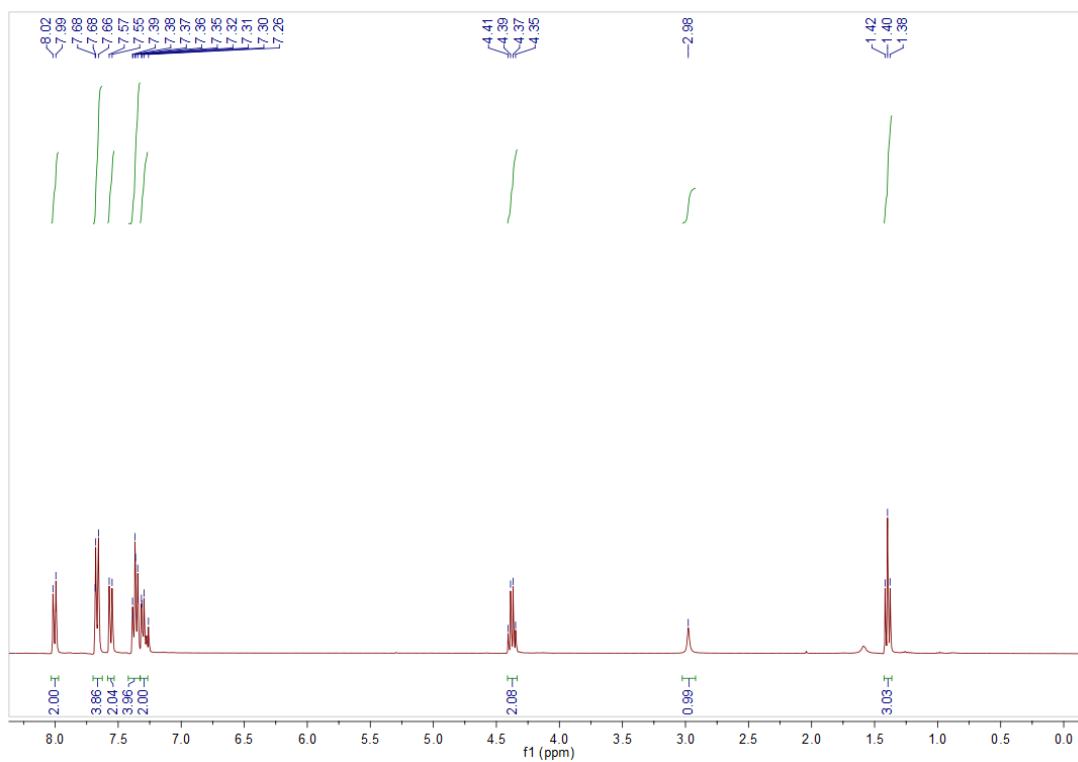


¹³C NMR spectrum of ethyl 4-ethynylbenzoate

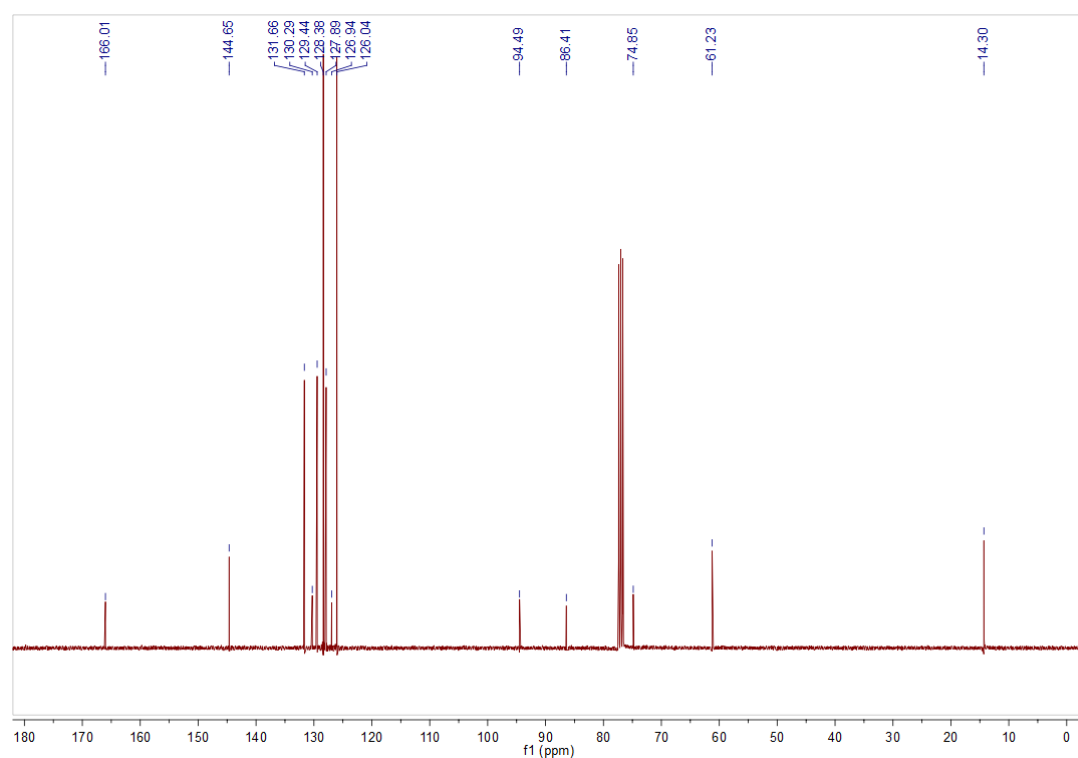


Ethyl-4-((trimethylsilyl)ethynyl)benzoate (1.27 g, 7.32 mmol, 1.0 equiv) was dissolved in dry THF (50 ml) under N₂. n-BuLi (3.2 mL (2.5 M), 8.05 mmol, 1.1 equiv) was added dropwise at -78°C. After 1 h, a solution of benzophenone (1.40 g, 7.69 mmol, 1.05 equiv.) in dry THF was added and the reaction mixture was allowed to reach room temperature for 1 h. The reaction mixture was quenched by addition of 1.0 M HCl and extracted with ethylacetate, dried over Na₂SO₄, and concentrated under reduced pressure. The crude material was crystallized by adding hexane affording 1.66 g (64%) as white solid. R_f = 0.70 (hexanes:EA = 5:1)

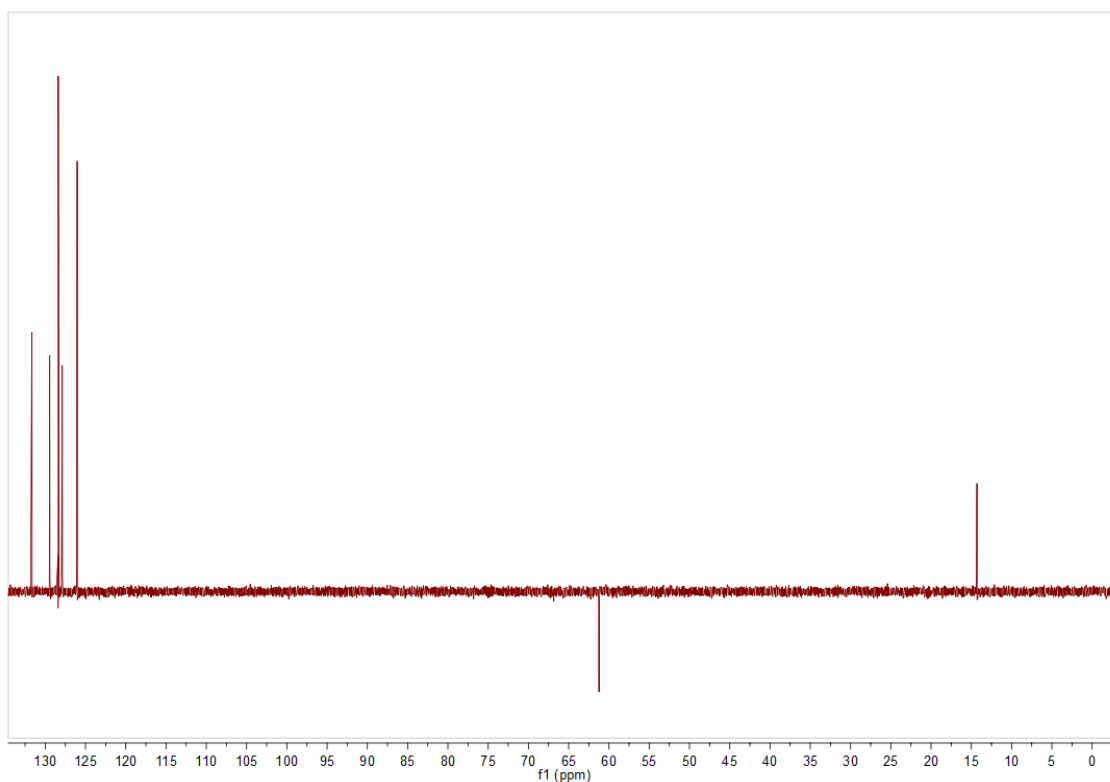
¹H NMR (360 MHz, CDCl₃) δ = 8.01 (d, J=8.4, 2H), 7.70 – 7.63 (m, 4H), 7.56 (d, J=8.4, 2H), 7.42 – 7.33 (m, 4H), 7.32 – 7.27 (m, 2H), 4.38 (q, J=7.1, 2H), 2.98 (s, 1H), 1.40 (t, J=7.1, 3H).
¹³C NMR (91 MHz, CDCl₃) δ = 166.01, 144.65, 131.66, 130.29, 129.44, 128.38, 127.89, 126.94, 126.04, 94.49, 86.41, 74.85, 61.23, 14.30.



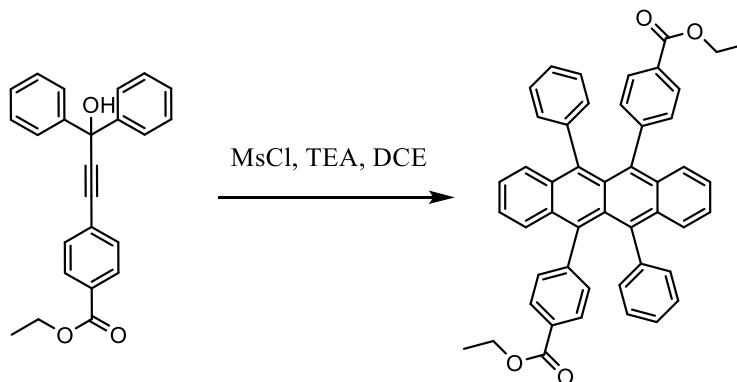
¹H NMR spectrum of ethyl 4-(3-hydroxy-3,3-diphenylprop-1-yn-1-yl)benzoate



¹³C NMR spectrum of ethyl 4-(3-hydroxy-3,3-diphenylprop-1-yn-1-yl)benzoate



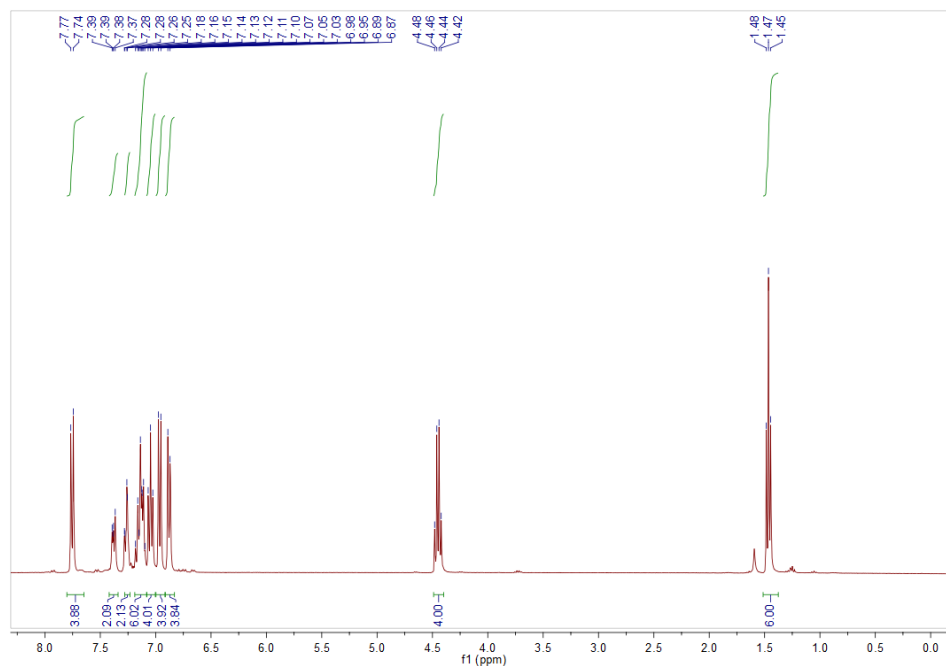
DEPT135 spectrum of ethyl 4-(3-hydroxy-3,3-diphenylprop-1-yn-1-yl)benzoate



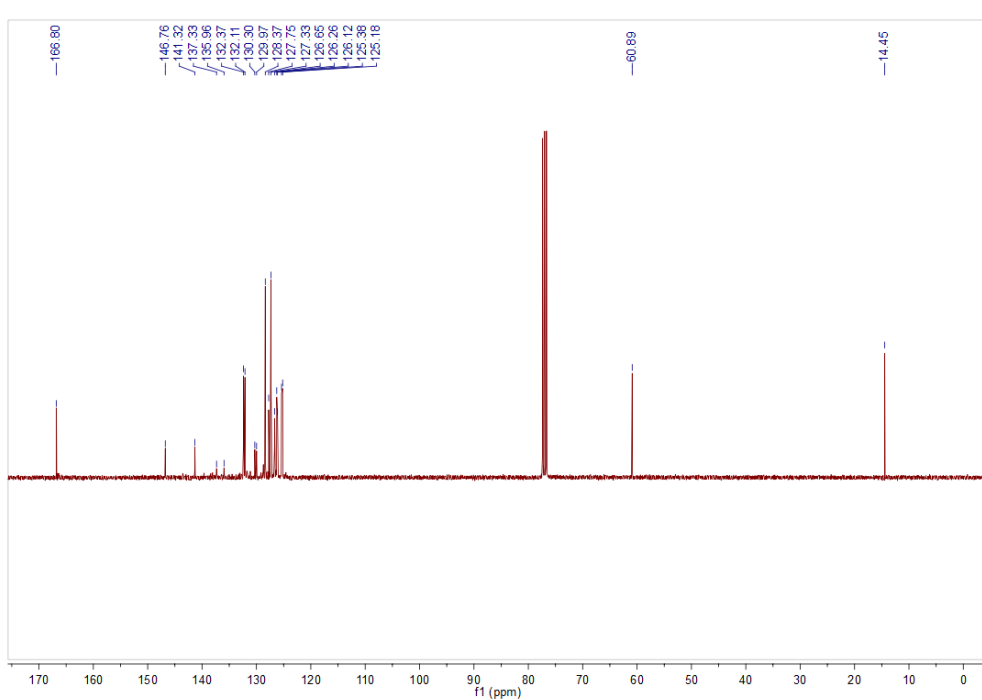
Ethyl 4-(3-hydroxy-3,3-diphenylprop-1-yn-1-yl)benzoate (250 mg, 0.7 mmol, 1.0 equiv.) was dissolved in dry DCE (5.0 mL) under argon. The mixture was cooled to 0 °C and then, TEA (177 mg, 1.75 mmol, 2.5 equiv.) was added followed by MsCl (0.064 mL, 0.8 mmol, 1.2 equiv.). After stirring at rt for 24 hr, the reaction mixture was heated at 110 °C for 24 hr. The volatiles were removed in vacuo and the crude was purified by flash chromatography (HEX/DCM → 10:1 → 5:1 → 2:1) affording 111.5 mg (23.5%) as orange solid. $R_f = 0.50$ (hexanes:EA = 5:1)

^1H NMR (360 MHz, CDCl_3) δ 7.76 (d, $J = 8.1$ Hz, 4H), 7.38 (dd, $J = 6.1, 4.1$ Hz, 2H), 7.26 (t, $J = 4.2$ Hz, 2H), 7.19 – 7.08 (m, 6H), 7.05 (t, $J = 7.5$ Hz, 4H), 6.96 (d, $J = 8.1$ Hz, 4H), 6.88 (d, $J = 7.1$ Hz, 4H), 4.45 (q, $J = 7.1$ Hz, 4H), 1.47 (t, $J = 7.1$ Hz, 6H).

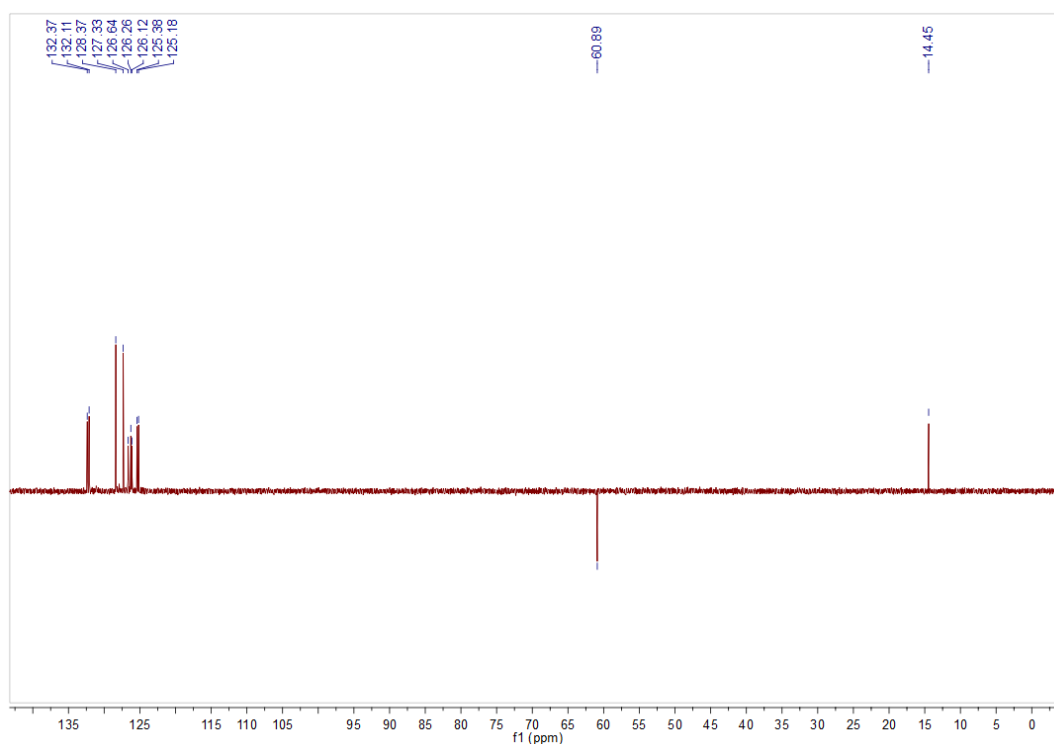
^{13}C NMR (91 MHz, CDCl_3) δ 166.80, 146.76, 141.32, 137.33, 135.96, 132.37, 132.11, 130.30, 129.97, 128.37, 127.75, 127.33, 126.65, 126.26, 126.12, 125.38, 125.18, 60.89, 14.45.



^1H NMR spectrum of diethyl 4,4'-(6,12-diphenyltetracene-5,11-diyl)dibenzoate

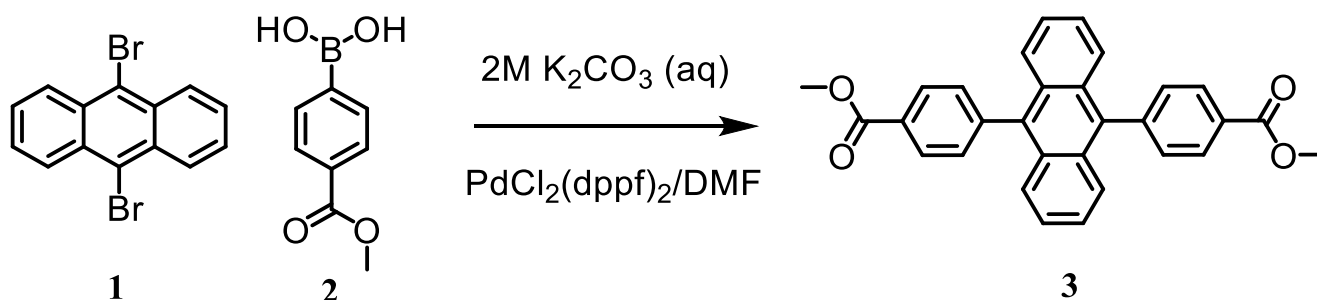


^{13}C NMR spectrum of diethyl 4,4'-(6,12-diphenyltetracene-5,11-diyl)dibenzoate



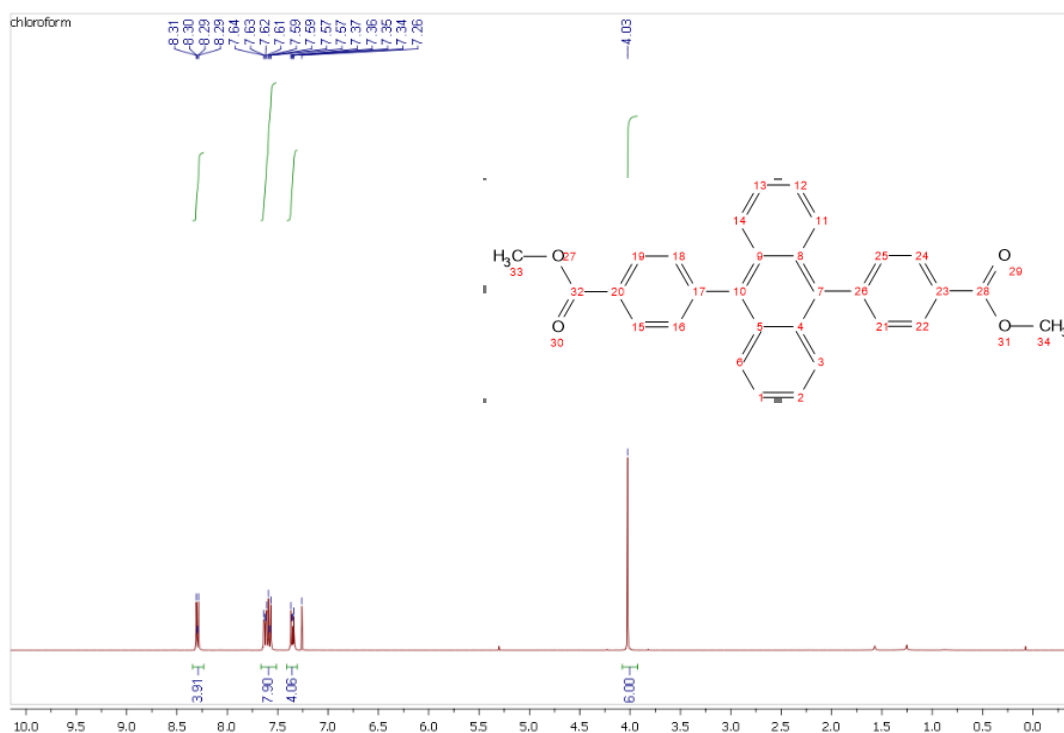
DEPT135 spectrum of diethyl 4,4'-(6,12-diphenyltetracene-5,11-diyl)dibenzoate

S1. Synthetic procedure and characterization

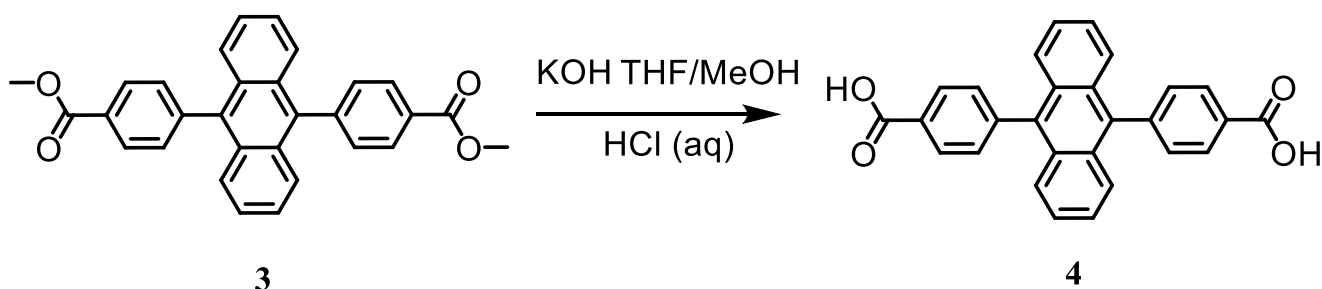


The mixture of **1** (9,10-dibromoanthracene, 250mg, 0.74mmol), **2** (4 - (methoxycarbonyl) phenyl) boronic acid, 335mg, 1.86mmol) and a catalytic amount of PdCl₂(dppf)₂ (54 mg, 0.074mmol) were dissolved in 20mL of degassed DMF. Then an aqueous 2 M K₂CO₃ solution was added to the mixture and the reaction was heated to 155 °C for 22 h until the anthracene was consumed. The crude product was purified by column chromatography using DCM to afford white solid compound **3** (224mg, 67.7 %).

¹H NMR (360 MHz, CDCl₃) δ 8.35 – 8.23 (m, 4H, H^{3,6,11,14}), 7.60 (ddd, J = 8.2, 6.6, 2.4 Hz, 8H, H^{15,16,18,19,21,22,24,25}), 7.35 (dd, J = 6.9, 3.3 Hz, 4H, H^{1,2,12,13}), 4.03 (s, 6H, H^{33,34}).

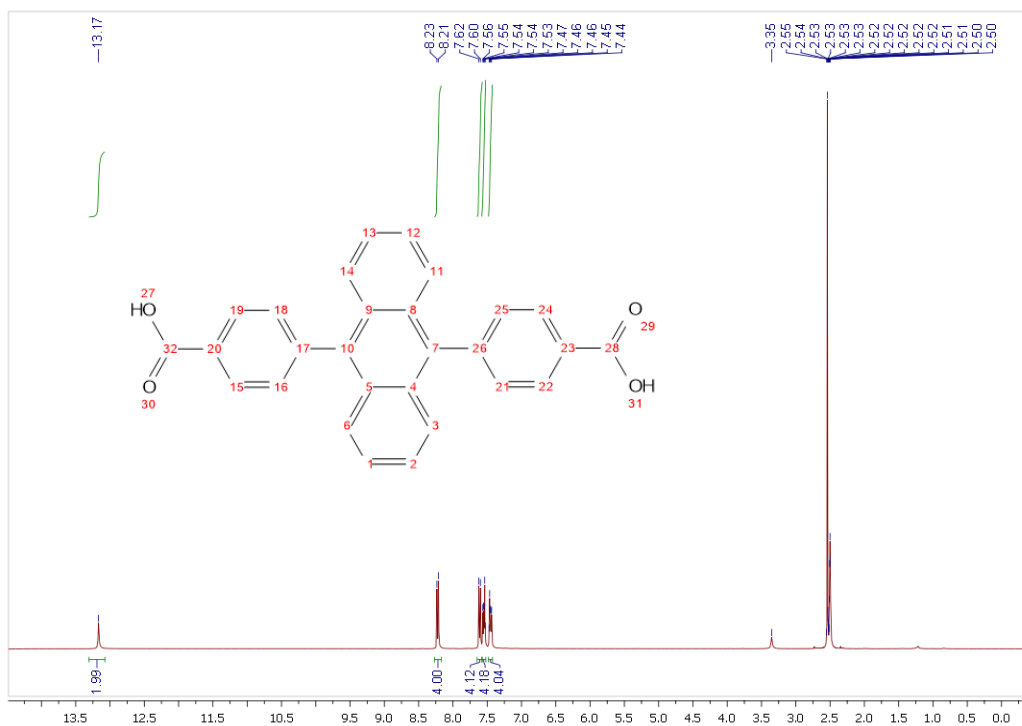


^1H NMR spectrum of 3

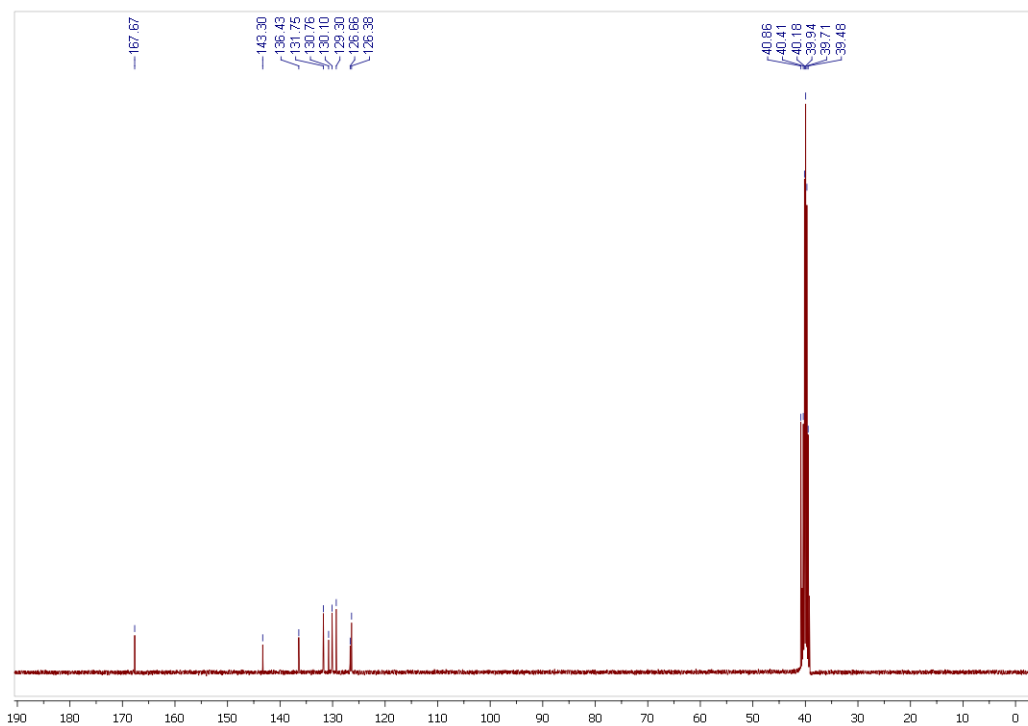


The 9,10-(methyl-4-carboxyphenyl) anthracene (217mg, 0.48mmol) was suspended in MeOH (15 mL), 1,4-dioxane (15 mL) and KOH aqueous (2M, 15 ml). The mixture was refluxed at 60 °C for 20 h. After cooling to the room temperature, the mixture was tuned to pH = 2 using 4 M hydrochloric acid. The precipitate was collected by filter affording white solid **4** (183 mg, 90.1%)

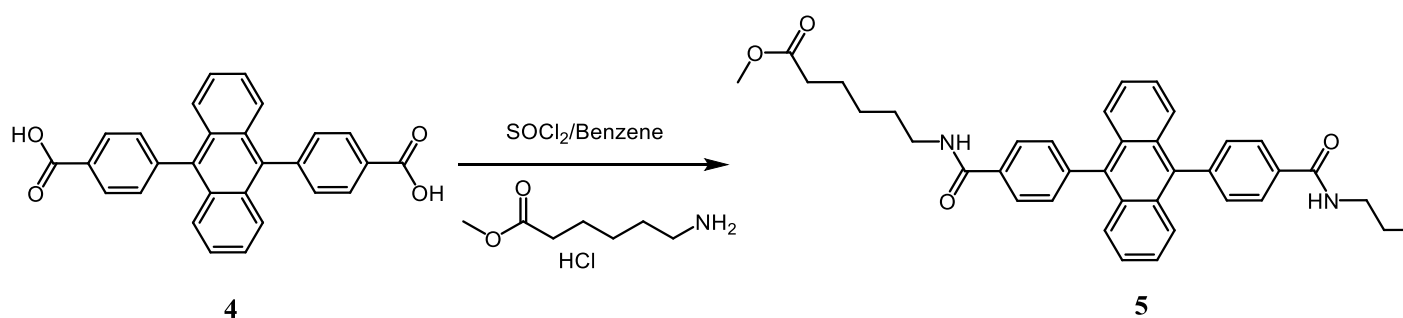
^1H NMR (360 MHz, $(\text{CD}_3)_2\text{SO}$) δ 13.17 (s, 2H, $\text{H}^{30,31}$), 8.22 (d, $J = 8.2$ Hz, 4H, $\text{H}^{3,6,11,14}$), 7.61 (d, $J = 8.2$ Hz, 4H, $\text{H}^{15,19,22,24}$), 7.58 – 7.52 (m, 4H, $\text{H}^{16,18,21,25}$), 7.48 – 7.42 (m, 4H, $\text{H}^{1,2,12,13}$).
 ^{13}C NMR (91 MHz, $(\text{CD}_3)_2\text{SO}$) δ 167.67 (s, $\text{C}^{28,32}$), 143.30 (s, $\text{C}^{17,26}$), 136.43 (s, $\text{C}^{7,10}$), 131.75 (s, $\text{C}^{4,5,8,9}$), 130.76 (s, $\text{C}^{15,19,22,24}$), 130.10 (s, $\text{C}^{3,6,11,14}$), 129.30 (s, $\text{C}^{20,23}$), 126.66 (s, $\text{C}^{16,18,21,25}$), 126.38 (s, $\text{C}^{1,2,12,13}$).



¹H NMR spectrum of 4



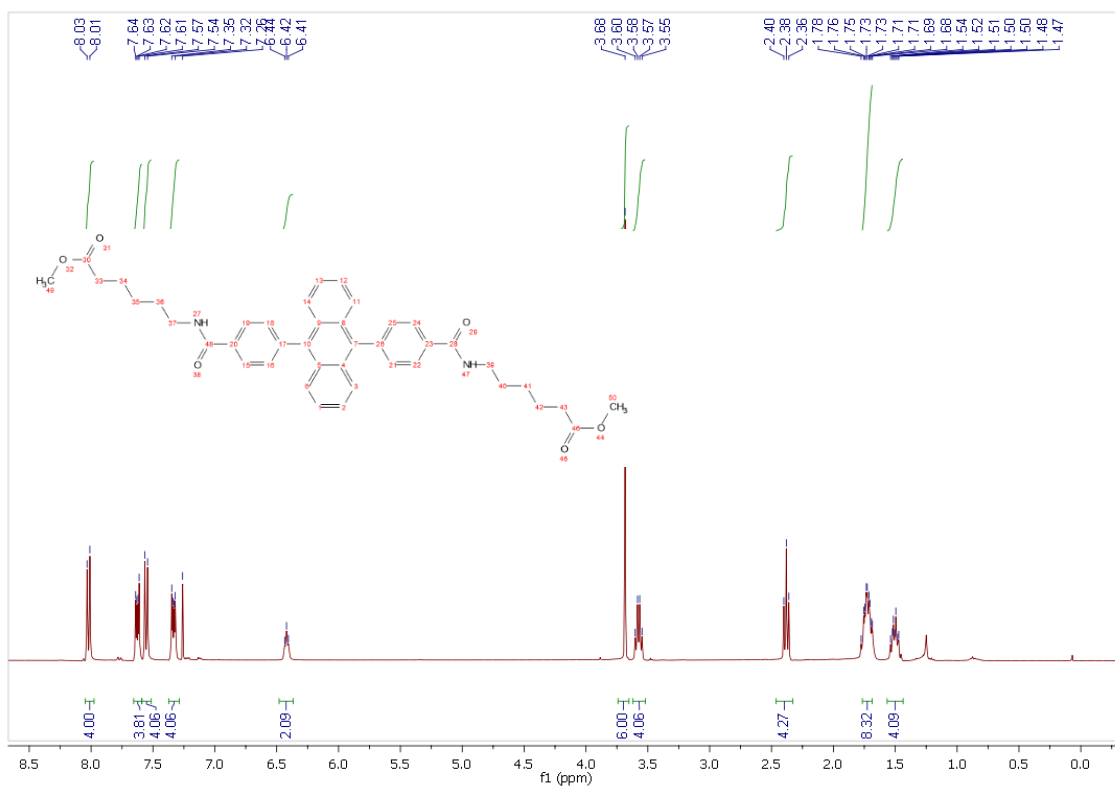
¹³C NMR spectrum of 4



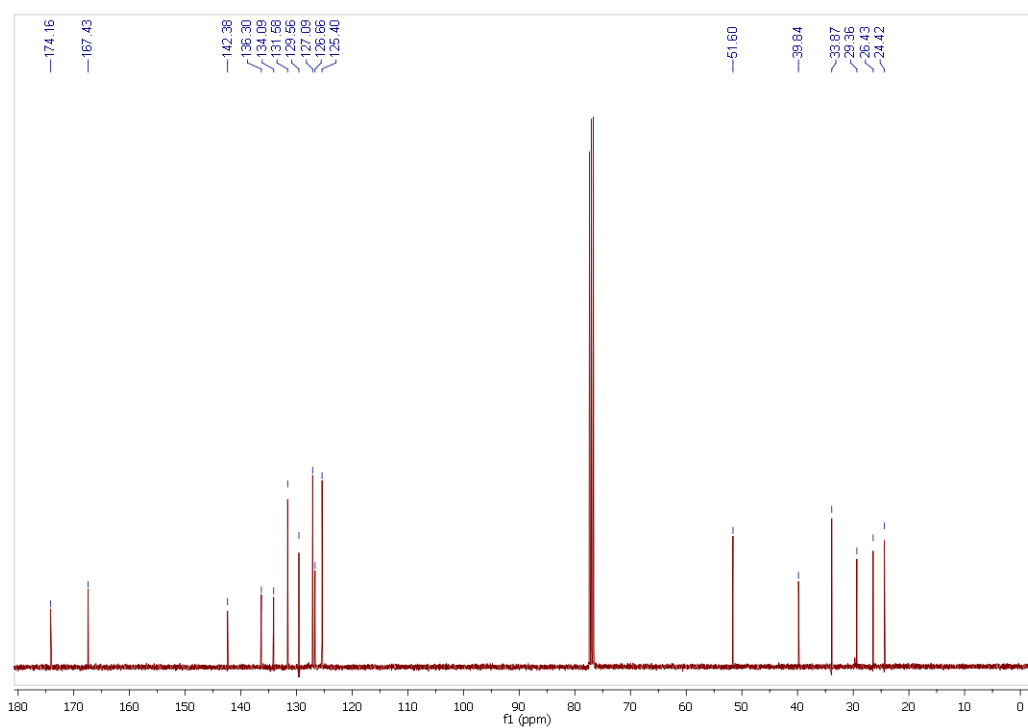
4 (4,4'-(anthracene-9,10-diyl) dibenzoic acid, 70 mg, 0.167 mmol) was placed in 10 mL 2-necked flask and benzene (5 mL) was added under N_2 protection. Then thionyl chloride was added to the suspension and refluxed for 5 h with catalyst quantity of anhydrous DMF. After removal of redundant thionyl chloride and benzene, the residue was dilute by dehydrated DCM and used directly for the next step affording white solid **5** (85 mg, 75.9%).

^1H NMR (360 MHz, CDCl_3) δ 8.02 (d, $J = 8.2$ Hz, 4H, $\text{H}^{3,6,11,14}$), 7.63 (dd, $J = 6.8, 3.3$ Hz, 4H, $\text{H}^{15,19,22,24}$), 7.55 (d, $J = 8.1$ Hz, 4H, $\text{H}^{16,18,21,25}$), 7.33 (dd, $J = 6.9, 3.2$ Hz, 4H, $\text{H}^{1,2,12,13}$), 6.42 (t, $J = 5.4$ Hz, 2H, $\text{H}^{27,47}$), 3.68 (s, 6H, $\text{H}^{49,50}$), 3.57 (dd, $J = 13.1, 6.8$ Hz, 4H, $\text{H}^{37,39}$), 2.38 (t, $J = 7.3$ Hz, 4H, $\text{H}^{33,43}$), 1.77 – 1.69 (m, 8H, $\text{H}^{34,36,40,42}$), 1.57 – 1.44 (m, 4H, $\text{H}^{35,41}$).

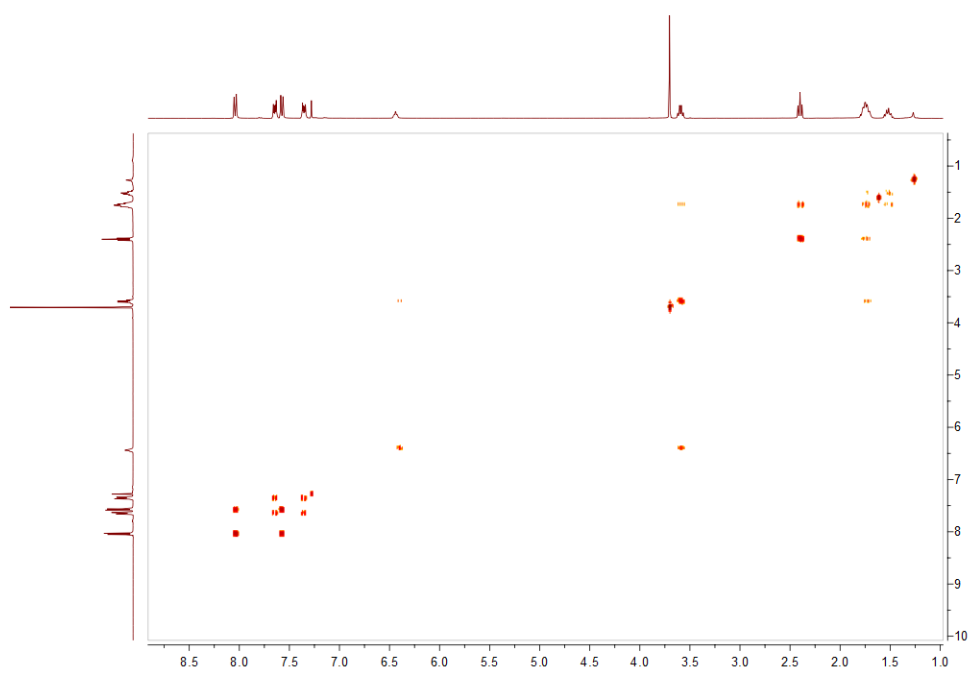
^{13}C NMR (91 MHz, CDCl_3) δ 174.16 (s, $\text{C}^{30,46}$), 167.43 (s, $\text{C}^{28,48}$), 142.38 (s, $\text{C}^{17,26}$), 136.30 (s, $\text{C}^{7,10}$), 134.09 (s, $\text{C}^{20,23}$), 131.58 (s, $\text{C}^{4,5,8,9}$), 129.56 (s, $\text{C}^{16,18,21,25}$), 127.09 (s, $\text{C}^{3,6,11,14}$), 126.66 (s, $\text{C}^{15,19,22,24}$), 125.40 (s, $\text{C}^{1,2,12,13}$), 51.60 (s, $\text{C}^{49,50}$), 39.84 (s, $\text{C}^{37,39}$), 33.87 (s, $\text{C}^{33,43}$), 29.36 (s, $\text{C}^{36,40}$), 26.43 (s, $\text{C}^{35,41}$), 24.42 (s, $\text{C}^{34,42}$). DEPT 135 (91 MHz, CDCl_3) δ 131.58 (s, $\text{C}^{16,18,21,25}$), 128.07 (s, $\text{C}^{3,6,11,14}$), 126.66 (s, $\text{C}^{15,19,22,24}$), 125.40 (s, $\text{C}^{1,2,12,13}$), 51.59 (s, $\text{C}^{49,50}$), 39.83 (s, 37,39), 33.86 (s, $\text{C}^{33,43}$), 29.35 (s, $\text{C}^{36,40}$), 26.42 (s, $\text{C}^{35,41}$), 24.42 (s, $\text{C}^{34,42}$).



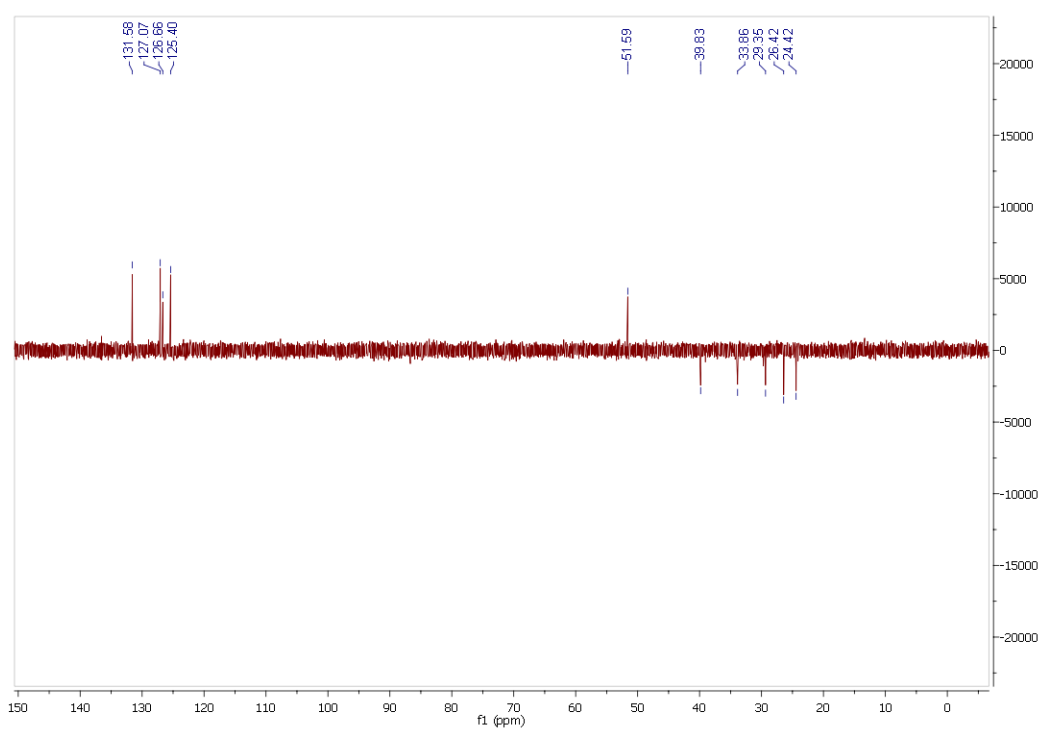
¹H NMR spectrum of **5**



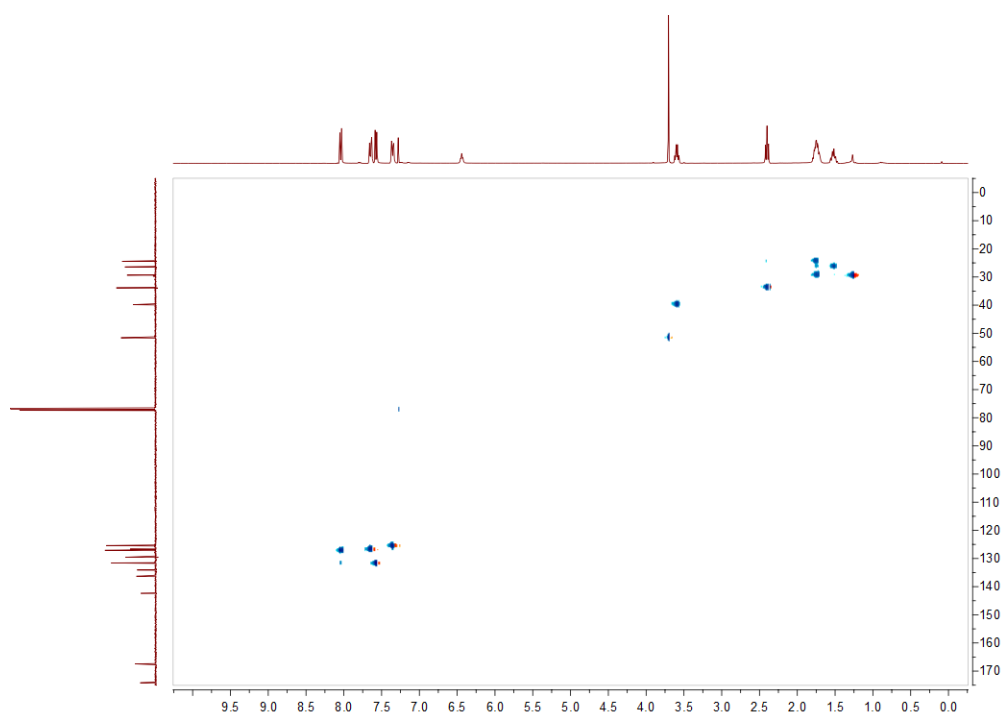
¹³C NMR spectrum of **5**



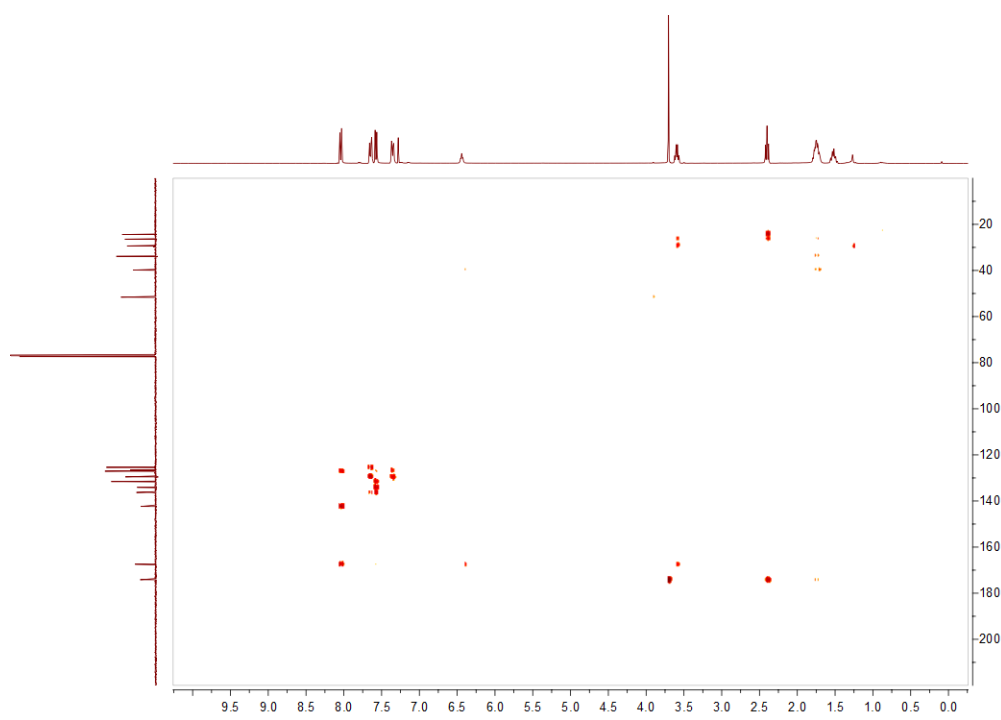
COSY spectrum of **5**



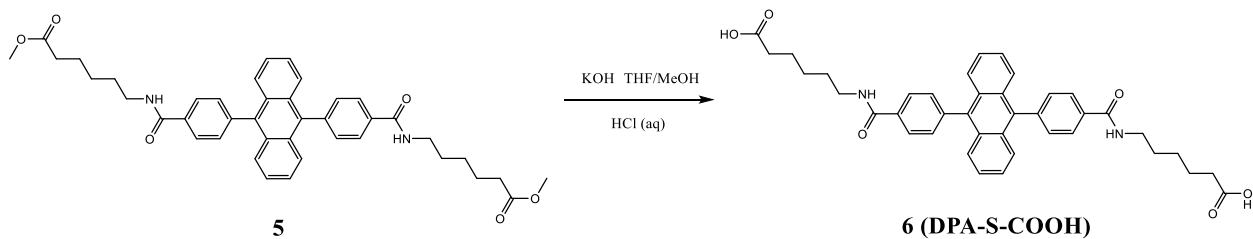
DEPT135 spectrum of **5**



HSQC spectrum of **5**



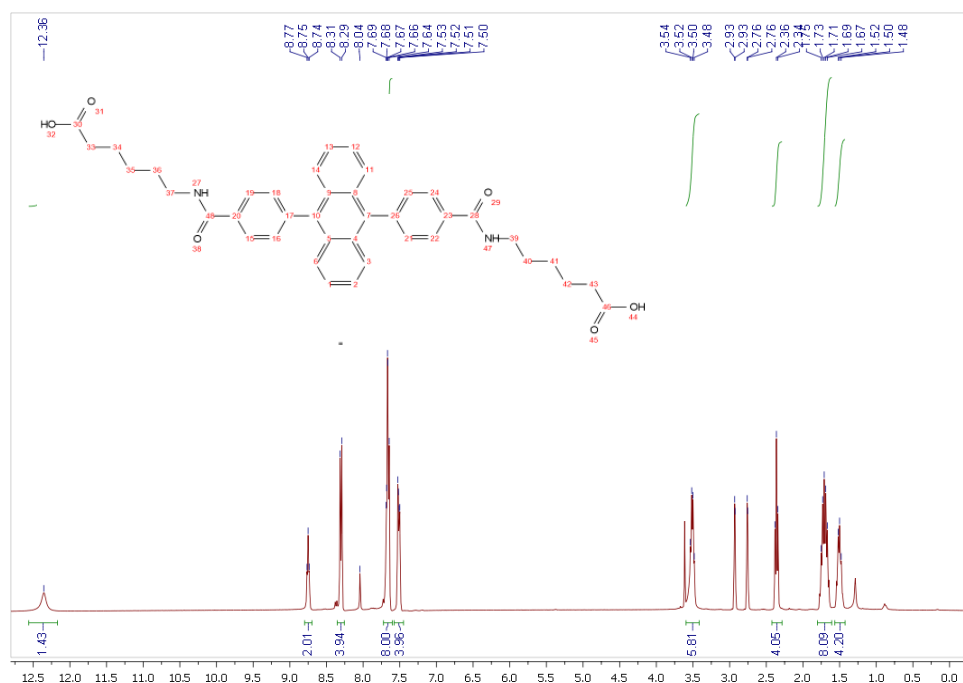
HMBC spectrum of **5**



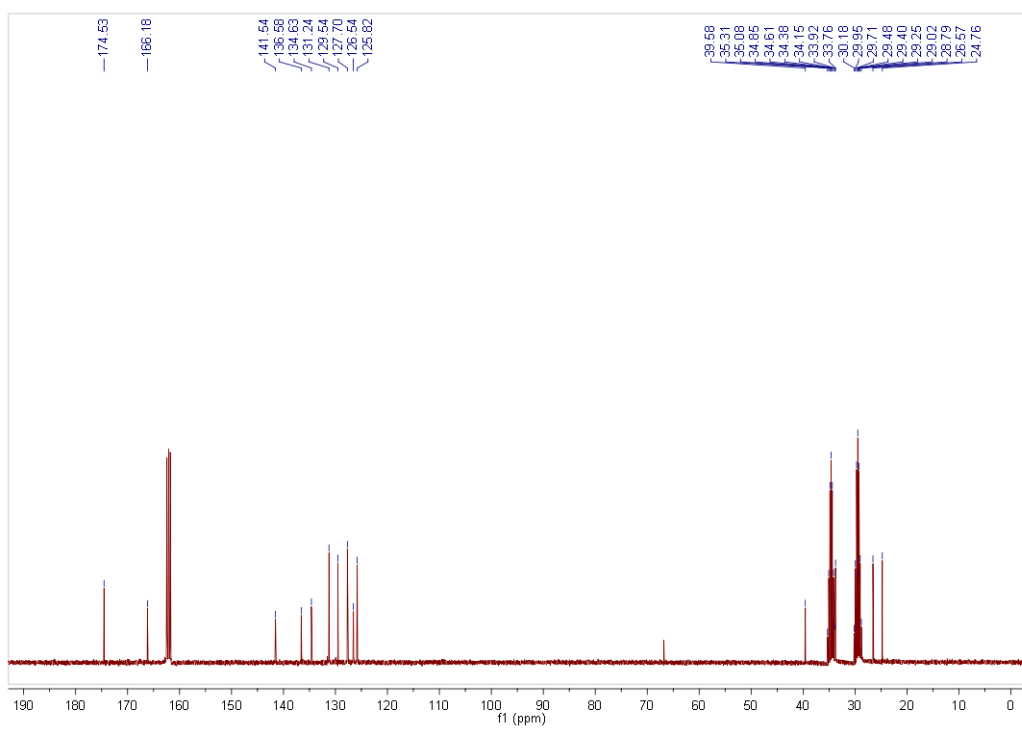
The **5** (85 mg, 0.13 mmol) was suspended in MeOH (15 mL). 1,4-dioxane (15ml) and KOH aqueous (2M, 15 mL). The mixture was refluxed at 60 °C for 20h. After cooling to room temperature, the mixture was tuned to pH = 2 using hydrochloric acid (4M). The precipitate was collected by filter affording the molecule **6** as a white solid (72.5 mg, 89.0%).

$^1\text{H NMR}$ (360 MHz, *N,N*-dimethyl-formamide- d_7): δ 12.36 (s, 2H, H^{32,44}), 8.75 (t, $J = 5.3$ Hz, 2H, H^{27,47}), 8.30 (d, $J = 8.1$ Hz, 4H, H^{3,6,11,14}), 7.72 – 7.60 (m, 8H H^{15,19,22,24,16,18,21,25}), 7.51 (dd, $J = 6.9, 3.1$ Hz, 4H, H^{1,2,12,13}), 3.51 (dd, $J = 12.6, 6.5$ Hz, 4H, H^{37,39}), 2.36 (t, $J = 7.3$ Hz, 4H, H^{33,43}), 1.71 (dt, $J = 15.3, 7.6$ Hz, 8H, H^{34,36,40,42}), 1.57 – 1.43 (m, 4H, H^{35,41}).

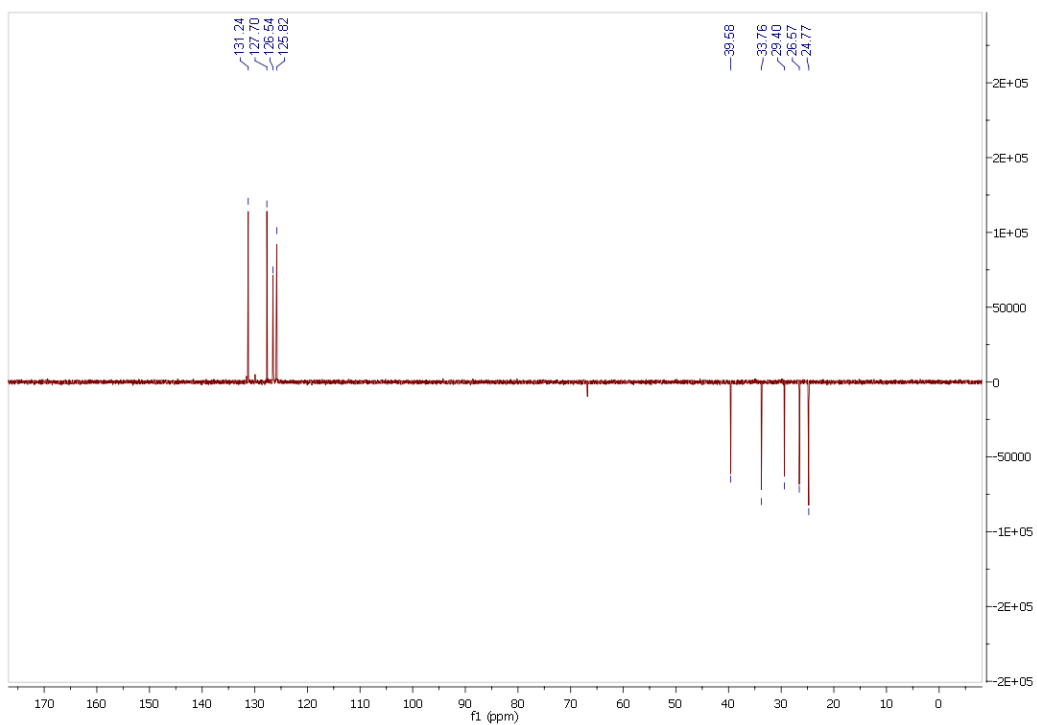
$^{13}\text{C NMR}$ (91 MHz, *N,N*-dimethyl-formamide- d_7): δ 174.53 (s, C^{30,46}), 166.18 (s, C^{28,48}), 141.54 (s, C^{17,26}), 136.58 (s, C^{7,10}), 134.63 (s, C^{20,23}), 131.24 (s, C^{4,5,8,9}), 129.54 (s, C^{16,18,21,25}), 127.70 (s, C^{3,6,11,14}), 126.54 (s, C^{15,19,22,24}), 125.82 (s, C^{1,2,12,13}), 39.58 (s, C^{37,39}), 35.08 (s, C^{33,43}), 29.95 (s, C^{36,40}), 26.57 (s, C^{35,41}), 24.76 (s, C^{34,42}). DEPT 135 (91 MHz, CDCl₃) δ 131.24 (s, C^{16,18,21,25}), 127.70 (s, C^{3,6,11,14}), 126.54 (s, C^{15,19,22,24}), 125.82 (s, C^{1,2,12,13}), 39.58 (s, C^{37,39}), 33.76 (s, C^{33,43}), 29.40 (s, C^{36,40}), 26.57 (s, C^{35,41}), 24.77 (s, C^{34,42}). MS-ESI (m/z): [M]⁻ Calcd. for C₄₀H₄₀N₂O₆⁻ 643.3, found 643.3.



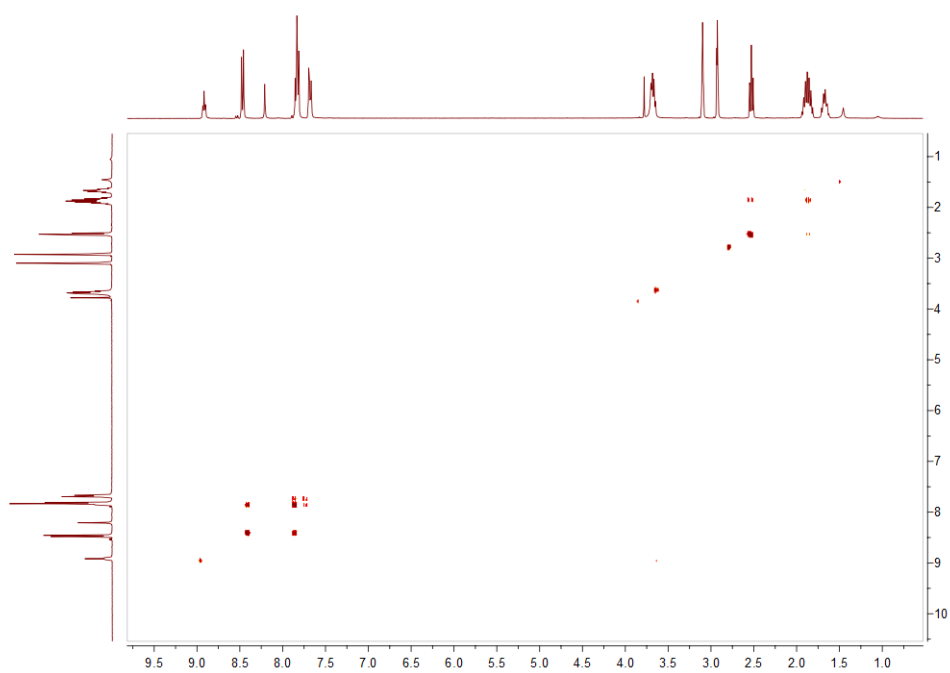
^1H NMR spectrum of **6**



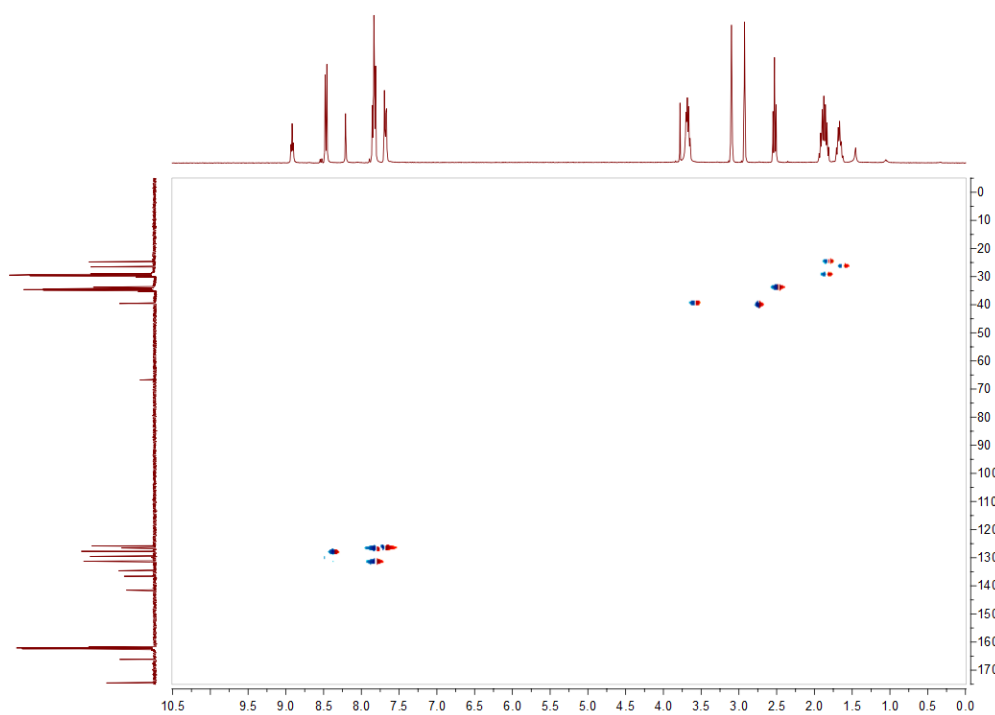
^{13}C NMR spectrum of **6**



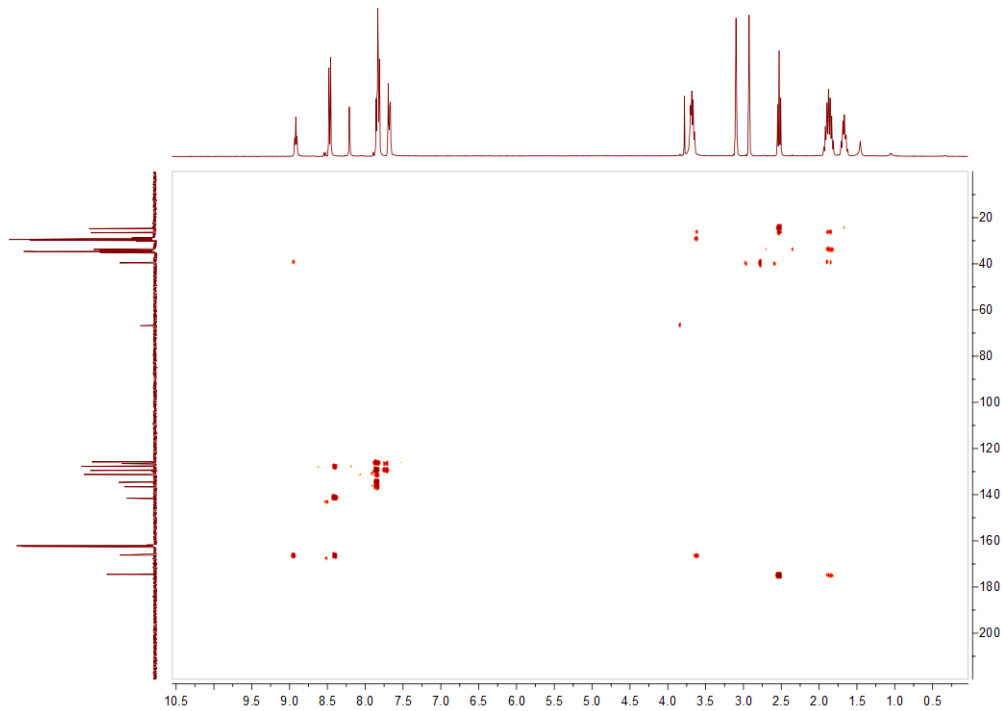
DPET135 spectrum of **6**



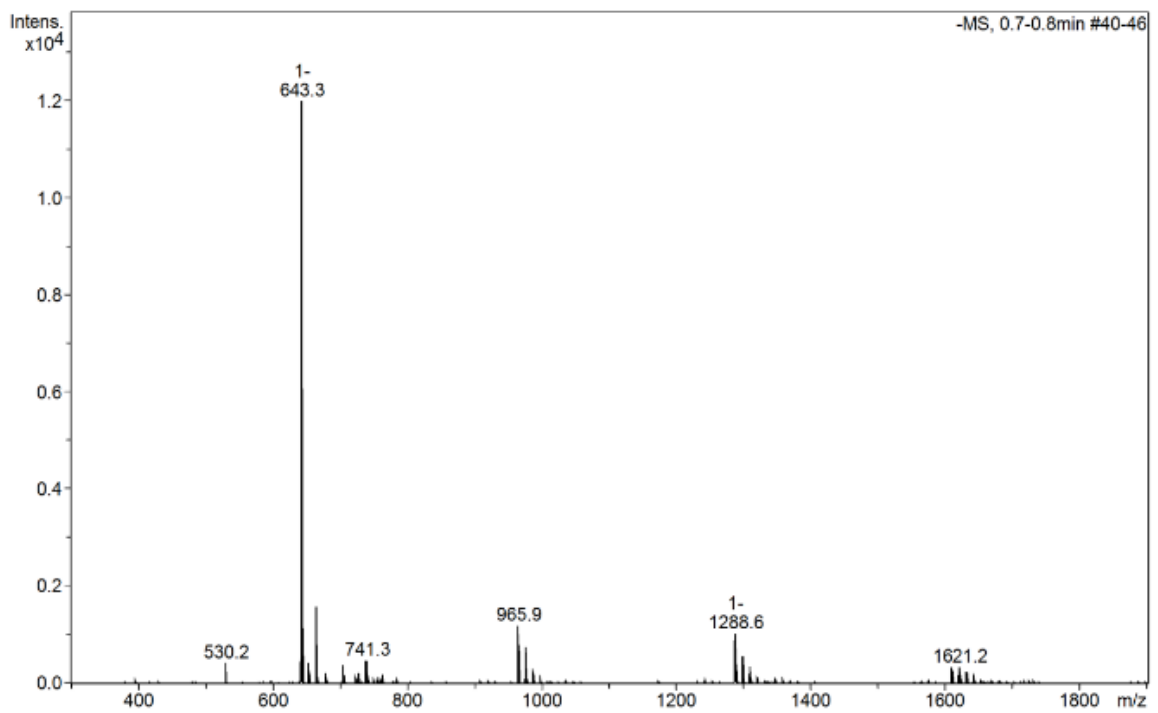
COSY spectrum of **6**



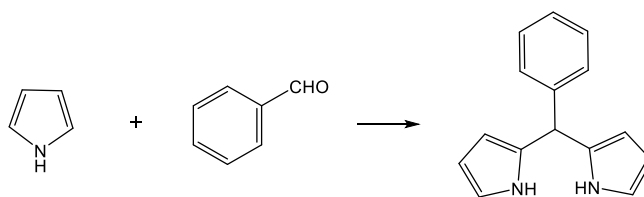
HSQC spectrum of **6**



HMBC spectrum of **6**

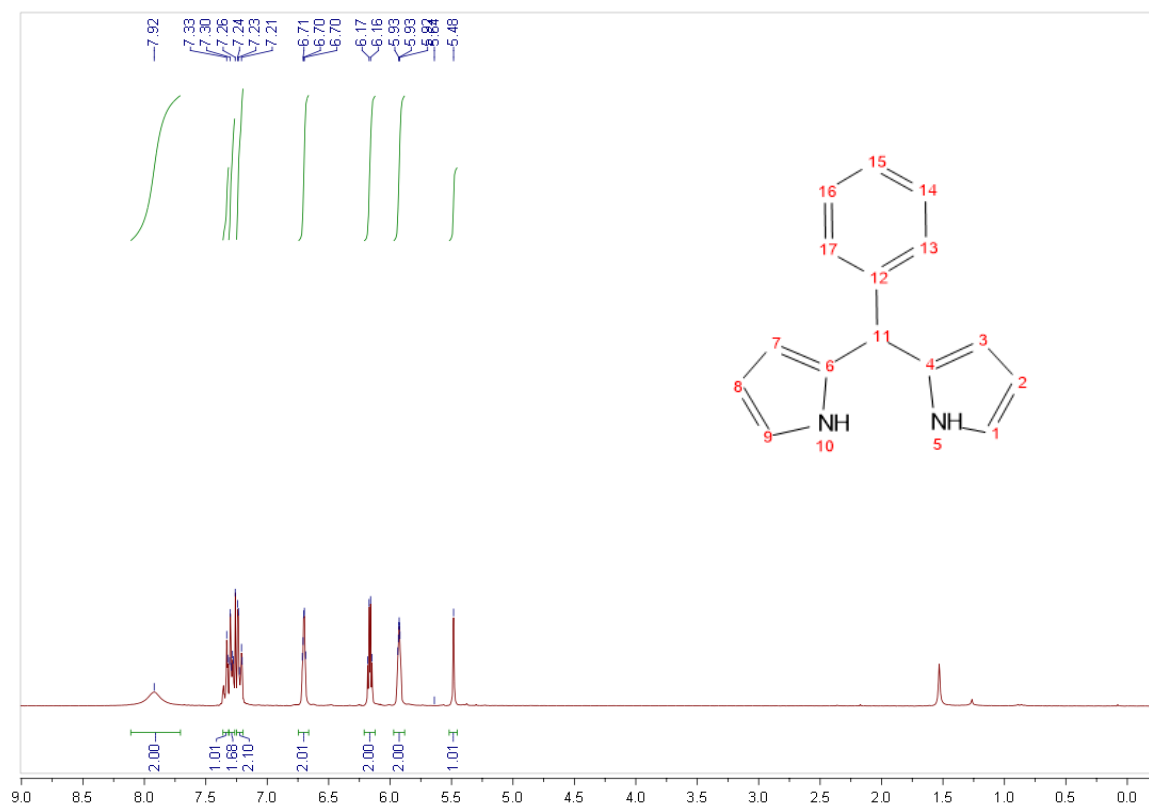


Mass spectrometry of **6**

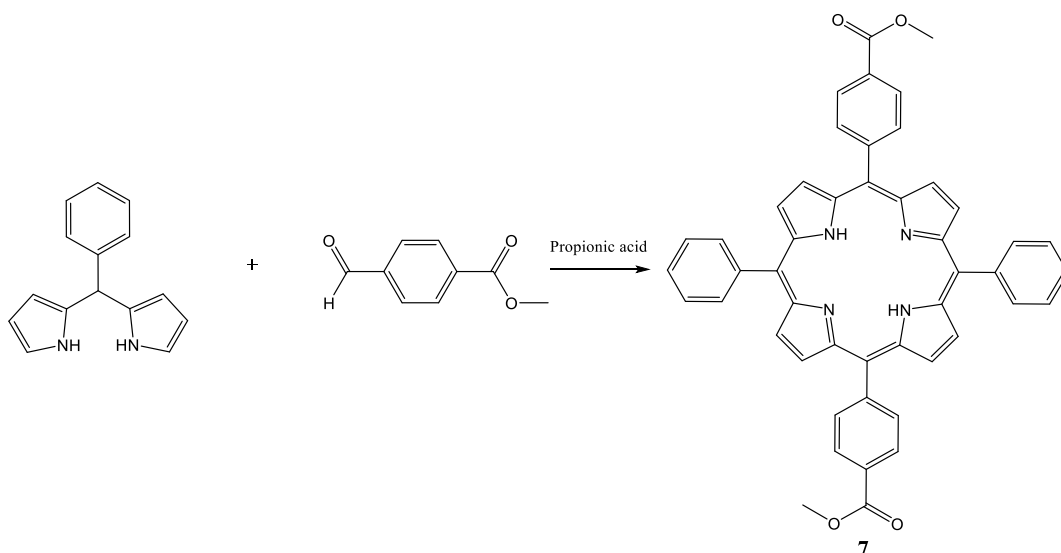


A mixture of benzaldehyde (2.0 g, 18 mmol) and pyrrole (30 mL, 0.44 mol) was treated with InCl_3 (0.2 g, 0.9 mmol) at room temperature under N_2 protection. After stirring for 6 h, NaOH (4.0 g, 0.1 mol) was added and the reaction mixture was stirred for 45 min. excess NaOH was filtered and excess pyrrole was removed by distillation under reduced pressure. The resulting black solid was purified by silica gel column chromatography with CH_2Cl_2 to afford a dark-brown solid dipyrroliphenylmethane (3.2 g, 76.0%).

^1H NMR (250 MHz, CDCl_3) δ 7.92 (s, 2H, $\text{H}^{5,10}$), 7.33 (d, $J = 1.9$ Hz, 1H, H^{15}), 7.31 – 7.26 (m, 2H, $\text{H}^{14,16}$), 7.25 – 7.20 (m, 2H, $\text{H}^{13,17}$), 6.70 (dt, $J = 4.2, 2.1$ Hz, 2H, $\text{H}^{1,9}$), 6.16 (dd, $J = 5.9, 2.8$ Hz, 2H, $\text{H}^{3,7}$), 5.97 – 5.88 (m, 2H, $\text{H}^{2,8}$), 5.48 (s, 1H, H^{11}).



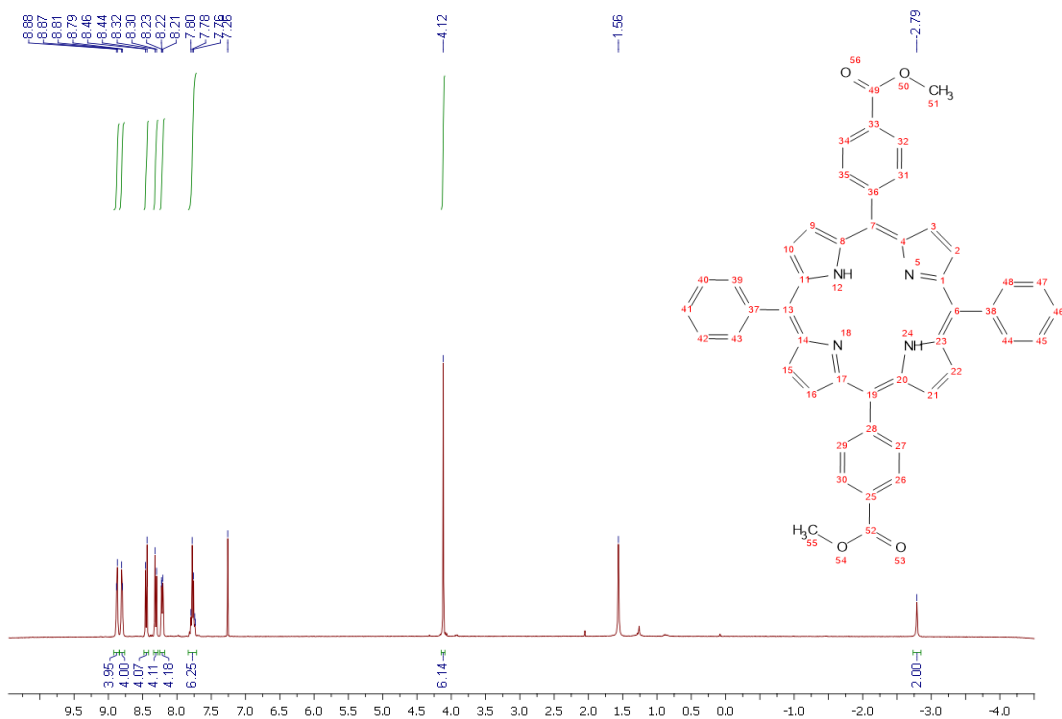
^1H NMR spectrum of dipyrroliphenylmethane



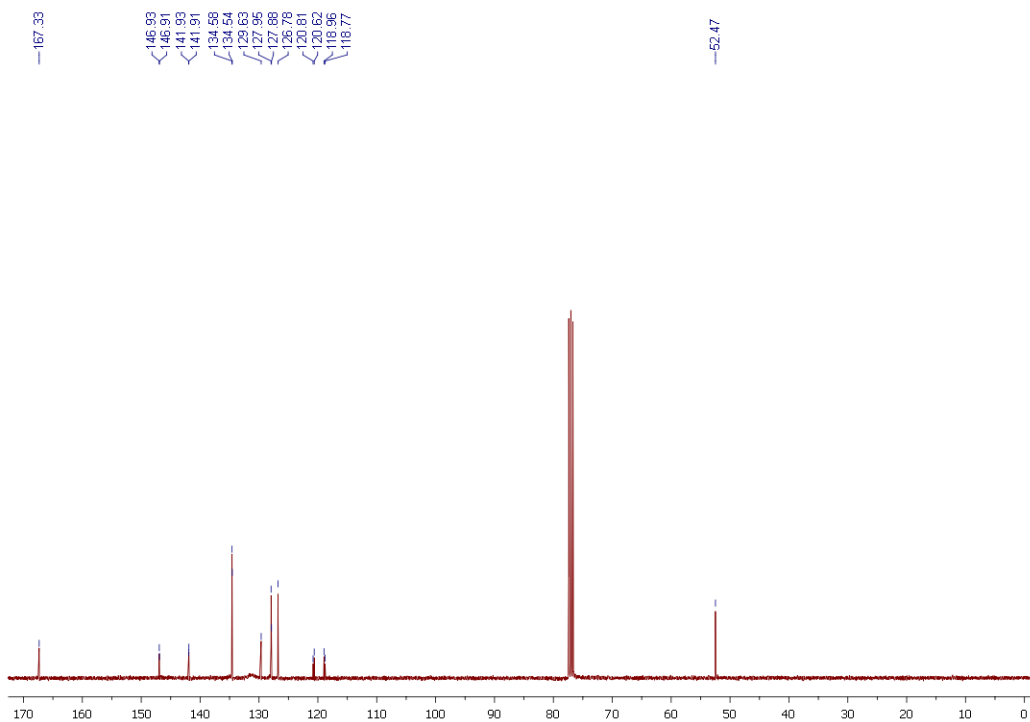
Dipyrrolophenylmethane (2.0 g, 9 mmol) and methyl 4-formylbenzoate (1.47 g, 9 mmol) were dissolved in 40 mL of propionic acid, and mixture was refluxing for 1 h. The solvent was evaporated under reduced pressure. Purification was done by silica gel column chromatography with CH_2Cl_2 to afford a purple solid (POR-ESTER, 470 mg, yield 7.1%)

^1H NMR (360 MHz, CDCl_3) δ 8.88 (d, $J = 4.9$ Hz, 4H, $\text{H}^{2,3,9,10}$), 8.80 (d, $J = 4.9$ Hz, 4H, $\text{H}^{15,16,21,22}$), 8.45 (d, $J = 8.2$ Hz, 4H, $\text{H}^{27,29,31,35}$), 8.31 (d, $J = 8.1$ Hz, 4H, $\text{H}^{26,30,32,34}$), 8.25 – 8.18 (m, 4H, $\text{H}^{40,42,45,47}$), 7.84 – 7.71 (m, 6H, $\text{H}^{39,41,43,44,46,48}$), 4.12 (s, 6H, $\text{H}^{51,55}$), -2.79 (s, 2H, $\text{H}^{12,24}$).

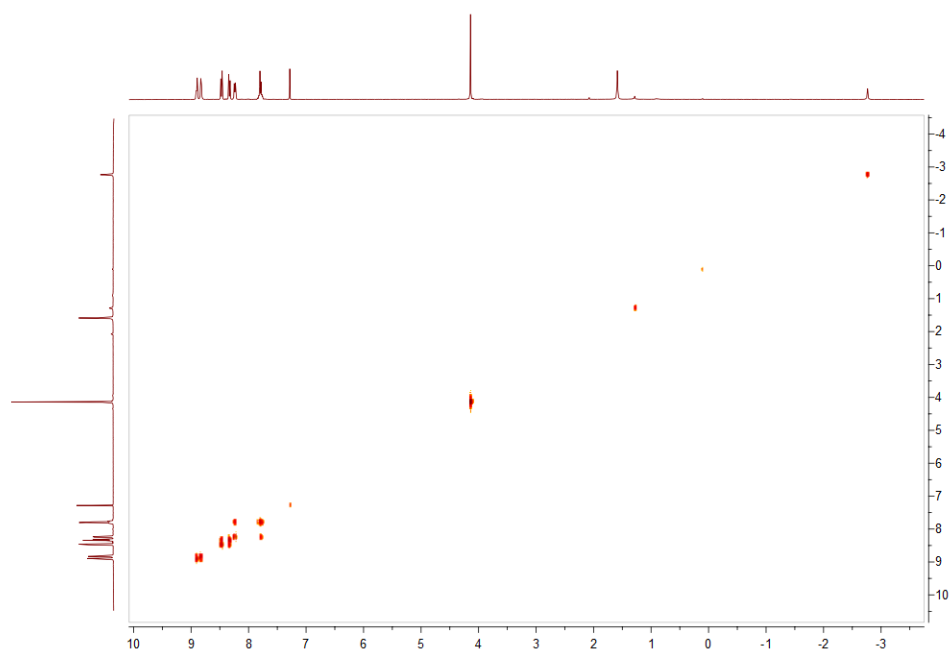
^{13}C NMR (91 MHz, CDCl_3) δ 167.33 (s, $\text{C}^{49,52}$), 146.93 (d, $J = 2.2$ Hz, $\text{C}^{1,11,14,23}$), 146.91 (d, $J = 2.2$ Hz, $\text{C}^{4,8,17,20}$), 141.93 (d, $J = 2.2$ Hz, $\text{C}^{7,19}$), 141.91 (d, $J = 2.2$ Hz, $\text{C}^{28,36}$), 134.58 (d, $J = 3.1$ Hz, $\text{C}^{37,38}$), 134.54 (d, $J = 3.1$ Hz, $\text{C}^{25,33}$), 129.63 (s, $\text{C}^{26,30,32,34}$), 127.95 (d, $J = 6.4$ Hz, $\text{C}^{27,29,31,35}$), 127.88 (d, $J = 6.4$ Hz, $\text{C}^{39,43,44,48}$), 126.78 (s, $\text{C}^{41,46}$), 120.81 (d, $J = 17.7$ Hz, $\text{C}^{40,42,45,47}$), 120.62 (d, $J = 17.7$ Hz, $\text{C}^{15,22,2,10}$), 118.96 (d, $J = 16.8$ Hz, $\text{C}^{3,9,16,21}$), 118.77 (d, $J = 16.8$ Hz, $\text{C}^{6,13}$), 52.47 (s, $\text{C}^{51,55}$).



^1H NMR spectrum of 7



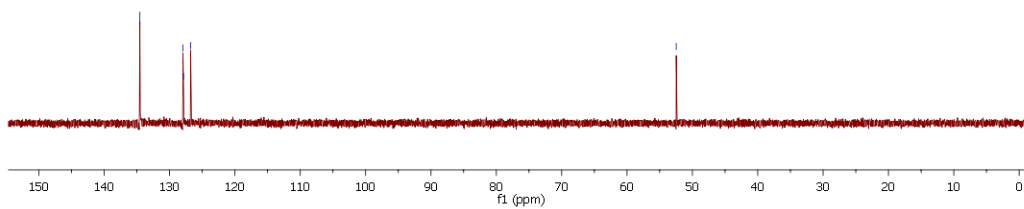
^{13}C NMR spectrum of 7



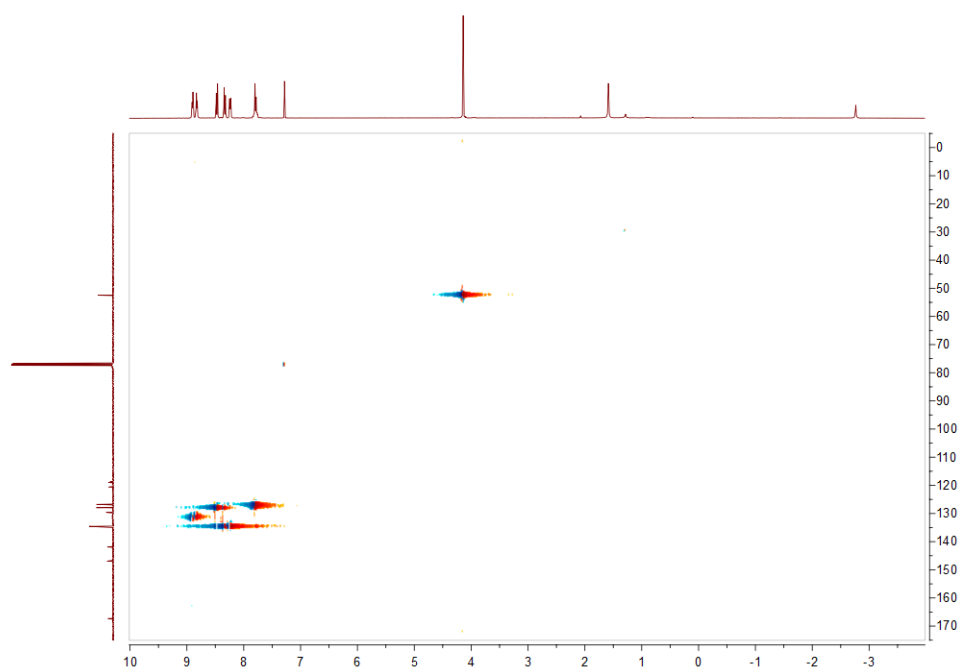
COSY spectrum of 7

134.57
134.54
127.94
127.87
126.77

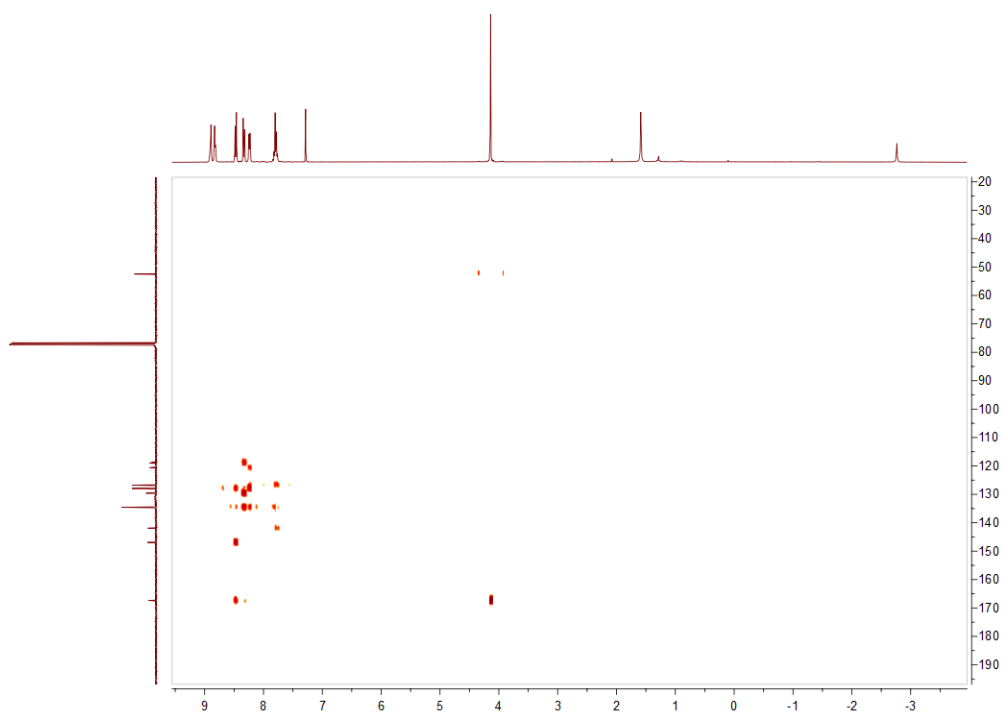
-52.47

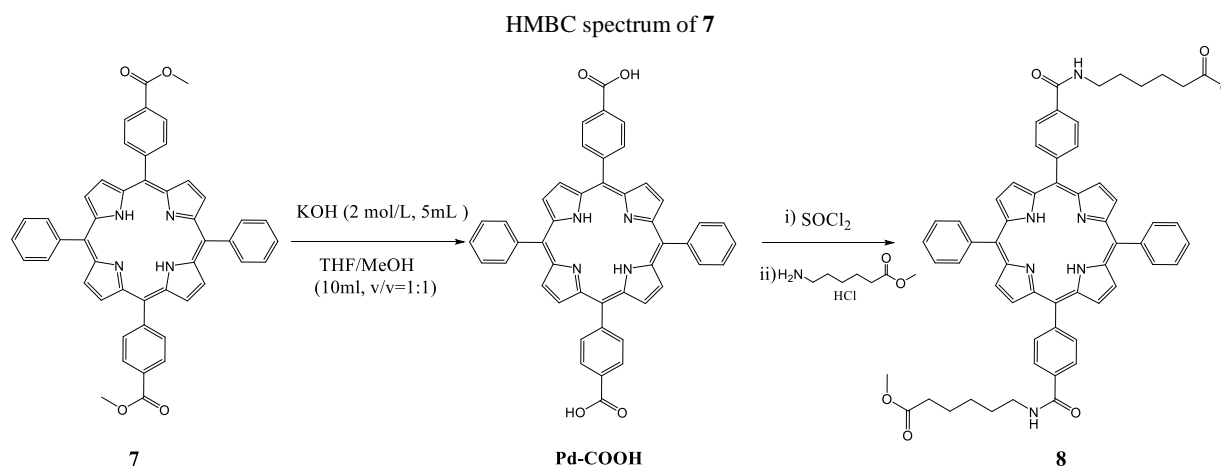


DEPT135 spectrum of 7



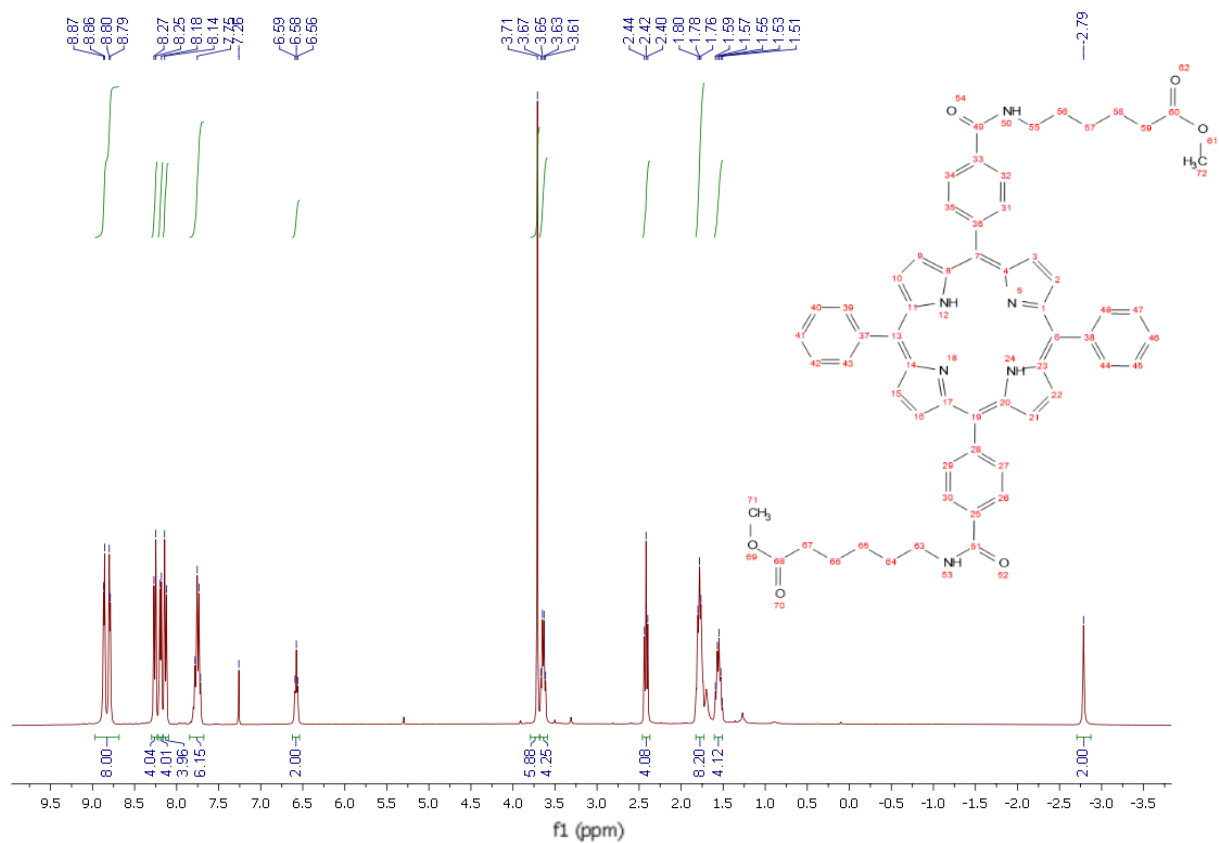
HSQC spectrum of 7



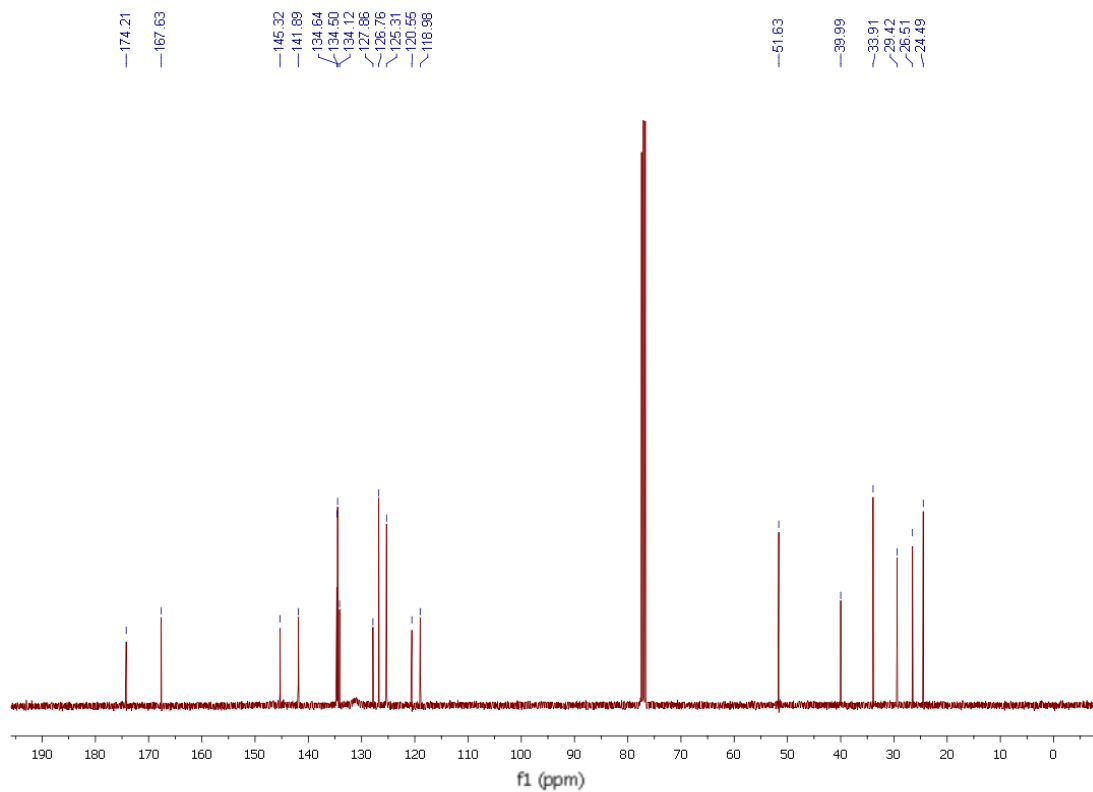


7 (40 mg, 0.055 mmol) was dissolved in 5 mL THF and 5 mL MeOH. KOH solution (2 M, 5 mL) was added to the previous solution refluxing for 6 h. After cooling to room temperature, the mixture was acidified with HCl (2 M) to the pH 2. The compound was collected by filtration to afford a dark-green solid (28 mg, yield 72.8%). Pd-COOH (450 mg, 0.64 mmol) was placed in 100 mL 2-necked flask and 50 mL of benzene were added under N₂ atmosphere. Then 10 mL of thionyl chloride was added to the suspension and refluxed for 5 h with catalytic quantity of dehydrated DMF. After removal of the solvent and redundant thionyl chloride under the reduced pressure, the residue was dissolved in 20 mL dehydrate CH₂Cl₂ and then added to the mixture of methyl 6-aminohexanoate hydrochloride (581 mg, 3.2 mmol) and triethylamine (323 mg, 3.2 mmol) which were previously dissolved in 20 mL CH₂Cl₂. After removal of the solvents under reduced pressure, the resulting mixture was purified by silica gel column chromatography with CH₂Cl₂ / MeOH, 100:1 v/v as eluent mixture, to afford the molecule **8** as a purple solid (436 mg, 71.1%).

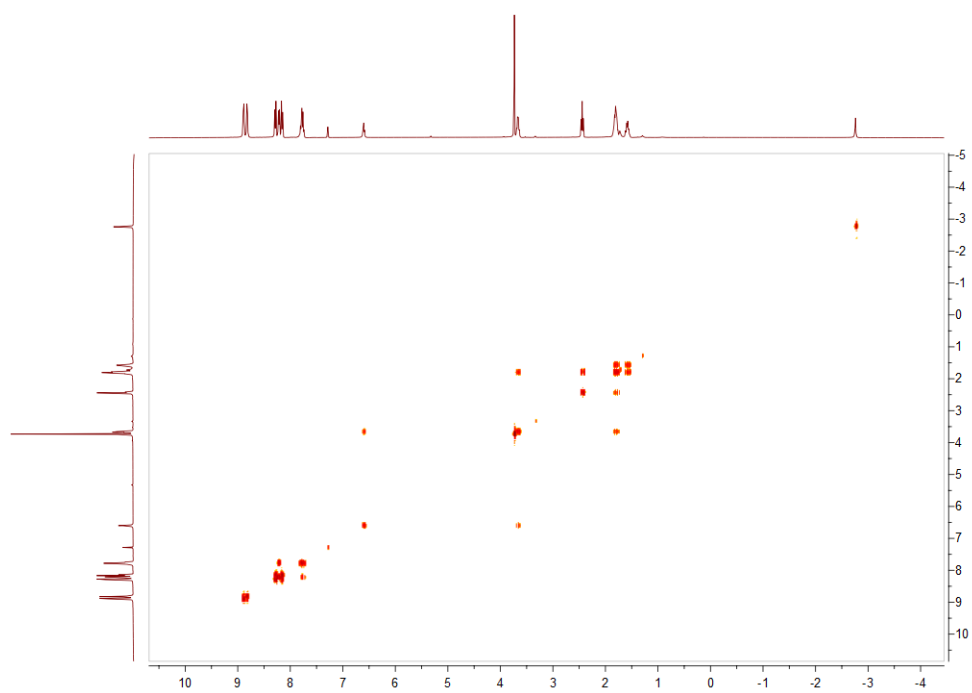
¹H NMR (360 MHz, CDCl₃) δ 8.83 (dd, J = 24.8, 4.6 Hz, 8H, H^{2,3,9,10,15,16,21,22}), 8.26 (d, J = 7.9 Hz, 4H, H^{27,29,31,35}), 8.19 (d, J = 6.8 Hz, 4H, H^{26,30,32,34}), 8.13 (d, J = 7.9 Hz, 4H, H^{40,42,45,47}), 7.85 – 7.68 (m, 6H, H^{39,41,43,44,46,48}), 6.58 (t, J = 5.6 Hz, 2H, H^{50,53}), 3.71 (s, 6H, H^{71,72}), 3.64 (dd, J = 13.0, 6.6 Hz, 4H, H^{55,63}), 2.42 (t, J = 7.3 Hz, 4H, H^{59,67}), 1.82 – 1.73 (m, 8H, H^{56,58,64,66}), 1.56 (dd, J = 15.2, 8.1 Hz, 4H, H^{57,65}), -2.79 (s, 2H, H^{12,24}). ¹³C NMR (91 MHz, CDCl₃) δ 174.21 (s, C^{60,68}), 167.63 (s, C^{49,51}), 145.32 (s, C^{1,11,14,23,4,8,17,20}), 141.89 (s^{7,19,28,36}), 134.57 (d, J = 12.5 Hz, C^{37,38}), 134.12 (s, C^{25,33}), 127.86 (s, C^{26,30,32,34}), 126.76 (s, C^{41,46}), 125.31 (s, C^{40,42,45,47}), 120.55 (s^{C15,22,2,10}), 118.98 (s, C^{3,9,16,21,6,13}), 51.63 (s, C^{71,72}), 39.99 (s, C^{55,63}), 33.91 (s, C^{59,67}), 29.42 (s, C^{56,64}), 26.51 (s, C^{57,65}), 24.49 (s, C^{58,66}). MS-ESI (*m/z*): [M]⁺ Calcd. for C₆₀H₅₆N₆O₆⁺ 957.4, found 957.4



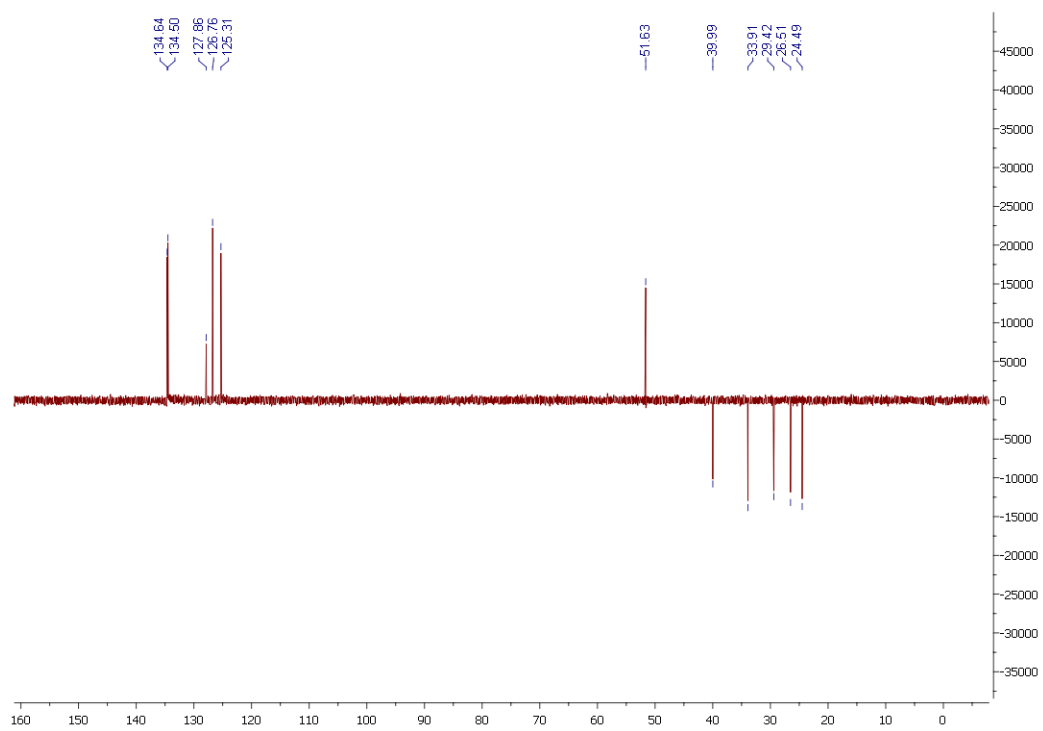
¹H NMR spectrum of 8



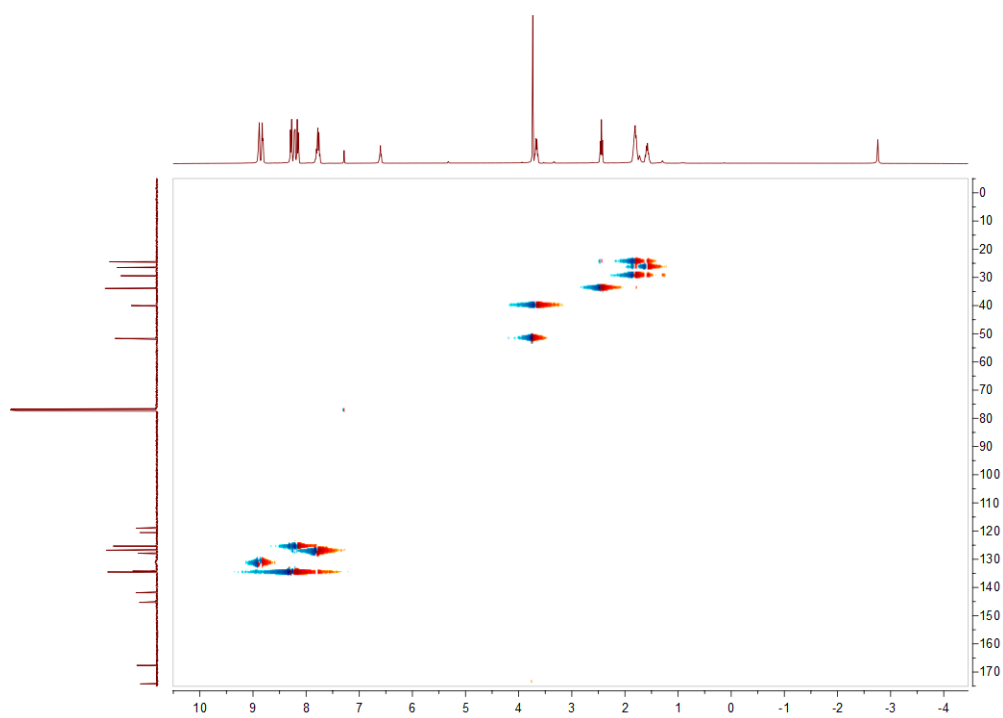
^{13}C NMR spectrum of **8**



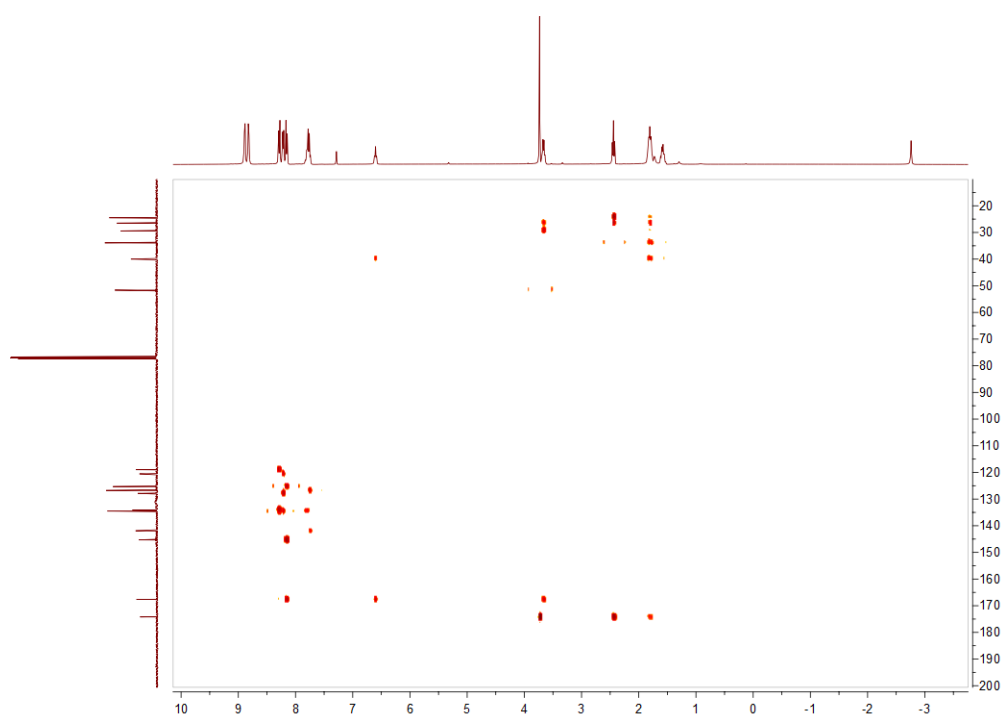
COSY spectrum of **8**



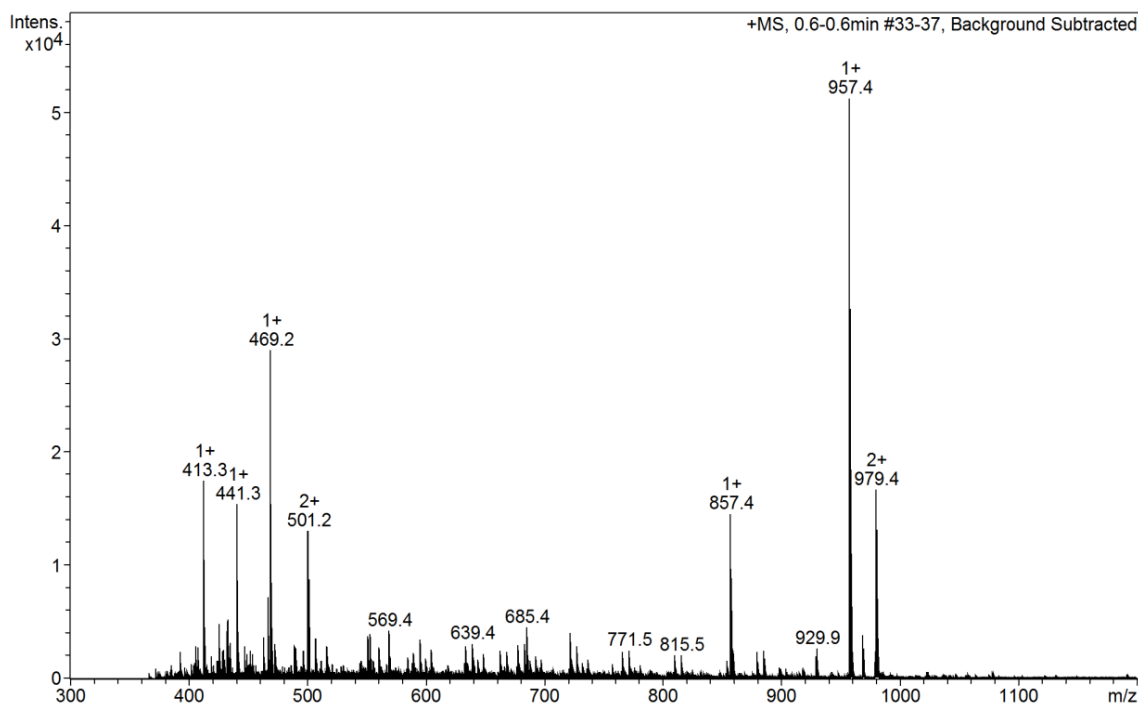
DEPT135 spectrum of **8**



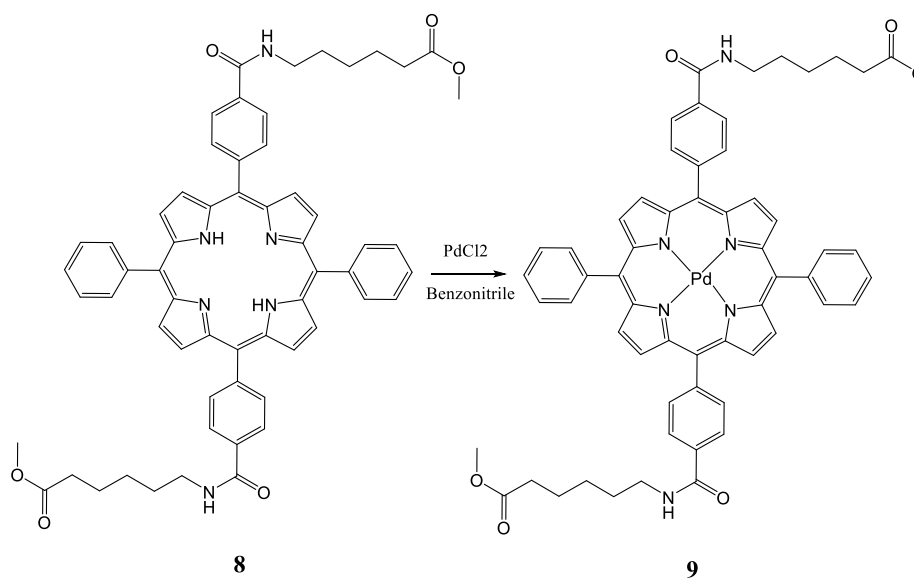
HSQC spectrum of **8**



HMBC spectrum of **8**

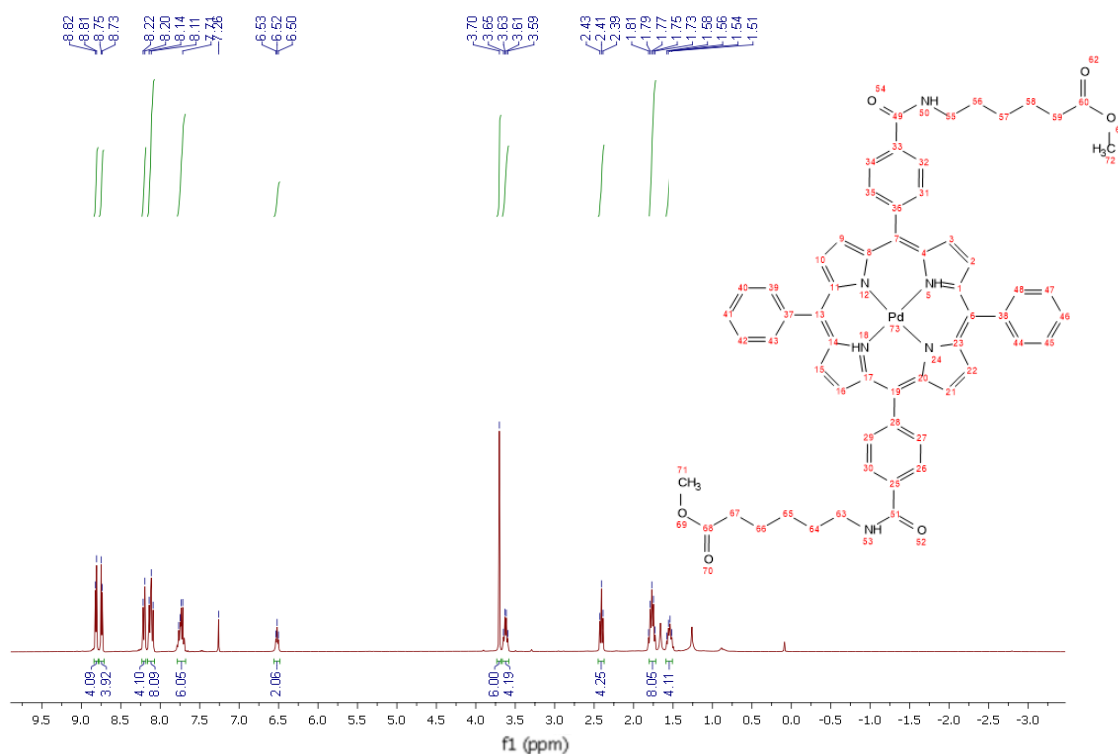


Mass spectrometry of **8**

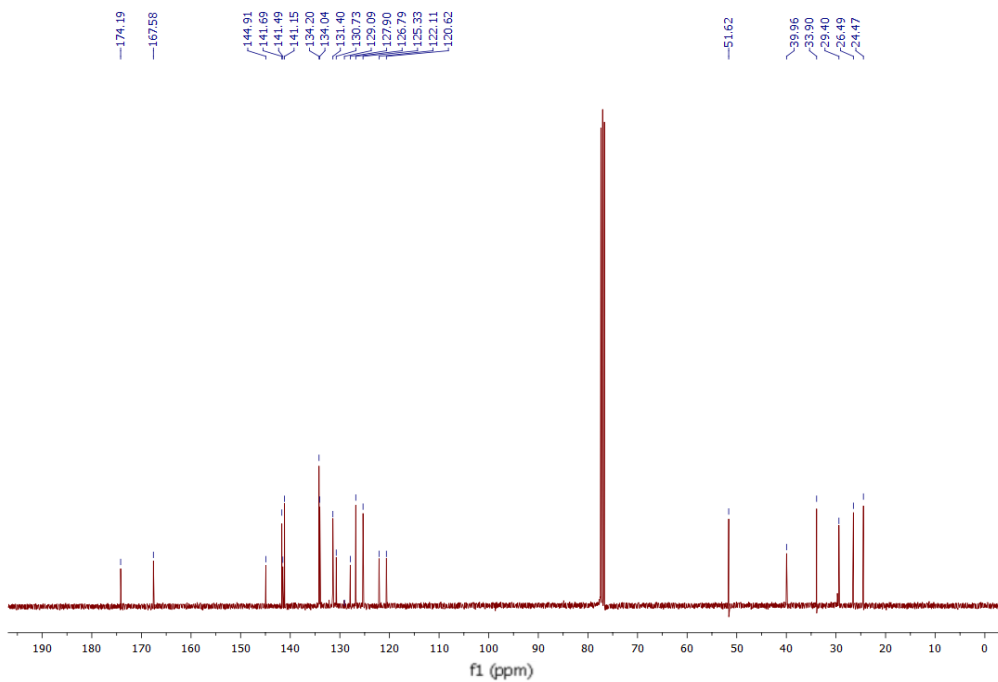


8 (70 mg, 0.073 mmol) and PdCl₂ (16 mg, 0.087 mmol) were dissolved in benzonitrile (30 mL) and refluxed for 4.5 h. After removal of the solvents under reduced pressure, the residue was purified by column chromatography on a silica gel using CH₂Cl₂ / MeOH, 100:1 v/v as eluent mixture, to obtain the molecule **9** (56 mg, 0.064 mmol, 72.2%) as an orange solid.

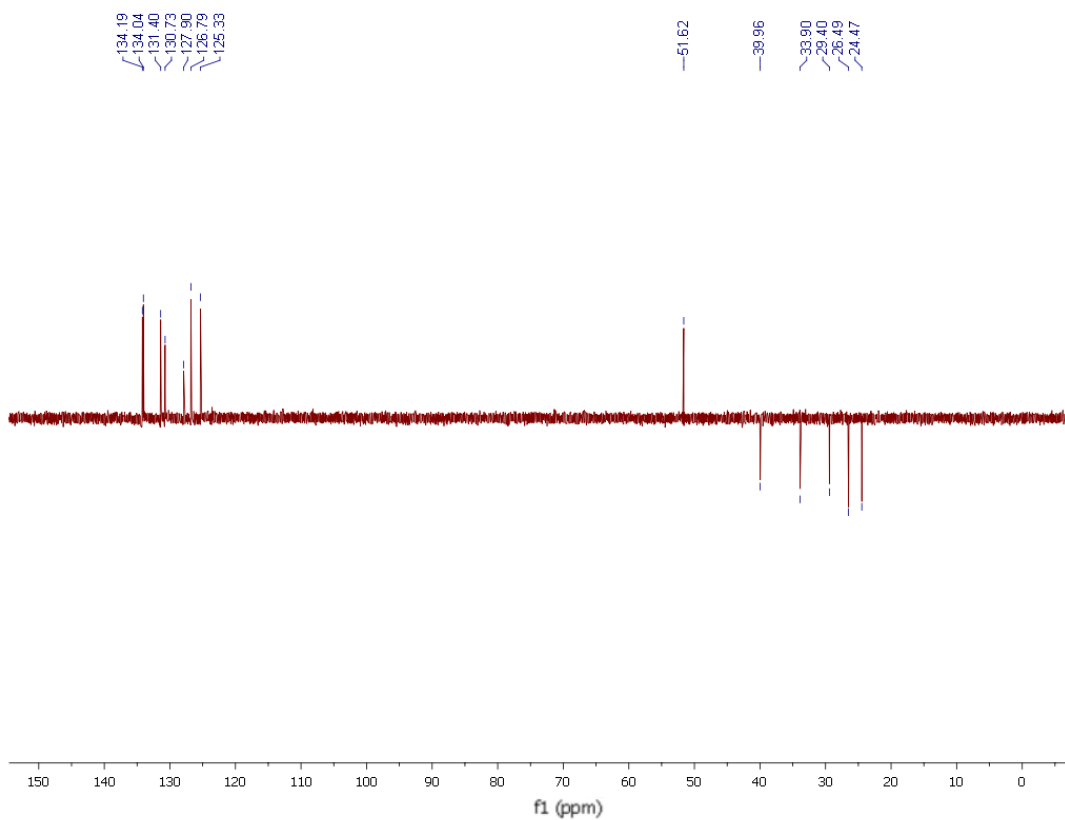
^1H NMR (360 MHz, CDCl_3) δ 8.81 (d, $J = 5.0$ Hz, 4H, $\text{H}^{2,3,9,10}$), 8.74 (d, $J = 5.0$ Hz, 4H, $\text{H}^{15,16,21,22}$), 8.21 (d, $J = 8.1$ Hz, 4H, $\text{H}^{26,30,32,34}$), 8.11 (t, $J = 9.1$ Hz, 8H, $\text{H}^{26,30,32,34,40,42,45,47}$), 7.74 (dd, $J = 11.4, 7.2$ Hz, 6H, $\text{H}^{39,41,43,44,46,48}$), 6.52 (t, $J = 5.7$ Hz, 2H, $\text{H}^{50,53}$), 3.70 (s, 6H, $\text{H}^{71,72}$), 3.62 (dd, $J = 13.0, 6.6$ Hz, 4H, $\text{H}^{55,63}$), 2.41 (t, $J = 7.3$ Hz, 4H, $\text{H}^{59,67}$), 1.76 (dd, $J = 14.9, 7.4$ Hz, 8H, $\text{H}^{56,58,64,66}$), 1.55 (dd, $J = 15.2, 8.3$ Hz, 4H, $\text{H}^{57,65}$). ^{13}C NMR (91 MHz, CDCl_3) δ 174.19 (s, $\text{C}^{60,68}$), 167.58 (s, $\text{C}^{49,51}$), 144.91 (s, $\text{C}^{1,11,14,23}$), 141.69 (s, $\text{C}^{4,8,17,20}$), 141.49 (s, $\text{C}^{28,36}$), 141.15 (s, $\text{C}^{37,38}$), 134.20 (s, $\text{C}^{15,22,2,10}$), 134.04 (s, $\text{C}^{26,30,32,34}$), 131.40 (s, $\text{C}^{41,46}$), 130.73 (s, $\text{C}^{40,42,45,47}$), 129.09 (s, $\text{C}^{25,33}$), 127.90 (s, $\text{C}^{3,9,16,21}$), 126.79 (s, $\text{C}^{29,27,31,35}$), 125.33 (s, $\text{C}^{3,9,16,21}$), 122.11 (s, $\text{C}^{7,19}$), 120.62 (s, $\text{C}^{6,13}$), 51.62 (s, $\text{C}^{71,72}$), 39.96 (s, $\text{C}^{55,63}$), 33.90 (s, $\text{C}^{59,67}$), 29.41 (s, $\text{C}^{56,64}$), 26.49 (s, $\text{C}^{57,65}$), 24.47 (s, $\text{C}^{58,66}$). DEPT135 (91 MHz, CDCl_3) δ 134.19 (s, $\text{C}^{15,22,2,10}$), 134.04 (s, $\text{C}^{26,30,32,34}$), 131.40 (s, $\text{C}^{41,46}$), 130.73 (s, $\text{C}^{40,42,45,47}$), 127.90 (s, $\text{C}^{3,9,16,21}$), 126.79 (s, $\text{C}^{29,27,31,35}$), 125.33 (s, $\text{C}^{3,9,16,21}$), 51.62 (s, $\text{C}^{71,72}$), 39.96 (s, $\text{C}^{55,63}$), 33.90 (s, $\text{C}^{59,67}$), 29.41 (s, $\text{C}^{56,64}$), 26.49 (s, $\text{C}^{57,65}$), 24.47 (s, $\text{C}^{58,66}$).



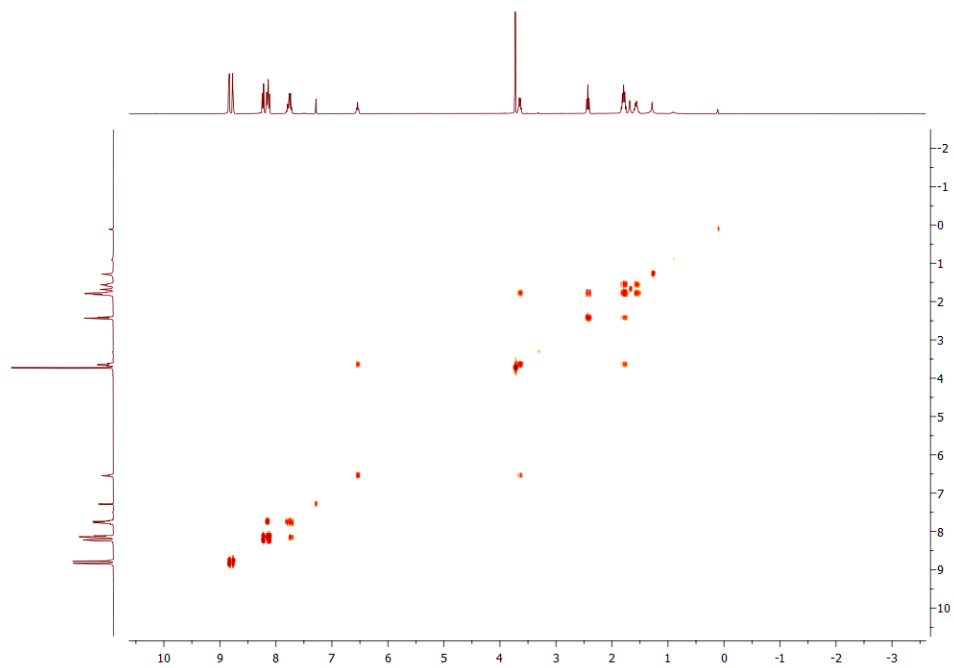
^1H NMR spectrum of **9**



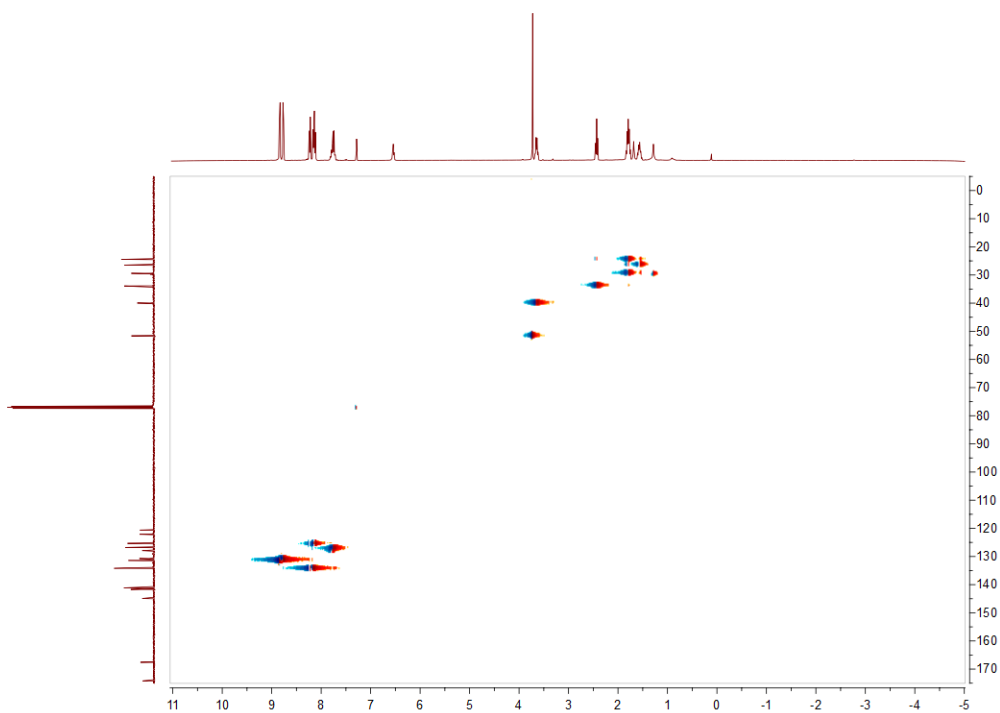
13C NMR spectrum of 9



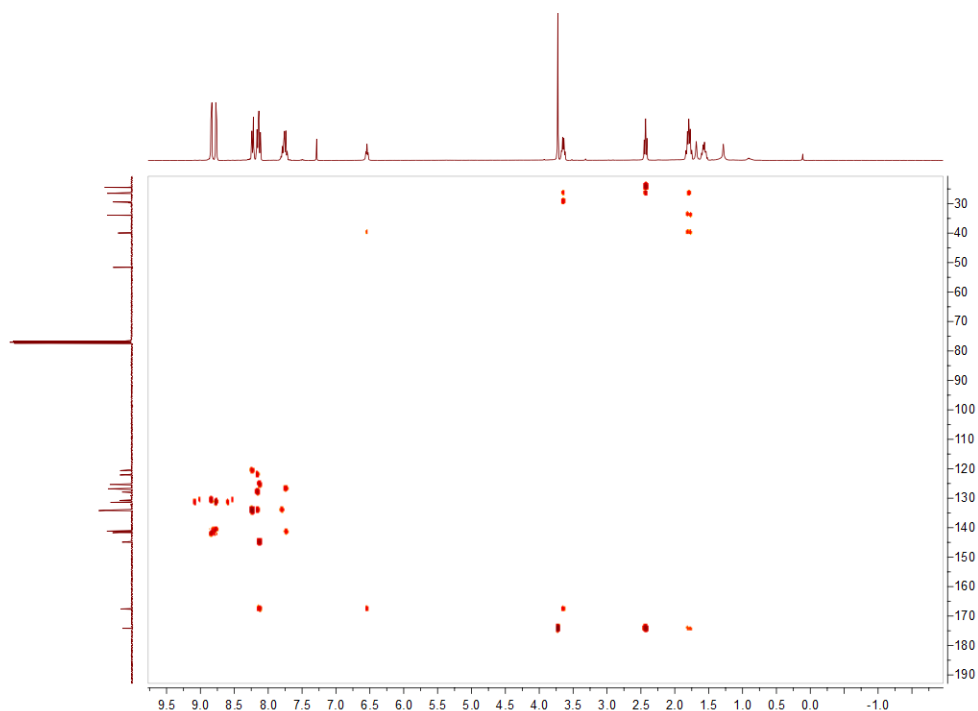
DEPT135 spectrum of 9



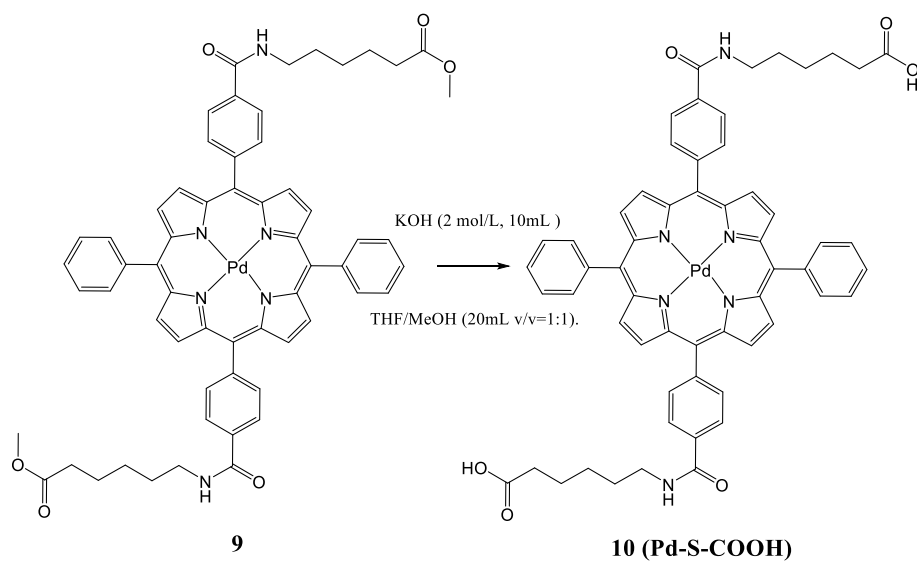
COSY spectrum of **9**



HSQC spectrum of **9**



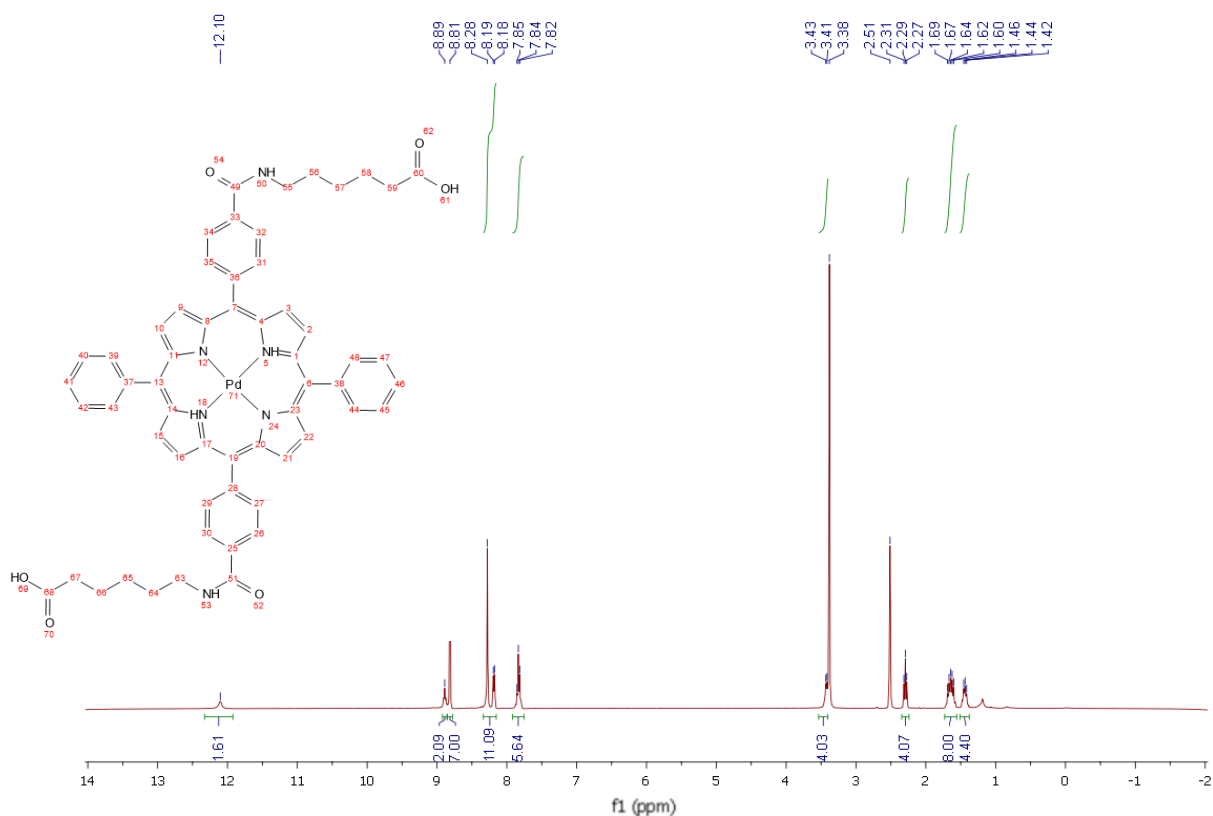
HMBC spectrum of **9**



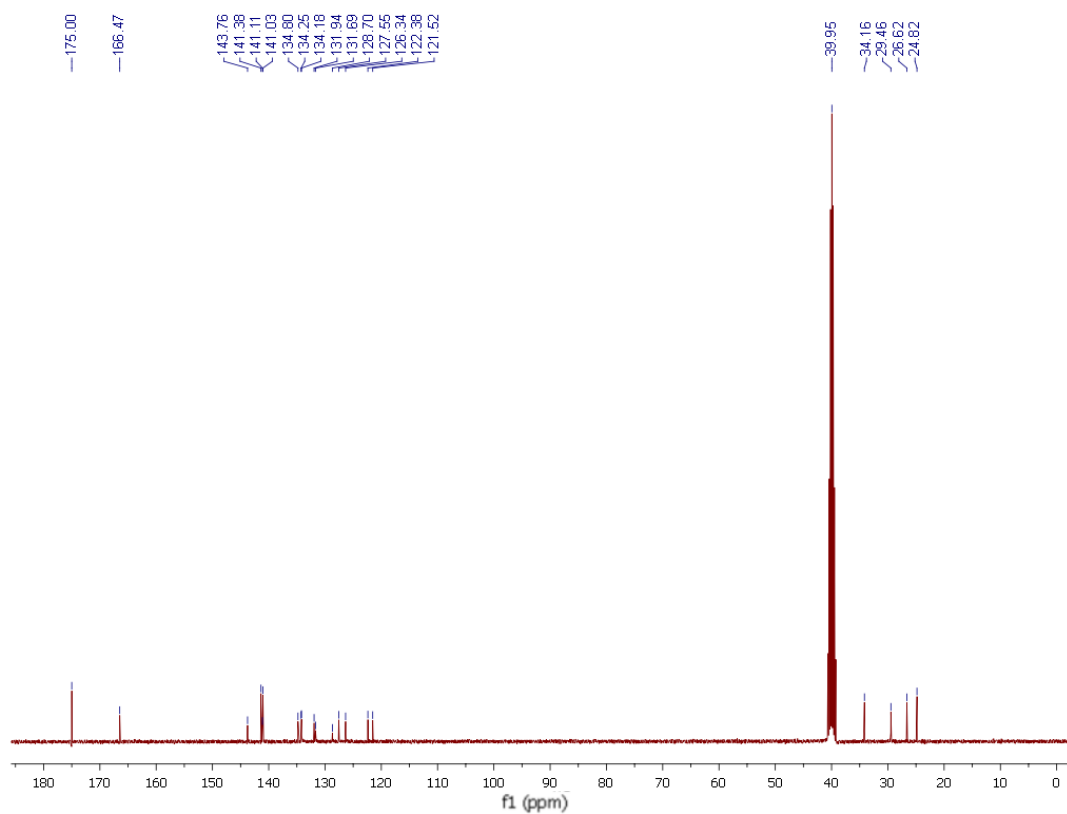
9 (56 mg, 0.053 mmol) was dissolved in 10 mL of THF and 10 mL of MeOH. Potassium hydroxide solution (2 mol/L, 10 mL) was added to the previous solution refluxing for 5 h. After cooling to room temperature, the mixture was acidified with HCl (1 mol/L) to pH 7. The compound was collected by filtration to afford the molecule **10** as an orange solid (50 mg, yield 91.7%).

$^1\text{H NMR}$ (360 MHz, $(\text{CD}_3)_2\text{SO}$) δ 12.10 (s, 2H, $\text{H}^{61,69}$), 8.89 (s, 2H, $\text{H}^{50,53}$), 8.81 (s, 7H, Ar-H), 8.34 – 8.15 (m, 11H, Ar-H), 7.83 (t, $J = 6.9$ Hz, 6H, $\text{H}^{39,41,43,44,46,48}$), 3.42 (d, $J = 6.2$ Hz, 4H,

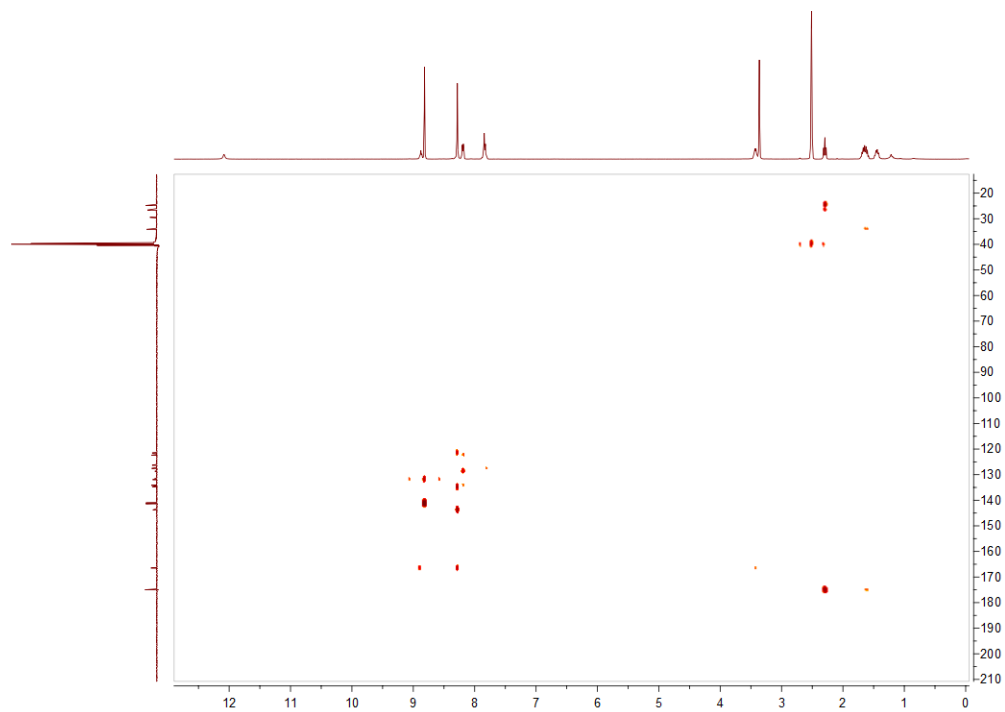
H^{55,63}), 2.29 (t, J = 7.3 Hz, 4H, H^{59,67}), 1.73 – 1.56 (m, 8H, H^{56,58,64,66}), 1.51 – 1.38 (m, 4H, H^{57,65}). ¹³C NMR (91 MHz, (CD₃)₂SO) δ 175.00 (s, C^{60,68}), 166.47 (s, C^{49,51}), 143.76 (s, C^{1,11,14,23}) 141.38 (s, C^{4,8,17,20}), 141.11 (s, C^{28,36}), 141.03 (s, C^{37,38}) 134.80 (s, C^{25,33}), 134.25 (s, C^{26,30,32,34}), 131.81 (s, C^{41,46}), 131.94 (s, C^{40,42,45,47}) 131.69 (s, C^{15,22,2,10}), 128.70 (s, C^{3,9,16,21}), 127.55 (s, C^{29,27,31,35}), 126.34 (s, C^{3,9,16,21}), 122.38 (s, C^{7,19}), 121.52 (s, C^{6,13}), 39.95 (s, C^{55,63}), 34.16 (s, C^{59,67}), 29.46 (s, C^{56,64}), 26.62 (s, C^{57,65}), 24.82 (s, C^{58,66}). MS-ESI (*m/z*): [M]⁺ Calc. for C₅₈H₅₀N₆O₆Pd⁻ 1031.3, found 1031.3



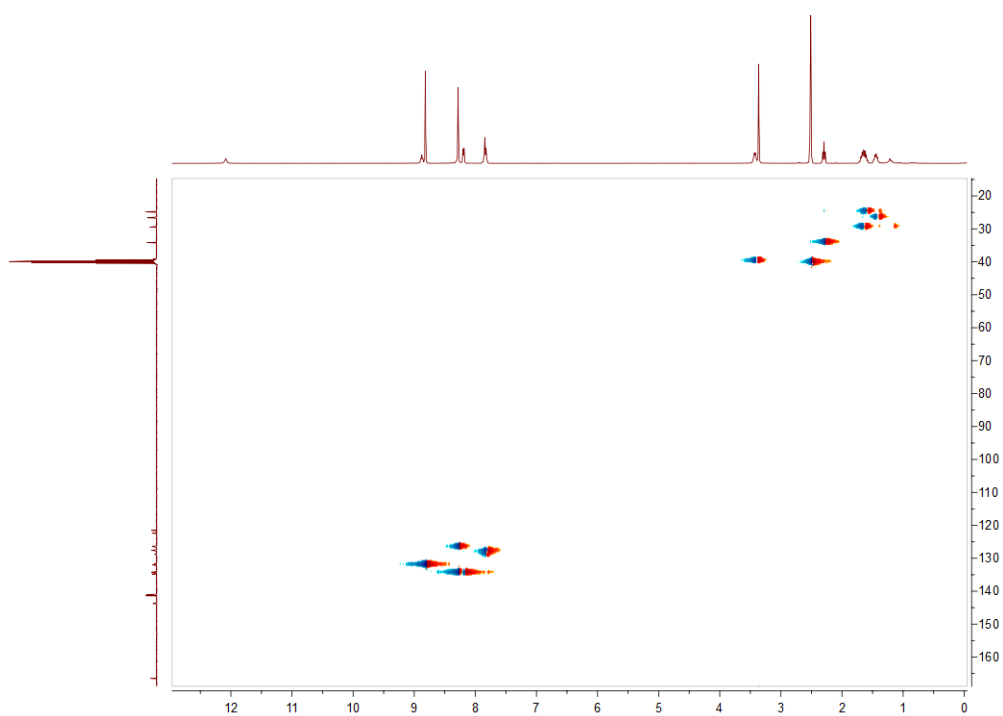
¹H NMR spectrum of **10**



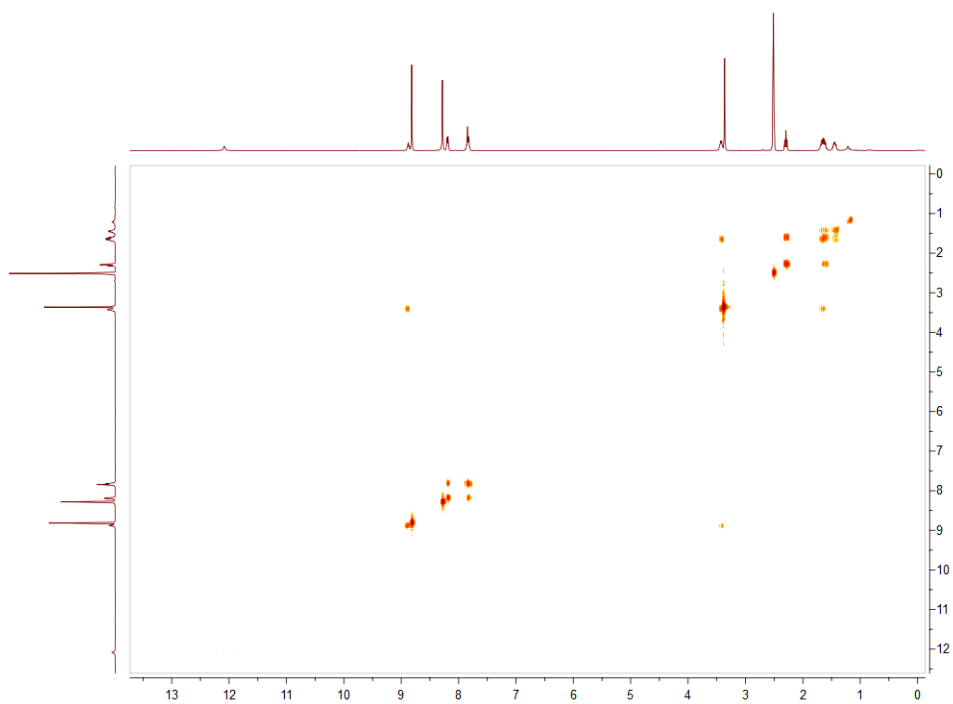
^{13}C NMR spectrum of **10**



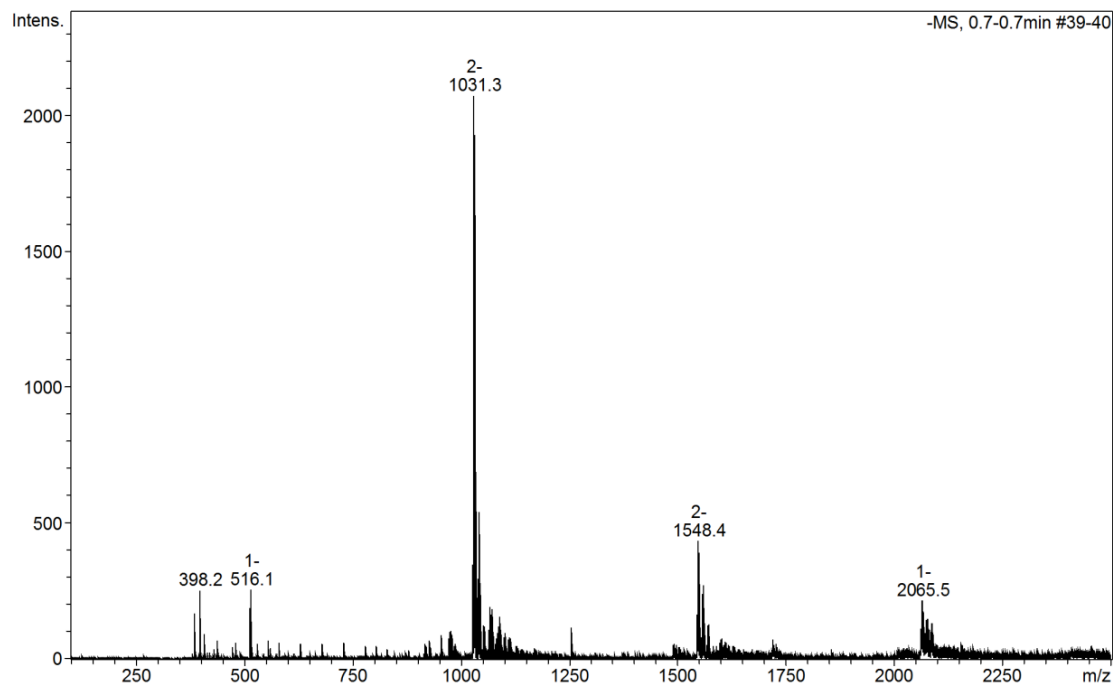
HMBC spectrum of **10**



HSQC spectrum of **10**

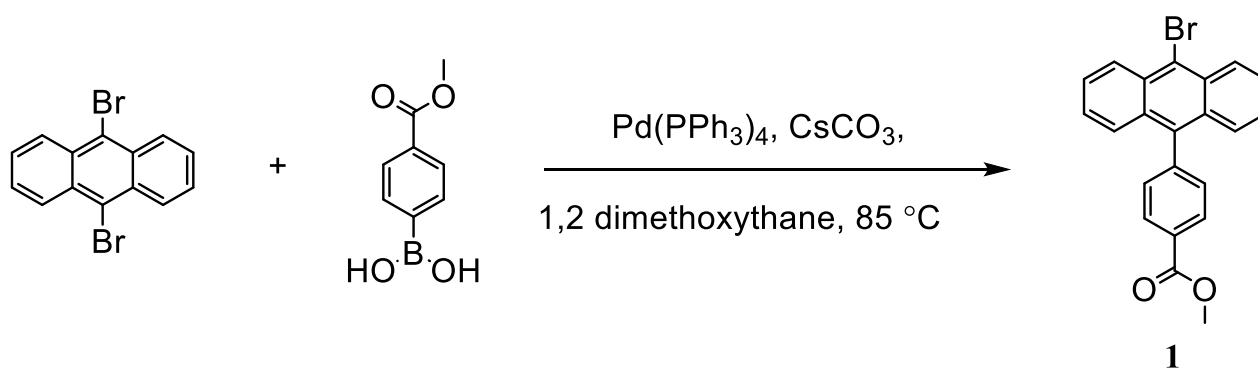


COSY spectrum of **10**



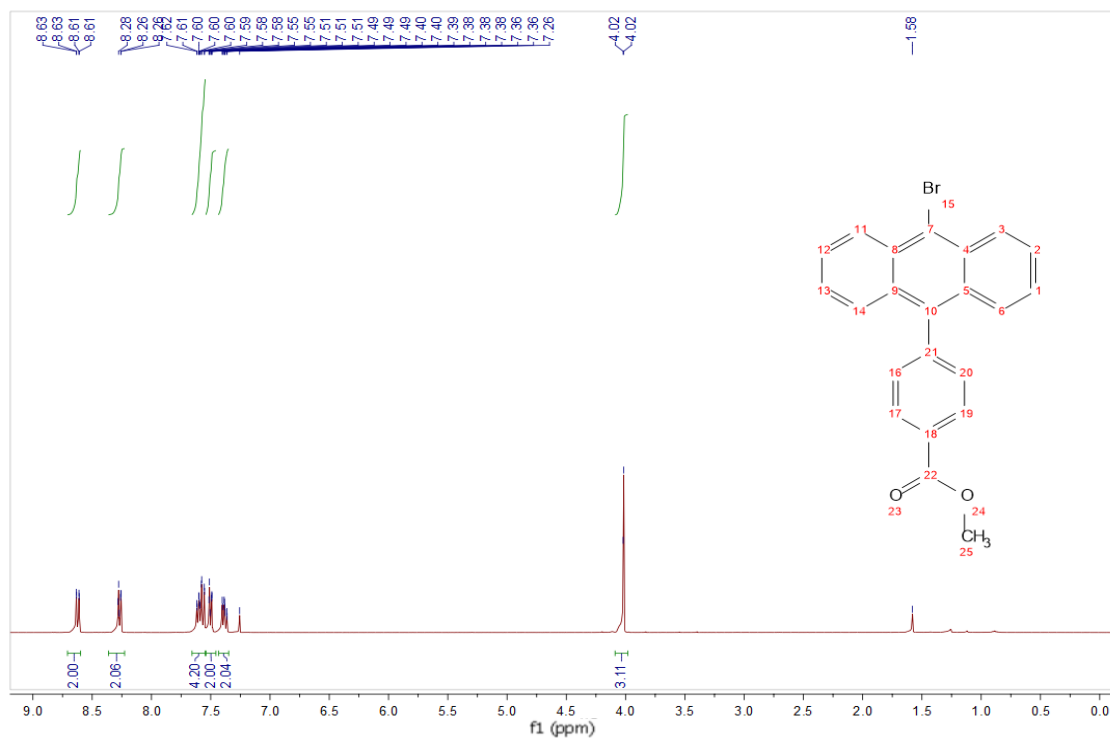
Mass spectrometry of **10**

Section 1. Synthetic procedure and characterization

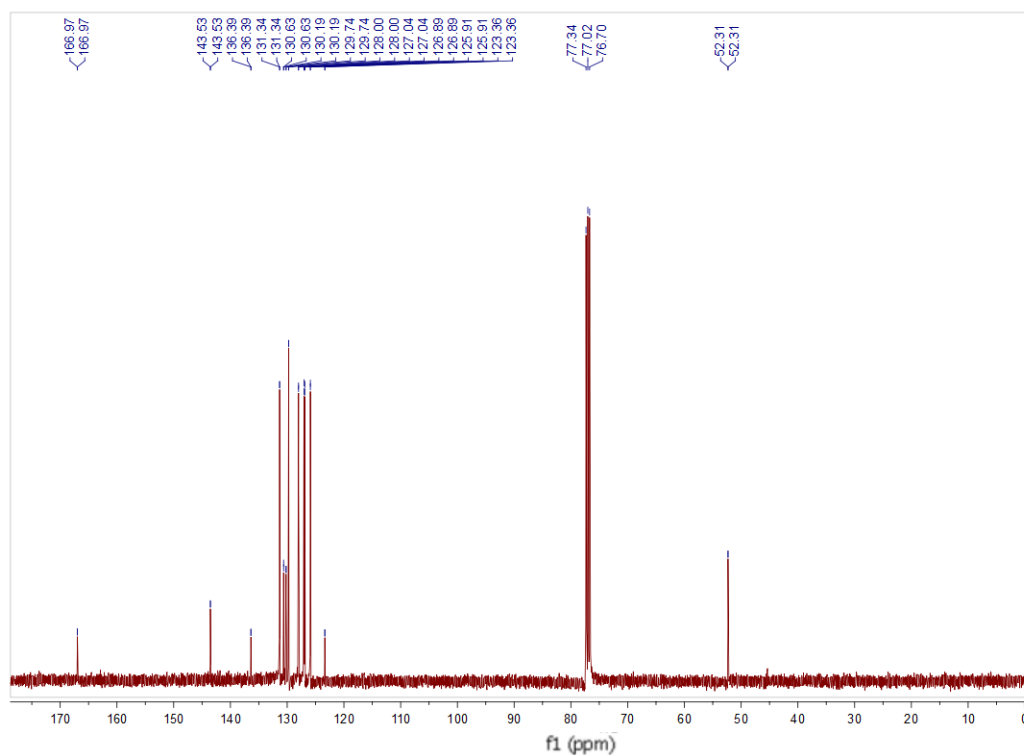


The mixture of 9,10-dibromoanthracene (4.0 g, 11.90 mmol), (4 - (methoxycarbonyl) phenyl) boronic acid (0.85 g, 4.76 mmol), CsCO_3 (4.0 g, 11.90 mmol) and a catalytic amount of $\text{Pd}(\text{PPh}_3)_4$ (192 mg, 0.016 mmol) were dissolved in 250 mL 1,2 dimethoxyethane. The reaction was heated to $85\text{ }^\circ\text{C}$ for 22 h under N_2 atmosphere. The crude product was purified by column chromatography using $\text{CHCl}_3/\text{Hexane} = 8/2$ to afford yellowish solid **1** (1.5 g, 45.7 %).

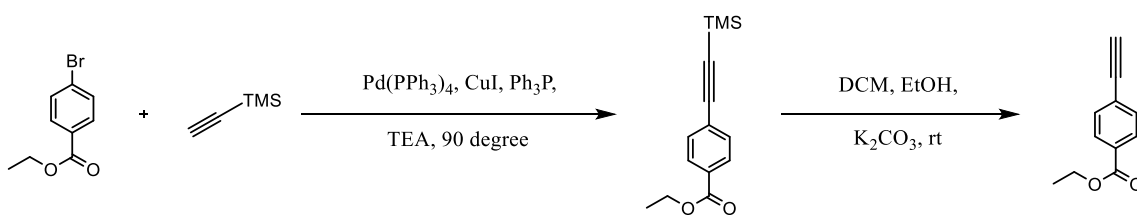
$^1\text{H NMR}$ (400 MHz, CDCl_3) δ 8.62 (d, $J = 8.9, 0.7\text{ Hz}$, 2H, $\text{H}^{3,11}$), 8.36 – 8.23 (m, 2H, $\text{H}^{6,14}$), 7.66 – 7.55 (m, 4H, $\text{H}^{16,17,19,20}$), 7.54 – 7.46 (m, 2H, $\text{H}^{2,12}$), 7.38 (m, $J = 8.8, 6.5, 1.1\text{ Hz}$, 2H, $\text{H}^{1,13}$), 4.02 (s, $J = 1.8\text{ Hz}$, 3H, H^{25}).



¹H NMR spectrum of **1**

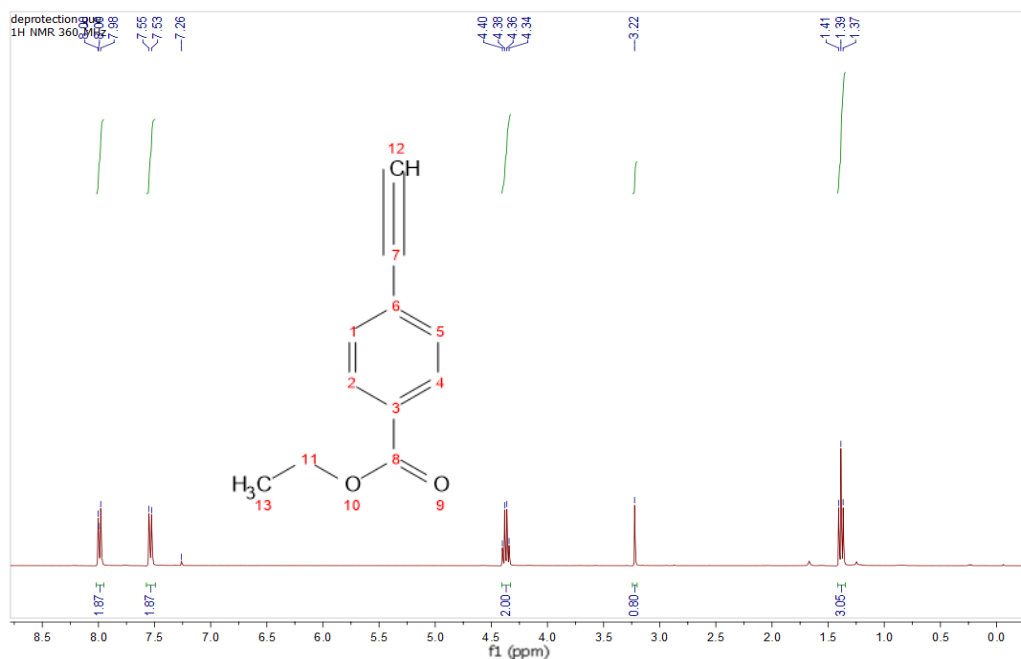


¹³C NMR spectrum of **1**

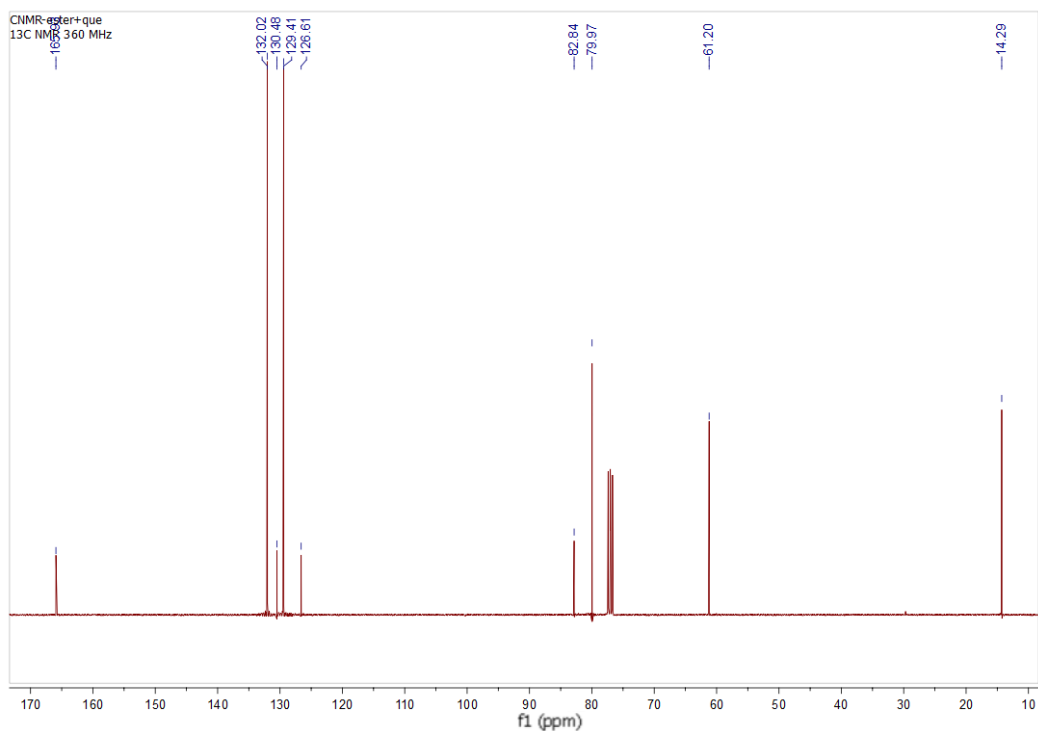


A mixture of ethyl 4-bromobenzoate (2.01 g, 8.77 mmol, 1.0 equiv), Pd(PPh₃)₄ (504 mg, 0.44 mmol, 0.05 equiv.), CuI (83 mg, 0.44 mmol, 0.05 equiv.) and PPh₃ (137 mg, 0.53 mmol, 0.06 equiv.) was dissolved in triethylamine (60 ml) under argon. Ethynyltrimethylsilane (1.03 g 10.49 mmol, 1.2 equiv) was added and the reaction mixture was heated at 90 °C for 17 hr. After cooling to rt, the mixture was filtered through CELITE and evaporated to dryness. To a solution of K₂CO₃ (2.33 g, 16.8 mmol, 2.0 equiv.) in EtOH/DCM (50 mL/10 mL) mixture ethyl-4-((trimethylsilyl)ethynyl)benzoate (2.08 g, 8.4 mmol, 1.0 equiv.) was added under argon. The reaction mixture was stirred for 4 h at rt, then filtered and evaporated to dryness. The crude was purified by flash chromatography to afford 1.27 g (86.7%). R_f = 0.40 (hexanes:DCM = 1:1).

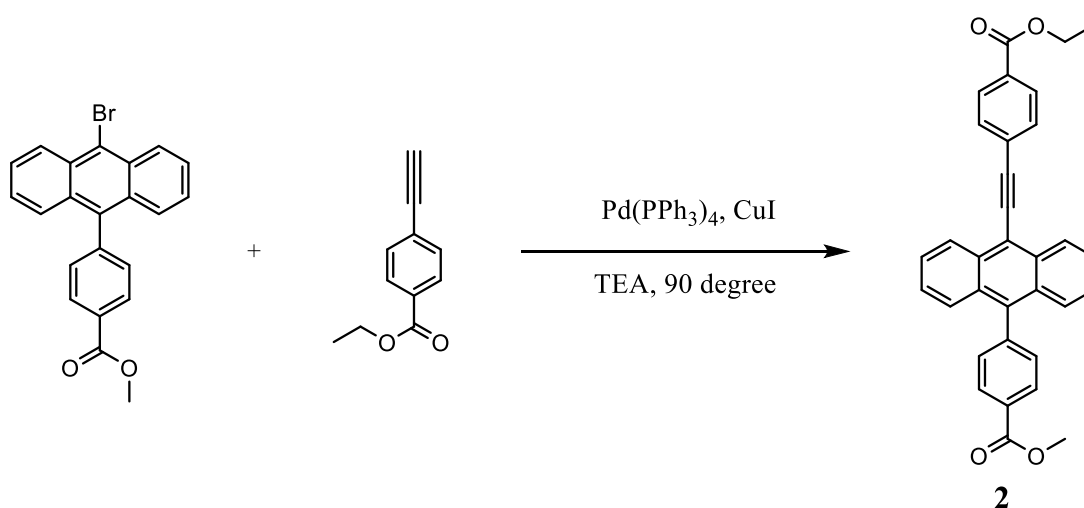
¹H NMR (360 MHz, CDCl₃) δ = 8.02 – 7.95 (m, 2H, H^{2,4}), 7.54 (d, J=8.3, 2H, H^{1,5}), 4.37 (q, J=7.1, 2H, H¹¹), 3.22 (s, 1H, H¹²), 1.39 (t, J=7.1, 3H, H¹³). ¹³C NMR (91 MHz, CDCl₃) δ = 165.93 (s, C⁸), 132.02 (s, C^{1,5}), 130.48 (s, C³), 129.41 (s, C^{2,4}), 126.61 (s, C⁶), 82.84 (s, C⁷), 79.97 (s, C¹²), 61.20 (s, C⁷⁷), 14.29 (s, C¹³)



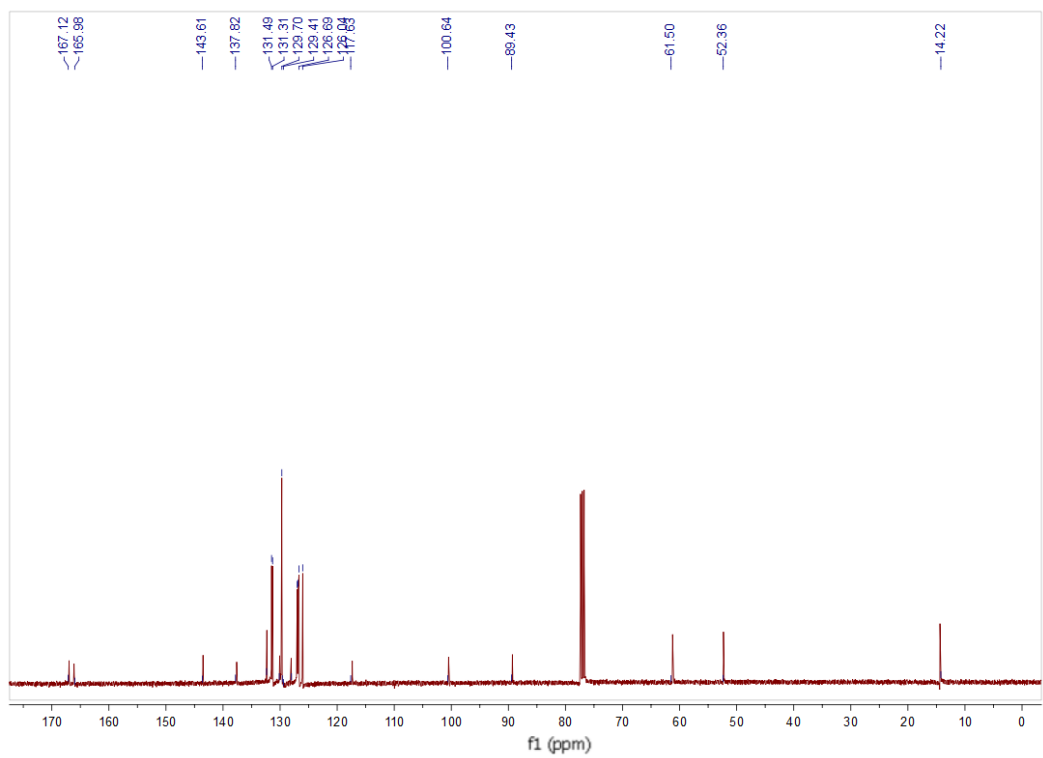
¹H NMR spectrum of ethyl 4-ethynylbenzoate



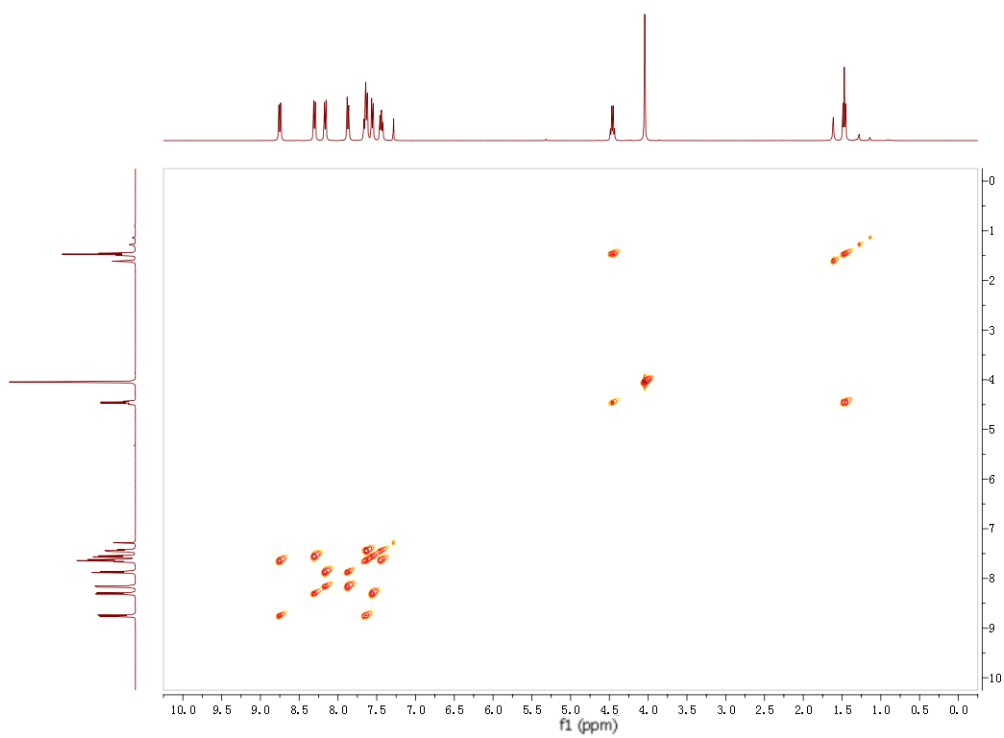
¹³C NMR spectrum of ethyl 4-ethynylbenzoate



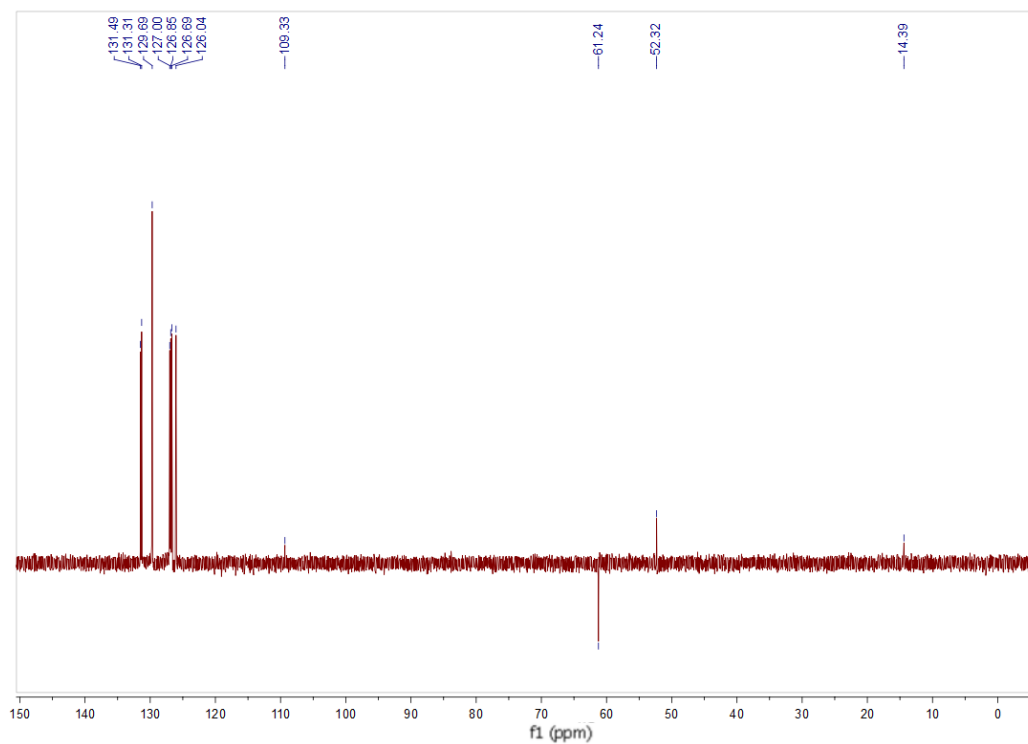
1 (1.5 g, 3.84 mmol), ethyl 4-ethynylbenzoate (0.855 g, 5.34 mmol), Pd(PPh₃)₄ (250 mg, 0.22 mmol) and CuI (55 mg, 0.28 mmol) were mixed in 60 mL THF and 60 mL di-isopropyl amine with N₂ protection. The reaction was refluxed for 24h. The solvent was removed and the reaction mixture was washed with H₂O and CHCl₃. The organic phase was dried, evaporated under vacuum and finally purified by column chromatography (hexane:DCM = 2:1) to afford **2** ([4-((10-(4-carboxyphenyl)anthracene-9-yl)ethynyl)benzoate) as a pale yellow solid. The solid was recrystallized from hot acetone. Yield: 1.3 g (73%).



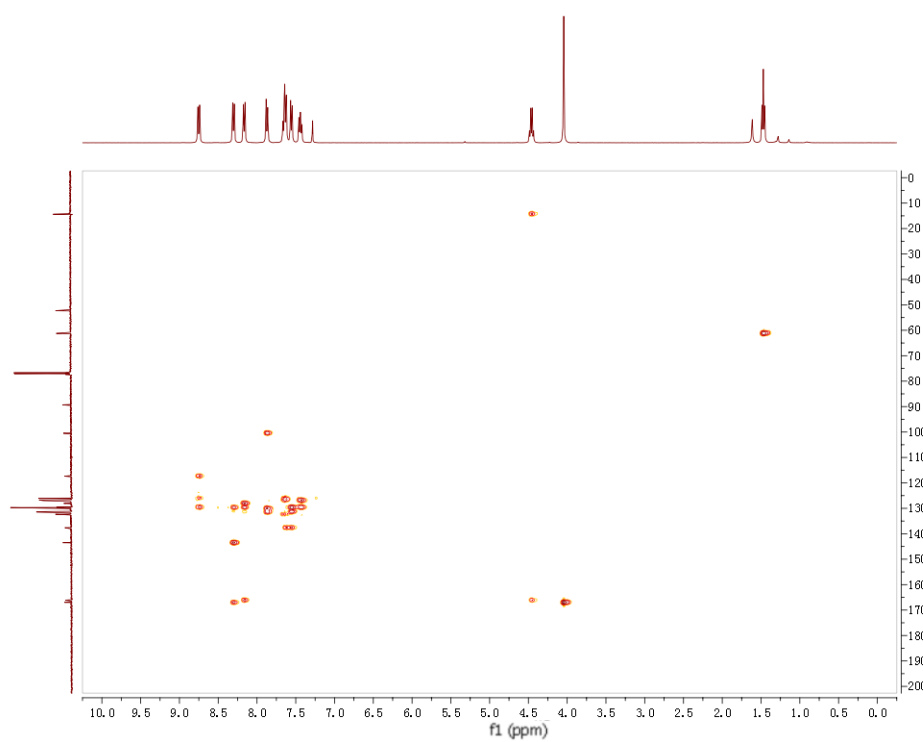
^{13}C NMR spectrum of **2**



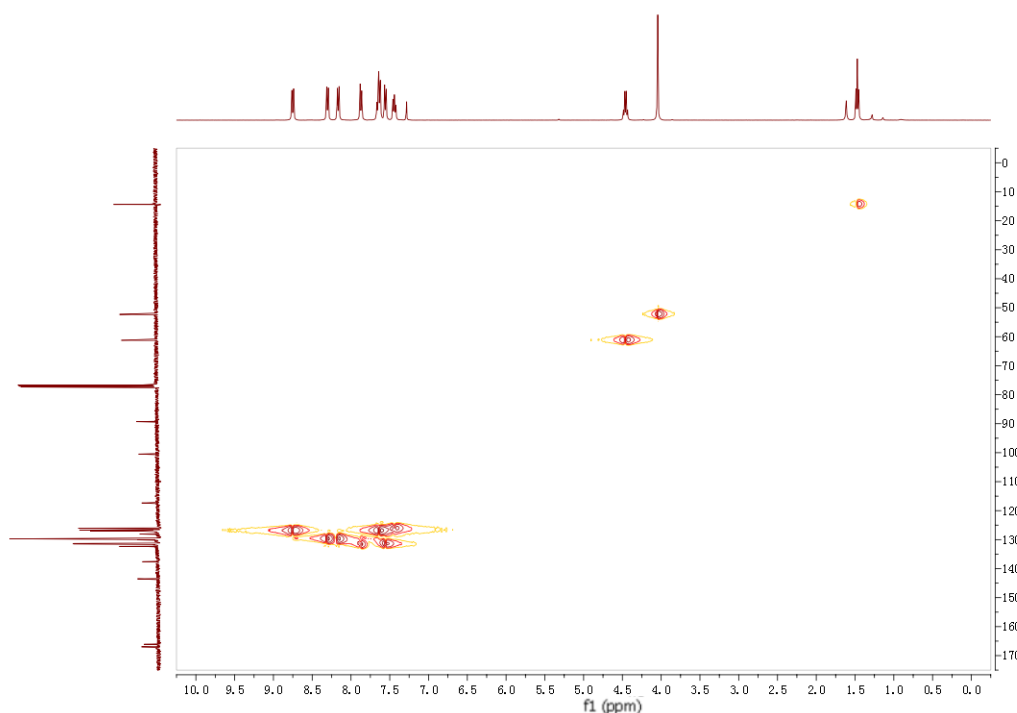
COSY spectrum of **2**



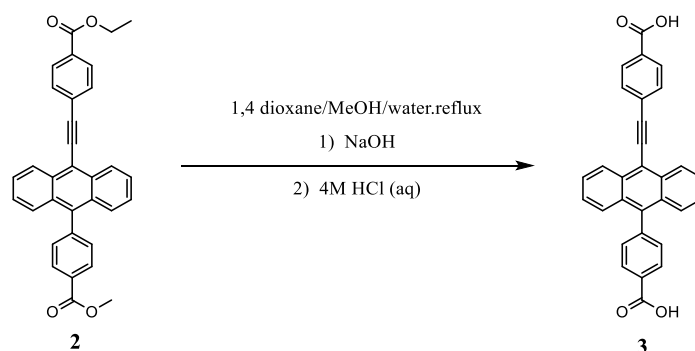
DEPT135 spectrum of **2**



HSQC spectrum of **2**



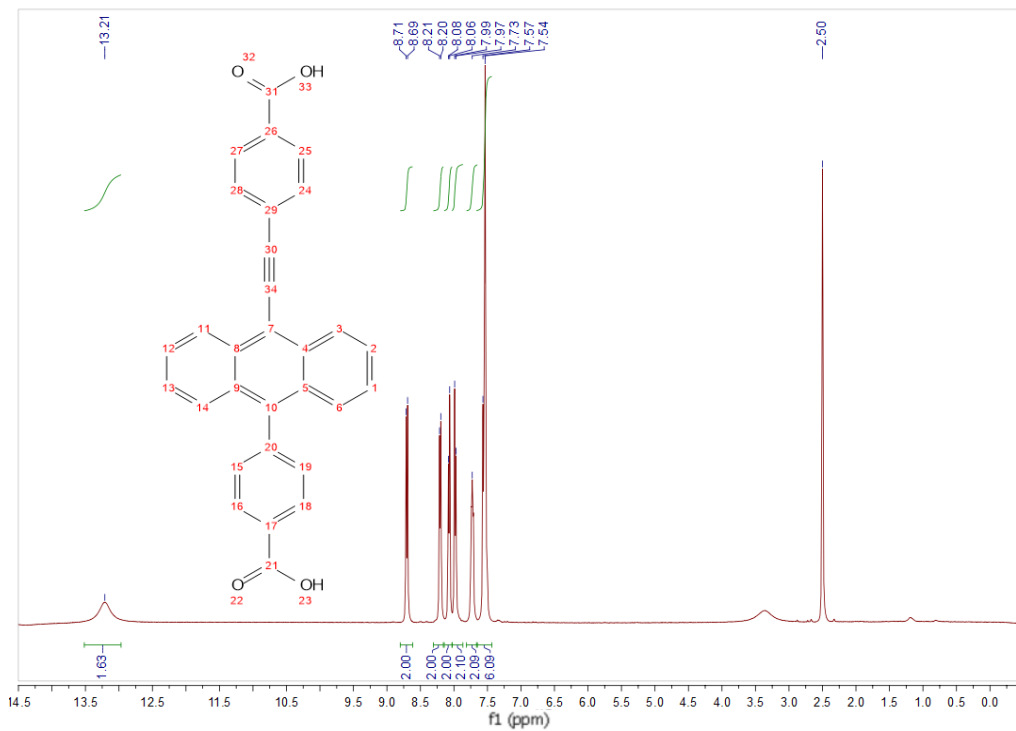
HMBC spectrum of **2**



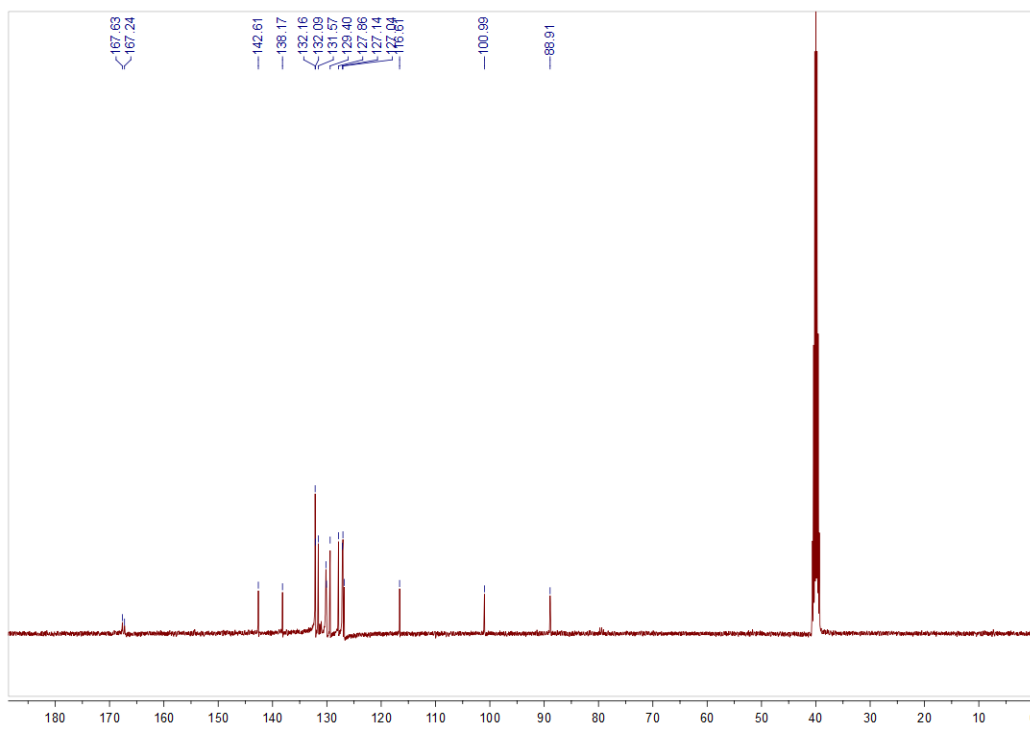
2 ((10-(4-carboxyphenyl)anthracene-9-yl)ethynyl)benzoate (1.0 g, 2.12 mmol) was suspended in 100 mL 1,4- dioxane/MeOH/water (v:v = 2:5:3) in a 250 mL flask. NaOH (8.0 mg, 200 mmol) was added and refluxed for 10 h at 60 °C. The reaction was monitored by TLC and when starting material was completely consumed, the pH value was adjusted to pH 2 by adding 2 M HCl. Yellowish precipitate **3** was collected by filtration. Yield: 0.85 mg (91.0%).

^1H NMR (400 MHz, $(\text{CD}_3)_2\text{SO}$): δ 13.21 (s, 2H, $\text{H}^{23,33}$), 8.70 (d, $J = 8.6$ Hz, 2H, $\text{H}^{6,14}$), 8.21 (d, $J = 7.4$ Hz, 2H, $\text{H}^{3,11}$), 8.07 (d, $J = 7.5$ Hz, 2H, $\text{H}^{16,18}$), 7.98 (d, $J = 7.6$ Hz, 2H, $\text{H}^{25,27}$), 7.73 (s, 2H, $\text{H}^{15,19}$), 7.55 (d, $J = 12.7$ Hz, 6H, $\text{H}^{1,2,12,13,24,28}$).

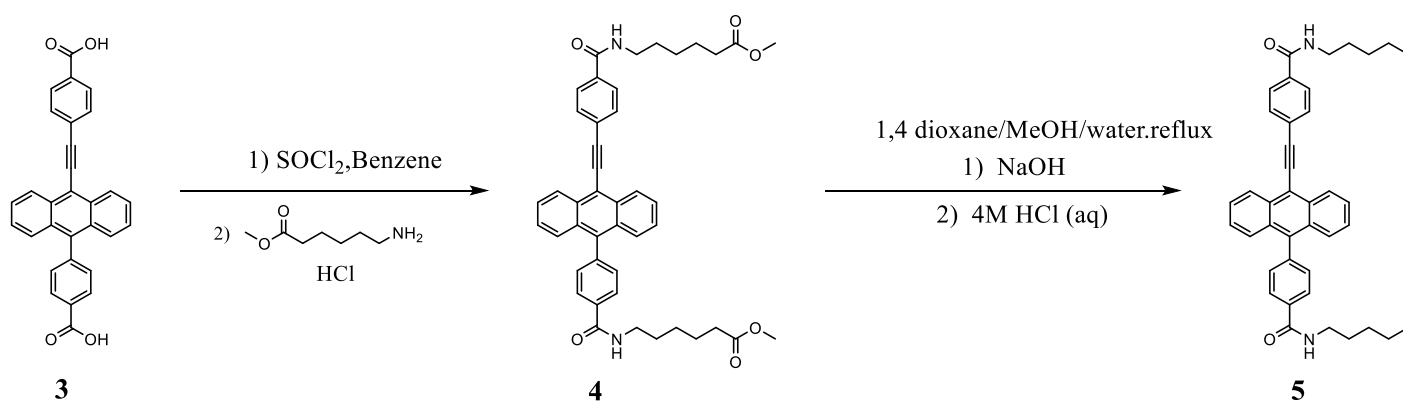
^{13}C NMR (101 MHz, DMSO) δ 167.63, 167.22, 142.61, 138.16, 132.15, 132.09, 131.57, 131.30, 131.02, 130.17, 130.07, 129.39, 127.86, 127.14, 127.04, 126.81, 116.61, 100.99, 88.91.



$^1\text{H NMR}$ spectrum of 3



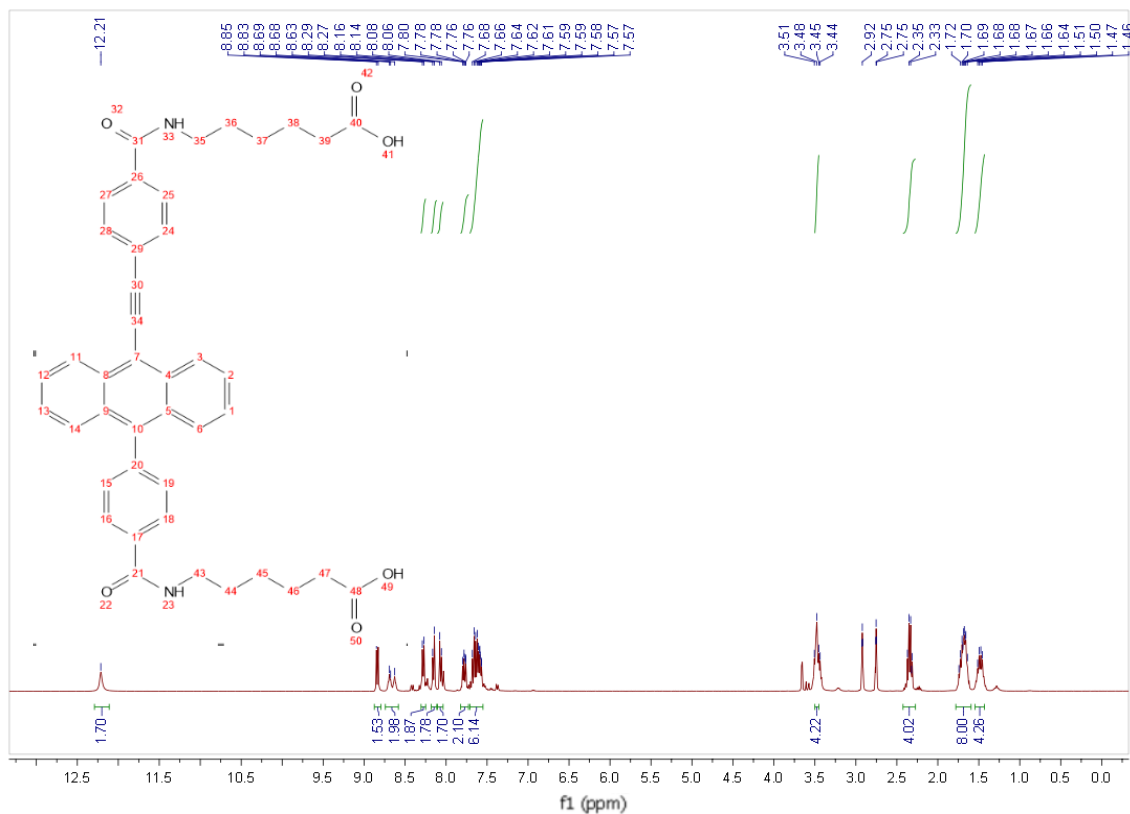
$^{13}\text{C NMR}$ spectrum of 3



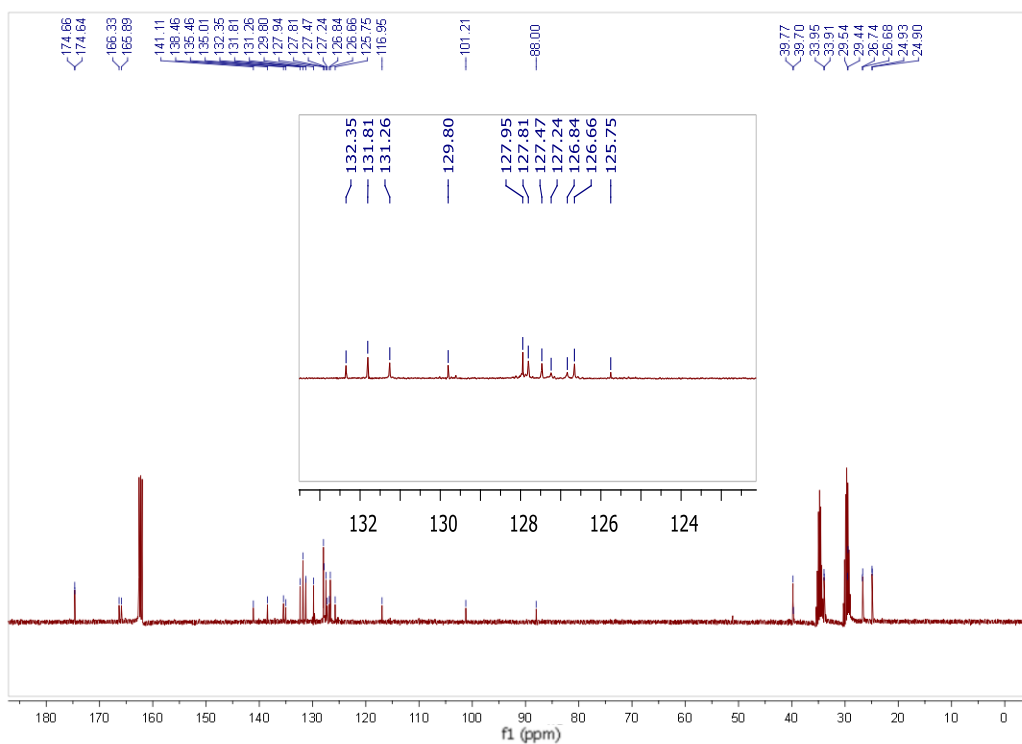
3 (70 mg, 0.167 mmol) was placed in 10 mL 2-necked flask and benzene (5 mL) was added under N₂ atmosphere. Then thionyl chloride was added to the suspension and refluxed for 5 h with catalytic amount of dehydrated DMF. After removing the redundant thionyl chloride and benzene, the residue was redispersed by anhydrous CH₂Cl₂ and used directly for the next step affording white solid **4** (85 mg, 75.9%). The **4** (85 mg, 0.13 mmol) was suspended in MeOH (15 mL). 1,4-dioxane (15 mL) and KOH aqueous (2M, 15 mL). The mixture was refluxed at 60 °C for 20h. After cooling to room temperature, the mixture was adjusted to pH 2 using 4 M hydrochloric acid. The precipitate was collected by filtration, achieving the molecule **5** as white solid after solvent evaporation (72.5 mg, 89.0%).

¹H NMR (400 MHz, *N,N*-dimethyl-formamide-*d*₇): δ 12.21 (s, 2H, H^{41,49}), 8.84 (d, *J* = 8.7 Hz, 2H, H^{6,14}), 8.65 (dd, *J* = 25.4, 5.1 Hz, 2H, H^{23,33}), 8.28 (d, *J* = 8.2 Hz, 2H, H^{3,11}), 8.15 (d, *J* = 8.3 Hz, 2H, H^{16,18}), 8.06 (d, *J* = 8.3 Hz, 2H, H^{25,27}), 7.83 – 7.72 (m, 2H, H^{15,19}), 7.71 – 7.53 (m, 6H, H^{1,2,12,13,24,28}), 3.46 (d, *J* = 9.6 Hz, 4H, H^{35,43}), 2.42 – 2.21 (m, 4H, H^{39,47}), 1.80 – 1.58 (m, 8H, H^{36,38,44,46}), 1.55 – 1.41 (m, 4H, H^{37,45}). ¹³C NMR (101 MHz, *N,N*-dimethyl-formamide-*d*₇): δ 174.66 (s, C⁴⁸), 174.64 (s, C⁴⁰), 166.33 (s, C³¹), 165.89 (s, C²¹), 141.11 (s, C²⁰), 138.46 (s, C¹⁰), 135.46 (s, C¹⁷), 135.01 (s, C²⁵), 132.35 (s, C^{4,8}), 131.81 (s, C^{5,9,15,19}), 131.26 (s, C^{24,28}), 129.80 (s, C^{5,9}), 127.94 (s, C^{2,12}), 127.81 (s, C^{16,18}), 127.47 (s, C^{25,27}), 127.24 (s, C^{1,13}), 126.84 (s, C^{6,14}), 126.66 (s, C^{3,11}), 125.75 (s, C²⁹), 116.95 (s, C⁷), 101.21 (s, C³⁴), 88.00 (s, C³⁰), 39.77 (s, C⁴³), 39.70 (s, C³⁵), 33.95 (s, C⁴⁵), 33.91 (s, C³⁷), 29.54 (s, C⁴⁶), 29.44 (s, C³⁸), 26.74 (s, C⁴⁴), 26.68 (s, C³⁶), 24.93 (s, C⁴⁷), 24.90 (s, C³⁹). DEPT 135 (101 MHz, *N,N*-dimethyl-formamide-*d*₇): δ 131.81 (s, C^{15,19}), 131.26 (s, C^{24,28}), 127.94 (s, C^{2,12}), 127.81 (s, C^{16,18}), 127.47 (s, C^{25,27}), 127.24 (s, C^{1,13}), 126.83 (s, C^{6,14}), 126.66 (s, C^{3,11}), 39.77 (s, C⁴³), 39.70 (s, C³⁵), 33.95 (s, C⁴⁵), 33.91 (s, C³⁷), 29.54 (s, C⁴⁶), 29.44 (s, C³⁸), 26.74 (s, C⁴⁴), 26.68

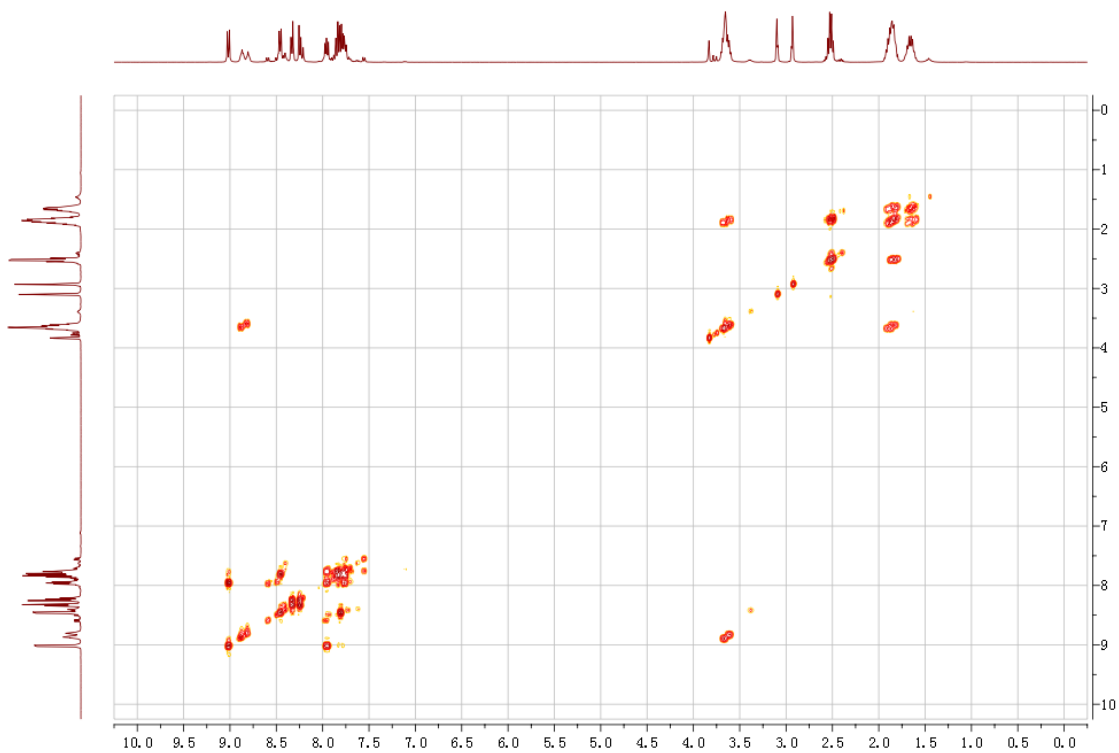
(s, C³⁶), 24.93 (s, C⁴⁷), 24.90 (s, C³⁹). MS-ESI (*m/z*): [M]⁻ Calcd. for C₄₂H₄₀N₂O₆ 667.3, found 667.3

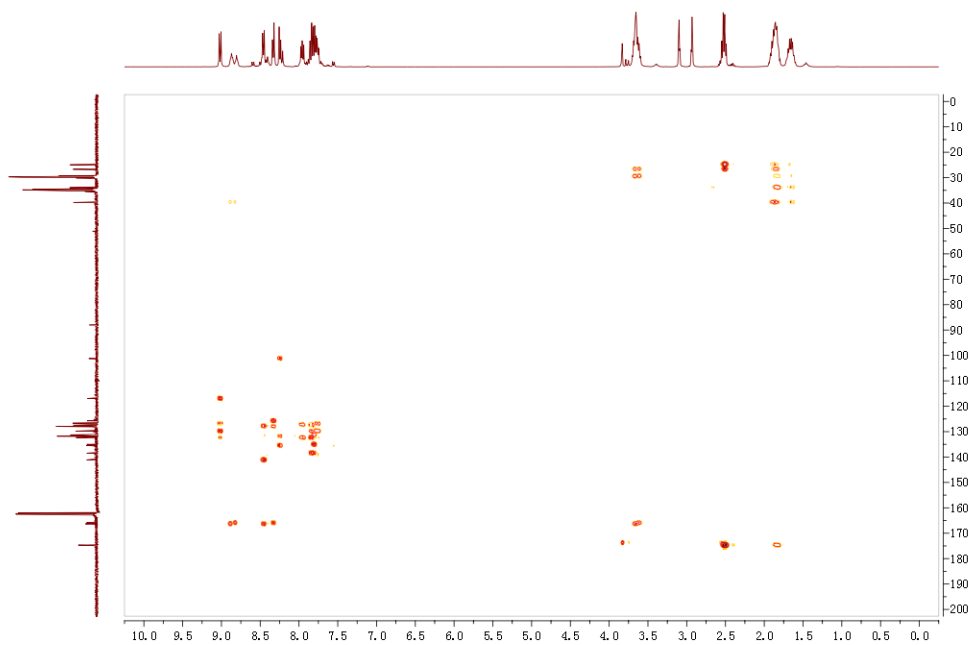


¹H NMR spectrum of 5

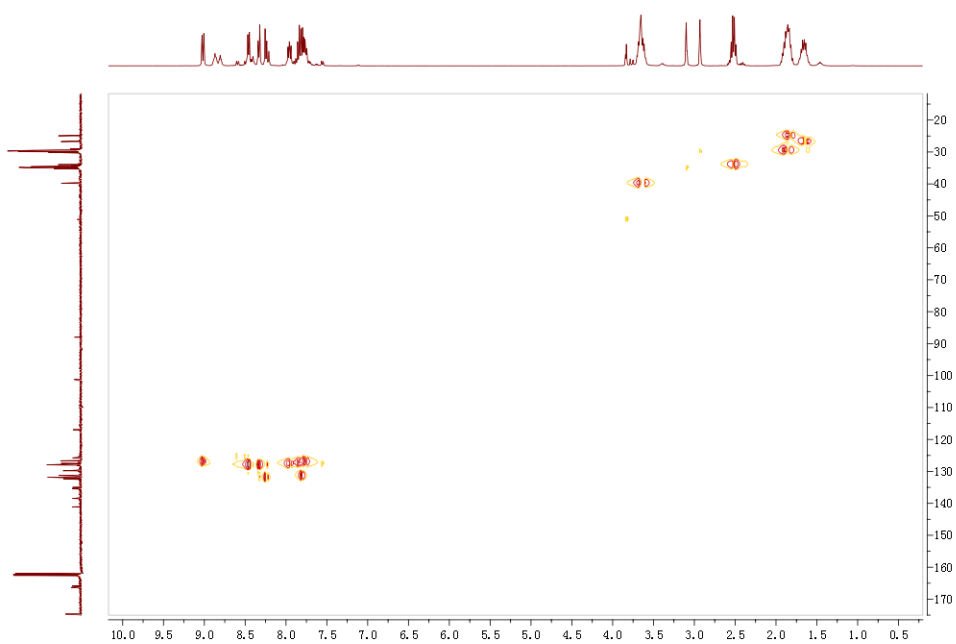


^{13}C NMR spectrum of **5**

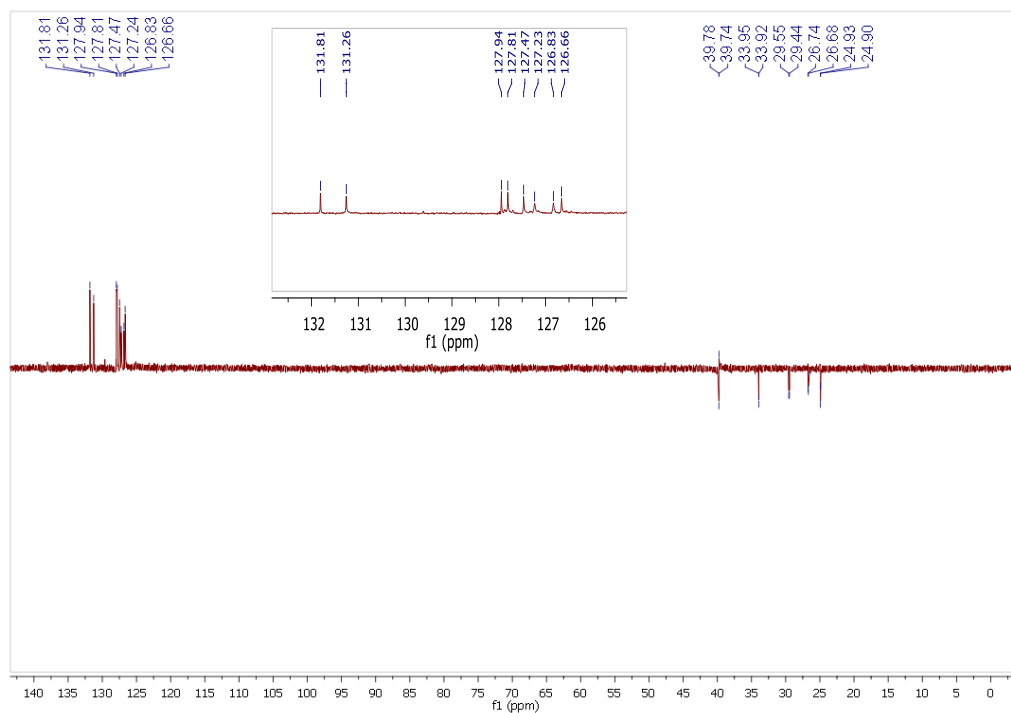




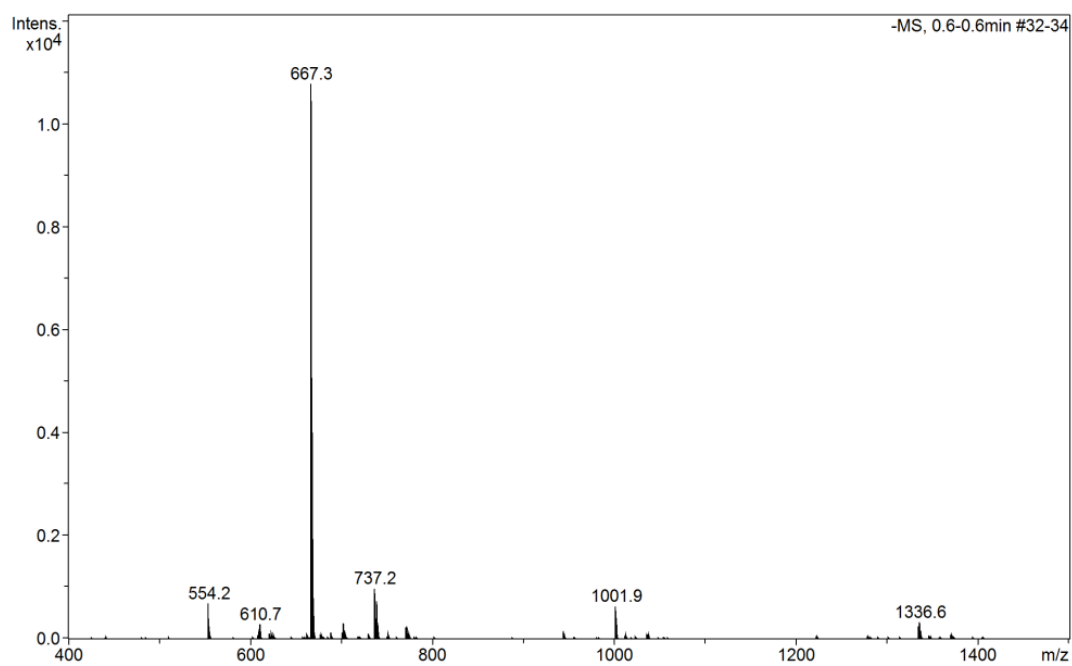
HSQC spectrum of 5



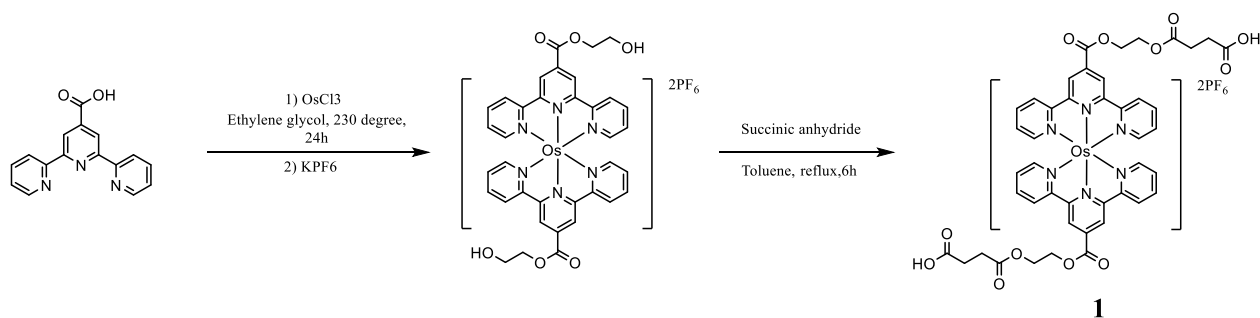
HMBC spectrum of 5



DEPT135 spectrum of 5

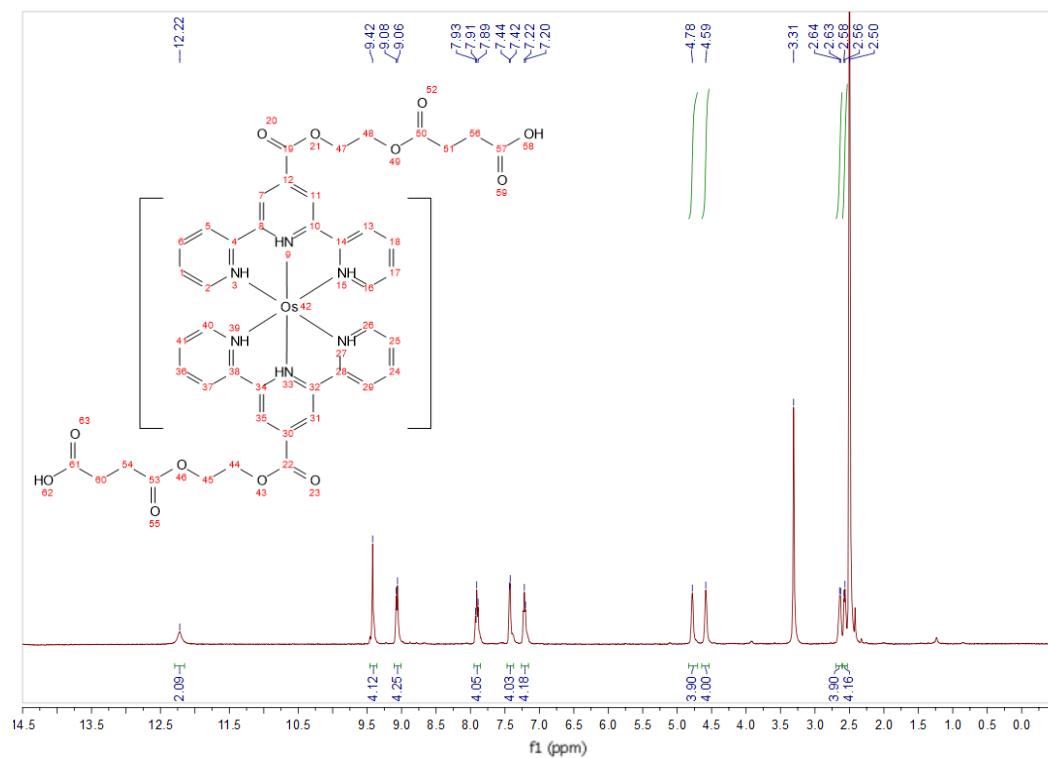


Mass spectrometry of 5

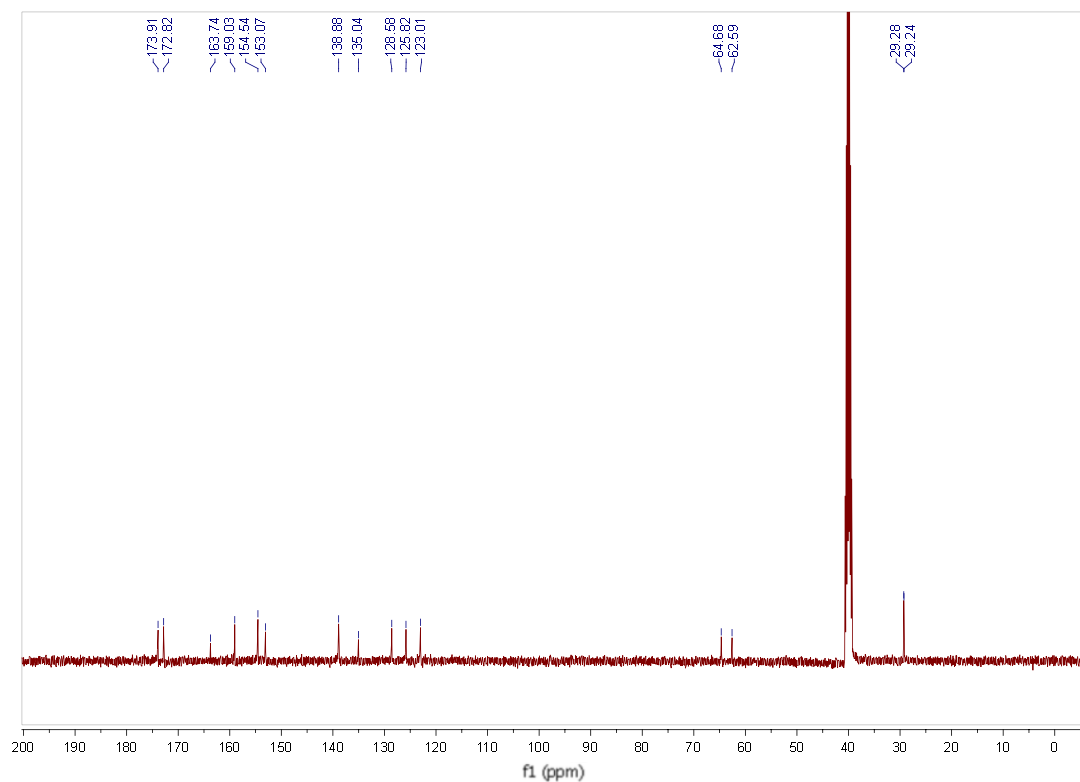


Osmium(III) chloride hydrate (100.0 mg, 0.34 mmol) and [2,2':6',2''-terpyridine]-4'-carboxylic acid (187.0 mg, 0.68 mmol) were refluxed in 6 mL ethylene glycol for 20 hours at 230 °C under continuous stirring. The black solution was obtained. After cooling to room temperature, KPF₆ in deionized water (15 mL) was added, giving black precipitates. The precipitates were filtrated and washed with water and MeOH (7:3). To the solution of affording black precipitates in toluene was added succinic anhydride (680 mg, 6.8 mmol). After refluxing for 8 hours, the solution was concentrated and resulting solid was washing by ethyl acetate to remove excess succinic anhydride affording **1** Os(tpy-sapcer-COOH)₂ · 2PF₆

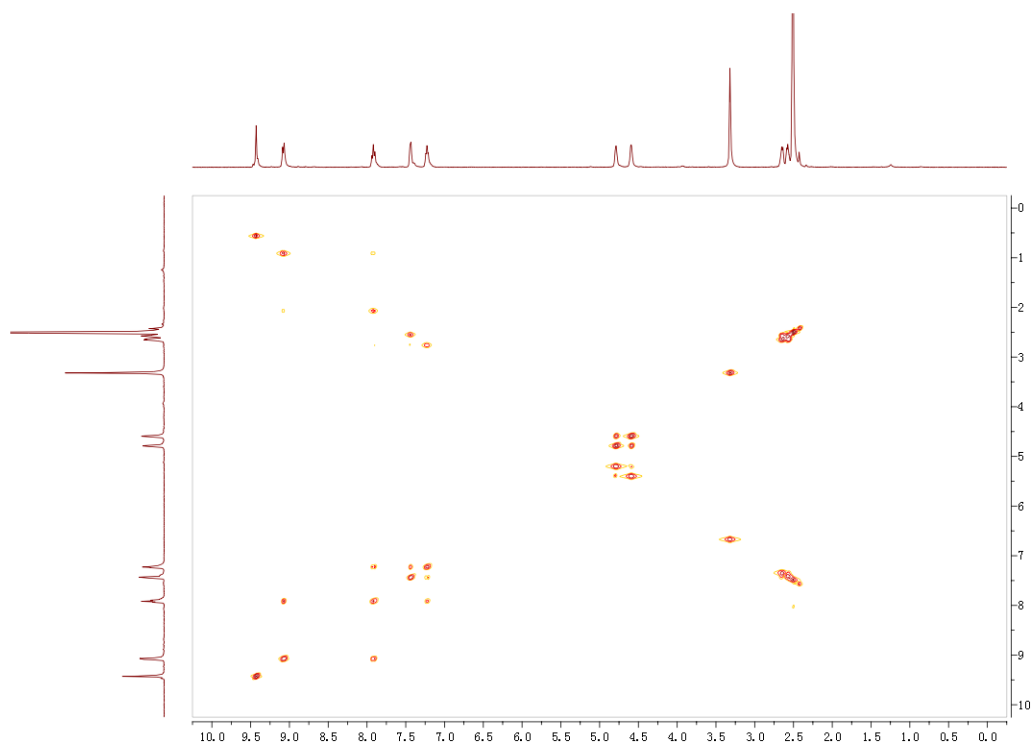
¹H NMR (400 MHz, (CD₃)₂SO) δ 12.22 (s, 2H, H^{58,62}), 9.42 (s, 4H, H^{7,11,31,35}), 9.07 (d, J = 7.7 Hz, 4H, H^{2,16,26,40}), 7.91 (t, J = 7.8 Hz, 4H, H^{5,13,29,37}), 7.43 (d, J = 5.0 Hz, 4H, H^{6,18,24,36}), 7.21 (d, J = 6.6 Hz, 4H, H^{1,17,25,41}), 4.78 (s, 4H, H^{44,47}), 4.59 (s, 4H, H^{45,48}), 2.64 (d, J = 6.4 Hz, 4H, H^{51,54}), 2.57 (d, J = 5.8 Hz, 4H, H^{56,60}). ¹³C NMR (101 MHz, (CD₃)₂SO) δ 173.91 (s, C^{57,61}), 172.82 (s, C^{50,53}), 163.74 (s, C^{19,22}), 159.03 (s, C^{4,14,28,38}), 154.54 (s, C^{2,16,36,40}), 153.07 (s, C^{8,10,32,34}), 138.88 (s, C^{6,18,24,36}), 135.04 (s, C^{12,30}), 128.58 (s, C^{1,17,25,41}), 125.82 (s, C^{7,11,31,35}), 123.01 (s, C^{5,13,29,37}), 64.68 (s, C^{44,47}), 62.59 (s, C^{45,48}), 29.28 (s, C^{51,54}), 29.24 (s, C^{56,60}). DEPT 135 (101 MHz, (CD₃)₂SO) δ 153.07 (s, C^{8,10,32,34}), 138.87 (s, C^{6,18,24,36}), 135.04 (s, C^{12,30}), 128.57 (s, C^{1,17,25,41}), 125.81 (s, C^{7,11,31,35}), 122.99 (s, C^{5,13,29,37}), 64.77 (s, C^{44,47}), 62.30 (s, C^{45,48}), 40.54 (s, C^{51,54}), 29.20 (s, C^{56,60}). MS-ESI (*m/z*): [M]⁺ Calcd. for (C₄₄H₃₈N₆O₁₂Os)/2⁺ 517.1, found 517.1



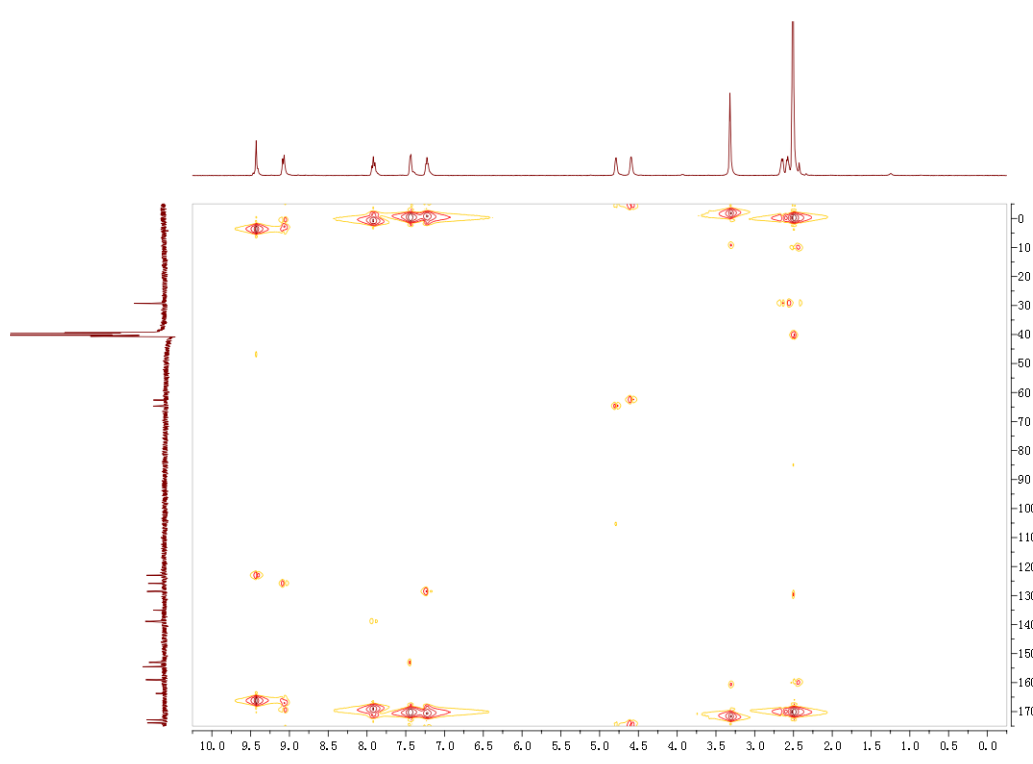
¹H NMR spectrum of 1



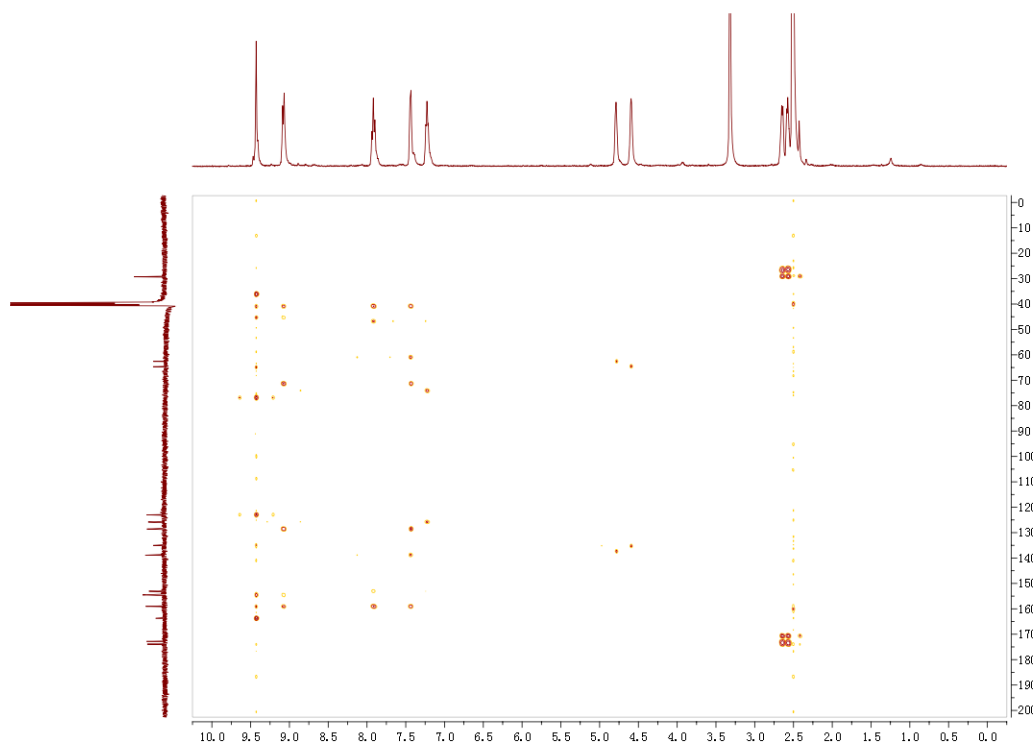
¹³C NMR spectrum of 1



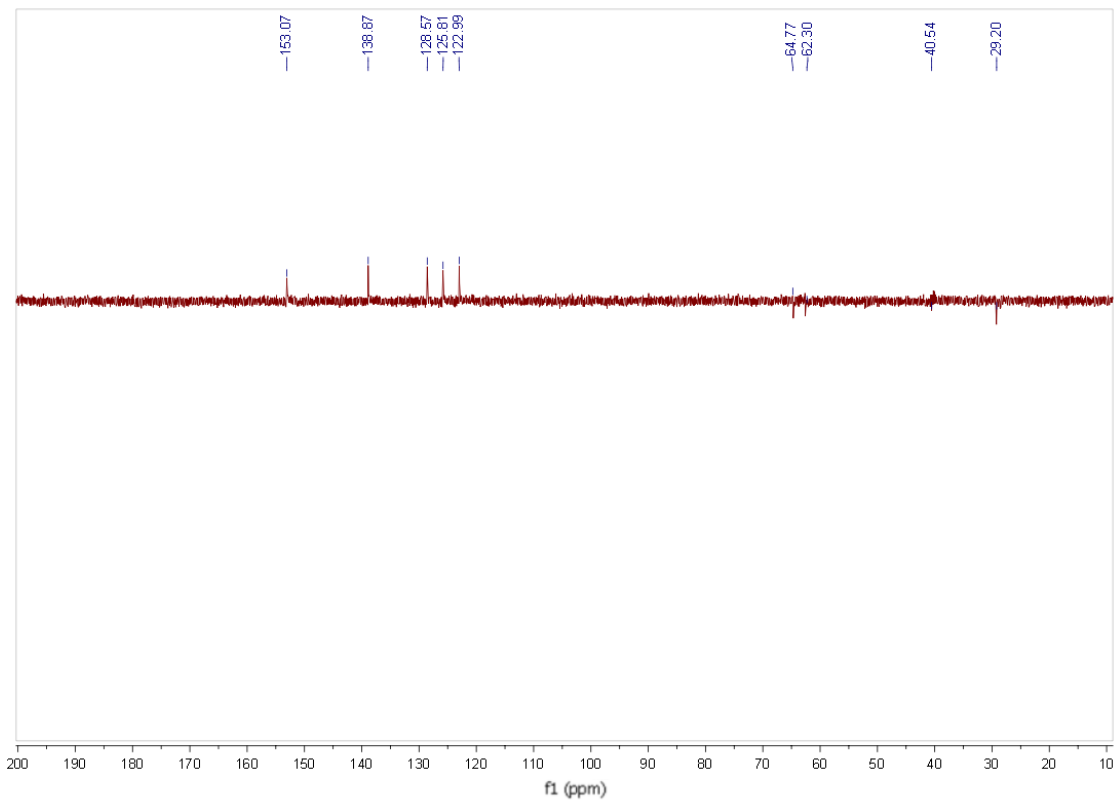
COSY spectrum of 1



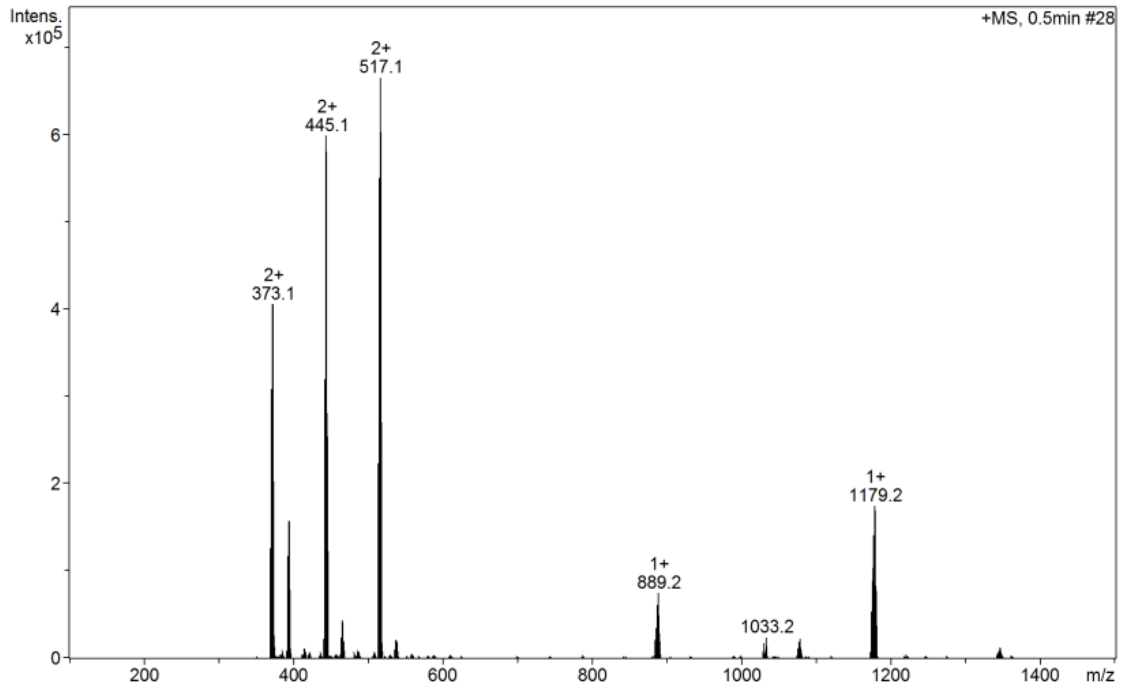
HSQC spectrum of 1



HMBC spectrum of 1



DEPT135 spectrum of 1



Mass spectrometry of **1**

4.6 Reference

1. Duan, C.; Liang, L.; Li, L.; Zhang, R.; Xu, Z. P., Recent progress in upconversion luminescence nanomaterials for biomedical applications. *J Mater Chem B* **2018**, *6* (2), 192-209.
2. Singh-Rachford, T. N.; Castellano, F. N., Photon upconversion based on sensitized triplet-triplet annihilation. *Coord. Chem. Rev.* **2010**, *254* (21-22), 2560-2573.
3. Zhang, F., General Introduction to Upconversion Luminescence Materials. In *Photon Upconversion Nanomaterials*, Springer Berlin Heidelberg: Berlin, Heidelberg, 2015; pp 1-20.
4. Liu, Q.; Yang, T.; Feng, W.; Li, F., Blue-emissive upconversion nanoparticles for low-power-excited bioimaging in vivo. *J. Am. Chem. Soc.* **2012**, *134* (11), 5390-7.
5. Mahboub, M.; Huang, Z.; Tang, M. L., Efficient Infrared-to-Visible Upconversion with Subsolar Irradiance. *Nano Lett.* **2016**, *16* (11), 7169-7175.
6. Wu, M.; Congreve, D. N.; Wilson, M. W. B.; Jean, J.; Geva, N.; Welborn, M.; Van Voorhis, T.; Bulović, V.; Bawendi, M. G.; Baldo, M. A., Solid-state infrared-to-visible upconversion sensitized by colloidal nanocrystals. *Nat. Photonics* **2015**, *10* (1), 31-34.
7. Bharmoria, P.; Bildirir, H.; Moth-Poulsen, K., Triplet-triplet annihilation based near infrared to visible molecular photon upconversion. *Chem. Soc. Rev.* **2020**, *49* (18), 6529-6554.
8. Aboshyan-Sorgho, L.; Besnard, C.; Pattison, P.; Kittilstved, K. R.; Aebischer, A.; Bunzli, J. C.; Hauser, A.; Piguet, C., Near-infrared-to-visible light upconversion in a molecular trinuclear d-f-d complex. *Angew. Chem. Int. Ed. Engl.* **2011**, *50* (18), 4108-12.
9. Auzel, F., Upconversion and anti-Stokes processes with f and d ions in solids. *Chem. Rev.* **2004**, *104* (1), 139-73.
10. Feng, W.; Sun, L.-D.; Zhang, Y.-W.; Yan, C.-H., Synthesis and assembly of rare earth nanostructures directed by the principle of coordination chemistry in solution-based process. *Coord. Chem. Rev.* **2010**, *254* (9-10), 1038-1053.
11. Wang, F.; Liu, X., Recent advances in the chemistry of lanthanide-doped upconversion nanocrystals. *Chem. Soc. Rev.* **2009**, *38* (4), 976-89.
12. Wang, G.; Peng, Q.; Li, Y., Lanthanide-doped nanocrystals: synthesis, optical-magnetic properties, and applications. *Acc. Chem. Res.* **2011**, *44* (5), 322-32.
13. Dong, H.; Sun, L. D.; Yan, C. H., Energy transfer in lanthanide upconversion studies for extended optical applications. *Chem. Soc. Rev.* **2015**, *44* (6), 1608-34.
14. Lingeshwar Reddy, K.; Balaji, R.; Kumar, A.; Krishnan, V., Lanthanide Doped Near Infrared Active Upconversion Nanophosphors: Fundamental Concepts, Synthesis Strategies, and Technological Applications. *Small* **2018**, *14* (37), e1801304.
15. Huang, S.; Cheng, Z.; Chen, Y.; Liu, B.; Deng, X.; Ma, P. a.; Lin, J., Multifunctional polyelectrolyte multilayers coated onto Gd₂O₃:Yb³⁺,Er³⁺@MSNs can be used as drug carriers and imaging agents. *RSC Adv.* **2015**, *5* (52), 41985-41993.
16. Yao, L.; Zhou, J.; Liu, J.; Feng, W.; Li, F., Iridium-complex-modified upconversion nanophosphors for effective LRET detection of cyanide anions in pure water. *Adv. Funct. Mater.* **2012**, *22* (13), 2667-2672.
17. Shin, J.; Kyhm, J.-H.; Hong, A.-R.; Song, J. D.; Lee, K.; Ko, H.; Jang, H. S., Multicolor tunable upconversion luminescence from sensitized seed-mediated grown LiGdF₄: Yb, Tm-based core/triple-shell nanophosphors for transparent displays. *Chem. Mater.* **2018**, *30* (23), 8457-8464.
18. Ding, M.; Dong, B.; Lu, Y.; Yang, X.; Yuan, Y.; Bai, W.; Wu, S.; Ji, Z.; Lu, C.; Zhang, K., Energy manipulation in lanthanide-doped core-shell nanoparticles for tunable dual-mode luminescence toward advanced anti-counterfeiting. *Adv. Mater.* **2020**, *32* (45), 2002121.
19. Xu, J.; Zhang, B.; Jia, L.; Fan, Y.; Chen, R.; Zhu, T.; Liu, B., Dual-mode, color-tunable, lanthanide-doped core-shell nanoarchitectures for anti-counterfeiting inks and latent fingerprint recognition. *ACS Appl. Mater. Interfaces* **2019**, *11* (38), 35294-35304.

-
20. Gao, L.; Shan, X.; Xu, X.; Liu, Y.; Liu, B.; Li, S.; Wen, S.; Ma, C.; Jin, D.; Wang, F., Video-rate upconversion display from optimized lanthanide ion doped upconversion nanoparticles. *Nanoscale* **2020**, *12* (36), 18595-18599.
21. Karunakaran, S. K.; Arumugam, G. M.; Yang, W.; Ge, S.; Khan, S. N.; Lin, X.; Yang, G., Research progress on the application of lanthanide-ion-doped phosphor materials in perovskite solar cells. *ACS Sustainable Chem. Eng.* **2021**, *9* (3), 1035-1060.
22. Li, Q.; Yuan, S.; Liu, F.; Zhu, X.; Liu, J., Lanthanide-Doped Nanoparticles for Near-Infrared Light Activation of Photopolymerization: Fundamentals, Optimization and Applications. *The Chemical Record* **2021**, *21* (7), 1681-1696.
23. Ge, X.; Wei, R.; Sun, L., Lanthanide nanoparticles with efficient near-infrared-II emission for biological applications. *J Mater Chem B* **2020**, *8* (45), 10257-10270.
24. Zhang, Q.; O'Brien, S.; Grimm, J., Biomedical Applications of Lanthanide Nanomaterials, for Imaging, Sensing and Therapy. *Nanotheranostics* **2022**, *6* (2), 184-194.
25. Seo, S. E.; Choe, H.-S.; Cho, H.; Kim, H.-i.; Kim, J.-H.; Kwon, O. S., Recent advances in materials for and applications of triplet-triplet annihilation-based upconversion. *J. Mater. Chem. C* **2022**.
26. Parker, C. A.; Hatchard, C. G.; Bowen, E. J., Delayed fluorescence from solutions of anthracene and phenanthrene. *Proc., Math. phys. sci.* **1997**, *269* (1339), 574-584.
27. Parker, C.; Hatchard, C., Delayed fluorescence from solutions of anthracene and phenanthrene. *Proc., Math. phys. sci.* **1962**, *269* (1339), 574-584.
28. Zhou, J.; Liu, Q.; Feng, W.; Sun, Y.; Li, F., Upconversion luminescent materials: advances and applications. *Chem. Rev.* **2015**, *115* (1), 395-465.
29. Vadrucci, R.; Weder, C.; Simon, Y. C., Organogels for low-power light upconversion. *Mater. Horiz.* **2015**, *2* (1), 120-124.
30. Filatov, M. A.; Balushev, S.; Landfester, K., Protection of densely populated excited triplet state ensembles against deactivation by molecular oxygen. *Chem. Soc. Rev.* **2016**, *45* (17), 4668-89.
31. Balushev, S.; Katta, K.; Avlasevich, Y.; Landfester, K., Annihilation upconversion in nanoconfinement: solving the oxygen quenching problem. *Mater. Horiz.* **2016**, *3* (6), 478-486.
32. Lewis, G. N.; Kasha, M., Phosphorescence and the Triplet State. *J. Am. Chem. Soc.* **2002**, *66* (12), 2100-2116.
33. Lewis, G. N.; Kasha, M., Phosphorescence in Fluid Media and the Reverse Process of Singlet-Triplet Absorption. *J. Am. Chem. Soc.* **2002**, *67* (6), 994-1003.
34. Kinoshita, T.; Fujisawa, J.; Nakazaki, J.; Uchida, S.; Kubo, T.; Segawa, H., Enhancement of Near-IR Photoelectric Conversion in Dye-Sensitized Solar Cells Using an Osmium Sensitizer with Strong Spin-Forbidden Transition. *J Phys Chem Lett* **2012**, *3* (3), 394-8.
35. Zhang, X.; Canton, S. E.; Smolentsev, G.; Wallentin, C. J.; Liu, Y.; Kong, Q.; Attenkofer, K.; Stickrath, A. B.; Mara, M. W.; Chen, L. X.; Warnmark, K.; Sundstrom, V., Highly accurate excited-state structure of [Os(bpy)₂dc bpy]²⁺ determined by X-ray transient absorption spectroscopy. *J. Am. Chem. Soc.* **2014**, *136* (24), 8804-9.
36. Felix, F.; Ferguson, J.; Güdel, H. U.; Ludi, A., Electronic spectra of M(bipy)₂³⁺ complexions (M = Fe, Ru and Os). *Chem. Phys. Lett.* **1979**, *62* (1), 153-157.
37. Kober, E. M.; Meyer, T. J., Concerning the absorption spectra of the ions M(bpy)₃²⁺ (M = Fe, Ru, Os; bpy = 2,2'-bipyridine). *Inorg. Chem.* **2002**, *21* (11), 3967-3977.
38. Joarder, B.; Mallick, A.; Sasaki, Y.; Kinoshita, M.; Haruki, R.; Kawashima, Y.; Yanai, N.; Kimizuka, N., Near-Infrared-to-Visible Photon Upconversion by Introducing an S-T Absorption Sensitizer into a Metal-Organic Framework. *ChemNanoMat* **2020**, *6* (6), 916-919.
39. Haruki, R.; Sasaki, Y.; Masutani, K.; Yanai, N.; Kimizuka, N., Leaping across the visible range: near-infrared-to-violet photon upconversion employing a silyl-substituted anthracene. *Chem. Commun.* **2020**, *56* (51), 7017-7020.
40. Kinoshita, M.; Sasaki, Y.; Amemori, S.; Harada, N.; Hu, Z.; Liu, Z.; Ono, L. K.; Qi, Y.; Yanai, N.; Kimizuka, N., Photon Upconverting Solid Films with Improved Efficiency for Endowing Perovskite Solar Cells with Near-Infrared Sensitivity. *ChemPhotoChem* **2020**, *4* (11), 5271-5278.

-
41. Lower, S. K.; El-Sayed, M. A., The Triplet State and Molecular Electronic Processes in Organic Molecules. *Chem. Rev.* **2002**, *66* (2), 199-241.
 42. Crosby, G. A.; Demas, J. N., Quantum efficiencies on transition metal complexes. II. Charge-transfer luminescence. *J. Am. Chem. Soc.* **2002**, *93* (12), 2841-2847.
 43. Balushev, S.; Yakutkin, V.; Miteva, T.; Avlasevich, Y.; Chernov, S.; Aleshchenkov, S.; Nelles, G.; Cheprakov, A.; Yasuda, A.; Mullen, K.; Wegner, G., Blue-green up-conversion: noncoherent excitation by NIR light. *Angew. Chem. Int. Ed. Engl.* **2007**, *46* (40), 7693-6.
 44. Singh-Rachford, T. N.; Castellano, F. N., Nonlinear photochemistry squared: quartic light power dependence realized in photon upconversion. *J. Phys. Chem. A* **2009**, *113* (33), 9266-9.
 45. Bennison, M. J.; Collins, A. R.; Zhang, B.; Evans, R. C., Organic Polymer Hosts for Triplet-Triplet Annihilation Upconversion Systems. *Macromolecules* **2021**, *54* (12), 5287-5303.
 46. Ronchi, A.; Monguzzi, A., Developing solid-state photon upconverters based on sensitized triplet-triplet annihilation. *J. Appl. Phys.* **2021**, *129* (5), 050901.
 47. v. Bünau, G., J. B. Birks: Photophysics of Aromatic Molecules. Wiley-Interscience, London 1970. 704 Seiten. Preis: 210s. *Berichte der Bunsengesellschaft für physikalische Chemie* **1970**, *74* (12), 1294-1295.
 48. Thomas, S. W., 3rd; Joly, G. D.; Swager, T. M., Chemical sensors based on amplifying fluorescent conjugated polymers. *Chem. Rev.* **2007**, *107* (4), 1339-86.
 49. Ma, X.; Sun, R.; Cheng, J.; Liu, J.; Gou, F.; Xiang, H.; Zhou, X., Fluorescence Aggregation-Caused Quenching versus Aggregation-Induced Emission: A Visual Teaching Technology for Undergraduate Chemistry Students. *J. Chem. Educ.* **2015**, *93* (2), 345-350.
 50. Kim, J. H.; Kim, J. H., Encapsulated triplet-triplet annihilation-based upconversion in the aqueous phase for sub-band-gap semiconductor photocatalysis. *J. Am. Chem. Soc.* **2012**, *134* (42), 17478-81.
 51. Lee, H.-L.; Lee, M.-S.; Park, H.; Han, W.-S.; Kim, J.-H., Visible-to-UV triplet-triplet annihilation upconversion from a thermally activated delayed fluorescence/pyrene pair in an air-saturated solution. *Korean J. Chem. Eng.* **2019**, *36* (11), 1791-1798.
 52. Marsico, F.; Turshatov, A.; Peköz, R.; Avlasevich, Y.; Wagner, M.; Weber, K.; Donadio, D.; Landfester, K.; Balushev, S.; Wurm, F. R., Hyperbranched unsaturated polyphosphates as a protective matrix for long-term photon upconversion in air. *J. Am. Chem. Soc.* **2014**, *136* (31), 11057-11064.
 53. Liu, Q.; Yin, B.; Yang, T.; Yang, Y.; Shen, Z.; Yao, P.; Li, F., A general strategy for biocompatible, high-effective upconversion nanocapsules based on triplet-triplet annihilation. *J. Am. Chem. Soc.* **2013**, *135* (13), 5029-37.
 54. Allen, T. M., Liposomes. Opportunities in drug delivery. *Drugs* **1997**, *54 Suppl 4* (4), 8-14.
 55. Lasic, D. D., Novel applications of liposomes. *Trends Biotechnol.* **1998**, *16* (7), 307-21.
 56. Bozzuto, G.; Molinari, A., Liposomes as nanomedical devices. *Int. J. Nanomed.* **2015**, *10*, 975-99.
 57. Crommelin, D. J. A.; van Hoogevest, P.; Storm, G., The role of liposomes in clinical nanomedicine development. What now? Now what? *J. Controlled Release* **2020**, *318*, 256-263.
 58. Kim, E. M.; Jeong, H. J., Liposomes: Biomedical Applications. *Chonnam Med. J.* **2021**, *57* (1), 27-35.
 59. Muthu, M. S.; Feng, S. S., Theranostic liposomes for cancer diagnosis and treatment: current development and pre-clinical success. *Expert Opin. Drug Delivery* **2013**, *10* (2), 151-5.
 60. Askes, S. H.; Bahreman, A.; Bonnet, S., Activation of a photodissociative ruthenium complex by triplet-triplet annihilation upconversion in liposomes. *Angew. Chem. Int. Ed. Engl.* **2014**, *53* (4), 1029-33.
 61. Petros, R. A.; DeSimone, J. M., Strategies in the design of nanoparticles for therapeutic applications. *Nat. Rev. Drug Discovery* **2010**, *9* (8), 615-27.
 62. Fujimoto, K.; Kawai, K.; Masuda, S.; Mori, T.; Aizawa, T.; Inuzuka, T.; Karatsu, T.; Sakamoto, M.; Yagai, S.; Sengoku, T.; Takahashi, M.; Yoda, H., Triplet-Triplet Annihilation-Based Upconversion Sensitized by a Reverse Micellar Assembly of Amphiphilic Ruthenium Complexes. *Langmuir* **2019**, *35* (30), 9740-9746.

-
63. Yamamoto, E.; Kuroda, K., Colloidal Mesoporous Silica Nanoparticles. *Bull. Chem. Soc. Jpn.* **2016**, *89* (5), 501-539.
64. Fang, X.; Zhao, X.; Fang, W.; Chen, C.; Zheng, N., Self-templating synthesis of hollow mesoporous silica and their applications in catalysis and drug delivery. *Nanoscale* **2013**, *5* (6), 2205-18.
65. Kankala, R. K.; Han, Y. H.; Na, J.; Lee, C. H.; Sun, Z.; Wang, S. B.; Kimura, T.; Ok, Y. S.; Yamauchi, Y.; Chen, A. Z.; Wu, K. C., Nanoarchitected Structure and Surface Biofunctionality of Mesoporous Silica Nanoparticles. *Adv. Mater.* **2020**, *32* (23), e1907035.
66. Li, Z.; Barnes, J. C.; Bosoy, A.; Stoddart, J. F.; Zink, J. I., Mesoporous silica nanoparticles in biomedical applications. *Chem. Soc. Rev.* **2012**, *41* (7), 2590-605.
67. Huang, L.; Zhao, Y.; Zhang, H.; Huang, K.; Yang, J.; Han, G., Expanding Anti-Stokes Shifting in Triplet-Triplet Annihilation Upconversion for In Vivo Anticancer Prodrug Activation. *Angew. Chem. Int. Ed. Engl.* **2017**, *56* (46), 14400-14404.
68. Lee, H. L.; Park, J. H.; Choe, H. S.; Lee, M. S.; Park, J. M.; Harada, N.; Sasaki, Y.; Yanai, N.; Kimizuka, N.; Zhu, J.; Bhang, S. H.; Kim, J. H., Upconverting Oil-Laden Hollow Mesoporous Silica Microcapsules for Anti-Stokes-Based Biophotonic Applications. *ACS Appl Mater Interfaces* **2019**, *11* (30), 26571-26580.
69. Kwon, O. S.; Kim, J. H.; Cho, J. K.; Kim, J. H., Triplet-triplet annihilation upconversion in CdS-decorated SiO₂ nanocapsules for sub-bandgap photocatalysis. *ACS Appl Mater Interfaces* **2015**, *7* (1), 318-25.
70. Kwon, O. S.; Song, H. S.; Conde, J.; Kim, H. I.; Artzi, N.; Kim, J. H., Dual-Color Emissive Upconversion Nanocapsules for Differential Cancer Bioimaging In Vivo. *ACS Nano* **2016**, *10* (1), 1512-21.
71. Keivanidis, P. E.; Balushev, S.; Miteva, T.; Nelles, G.; Scherf, U.; Yasuda, A.; Wegner, G., Up-Conversion Photoluminescence in Polyfluorene Doped with Metal(II)-Octaethyl Porphyrins. *Adv. Mater.* **2003**, *15* (24), 2095-2098.
72. Jiang, X.; Guo, X.; Peng, J.; Zhao, D.; Ma, Y., Triplet-Triplet Annihilation Photon Upconversion in Polymer Thin Film: Sensitizer Design. *ACS Appl Mater Interfaces* **2016**, *8* (18), 11441-9.
73. Zhou, H. C.; Long, J. R.; Yaghi, O. M., Introduction to metal-organic frameworks. *Chem. Rev.* **2012**, *112* (2), 673-4.
74. Monguzzi, A.; Ballabio, M.; Yanai, N.; Kimizuka, N.; Fazzi, D.; Campione, M.; Meinardi, F., Highly Fluorescent Metal-Organic-Framework Nanocomposites for Photonic Applications. *Nano Lett.* **2018**, *18* (1), 528-534.
75. Park, J.; Xu, M.; Li, F.; Zhou, H. C., 3D Long-Range Triplet Migration in a Water-Stable Metal-Organic Framework for Upconversion-Based Ultralow-Power in Vivo Imaging. *J. Am. Chem. Soc.* **2018**, *140* (16), 5493-5499.
76. Roy, I.; Goswami, S.; Young, R. M.; Schlesinger, I.; Mian, M. R.; Enciso, A. E.; Zhang, X.; Hornick, J. E.; Farha, O. K.; Wasielewski, M. R., Photon upconversion in a glowing metal-organic framework. *J. Am. Chem. Soc.* **2021**, *143* (13), 5053-5059.
77. Oldenburg, M.; Turshatov, A.; Busko, D.; Wollgarten, S.; Adams, M.; Baroni, N.; Welle, A.; Redel, E.; Woll, C.; Richards, B. S.; Howard, I. A., Photon Upconversion at Crystalline Organic-Organic Heterojunctions. *Adv. Mater.* **2016**, *28* (38), 8477-8482.
78. Hill, S. P.; Banerjee, T.; Dilbeck, T.; Hanson, K., Photon upconversion and photocurrent generation via self-assembly at organic-inorganic interfaces. *J Phys Chem Lett* **2015**, *6* (22), 4510-7.
79. Mattiello, S.; Monguzzi, A.; Pedrini, J.; Sassi, M.; Villa, C.; Torrente, Y.; Marotta, R.; Meinardi, F.; Beverina, L., Self-Assembled Dual Dye-Doped Nanosized Micelles for High-Contrast Up-Conversion Bioimaging. *Adv. Funct. Mater.* **2016**, *26* (46), 8447-8454.
80. Askes, S. H. C.; Meijer, M. S.; Bouwens, T.; Landman, I.; Bonnet, S., Red Light Activation of Ru(II) Polypyridyl Prodrugs via Triplet-Triplet Annihilation Upconversion: Feasibility in Air and through Meat. *Molecules* **2016**, *21* (11), 1460.
81. Dartar, S.; Ucuncu, M.; Karakus, E.; Hou, Y.; Zhao, J.; Emrullahoglu, M., BODIPY-vinyl dibromides as triplet sensitizers for photodynamic therapy and triplet-triplet annihilation upconversion. *Chem. Commun.* **2021**, *57* (49), 6039-6042.

-
82. Di, D.; Yang, L.; Richter, J. M.; Meraldi, L.; Altamimi, R. M.; Alyamani, A. Y.; Credgington, D.; Musselman, K. P.; MacManus-Driscoll, J. L.; Friend, R. H., Efficient Triplet Exciton Fusion in Molecularly Doped Polymer Light-Emitting Diodes. *Adv. Mater.* **2017**, *29* (13), 1605987.
83. Kukhta, N. A.; Matulaitis, T.; Volyniuk, D.; Ivaniuk, K.; Turyk, P.; Stakhira, P.; Grazulevicius, J. V.; Monkman, A. P., Deep-Blue High-Efficiency TTA OLED Using Para- and Meta-Conjugated Cyanotriphenylbenzene and Carbazole Derivatives as Emitter and Host. *J Phys Chem Lett* **2017**, *8* (24), 6199-6205.
84. Nattestad, A.; Cheng, Y. Y.; MacQueen, R. W.; Schulze, T. F.; Thompson, F. W.; Mozer, A. J.; Fuckel, B.; Houry, T.; Crossley, M. J.; Lips, K.; Wallace, G. G.; Schmidt, T. W., Dye-Sensitized Solar Cell with Integrated Triplet-Triplet Annihilation Upconversion System. *J Phys Chem Lett* **2013**, *4* (12), 2073-8.
85. Zhou, Y.; Ruchlin, C.; Robb, A. J.; Hanson, K., Singlet Sensitization-Enhanced Upconversion Solar Cells via Self-Assembled Trilayers. *ACS Energy Lett.* **2019**, *4* (6), 1458-1463.
86. Hill, S. P.; Dilbeck, T.; Baduell, E.; Hanson, K., Integrated Photon Upconversion Solar Cell via Molecular Self-Assembled Bilayers. *ACS Energy Lett.* **2016**, *1* (1), 3-8.
87. Dilbeck, T.; Hanson, K., Molecular Photon Upconversion Solar Cells Using Multilayer Assemblies: Progress and Prospects. *J Phys Chem Lett* **2018**, *9* (19), 5810-5821.
88. Hill, S. P.; Hanson, K., Harnessing Molecular Photon Upconversion in a Solar Cell at Sub-solar Irradiance: Role of the Redox Mediator. *J. Am. Chem. Soc.* **2017**, *139* (32), 10988-10991.
89. Suo, H.; Zhu, Q.; Zhang, X.; Chen, B.; Chen, J.; Wang, F., High-security anti-counterfeiting through upconversion luminescence. *Materials Today Physics* **2021**, *21*, 100520.
90. Hagstrom, A. L.; Lee, H. L.; Lee, M. S.; Choe, H. S.; Jung, J.; Park, B. G.; Han, W. S.; Ko, J. S.; Kim, J. H.; Kim, J. H., Flexible and Micropatternable Triplet-Triplet Annihilation Upconversion Thin Films for Photonic Device Integration and Anticounterfeiting Applications. *ACS Appl Mater Interfaces* **2018**, *10* (10), 8985-8992.
91. Braga, D.; Jaafari, A.; Miozzo, L.; Moret, M.; Rizzato, S.; Papagni, A.; Yassar, A., The Rubrenic Synthesis: The Delicate Equilibrium between Tetracene and Cyclobutene. *Eur. J. Org. Chem.* **2011**, *2011* (22), 4160-4169.
92. Ragon, F.; Campo, B.; Yang, Q.; Martineau, C.; Wiersum, A. D.; Lago, A.; Guillermin, V.; Hemsley, C.; Eubank, J. F.; Vishnuvarthan, M.; Taulelle, F.; Horcajada, P.; Vimont, A.; Llewellyn, P. L.; Daturi, M.; Devautour-Vinot, S.; Maurin, G.; Serre, C.; Devic, T.; Clet, G., Acid-functionalized UiO-66(Zr) MOFs and their evolution after intra-framework cross-linking: structural features and sorption properties. *Journal of Materials Chemistry A* **2015**, *3* (7), 3294-3309.
93. DeCoste, J. B.; Peterson, G. W.; Jasuja, H.; Glover, T. G.; Huang, Y.-g.; Walton, K. S., Stability and degradation mechanisms of metal-organic frameworks containing the Zr₆O₄(OH)₄ secondary building unit. *Journal of Materials Chemistry A* **2013**, *1* (18), 5642.
94. Abdelhameed, R. M.; Rehan, M.; Emam, H. E., Figuration of Zr-based MOF@cotton fabric composite for potential kidney application. *Carbohydr. Polym.* **2018**, *195*, 460-467.
95. Monguzzi, A.; Mezyk, J.; Scotognella, F.; Tubino, R.; Meinardi, F., Upconversion-induced fluorescence in multicomponent systems: Steady-state excitation power threshold. *Phys. Rev. B* **2008**, *78* (19), 195112.
96. Ye, C.; Zhou, L.; Wang, X.; Liang, Z., Photon upconversion: from two-photon absorption (TPA) to triplet-triplet annihilation (TTA). *PCCP* **2016**, *18* (16), 10818-10835.
97. Irie, M., Photochromism: Memories and Switches-Introduction. *Chem. Rev.* **2000**, *100* (5), 1683-1684.
98. Nigel Corns, S.; Partington, S. M.; Towns, A. D., Industrial organic photochromic dyes. *Coloration Technology* **2009**, *125* (5), 249-261.
99. Huang, Y.; Li, L.; Liu, X.; Li, Z., Photobase-catalysed anionic thiol-epoxy click photopolymerization under NIR irradiation: from deep curing to shape memory. *Polymer Chemistry* **2022**, *13* (21), 3048-3052.

-
100. Pang, Y.; Fan, S.; Wang, Q.; Oprych, D.; Feilen, A.; Reiner, K.; Keil, D.; Slominsky, Y. L.; Popov, S.; Zou, Y., NIR-Sensitized Activated Photoreaction between Cyanines and Oxime Esters: Free-Radical Photopolymerization. *Angew. Chem.* **2020**, *132* (28), 11537-11544.
101. Wang, Q.; Popov, S.; Feilen, A.; Strehmel, V.; Strehmel, B., Rational Selection of Cyanines to Generate Conjugate Acid and Free Radicals for Photopolymerization upon Exposure at 860 nm. *Angew. Chem. Int. Ed.* **2021**, *60* (51), 26855-26865.
102. Corrigan, N.; Yeow, J.; Judzewitsch, P.; Xu, J.; Boyer, C., Seeing the light: advancing materials chemistry through photopolymerization. *Angew. Chem. Int. Ed.* **2019**, *58* (16), 5170-5189.
103. Ahmad, I.; Iqbal, K.; Sheraz, M. A.; Ahmed, S.; Ali, S. A.; Kazi, S. H.; Mirza, T.; Bano, R.; Aminuddin, M., Solvent Effect on Photoinitiator Reactivity in the Polymerization of 2-Hydroxyethyl Methacrylate. *Adv. Phys. Chem.* **2013**, *2013*, 1-6.
104. Szwarc, M., Living polymers. Their discovery, characterization, and properties. *J. Polym. Sci., Part A: Polym. Chem.* **1998**, *36* (1), IX-XV.
105. Torres-Pierna, H.; Ruiz-Molina, D.; Roscini, C., Highly transparent photochromic films with a tunable and fast solution-like response. *Mater. Horiz.* **2020**, *7* (10), 2749-2759.
106. Otaegui, J. R.; Ruiz-Molina, D.; Latterini, L.; Hernando, J.; Roscini, C., Thermoresponsive multicolor-emissive materials based on solid lipid nanoparticles. *Mater Horiz* **2021**, *8* (11), 3043-3054.
107. Amemori, S.; Sasaki, Y.; Yanai, N.; Kimizuka, N., Near-infrared-to-visible photon upconversion sensitized by a metal complex with spin-forbidden yet strong S₀-T₁ absorption. *J. Am. Chem. Soc.* **2016**, *138* (28), 8702-8705.
108. Lim, M.; Kwon, H.; Kim, D.; Seo, J.; Han, H.; Khan, S. B., Highly-enhanced water resistant and oxygen barrier properties of cross-linked poly (vinyl alcohol) hybrid films for packaging applications. *Prog. Org. Coat.* **2015**, *85*, 68-75.
109. Dzebo, D.; Moth-Poulsen, K.; Albinsson, B., Robust triplet-triplet annihilation photon upconversion by efficient oxygen scavenging. *Photochem. Photobiol. Sci.* **2017**, *16* (8), 1327-1334.
110. Askes, S. H.; Bonnet, S., Solving the oxygen sensitivity of sensitized photon upconversion in life science applications. *Nat. Rev. Chem.* **2018**, *2* (12), 437-452.

Chapter 5

Coordination polymers nanoparticles for singlet oxygen storage and release

5.1 Introduction

Photodynamic therapy (PDT) has been investigated over the past three decades and is currently an approved therapeutic modality for skin cancer,¹⁻³ the treatment of superficial bladder,⁴⁻⁶ early lung and advanced esophageal cancers,⁷⁻⁹ and age-related macular degeneration in a number of countries.¹⁰⁻¹¹ Basically, in a PDT process, a photosensitizer (PS) exhibits no or low toxicity by itself, but in the presence of light excitation and oxygen molecules, reactive oxygen species (ROS) are generated to cause damage to proteins, nucleic acids, lipids, membranes, and organelles, leading to irreversible destruction of the treated tissue.

Under the irradiation of light with a specific wavelength, an excited singlet state of a PS is initially populated. The generated singlet excited state of the PS rapidly relaxes to the lowest singlet excited state S_1 , which undergoes intersystem crossing, populating the lowest triplet excited state (T_1) of the PS (ISC, $S_1 \rightarrow T_1$). The obtained triplet state can then proceed to the following processes:

- react with substrates and O_2 to generate free radicals, such as superoxide radical ($\cdot O_2^-$) and hydroxyl radical ($\cdot OH$) (type I reaction).
- transfer its energy to the molecular O_2 (in its triplet ground state) to form highly reactive singlet oxygen (1O_2), resulting in the significant cellular toxicity (type II reaction) (Figure 5.1).

The mechanisms of tumor ablation is occurring through (1) direct cytotoxic effects on tumor cells, (2) indirect damage to the tumor vasculature, and (3) induction of an inflammatory response that activates the immune system.

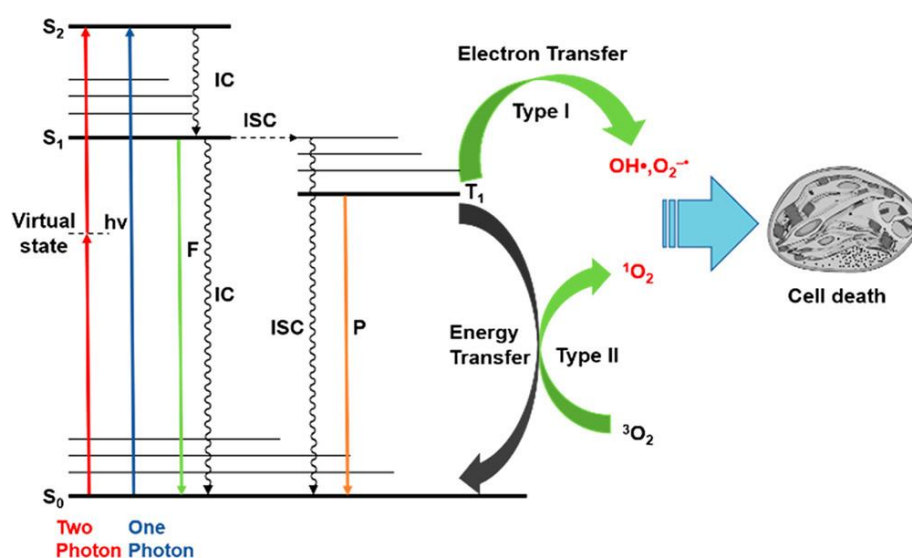


Figure 5.1: One-photon-excited and two-photon-excited PDT with two mechanisms (types I and II). Image extracted from reference.¹²

Numerous solid tumors have been treated with hundreds of PSs in clinical settings during the past 30 years, including BODIPY, phthalocyanine, chlorin, and tetrapyrrole.¹³⁻¹⁶ Additionally, nile blue compounds,¹⁷⁻¹⁸ rose bengal,¹⁹⁻²⁰ hypericin²¹⁻²² are commercially accessible and often utilized in clinical trials. A variety of PSs have been used till now in clinical trials and reported to enhance PS efficiency. Compared to other traditional treatments, such as surgery and radiotherapy, PDT has several main advantages:

(1) PSs only displays high toxicity after being activated by exposure to a certain wavelength of light, which reduces systemic toxicity during internalization and boosts selectivity.

(2) Because ROS harm various cell types, PDT offers a wide range of possible uses.

(3) PDT is a minimally invasive procedure as it.....

(4) By using nanomaterials PDT can be a synergetic therapy when combined with other forms of treatment including surgery and chemotherapy. For in vivo biological applications, such as the increased permeability and retention (EPR) effect.

Apart from these advantages, PDT has various limitations that needs to be overcome:

(1) Traditional porphyrin-like derivatives have very poor water solubility and are difficult to produce and purify.

(2) Due to their complicated structural makeup and high triplet yields, metal-coordinated photosensitizers are especially challenging to synthesis.

(3) Many metal-based sensitizers, also demonstrated substantial cytotoxicity when not exposed to light. (3) Because inorganic nanoparticle-based PSs are nonbiodegradable and have very short excitation wavelengths that have high energy and produce significant phototoxicity, they are difficult to use in biological applications.²³

5.1.1 Synthetic strategies for efficient photosensitizer design

5.1.1.1 Introducing heavy atoms.

Many different photosensitizers for PDT have been developed during the years. Johannes and colleagues have synthesized homoleptic iodinated bis(dipyrrinato) zinc(II) complexes with exceptionally extended excited-state lifetimes (the lifespan of metal complexes ranges from 207 to 559 ns). The ISC process is promoted by the iodine atoms (heavy atom), due to the spin-orbit coupling. Thus, when exposed to light at therapeutically significant longer wavelengths, the formed excited state of the complexes were found to interact with the molecular oxygen to produce $^1\text{O}_2$.²⁴ Additionally, as the energy of the excited states of thiocarbonyl compounds are lower than those of the carbonyl compounds, sulfur substitution of the oxygen within the fluorophore molecules causes a redshift of the absorption spectrum, allowing to use excitation wavelengths of deeper penetration.²⁵ Juan and coworkers have developed a general strategy for sulfur replacement of different molecules, *via* one-pot reaction. With this strategy, a set of thio-based PSs of different absorption spectra, able to generate efficiently singlet oxygen (Figure 6.2).²⁶

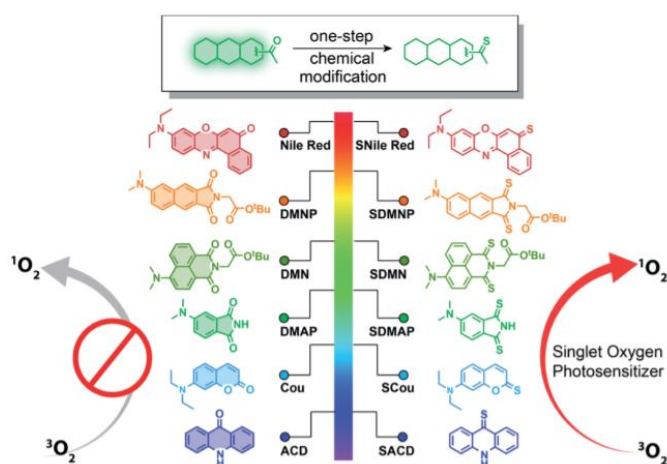


Figure 5.2: Design of thio-based PSs. Thiocarbonyl substitution at the carbonyl group of a variety of fluorophores can dramatically enhance their abilities to generate ROS. Illustrated are structures of the starting (left) and thio-based fluorophores (right) described in this study. Images extracted from reference. ²⁶

5.1.1.2 Energy transfer-based strategies

Donor-acceptor-donor (D–A–D) PSs having large conjugation system is a way to enhance fluorescence and $^1\text{O}_2$ generation. Apart from this, to enhance the visible/near-infrared absorbance, strategies such as Förster resonance energy transfer (FRET) or bond energy

transfer (TBET) have been considered another approach to develop PSs for high PDT efficiency fluorescent molecular arrays. For example, Zheng and coworkers designed an unquenched activatable PS based on the conjugation of porphyrin pyropheophorbide (pyro) as a FRET acceptor and 5-carboxy-X-rhodamine (Rox) as a FRET donor with a caspase-3-specific peptide sequence as a linker. This structure allowed to induce apoptosis through $^1\text{O}_2$ generation.²⁷

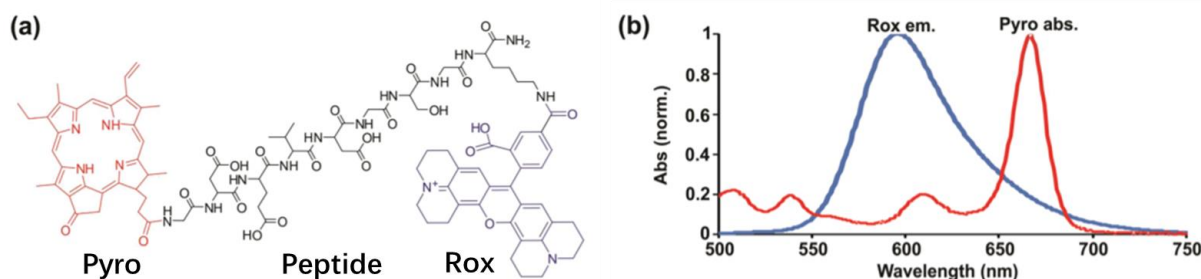


Figure 5.3: Structure of a QUaPS with Pyro shown in red and Rox shown in blue. (b) Normalized spectra of Rox donor emission and Pyro acceptor Q-band absorption. Images extracted from reference.²⁷

5.1.1.3 Activatable PSs

Many effective PSs have been obtained to date, based on several different molecules, though many of these lack selectivity towards particular tumor cells. Having PSs with high ROS generation efficiency and high selectivity towards cancer cells still represent a great challenge. Chen and coworkers achieved a phthalocyanine-based photosensitizer ($\text{ZnPc}(\text{TAP})_4$) that is non-toxic and has high anti-tumor action at pH 6.5 (under slightly acidic conditions) and low photocytotoxicity at pH 7.4. This photosensitizer enables tumor imaging-guided anticancer therapy (Figure 6.4a).²⁸ In other studies, Lo and coworkers designed a new pH-responsive fluorescence probe and photosensitizer based on the phthalocyanine units' self-quenching process (Figure 6.4b). Due to the sensitivity of the linker towards acidity, this dimer exhibits increased fluorescence emission and singlet oxygen production making it switchable for possible application.²⁹ Other types of activatable PSs, such as protein-activated PSs,³⁰⁻³¹ Photoactivated PSs,³²⁻³³ H_2O_2 -Activated PSs,³⁴⁻³⁵ are also novel designs for efficient photosensitizers.

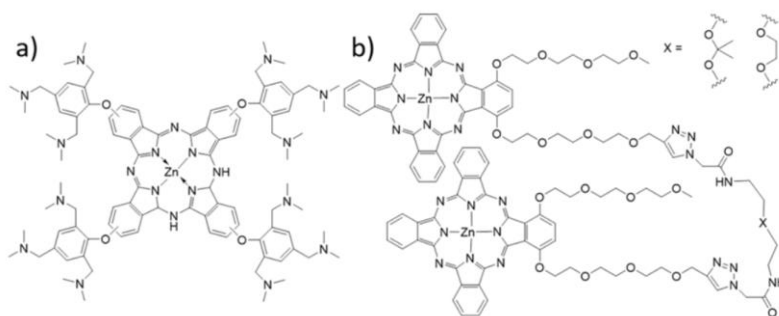


Figure 5.4: Chemical structures of (a) ZnPc(TAP)₄ and (b) pH-responsive probe.

5.1.2 Nanomaterials for PDT

Many first-generation PSs have already received clinical approval. However, most of these still present several disadvantages, such as hydrophobicity and shallow penetration depth, low uptake, and lack of selectivity. Thus, nanomaterials have been explored to obtain PDT. Over the past few years, different types of nanomaterials have been developed as carriers or PSs for PDT. These nanomaterials show enhanced properties that make them more effective for PDT than organic PSs.

5.1.2.1 Carbon-based nanomaterials for PDT

Carbon nanotubes (CNTs) absorb light and produce ¹O₂, which makes them competitive for the use of PDT. The versatile surface modifications of CNTs can turn them into outstanding PDT agents. Wang and coworkers reported a surface modified single wall carbon nanotubes (SWCNTs) with a conclusion that surface functionalization affected the photodynamic ability, showing different photodynamic efficiency *in vivo* and *in vitro* depending on the method of function (Figure 5.5).³⁶

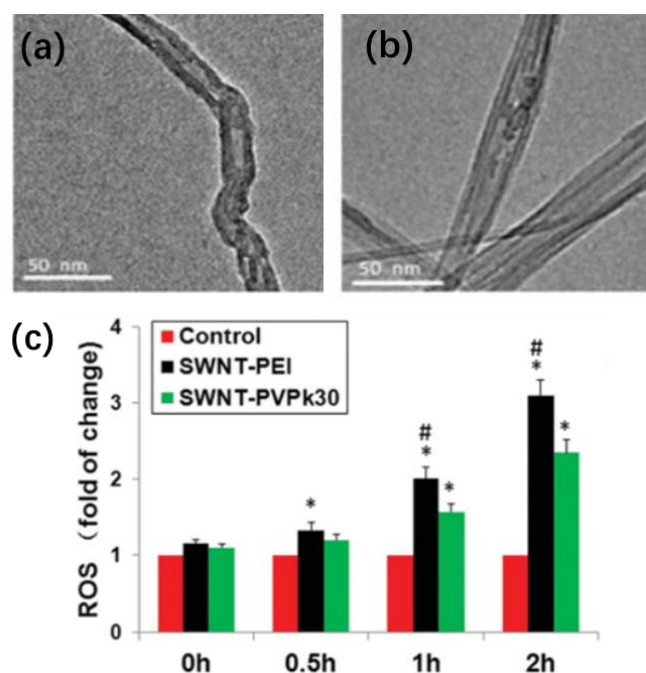


Figure 5.5: TEM pictures of (b) SWCNT functionalized with PEI and (e) SWCNT functionalized with PVPk30; (c) ROS generations are expressed as fold-change over control. Images extracted from reference. ³⁶

5.1.2.2 Gold-based nanomaterials for PDT

Gold-based nanomaterials possess promising a variety of promising characteristics, such as high surface areas, good photophysical property, good biocompatibility, ease of surface modification via goldthiol chemistry, and morphology tunability inducing absorption change.³⁷⁻³⁹ Thus, gold-based materials have been well-studied and become good alternatives for PDT. Chiang and coworkers presented a series of gold nanomaterials, such as nanocages (Au NCs), nanorods in shells (NR shell), and nanoparticles in shells (NP shell), which are ideal multi-functional theranostic nanomaterials. These materials can act as fluorescent cellular markers and impose synergic effects (photothermal and photodynamic therapy) on the destruction of tumors in mice when exposed to very low doses of NIR light leading anew discovery in the treatment of future cancer therapy.⁴⁰

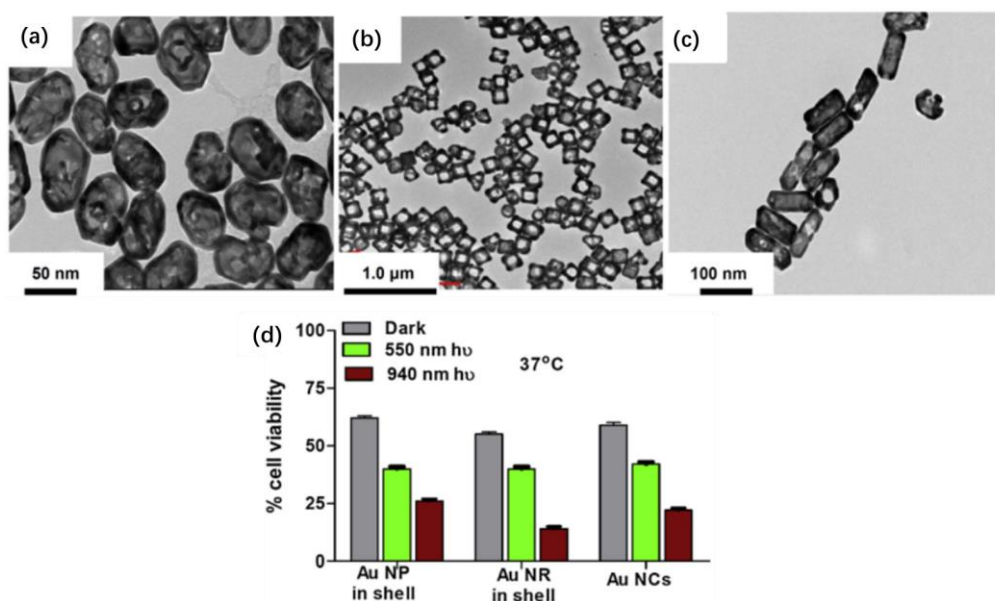


Figure 5.5: (a), (b) and (c) represent the transmission electron microscopic images of gold nanoparticle-in-shell, nanocages and nanorod-in-shell. (d) Cell viabilities of HeLa cells incubated with different lipid-coated gold nanoshells under dark and photoirradiation conditions at 37 C. Images extracted from reference.⁴⁰

5.1.2.3 MOFs-based nanomaterials for PDT

Nanoscale **MOFs** (NMOFs) have become a brilliant delivery platform for PDT due to versatile functionalities of materials, the well-defined crystalline structures, high porosity, and tunable framework stability. Li and coworkers presented NMOFs constructed by H₂DBP (5,15-di(p-benzoato)porphyrin) and Hf⁴⁺, which showed high PDT efficacy *in vivo* with half of the mice (subcutaneous xenograft murine models) with 50 times tumor volume reduction and half of the mice with complete tumor eradication, comparing to the mice treated with H₂DBP with no therapeutic effect.⁴¹

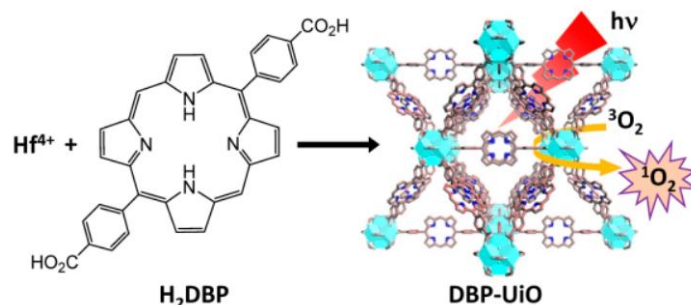


Figure 5.6: Synthesis of NMOF and the schematic description of singlet oxygen generation process. Image extracted from reference.⁴¹

5.2 Objectives

Polycyclic aromatic hydrocarbons such as anthracenes or rubrene are commonly used as $^1\text{O}_2$ trappers forming endoperoxide on its molecular π surface with the singlet oxygen. While the endoperoxide can be broken after heating to release singlet oxygen again, which can be utilized for PDT (Figure 5.7).⁴²⁻⁴⁴ However, most of the cases using anthracenes as $^1\text{O}_2$ carriers are molecular level⁴⁵ and host-guest structured.⁴⁶ A coordinated nanostructured singlet oxygen-trapping **MOFs** was reported, but due to the lack of internal thermal trigger, this material can not be used for biological application.⁴⁴

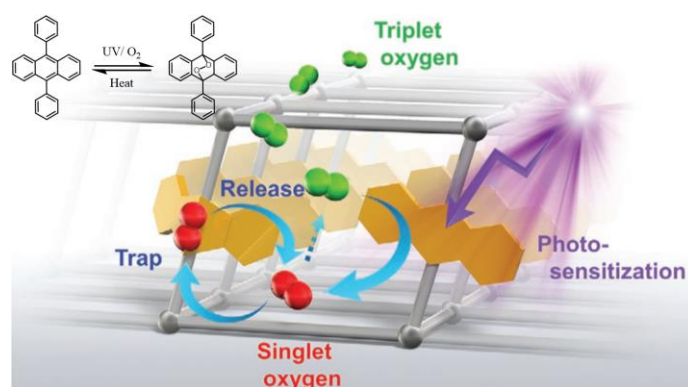


Figure 5.7: Schematic image to trap dissolved oxygen using a nanoconstructed with dpa, which has photosensitizing and trapping abilities with oxygen. Image extracted from reference.⁴⁴

The general aim of the work reported in this chapter is the preparation of the coordination polymer nanoparticles (**CPNs**) for photodynamic therapy, which are able to store molecular oxygen, and release it as singlet oxygen, at will, upon radiation.

To achieve nanoparticles with these properties the following specific objectives need to be fulfilled:

- The monomeric units of the **CPNs** is constituted by a chemically functionalized anthracene (**DPA-S-COOH**), synthesized in Chapter 4. ZrClO_2 is used
- The corresponding **DPA-S-CPNs** are expected to react with oxygen upon their irradiation with UV light, in air atmosphere. In this way the **DPA-S-CPNs** are able to chemically store a high amount of oxygen within the nanostructure, forming the corresponding endoperoxides for each anthracene monomer.
- Singlet oxygen must released from the endoperoxide upon heating.
- **DPA-S-CPNs** are then synthesized to incorporate photothermal agents (e.g. gold nanoshell) to induce the photothermal release of singlet oxygen (**DPA-S-**

COOH@Au). In this way, due to the high concentration of $^1\text{O}_2$ trapped in the nanoparticle, we expect the particles release sudden and high amount of $^1\text{O}_2$ upon visible or near infrared irradiation. (Figure 5.8).

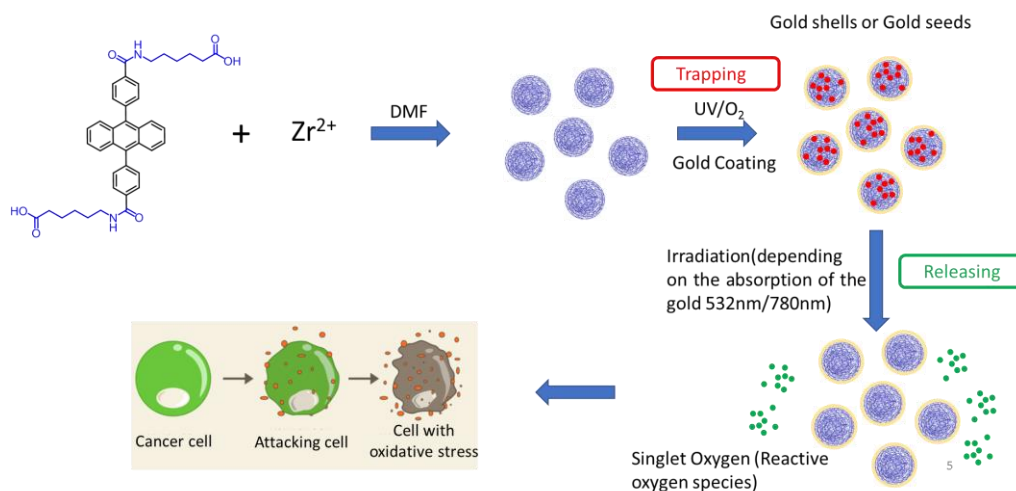


Figure 5.8: Schematic image of trapping and releasing process of gold-coated DPA-S-CPNs to induce cell apoptosis.

5.3 Result and discussion

5.3.1 DPA-S-COOH singlet oxygen trapping and releasing monitoring by NMR

Before the synthesis of **DPA-S-CPNs**, we firstly verified the molecule **DPA-S-COOH** singlet oxygen trapping ability. A few milligram of DPA-S-COOH was dissolved in deuterated DMF and its NMR spectra was recorded as time 0 min. Afterwards, the containing NMR tube was irradiated by 450 nm laser for 15h where the NMR spectra appeared three new picks marked with red dots and one pick at 7.5 ppm disappeared, which is a typical oxygen trapping spectra change based on the reported reference.⁴⁴ Later on, a recovery process was also monitored by heating the irradiated NMR tube at 100 degree for 10h revealed by NMR spectra. Although there were some impurities observed, the main peak at around 7.5 is recovered, indicating the a structure restore (Figure 5.9).⁴⁴

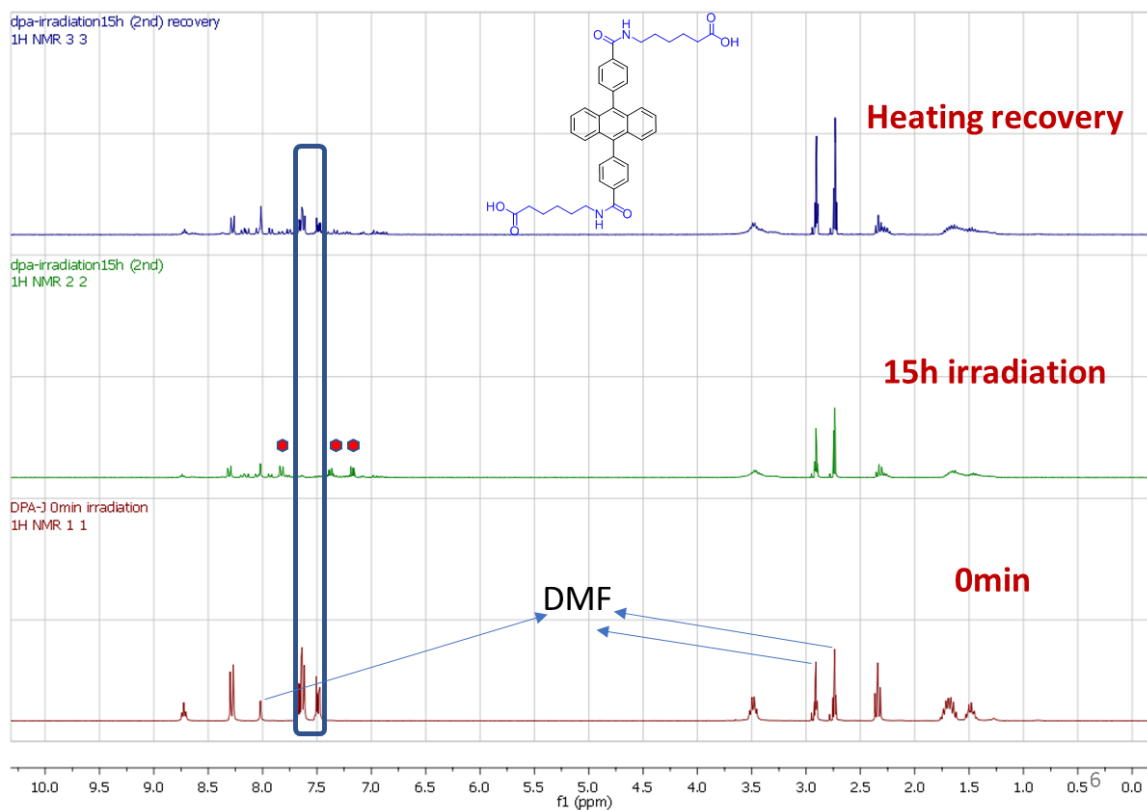


Figure 5.9: NMR spectrum monitoring of DPA-S-CPNs trapping and recovery process.

5.3.2 Absorption change of DPA-S-COOH upon light irradiation

Structural change of the conjugation system causes the absorption change because of the formation of endoperoxide, which revealed by the UV-vis measurements. The DMF solution of **DPA-S-COOH** was irradiated by 450 nm laser for 12h, and the absorption decreased significantly, which can be seen in Figure 5.10a,b. To enhance practical use and accelerate the singlet oxygen trapping process, solar simulator was used. The result turned out that 2h irradiation can dramatically reduce the absorption, which significantly speed up the process indicating an efficient oxygen trapping for easy manipulation (Figure 5.10).

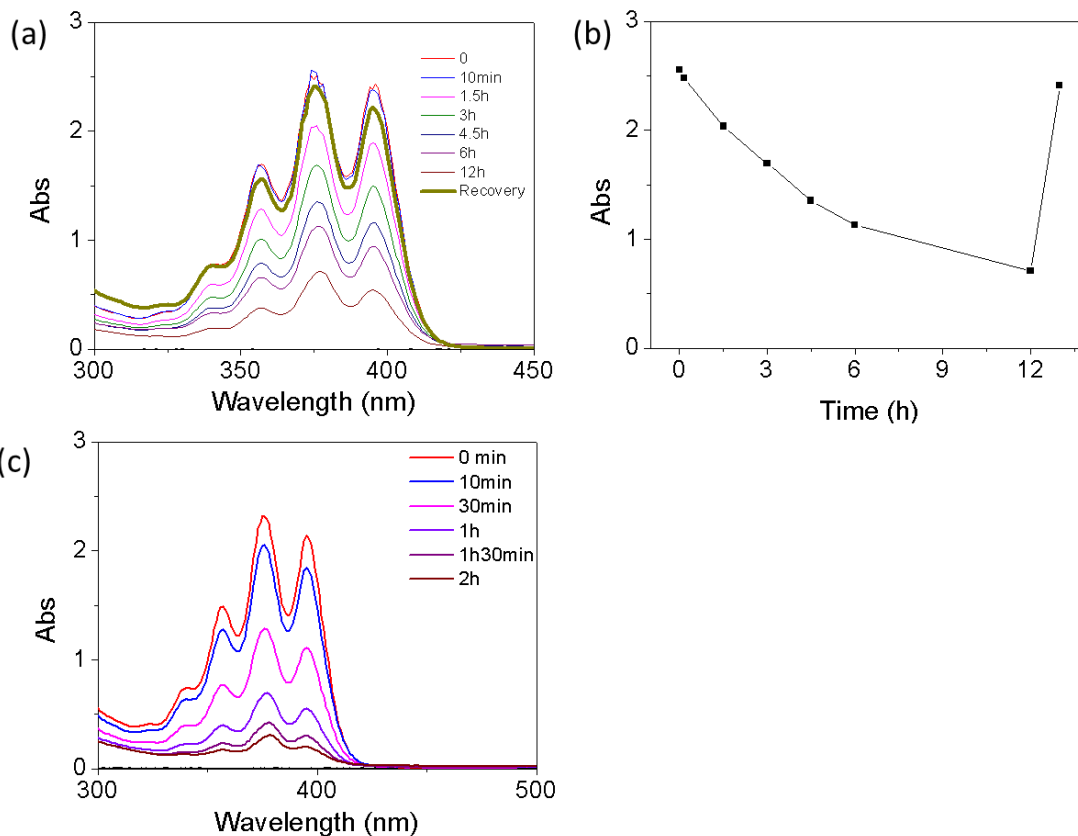


Figure 5.10: (a) UV-vis of DPA-S-COOH trapping and recovery process irradiated by 450 nm laser. (b) Plot of irradiation and recovery absorption change at 375 nm. (c) UV-vis of DPA-S-COOH trapping process irradiated by solar simulator.

5.3.3 Photothermal induced fluorescence enhancement in molecular level

Due to the formation change of aromatic rings, the fluorescence of **DPA-S-COOH** has been quenched. Thus, to verify the feasibility that if the heat generated by gold shells can trigger the cleavage of endoperoxide. An attempt was carried out:

DPA-S-COOH was firstly dissolved in DMF solution and irradiated by solar simulator recorded by fluorometer as time 0. Afterwards, gold nanoshells (0.15mg/mL) were added in DMF with following NIR excitation (780nm). In the first 30 min irradiation, the fluorescence was increased. However when the irradiation time prolonged to 1h, the fluorescence was decreased with gold shells aggregates observed (Figure 5.11). Although the fluorescence increase was stopped, a conclusion can be made that, upon 780 nm irradiation, the heat generated from gold is able to cut the endoperoxide and recover the aromatic structure with a fluorescence restore.

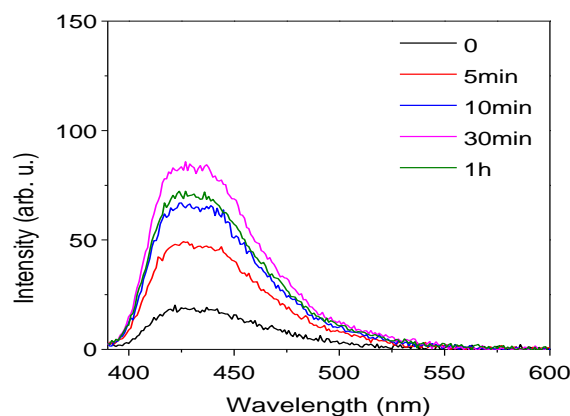


Figure 5.11: Fluorescence recovery of irradiated **DPA-S-COOH** and gold shells in DMF upon NIR irradiation (780nm)

5.3.4 Photothermal induced fluorescence enhancement investigation in nanoscale level

Given the preliminary molecular-level verification, we wanted to know if the fluorescence restore can take place in nanoscale level. The straightforward attempt is to simply mix **DPA-S-CPNs** with gold nanoshell. The absorption of the mixture suspension is showing two typical bands of 375 nm and 780 nm which corresponding to **DPA-S-CPNs** and gold nanoshells respectively (Figure 5.12a). To investigate the fluorescence change, the emission of **DPA-S-CPNs** was measured before and after solar simulator irradiation ($\lambda_{Exc} = 375$ nm, Figure 5.12b). From the spectra, it showed a emission decrease after oxygen trappment. At the same time, the small window (before and after) indicates poor fluorescence and limit of detection probably because of ACQ. Even though, 40 min irradiation ($\lambda_{Exc} = 780$ nm) was used to see emission change. Unfortunately, emission enhancement was not observed (Figure 5.12c)

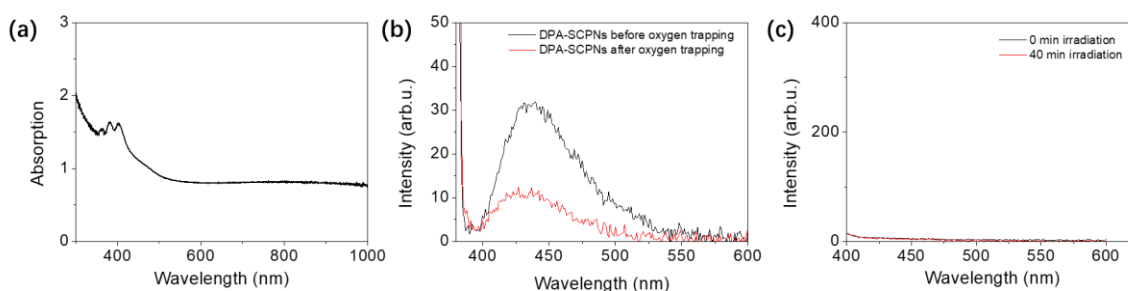


Figure 5.12: (a) Absorption of mixture of **DPA-S-COOH** and gold shells in waster. (b) Emission spectrum of **DPA-S-CPNs** before/after solar simulator irradiation. (c) Fluorescence change of mixture of **DPA-S-COOH** and gold shells in waster after 40min irradiation ($\lambda_{Exc} = 780$ nm)

For a further trying, we then used methods reported in the literature⁴⁷ to synthesize nanoshells in the presence of **DPA-S-CPNs** tryng to have nanoparticles encapsulated within the

hollow gold nanoshells. However, the absorption of resulting suspension shifted from anticipated 780 nm (absorption of gold nanoshells) to 555 nm (Figure 5.13a), which can be speculated that the solid gold was formed along with verification of transmission electron microscopy (TEM) indicating gold seeds forming (Figure 5.13b). Even though, a laser ($\lambda_{\text{Exc}} = 532 \text{ nm}$) was used for trying. Unfortunately, emission recovery has not been observed even with a higher concentration of gold seeds.

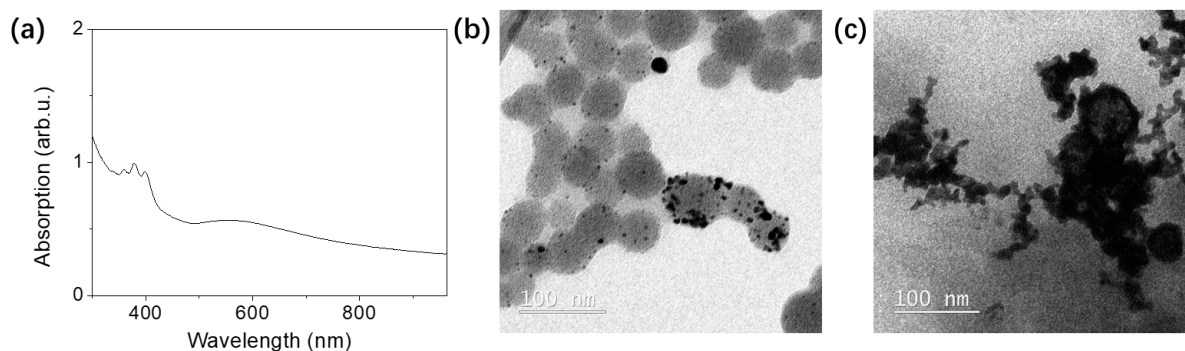


Figure 5.13: (a) Absorption of mixture of **DPA-S-COOH** and gold particles through *in situ* synthesis. (b,c) TEM images of the resulting **DPA-S-COOH@Au**

5.4 Future work

Given to the preliminary result, monitoring the emission of **DPA-S-COOH** to evaluate **DPA-S-CPNs** is not a good approach not only because of low efficiency of heat transfer but also the small detection window caused by ACQ. Therefore, a new method has to be used, for example The energy level of the singlet oxygen $^1\text{O}_2$ is 94.29 kJ/mol above the triplet ground state. The energy level corresponds to a transition at about 1270 nm in the near-infrared spectrum. Consequently, a direct phosphorescence measurement of the emission at 1270 nm is one way to find singlet oxygen.⁴⁸ In addition, the thermal trigger can be extend to organic small molecule-based photothermal agents that could be incorporated with the **DPA-S-CPNs**, which may induce the heat from inner part to the outside part of the particle realizing complete heat transfer. The possible candidates molecule can be chemical modified Bodipy or tannic acid.⁴⁹⁻

5.5 Reference

1. Robertson, C. A.; Evans, D. H.; Abrahamse, H., Photodynamic therapy (PDT): a short review on cellular mechanisms and cancer research applications for PDT. *Journal of Photochemistry and Photobiology B: Biology* **2009**, *96* (1), 1-8.
2. Braathen, L. R.; Szeimies, R.-M.; Basset-Seguín, N.; Bissonnette, R.; Foley, P.; Pariser, D.; Roelandts, R.; Wennberg, A.-M.; Morton, C. A., Guidelines on the use of photodynamic therapy for nonmelanoma skin cancer: an international consensus. *Journal of the American Academy of Dermatology* **2007**, *56* (1), 125-143.
3. Christensen, E.; Warloe, T.; Kroon, S.; Funk, J.; Helsing, P.; Soler, A.; Stang, H.; Vatne, Ø.; Mørk, C., Guidelines for practical use of MAL-PDT in non-melanoma skin cancer. *Journal of the European Academy of Dermatology and Venereology* **2010**, *24* (5), 505-512.
4. Berndt-Paetz, M.; Schulze, P.; Stenglein, P. C.; Weimann, A.; Wang, Q.; Horn, L.-C.; Riyad, Y. M.; Griebel, J.; Hermann, R.; Glasow, A., Reduction of Muscle-Invasive Tumors by Photodynamic Therapy with Tetrapyrrole-Tetratosylat in an Orthotopic Rat Bladder Cancer Model Effective Bladder Tumor Growth Control by PDT with THPTS. *Molecular Cancer Therapeutics* **2019**, *18* (4), 743-750.
5. Marcus, S. L., Clinical photodynamic therapy: the continuing evolution. In *Photodynamic therapy*, CRC Press: 2020; pp 219-268.
6. Dougherty, T. J.; Marcus, S. L., Photodynamic therapy. *European Journal of Cancer* **1992**, *28* (10), 1734-1742.
7. Wang, K.; Yu, B.; Pathak, J. L., An update in clinical utilization of photodynamic therapy for lung cancer. *Journal of Cancer* **2021**, *12* (4), 1154.
8. Yano, T.; Wang, K. K., Photodynamic therapy for gastrointestinal cancer. *Photochem. Photobiol.* **2020**, *96* (3), 517-523.
9. Wu, H.; Minamide, T.; Yano, T., Role of photodynamic therapy in the treatment of esophageal cancer. *Digestive Endoscopy* **2019**, *31* (5), 508-516.
10. Gao, Y.; Yu, T.; Zhang, Y.; Dang, G., Anti-VEGF monotherapy versus photodynamic therapy and anti-VEGF combination treatment for neovascular age-related macular degeneration: a meta-analysis. *Investigative Ophthalmology & Visual Science* **2018**, *59* (10), 4307-4317.
11. Su, Y.; Wu, J.; Gu, Y., Photodynamic therapy in combination with ranibizumab versus ranibizumab monotherapy for wet age-related macular degeneration: A systematic review and meta-analysis. *Photodiagnosis and photodynamic therapy* **2018**, *22*, 263-273.
12. Pham, T. C.; Nguyen, V.-N.; Choi, Y.; Lee, S.; Yoon, J., Recent Strategies to Develop Innovative Photosensitizers for Enhanced Photodynamic Therapy. *Chem. Rev.* **2021**, *121* (21), 13454-13619.
13. Del Governatore, M.; Hamblin, M. R.; Shea, C. R.; Rizvi, I.; Molpus, K. G.; Tanabe, K. K.; Hasan, T., Experimental photoimmunotherapy of hepatic metastases of colorectal cancer with a 17.1 A chlorin e6 immunoconjugate. *Cancer research* **2000**, *60* (15), 4200-4205.
14. Plekhova, N.; Shevchenko, O.; Korshunova, O.; Stepanyugina, A.; Tananaev, I.; Apanasevich, V., Development of Novel Tetrapyrrole Structure Photosensitizers for Cancer Photodynamic Therapy. *Bioengineering* **2022**, *9* (2), 82.
15. Zheng, B.-D.; Ye, J.; Zhang, X.-Q.; Zhang, N.; Xiao, M.-T., Recent advances in supramolecular activatable phthalocyanine-based photosensitizers for anti-cancer therapy. *Coord. Chem. Rev.* **2021**, *447*, 214155.
16. Nguyen, V.-N.; Ha, J.; Cho, M.; Li, H.; Swamy, K.; Yoon, J., Recent developments of BODIPY-based colorimetric and fluorescent probes for the detection of reactive oxygen/nitrogen species and cancer diagnosis. *Coord. Chem. Rev.* **2021**, *439*, 213936.
17. Wang, B.; Fan, J.; Wang, X.; Zhu, H.; Wang, J.; Mu, H.; Peng, X., A Nile blue based infrared fluorescent probe: imaging tumors that over-express cyclooxygenase-2. *Chem. Commun.* **2015**, *51* (4), 792-795.
18. Lozano-Torres, B.; Blandez, J. F.; Galiana, I.; García-Fernández, A.; Alfonso, M.; Marcos, M. D.; Orzáez, M.; Sancenón, F.; Martínez-Máñez, R., Real-Time In Vivo Detection of Cellular Senescence

through the Controlled Release of the NIR Fluorescent Dye Nile Blue. *Angew. Chem. Int. Ed.* **2020**, *59* (35), 15152-15156.

19. Wang, J.-H.; Wang, B.; Liu, Q.; Li, Q.; Huang, H.; Song, L.; Sun, T.-Y.; Wang, H.; Yu, X.-F.; Li, C., Bimodal optical diagnostics of oral cancer based on Rose Bengal conjugated gold nanorod platform. *Biomaterials* **2013**, *34* (17), 4274-4283.
20. Wang, B.; Wang, J.-H.; Liu, Q.; Huang, H.; Chen, M.; Li, K.; Li, C.; Yu, X.-F.; Chu, P. K., Rose-bengal-conjugated gold nanorods for in vivo photodynamic and photothermal oral cancer therapies. *Biomaterials* **2014**, *35* (6), 1954-1966.
21. Dong, X.; Zeng, Y.; Zhang, Z.; Fu, J.; You, L.; He, Y.; Hao, Y.; Gu, Z.; Yu, Z.; Qu, C., Hypericin-mediated photodynamic therapy for the treatment of cancer: A review. *J. Pharm. Pharmacol.* **2021**, *73* (4), 425-436.
22. Agostinis, P.; Vantieghem, A.; Merlevede, W.; de Witte, P. A., Hypericin in cancer treatment: more light on the way. *The international journal of biochemistry & cell biology* **2002**, *34* (3), 221-241.
23. Chen, J.; Fan, T.; Xie, Z.; Zeng, Q.; Xue, P.; Zheng, T.; Chen, Y.; Luo, X.; Zhang, H., Advances in nanomaterials for photodynamic therapy applications: Status and challenges. *Biomaterials* **2020**, *237*, 119827.
24. Karges, J.; Basu, U.; Blacque, O.; Chao, H.; Gasser, G., Polymeric Encapsulation of Novel Homoleptic Bis(dipyrinato) Zinc(II) Complexes with Long Lifetimes for Applications as Photodynamic Therapy Photosensitisers. *Angew. Chem. Int. Ed. Engl.* **2019**, *58* (40), 14334-14340.
25. Maciejewski, A.; Steer, R. P., The photophysics, physical photochemistry, and related spectroscopy of thiocarbonyls. *Chem. Rev.* **2002**, *93* (1), 67-98.
26. Tang, J.; Wang, L.; Loreda, A.; Cole, C.; Xiao, H., Single-atom replacement as a general approach towards visible-light/near-infrared heavy-atom-free photosensitizers for photodynamic therapy. *Chem Sci* **2020**, *11* (26), 6701-6708.
27. Lovell, J. F.; Chan, M. W.; Qi, Q.; Chen, J.; Zheng, G., Porphyrin FRET acceptors for apoptosis induction and monitoring. *J. Am. Chem. Soc.* **2011**, *133* (46), 18580-18582.
28. Yan, S.; Chen, J.; Cai, L.; Xu, P.; Zhang, Y.; Li, S.; Hu, P.; Chen, X.; Huang, M.; Chen, Z., Phthalocyanine-based photosensitizer with tumor-pH-responsive properties for cancer theranostics. *J Mater Chem B* **2018**, *6* (38), 6080-6088.
29. Ke, M. R.; Ng, D. K.; Lo, P. C., A pH-responsive fluorescent probe and photosensitizer based on a self-quenched phthalocyanine dimer. *Chem. Commun.* **2012**, *48* (72), 9065-7.
30. Li, X.; Kim, C. Y.; Lee, S.; Lee, D.; Chung, H. M.; Kim, G.; Heo, S. H.; Kim, C.; Hong, K. S.; Yoon, J., Nanostructured Phthalocyanine Assemblies with Protein-Driven Switchable Photoactivities for Biophotonic Imaging and Therapy. *J. Am. Chem. Soc.* **2017**, *139* (31), 10880-10886.
31. Li, X.; Yu, S.; Lee, Y.; Guo, T.; Kwon, N.; Lee, D.; Yeom, S. C.; Cho, Y.; Kim, G.; Huang, J. D.; Choi, S.; Nam, K. T.; Yoon, J., In Vivo Albumin Traps Photosensitizer Monomers from Self-Assembled Phthalocyanine Nanovesicles: A Facile and Switchable Theranostic Approach. *J. Am. Chem. Soc.* **2019**, *141* (3), 1366-1372.
32. Respondek, T.; Garner, R. N.; Herroon, M. K.; Podgorski, I.; Turro, C.; Kodanko, J. J., Light activation of a cysteine protease inhibitor: caging of a peptidomimetic nitrile with Ru(II)(bpy)₂. *J. Am. Chem. Soc.* **2011**, *133* (43), 17164-7.
33. Arora, K.; Herroon, M.; Al-Afyouni, M. H.; Toupin, N. P.; Rohrabough, T. N., Jr.; Loftus, L. M.; Podgorski, I.; Turro, C.; Kodanko, J. J., Catch and Release Photosensitizers: Combining Dual-Action Ruthenium Complexes with Protease Inactivation for Targeting Invasive Cancers. *J. Am. Chem. Soc.* **2018**, *140* (43), 14367-14380.
34. Xu, F.; Li, H.; Yao, Q.; Ge, H.; Fan, J.; Sun, W.; Wang, J.; Peng, X., Hypoxia-activated NIR photosensitizer anchoring in the mitochondria for photodynamic therapy. *Chem Sci* **2019**, *10* (45), 10586-10594.
35. Zeng, Q.; Zhang, R.; Zhang, T.; Xing, D., H₂O₂-responsive biodegradable nanomedicine for cancer-selective dual-modal imaging guided precise photodynamic therapy. *Biomaterials* **2019**, *207*, 39-48.

-
36. Wang, L.; Shi, J.; Liu, R.; Liu, Y.; Zhang, J.; Yu, X.; Gao, J.; Zhang, C.; Zhang, Z., Photodynamic effect of functionalized single-walled carbon nanotubes: a potential sensitizer for photodynamic therapy. *Nanoscale* **2014**, *6* (9), 4642-4651.
37. Ghosh, P.; Han, G.; De, M.; Kim, C. K.; Rotello, V. M., Gold nanoparticles in delivery applications. *Advanced Drug Delivery Reviews* **2008**, *60* (11), 1307-1315.
38. Jain, P. K.; Huang, X.; El-Sayed, I. H.; El-Sayed, M. A., Noble Metals on the Nanoscale: Optical and Photothermal Properties and Some Applications in Imaging, Sensing, Biology, and Medicine. *Acc. Chem. Res.* **2008**, *41* (12), 1578-1586.
39. Ackerson, C. J.; Jadzinsky, P. D.; Kornberg, R. D., Thiolate Ligands for Synthesis of Water-Soluble Gold Clusters. *J. Am. Chem. Soc.* **2005**, *127* (18), 6550-6551.
40. Vankayala, R.; Lin, C.-C.; Kalluru, P.; Chiang, C.-S.; Hwang, K. C., Gold nanoshells-mediated bimodal photodynamic and photothermal cancer treatment using ultra-low doses of near infra-red light. *Biomaterials* **2014**, *35* (21), 5527-5538.
41. Lu, K.; He, C.; Lin, W., Nanoscale Metal–Organic Framework for Highly Effective Photodynamic Therapy of Resistant Head and Neck Cancer. *J. Am. Chem. Soc.* **2014**, *136* (48), 16712-16715.
42. Asadirad, A. M.; Erno, Z.; Branda, N. R., Photothermal release of singlet oxygen from gold nanoparticles. *Chem. Commun.* **2013**, *49* (50), 5639-41.
43. Bresoli-Obach, R.; Nos, J.; Mora, M.; Sagrista, M. L.; Ruiz-Gonzalez, R.; Nonell, S., Anthracene-based fluorescent nanoprobe for singlet oxygen detection in biological media. *Methods* **2016**, *109*, 64-72.
44. Fujimura, M.; Kusaka, S.; Masuda, A.; Hori, A.; Hijikata, Y.; Pirillo, J.; Ma, Y.; Matsuda, R., Trapping and Releasing of Oxygen in Liquid by Metal-Organic Framework with Light and Heat. *Small* **2021**, *17* (22), e2004351.
45. Zhu, J.; Zou, J.; Zhang, J.; Sun, Y.; Dong, X.; Zhang, Q., An anthracene functionalized BODIPY derivative with singlet oxygen storage ability for photothermal and continuous photodynamic synergistic therapy. *J. Mater. Chem. B* **2019**, *7* (20), 3303-3309.
46. Zou, J.; Li, L.; Zhu, J.; Li, X.; Yang, Z.; Huang, W.; Chen, X., Singlet Oxygen "Afterglow" Therapy with NIR-II Fluorescent Molecules. *Adv. Mater.* **2021**, *33* (44), e2103627.
47. Guan, Y.; Xue, Z.; Liang, J.; Huang, Z.; Yang, W., One-pot synthesis of size-tunable hollow gold nanoshells via APTES-in-water suspension. *Colloids and Surfaces A: Physicochemical and Engineering Aspects* **2016**, *502*, 6-12.
48. Krajczewski, J.; Rucińska, K.; Townley, H. E.; Kudelski, A., Role of various nanoparticles in photodynamic therapy and detection methods of singlet oxygen. *Photodiagnosis and Photodynamic Therapy* **2019**, *26*, 162-178.
49. Ding, Z.; Gu, Y.; Zheng, C.; Gu, Y.; Yang, J.; Li, D.; Xu, Y.; Wang, P., Organic small molecule-based photothermal agents for cancer therapy: Design strategies from single-molecule optimization to synergistic enhancement. *Coord. Chem. Rev.* **2022**, *464*, 214564.
50. Liu, T.; Liu, W.; Zhang, M.; Yu, W.; Gao, F.; Li, C.; Wang, S.-B.; Feng, J.; Zhang, X.-Z., Ferrous-supply-regeneration nanoengineering for cancer-cell-specific ferroptosis in combination with imaging-guided photodynamic therapy. *Acs Nano* **2018**, *12* (12), 12181-12192.

Chapter 6

General Conclusions

In the present Thesis, the rational design of coordination polymer nanoparticles have been exploited for the development and study of functional materials for their potential application, such as biological and device application. For achieving this challenging objective, the complete characterisation in a wide range of methodologies and functional validation was performed. The results are summarized next:

1. For the first time, PACT coordination polymer particles (**RuBIS-CPNs**) have been developed. The DLS and UV-vis measurements demonstrated the nanoscale size, stability and photoactivity upon 532 nm irradiation.
2. For the first time photocleavage process was precisely quantified by using HPLC technique.
3. *In vitro* studies demonstrated that **RuBIS-CPNs** have an 11-fold increased uptake in comparison to related monomeric complexes thanks to the energy-dependent endocytosis uptake pathway triggered by the **CPNs** formulation.
4. This fact determined a substantial increase in phototoxicity index in comparison with monomeric species and a light-selective cytotoxic effect close to the gold standard cisplatin. Thus, **RuBIS-CPNs** demonstrates the potential of photoactivated **CPNs** for PACT anticancer treatments.
5. Two pairs of upconversion dyes have been designed, synthesized and characterized (**DPA-S-COOH**, **Pd-S-COOH**, **CAEBD-S-COOH**, and **Os-SCOOH**). In addition, with chemical functionalization, the upconversion between emitters and sensitizers still remains, which indicates the successful dyes synthesis for the upconversion.
6. We have demonstrated how the introduction of long alkyl chains within the emitter and sensitizer has allowed for the fabrication of nanoscaled amorphous coordination polymers with high dyes density and easy dyes-ratio tunability. This approach prevents dyes migration and phase segregation of the dyes in polymer material and allows the optimization of the dye interactions and the consequent energy transfer processes involved in the TTA-UC.
7. We proved the approach can be generalized to upconvert photons from/to different spectral regions and through distinct mechanisms (intersystem-crossing or direct singlet-to-triplet absorption). Given their chemical and colloidal stability in water, these **CPNs** could be considered the organic counterpart of the lanthanide-based inorganic nanomaterials, but with lower excitation intensity thresholds.
8. Last, but not least, their colloidal stability facilitated their application on different areas otherwise difficult to achieve: i) water-borne security inks for advanced anticounterfeiting technologies where printed messages could be decrypted upon UC

emission; ii) the fabrication of transparent films, in which the local high dyes density within the **CPNs** assures UC is preserved once they are embedded in polymer matrices even at low **CPNs** concentration. These films also showed concentrated emission in the edges, of interest for future luminescent solar concentrators.

9. Utilizing the oxygen trapping ability of anthracene upon light irradiation, we extend the possible application of **DPA-S-CPNs** to explore the singlet oxygen release for photodynamic therapy.

The versatility and simplicity of the approaches used for the formation of the water-dispersible CPs nanostructures presented in this Thesis, demonstrated the potential applications offered by the rational design allowing the development of functional materials. The results presented in this Thesis represent new examples for the formation of nanostructured materials and its application that could lead to the improvement of current systems.